A Dissertation approved by the department of Material Science
In fulfillment of the requirements for the degree of Doktor−Ingenieur (Dr.-Ing.)

Nanodomain Structure and Energetics of Carbon Rich SiCN and SiBCN Polymer-Derived Ceramics

M. Sc. Yan Gao
from Xinjiang, China
Matrikel-Nr. 1592533

TECHNISCHE
UNIVERSITÄT
DARMSTADT

Referee: Prof. Dr. Ralf Riedel
Co-referee: Prof. Dr. Wolfgang Ensinger

Fachbereich Material- und Geowissenschaften
Technische Universität Darmstadt

Date of submission: 09.10.2013
Date of oral examination: 27.11.2013

Darmstadt 2014
D17

Acknowledgments

The Ph.D. thesis represents the work performed at TU Darmstadt between April 2010 and June 2013.

I would like to give my sincere thanks to the people who have helped me during this Ph.D. work:

- Many thanks to Prof. Ralf Riedel, who gave me the chance to work in his group and on this interesting topic. Moreover, warm thanks for his supervision and mentorship during my research, for his help and support during my entire Ph.D. time, especially when I was sick, thanks for his great understanding.
- Warm thanks to Dr. Gabriela Mera for the suggestions to my work and many interesting discussions, and help with the Raman measurements.
- Lots of thanks to Dipl.-Ing. Hong Nguyen for her assistance with polymer synthesis, and for giving me help and care in both my work and my life.
- Thanks to Prof. Alexandra Navrotsky, Prof. Sabyasachi Sen, Dr. Tien Tran, Dr. Amir Hossein Tavakoli, Dr. Scarlett Widgeon, Dr. Emil Stoyanov for calorimetry and MAS NMR support, and for help during my visit at UC Davis.
- Thanks to Prof. Hans-Joachim Kleebe and M. Sc. Stefania Hapis, Dipl.-Ing. Mathis M. Müller for TEM measurements.
- Thanks to Dr. Yeping Xu for MAS NMR measurements.
- Thanks to Dipl.-Ing. Claudia Fasel for TG/MS measurements and a lot of technical help in daily lab work.
- Thanks to Dr. Koji Morita for TEM investigations.
- Thanks to Jean-Christophe Jaud and Dr. Joachim Brötz for the XRD measurements.
- Thanks to Dipl.-Ing. Mirko Reinold and Dr. Magdalena Graczyk-Zajac for eletrochemical study, M. Sc. Mahdi Seifollahi Bazarjani for SAXS measurements, Dipl.-Ing. Jiadong Zang for impedance spectroscopy measurements, Dr. Tinka Spehr for SAXS measurements, Prof. Weiyou Yang for TEM investigation, Prof. Sabyasachi Sen for checking SAXS interpretation, Dr. Magdalena Graczyk-Zajac, Prof. Linan An, Dr.-Ing. Holger Maune and Dr. Ming Li for the discussion on impedance spectroscopy, Dr. Benjamin Papendorf for helping with “Zusammenfassung”, M. Sc. Jia Yuan for helping with lab works, Su-Chen Chang for helps with documentation.
- Thanks to my officemates Dr. Magdalena Graczyk-Zajac, Dipl.-Ing. Jan Kaspar, Dipl.-Ing. Mirko Reinold who are companying me, helping me, comforting me and supporting me.
- Thanks to all the DF members who gave me such warm atmosphere and lots of helps. I cannot accomplish anything without you guys.
- Thanks to the Hiwis Shenshen He, Daniel Bick and Senan Jadeed.

I also greatly thank the DFG-NSF project for the financial support.

I give my special thanks to my family: my mother Hong Zhao, my sister Juan Gao, and my nephew Gaocheng Li. Thank you for being with me all the time no matter what I am and where I am. I would not be so happy without your support.

Table of contents

Abstract I

Zusammenfassung III

1. Introduction and motivation 1

2. Literature review 6

  2.1 Synthesis of Si-based preceramic polymers 6
  2.2 Processing of polymer-derived ceramic bulks 8
  2.3 Energetics of PDCs from calorimetry 9
  2.4 Nanodomain structure of Si(B)CN ceramics 11
  2.5 Impedance spectroscopy and its use in PDCs 13
  2.6 Electrochemistry of SiCN ceramics as anode material in lithium-ion batteries 15

3. Experimental 17

  3.1 Chemicals 17
  3.2 Synthesis of Si-based preceramic polymers 17
    3.2.1 Synthesis of polysilylcarbodiimides 19
    3.2.2 Synthesis of polyborosilylcarbodiimides 20
    3.2.3 Synthesis of polysilazanes 21
    3.2.4 Synthesis of polyborosilazanes 21
    3.2.5 Synthesis of polyphenylsilsesquicarbodiimides 22
    3.2.6 Synthesis of polyphenylsilsesquiazane 23
  3.3 Pyrolysis of polymers 23
  3.4 Bulk ceramic processing 24
  3.5 Annealing of ceramics 26
  3.6 Characterization techniques 26
  3.7 Characterization of ceramics prepared at selected temperatures 29

4. Results and discussion 33

  4.1 Polymer synthesis and processing 33
    4.1.1 Synthesis of poly(boro)silylcarbodiimides and bulk ceramic processing 33
    4.1.2 Synthesis of poly(boro)silazanes and bulk ceramic processing 35
    4.1.3 Polysilsesquicarbodiimide and $^{13}C/^{15}N$ isotope-enriched polysilsesquicarbodiimide 45
    4.1.4 Summary 51
  4.2 Effect of processing route 52
    4.2.1 Effect of processing route on the nanostructure — Low temperature thermal transformation 52
    4.2.2 Effect of processing route on the nanostructure — Thermal transformation up to 2100°C 62
    4.2.3 Summary 68
  4.3 Thermodynamic stability 69
    4.3.1 Structure and energetics of polysilylcarbodiimide-derived SiCN ceramics 69
    4.3.2 Structure and energetics of poly(boro)silazane-derived Si(B)CN ceramics 78
    4.3.3 Summary 82
  4.4 Solid state structure and microstructure of Si(B)CN ceramics 83
    4.4.1 Solid state structure of Si(B)CN ceramics 83
    4.4.2 Microstructure of Si(B)CN ceramics 96
    4.4.3 Summary 103
  4.5 Electrical / electrochemical properties 105
    4.5.1 Complex impedance spectra of selected polymer-derived ceramics 105
    4.5.2 Carbon-rich SiCN ceramics as anode material for lithium-ion batteries 113
    4.5.3 Summary 115

5. Conclusion 117

6. Outlook 120

References 121

Curriculum Vitae 128

- Personal status 128
- Scientific background 128
- Research experiences 128
- Working experience 129
- Activities 130
- Publications 130
- Awards & Honors 131

Eidesstattliche Erklärung 132

Abstract

This Ph.D. thesis focuses on the synthesis, processing, solid state structure, nanodomain structure, structural evolution, thermodynamic stability, and functional properties of carbon rich SiCN and SiBCN ceramics derived from preceramic polymers with tailored compositions and structures. The main objective of the studies is to better understand the effects of the composition and structure of the starting precursors, on the behavior of the resultant ceramics.

First, a set of preceramic polymers with systematically varied compositions and structures were synthesized. They are linear polysilylcarbodiimides and polysilazanes, and their boron modified counterparts; branched polysilsesquicarbodiimide and its $^{13}C/^{15}N$ isotope-enriched counterpart; and branched polysilsesquiazane. The synthesis of these polymers was investigated using NMR, FT-IR, Raman and TG/DTG. The results demonstrate that the obtained precursors exhibit the expected compositions and structures.

Then, the effects of processing route on the thermal stability of PDCs were studied by comparing bulk ceramics with their powder counterparts. The thermal transformation was investigated using FT-IR, Raman spectroscopy, XRD, TG/DTG and TEM. The results reveal that bulk ceramics are more thermally stable than their powder counterparts in terms of resistance to crystallization and decomposition. The Si(B)CN ceramic powders derived from poly(boro)phenylvinylsilylcarbodiimide contain α/β-SiC crystallites when heat treated at 1400ºC, while their bulk counterparts prepared at the same temperature remain completely amorphous. It is also found that bulk ceramics exhibit less weight loss than their powder analogues at temperatures up to 2100°C, especially in the case of SiCN bulk ceramics. The higher thermal stability of bulk ceramics as compared with the powder counterparts is likely due to the powders have greater surface area which enhances the carbothermal reaction and silicon carbide crystallization. In addition, the boron modification impedes the degradation of silicon nitride in both bulk and powder samples, similar to previously reported results.

Next, the energetics of PDCs was investigated using high temperature oxidative drop solution calorimetry on (i) ceramics derived from branched and linear polysilylcarbodiimide; (ii) ceramics derived from poly(boro)silazanes pyrolyzed at different temperatures. The results reveal that the ceramics derived from the branched polymer is energetically more stable than those from the linear polymer. Structural analysis using MAS NMR suggests that the increased energetic stability of the ceramics derived from the branched polymer is likely due to the presence of hydrogen at the mixed bonding environments consisting of N, C and Si atoms. These environments make up the interfacial region between the Si_3N_4 and "free" carbon nanodomains. For both the linear and branched polymers, the ceramics derived at 800 ºC are energetically more stable than those derived at 1100 ºC. The study of group (ii) reveals the effect of the pyrolysis temperature on the structural evolution and energetics of poly(boro)silazane-derived Si(B)CN ceramics. These ceramics contain mixed SiC_xN_{4-x}(x=0-4)

tetrahedra. MAS NMR spectroscopy of the 1100ºC and 1400ºC ceramics reveals that the structural evolution involves the following processes: (i) the demixing of SiC_xN_{4-x} mixed bonding environments, (ii) the cleavage of mixed bonds at the interdomain regions, and (iii) the coarsening of domains. Calorimetry results demonstrate that this structural evolution is favorable in both enthalpy and free energy.

We also investigated the solid state structures and nanodomain structures of the ceramics derived from the tailored polymers. The MAS NMR results indicate that the SiCN ceramics derived from polyphenylvinylsilylcarbodiimide and polymethylvinylsilylcarbodiimide both contain nanodomains of silicon nitride and “free” carbon. In the ceramics prepared from the phenyl-containing polymer, the “free” carbon and silicon nitride domains are basically isolated, while in the ceramics derived from the methyl-containing polymer, “free” carbon and silicon nitride domains are connected via C-N bonds. The SiBCN ceramics derived from boron-modified polysilylcarbodiimides have an additional B-containing phase which is located at the interface between the silicon nitride and the “free” carbon phase. On the other hand, the SiCN ceramics derived from polysilazanes contain “free” carbon and mixed bonded SiC_xN_{4-x}(x=0-4) nanodomains. The SiC_xN_{4-x} (x=0-4) domain consists of a core of SiN_4 tetrahedra, which connect to “free” carbon domain via SiN_3C, SiN_2C_2, $SiNC_3$, and SiC_4 tetrahedra. SiC_4 tetrahedra make up the most outer shell of mixed bonded SiC_xN_{4-x}(x=0-4) nanodomains. The SiBCN ceramics derived from boron-modified polysilazanes have an additional B-containing phase which connects the SiC_4 with the “free” carbon domains. SAXS results indicate that (i) the size of Si-containing nanodomains in SiCN ceramic is larger than in their SiBCN counterparts; (ii) the ceramics derived from phenyl-containing polymers exhibit smaller Si-containing nanodomains than those derived from methyl-containing polymers; and (iii) the size of Si-containing domains increases with pyrolysis temperature in all ceramics.

Finally, some functional behaviors of the resultant ceramics were investigated. The electrochemical properties of the ceramics were investigated to explore their applicability as anode materials for lithium-ion batteries. The results reveal that the SiCN ceramics derived from both linear and branched polymers are suitable anode materials for lithium-ion batteries. In particular, the SiCN ceramics derived from linear polyphenylvinylsilazane demonstrate outstanding performance in terms of cycling stability and capacity at high currents. In addition, the AC conductivity was characterized using impedance spectroscopy. It is found that the impedance spectra vary in accordance to the different microstructures of the ceramics, which, in turn, are related to the chemistry of the precursors. Conduction in SiCN ceramics is dominated via “free” carbon and SiC phases in series, as analyzed by two semicircles in the Nyquist plot. Conduction in SiBCN ceramics is dominated by one phase, and is thus represented by one semicircle in the Nyquist plot. Nonconducting BN forms the interfacial phase between the “free” carbon and SiC phases, and isolates the discontinuous phase from the continuous phase. Therefore, conduction in SiBCN ceramics is dominated by the continuous phase, whether it is “free carbon” or SiC.

Zusammenfassung

Die vorliegende Dissertation thematisiert die Synthese, Herstellung, Mikro- und Nanostruktur, strukturelle Entwicklung, thermodynamische Stabilität und funktionellen Eigenschaften von kohlenstoffreichen SiCN und SiBCN Keramiken, die von präkeramischen Polymeren mit maßgeschneiderter Zusammensetzung und räumlicher Struktur abgeleitet worden sind. Das Hauptanliegen der Arbeit ist es, zu ermitteln, inwieweit die Zusammensetzung und Struktur der polymeren Vorstufen die Eigenschaften der finalen Keramik beeinflussen.

Zu Beginn wurde eine Reihe von präkeramischen Polymeren mit systematisch variierten Zusammensetzungen und Strukturen synthetisiert. Dazu gehören lineare Polysilylcarbodiimide und Polysilazane sowie deren bormodifizierte Äquivalente, verzweigte Polysilsesquicarbodiimide und deren $^{13}C/^{15}N$ isotopenangereichertes Pendant als auch verzweigte Polysilsesquiazane. Die synthetisierten Polymere wurden unter Verwendung von NMR, FT-IR, Raman und TG/DTG charakterisiert.

Anschließend wurde der Einfluss des Herstellungsverfahrens auf die thermische Stabilität der polymerabgeleiteten Keramiken untersucht, indem die weitere Aufarbeitung des Materials entweder als Bulkmaterial oder als Pulver erfolgte. Die thermische Umwandlung wurde mit Hilfe von FT-IR- und Raman-Spektroskopie, XRD, STA und TEM untersucht. Die Ergebnisse zeigen, dass die Keramiken als Bulkmaterial thermisch stabiler sind als in Form von Pulvern in Bezug auf Kristallisationsbeständigkeit und Zersetzung. Die von Poly(boro)phenylvinylsilylcarbodiimid abgeleiteten keramischen Si(B)CN Pulver enthalten nach thermischer Auslagerung bei 1400 °C α/β-SiC Kristallite, während das Bulkmaterial nach Auslagerung unter denselben Bedingungen vollständig amorph bleibt. Zusätzlich wurde festgestellt, dass die Keramiken als Bulkmaterial nach der Auslagerung bei 2100 °C einen geringeren Massenverlust als die Pulverkeramiken aufweisen, insbesondere für den Fall einer SiCN basierten Matrix. Die höhere thermische Stabilität der Bulkkeramiken im Vergleich zu den Pulverkeramiken ist sehr wahrscheinlich auf die größere Oberfläche der Pulver zurückzuführen, welche die carbothermische Reaktion und Kristallisation von Siliciumcarbid begünstigen. Die Modifikation mit Bor verhindert außerdem die Zersetzung des Siliciumnitrids sowohl im Pulver- als auch im Bulkmaterial, ähnlich wie es bereits in früheren Publikationen berichtet wurde.

Außerdem erfolgte die thermodynamische Charakterisierung der polymerabgeleiteten Keramiken mittels oxidativer Hochtemperatur-Tropfenlösungskalorimetrie von (i) Keramiken abgeleitet von verzweigten und linearen Polysilylcarbodiimiden und (ii) Keramiken abgeleitet von Poly(boro)silazanen, pyrolysiert bei verschiedenen Temperaturen. Die Ergebnisse zeigen, dass die von verzweigten Polymeren abgeleiteten Keramiken energetisch stabiler sind als diejenigen, die auf linearen Polymeren basieren. Strukturanalysen mittels MAS-NMR lassen vermuten, dass die größere energetische Stabilität der von verzweigten Polymeren

abgeleiteten Keramiken sehr wahrscheinlich auf die Präsenz von Wasserstoff und von gemischten Bindungen – bestehend aus N, C und Si – zurückzuführen ist. Die gemischten Bindungen bilden die Grenzfläche zwischen Si_3N_4 und „freien“ Kohlenstoff Nanodomänen. Unabhängig davon, ob von linearen oder verzweigten Polymeren ausgegangen wird, sind die Keramiken nach der Pyrolyse bei 800 °C energetisch stabiler als nach 1100 °C. Der Effekt der Pyrolysetemperatur auf die strukturelle Entwicklung und Energetik der von Poly(boro)-silazanen abgeleiteten Si(B)CN Keramiken wurde ebenfalls untersucht. Die Matrix dieser Keramiken besteht aus gemischten SiC_xN_{4-x} (x=0-4) Tetraedern. MAS-NMR Spektroskopie von Keramiken, die bei 1100 °C und 1400 °C pyrolysiert worden sind, zeigt, dass die strukturelle Entwicklung wie folgt abläuft: (i) eine Phasenseparation gemischter SiC_xN_{4-x} Bindungen, (ii) die Spaltung gemischter Bindungen an den Domänengrenzen und (iii) ein Domänenwachstum. Kalorimetrische Messungen belegen die Favorisierung dieser strukturellen Entwicklung in Bezug auf die Enthalpie und freie Energie.

Die Mikro- und Nanodomänenstruktur der polymerabgeleiteten Keramiken wurde ebenso untersucht. Die MAS-NMR Messungen belegen, dass die von Polyphyenylvinylsilylcarbodiimid und Polymethylvinylsilylcarbodiimid abgeleiteten SiCN Keramiken in beiden Fällen Nanodomänen enthalten, welche aus Siliciumnitrid und „freiem“ Kohlenstoff bestehen. Werden die Keramiken aus phenylhaltigen Polymeren hergestellt, sind die Domänen aus „freiem“ Kohlenstoff und Siliciumnitrid grundsätzlich isoliert, wohingegen diese via C-N Bindungen miteinander verbunden sind, sofern von methylhaltigen Polymeren ausgegangen wird. Die aus bormodifizierten Polysilylcarbodiimiden abgeleiteten Keramiken enthalten zusätzlich eine borhaltige Phase, die an der Grenzfläche zwischen Siliciumnitrid und „freiem“ Kohlenstoff lokalisiert sein kann. Andererseits enthalten die von Polysilazanen abgeleiteten SiCN Keramiken Nanodomänen von „freiem“ Kohlenstoff und von gemischten SiC_xN_{4-x} (x=0-4) Bindungen. Die SiC_xN_{4-x} (x=0-4) Domänen bestehen aus einem Kern von SiN_4 Tetraedern, die mit dem „freien“ Kohlenstoff über SiN_3C, SiN_2C_2, $SiNC_3$, und SiC_4 Tetraeder miteinander verknüpft sind. Die äußere Schicht der SiC_xN_{4-x} (x=0-4) Nanodomänen bildet größtenteils SiC_4 Tetraeder aus. Die von bormodifizierten Polysilazanen abgeleiteten SiBCN Keramiken besitzen zusätzlich eine borhaltige Phase, welche die SiC_4 und „freien“ Kohlenstoffdomänen miteinander verbindet. SAXS Messungen belegen, dass (i) die Größe der Si-haltigen Nanodomänen in SiCN Keramiken größer als in SiBCN Keramiken ist, (ii) die von phenylhaltigen Polymeren abgeleiteten Keramiken kleinere Si-haltige Nanodomänen aufweisen als die von methylhaltigen Polymeren abgeleiteten Keramiken und (iii) in allen Keramiken die Größe der Si-haltigen Domänen mit Erhöhung der Pyrolysetemperatur zunimmt.

Zuletzt wurde das Funktionsverhalten der resultierenden Keramiken untersucht. Die elektrochemischen Eigenschaften der Keramiken wurden untersucht, um die Anwendbarkeit als Anodenmaterial in Lithium-Ionen Batterien zu evaluieren. Die Ergebnisse zeigen, dass die von linearen und vernetzten Polymeren abgeleiteten SiCN Keramiken als Anodenmaterial für Lithium-Ionen Batterien geeignet sind. Insbesondere zeigen die von linearen

Polyphenylvinylsilazanen abgeleiteten SiCN Keramiken eine hervorragende Leistung in Bezug auf Zyklenbeständigkeit und Kapazität bei hohen Stromstärken. Zusätzlich wurde die Wechselstrom-Leitfähigkeit mittels Impedanzspektroskopie untersucht. Es wird festgestellt, dass sich die Impedanzspektren in Übereinstimmung mit den verschiedenen Mikrostrukturen der Keramiken verändern, die wiederum von der Chemie der polymeren Vorstufen abhängig sind. Die Leitfähigkeit in SiCN Keramiken wird von „freiem“ Kohlenstoff und SiC Phasen bestimmt, wie im Nyquist-Diagramm durch das Auftreten zweier Halbkreise belegt wird. Hingegen wird die Leitfähigkeit in SiBCN Keramiken durch eine einzelne Phase bestimmt, da die Signalantwort im Nyquist-Diagramm einen einfachen Halbkreis beschreibt. Nichtleitendes BN bildet die Grenzfläche zwischen dem „freien“ Kohlenstoff und den SiC Phasen und isoliert die diskontinuierliche Phase von der kontinuierlichen. Daher wird die Leitfähigkeit in SiBCN Keramiken allein von einer kontinuierlichen Phase bestimmt, unabhängig davon ob es sich um „freien“ Kohlenstoff oder SiC handelt.

1. Introduction and motivation

Studies of polymer-derived ceramics (PDCs) have been undertaken for decades and have achieved substantial progress in understanding and utilization this unique class of amorphous ceramics. PDCs possess a set of outstanding properties, e.g. high strength, high creep resistance, excellent oxidation and corrosion resistance, and outstanding stability against crystallization and decomposition. Therefore, they are promising materials for widespread applications, including high strength fibers, coatings, ignition plugs, MEMS devices, as well as anode materials for lithium-ion batteries [1]. These outstanding properties are attributed to a unique microstructure of the PDCs, which can only be obtained by thermolyzing polymeric precursors at moderate temperatures, and cannot be prepared from ceramic powders using conventional ceramic sintering routes or traditional physical/chemical deposition processes.

Deeper investigations of PDCs reveal that the X-ray amorphous materials actually contain various nanodomain structures. The constitution of the nanodomain structures strongly depends on the material system, the characteristics of the precursors, and the processing conditions [2–4]. The nanoscale heterogeneity and the characteristics of the nanodomains have attracted extensive attention because they greatly influence the structure and properties of the ceramics at a larger/macroscopic scale.

Among all PDCs, SiCN and SiBCN are well known for their outstanding thermal stability against crystallization and decomposition up to extremely high temperatures. A variety of polymers, including typical polysilazanes and polysilylcarbodiimides were developed and used in preparing SiCN ceramics. These polymers were then modified with boron through, for example, hydroboration reactions to produce SiBCN ceramics. The microstructure of low-carbon SiCN synthesized from polysilylcarbodiimides is characterized by the presence of two amorphous phases, namely amorphous Si_3N_4 and amorphous carbon. On the other hand, carbon-rich SiCN prepared from polysilylcarbodiimides are composed of three amorphous phases, Si_3N_4, SiC and carbon [2,5]. It is found that introducing of excess amounts of carbon leads to higher thermal stability in SiCN PDCs [5,6]. In SiBCN PDCs, boron is present as a BCN phase coexisting with the Si_3N_4, SiC and carbon phases. Studies on SiBCN ceramics showed that the decomposition temperature of SiBCN is even higher. Some claimed that the improved stability is due to the increased nitrogen partial pressure in the vicinity of Si_3N_4 [7,8], while others believe that it is due to the decrease of carbon activity because of the dissolution of carbon in BNC layers [7,9]. In both scenarios the equilibrium temperature of the carbothermal reaction is increased, thus Si_3N_4 is stable at higher temperatures.

Recently the use of calorimetry makes it possible to obtain thermochemical data for PDC materials. It is found that relative to a mixture of crystalline components with the same composition, the ternary amorphous polymer-derived ceramics have exothermic heats of formation. This phenomenon was found over a large range of compositions in the SiOC, SiCN, SiCNO and SiBCN systems [10–13], suggesting that the amorphous PDCs are thermodynamically stable compared to their crystalline counterparts. Such stability is attributed to the unique structure of the PDCs, particularly the nature of their nanodomains and interfaces. Studies of certain SiOC PDCs revealed that mixed bonds in the interdomain regions were the source of the negative enthalpy, perhaps because they experience far less strain in an amorphous structure than in a crystalline one [14]. Further studies found that hydrogen release and phase separation could also stabilize the structure [12]. The lack of mixed bonds reduced the thermodynamic stability in some polysilylcarbodiimide-derived carbon-rich SiCN ceramics [10]. Moreover, regarding SiBCN which shows extraordinary resistance to decomposition with the presence of boron, calorimetry data show that thermodynamic stability diminishes with an increase in boron content [13].

PDCs are fascinating also because the compositions of the ceramics can be tailored by changing the structure and chemistry of the precursors. Carbon and boron contents have been the primary focus in studying these ternary and quaternary materials. High amounts of excess carbon inhibit the crystallization of Si_3N_4 in SiCN ceramics, leading to greater resistance to thermolysis than in ceramics containing lower carbon amounts [5]. Boron increases the stability of SiBCN PDCs against decomposition [13,15,16]. When the two factors exist concomitantly, a high “free” carbon concentration and boron-modification is assumed to improve the thermal stability of the SiBCN materials [17–19].

To better understand and use SiCN and SiBCN PDCs, it is important to verify how the unique nanodomain structures influence the energetics of these PDCs, and to understand the effect of carbon, boron, etc. on the performance of PDCs.

In this Ph.D. work, two classes of polymers, namely polysilazanes and polysilylcarbodiimides, as well as their boron-modified counterparts, were designed and synthesized. In addition, carbon contents were modified by replacing methyl groups attached to Si atoms with phenyl groups, assuming that the phenyl groups will produce more carbon than the methyl groups. In this way, the precursors were obtained with systematically varied molecular architecture, carbon content, and boron modification. The resultant amorphous SiCN and SiBCN ceramics consisted of Si_3N_4-SiC-C and Si_3N_4-SiC-C-BN phase system, respectively, in terms of stoichiometric components.

Both bulk and powder ceramics were prepared from these precursors. First, bulk ceramics were prepared from the aforementioned precursors. While PDC route is promising to produce bulk ceramics by plastic techniques [1,20], the main challenge is the evolution of gas during pyrolysis and the accompanied shrinkage, deformation, pore formation and cracking. There are various methods for forming bulk ceramics [21–32], and warm-pressing is one of the most commonly used and effective routes. For the successful usage of this technique, processing parameters, e.g. pressing pressure, heating temperature, and holding time must be optimized in accordance with the features of each precursor. In a typical warm-pressing, concomitant polymer crosslinking is required for obtaining the greenbody shape. Extra pre-crosslinking is needed for liquid (honey-like) polymers i.e. polysilylcarbodiimides and polysilazanes. The parameters for this essential step must be optimized in order to not only produce solidified pre-crosslinked polymer for the subsequent warm-pressing, but also to preserve certain reactivity in the warm-pressing procedure. For the polyborosilazanes synthesized in this work, bulk samples cannot be prepared directly by warm-presssing due to their thermoplastic behavior. Therefore, the self-filler route was introduced. The preparation of the self-filler and the ratio between the original polymer and the fillers are also required to be optimized.

PDC powders were also prepared in this work. Obviously, bulk ceramics have much lower surface area than their powder counterparts. Previous studies on the effect of particle size found that for SiBCN ceramics, increasing surface areas enhanced the carbothermal reaction, thus reduced the crystallization temperature of the materials [33,34]. It was found that poly(boro)phenylvinylsilylcarbodiimide-derived carbon-rich SiCN and SiBCN bulk ceramics exhibited considerably different microsctures as compared to the powder samples. The final microstructure, crystallinity, and resistance to thermal decomposition are strongly influenced by the precursor chemistry, the processing route, the thermolysis temperature, the presence of boron, and the “free” carbon content of these materials. Therefore, the properties of PDCs and their potential applications depend, to a great extent, on the chemistry of the precursors and their processing history.

Thermodynamic stability is the physiochemical reason for the formation of certain structures. Two groups of samples were selected for calorimetry measurement, namely i) branched polysilsesquicarbodiimide- and linear polysilylcarbodiimide-derived SiCN ceramics pyrolyzed at 800ºC and 1100ºC, and ii) polysilazane-derived SiCN and polyborosilazane-derived SiBCN ceramics pyrolyzed at 1100ºC and 1400ºC. The first group was studied to clarify the effect of polymer structure, i.e. branched versus linear, on the energetics of the derived ceramics. The second group was selected to understand the energetic of the microstructural evolution as a response to heat treatment, as well as the role of boron in this respect. With the help of MAS NMR spectrocopy, the structures of these ceramic samples were comprehensively evaluated. The compositions of the nanodomains as well as the interdomain regions were probed in order to better interpret differences in the energetic stability of the materials.

Since different precursors result in very different nanodomain structures, the overarching aim of this work is to develop structural models for ceramics derived from tailored polymers. Therefore, characterizing the structures becomes very important. In this work, many powerful techniques were utilized to characterize the structures of the resultant ceramics at different length scales, including MAS NMR, XRD, Raman, TEM, and SAXS. The integration of all of these methods enables a deep understanding of the nanodomain structure in terms of domain type, domain size, chemical bonding at domain interfaces, etc.

The ceramic structures show strong dependance on their precursors. Considering their varied molecular architectures, carbon content, and boron presence, different polymers result in ceramics with unique features. This phenomenon can be explained by the nature of the starting polymers, as well as the polymer to ceramic transformation.

With a comprehensive understanding of the nanodomain structures in these ceramics, the electrical properties were finally characterized by impedance spectroscopy (IS). IS is a very sensitive electrochemical technique which allows the simple treatment of carrier transport processes and reactions in complex situations, such as in intrinsically disordered material components [35]. The greatest benefit of using IS to study the conduction behavior of PDCs is the possibility to distinguish the effects of different phases. For this reason, it is also a commonly used technique for measuring the electrical properties of multiphase ceramics. There have been a few reports using impedance spectroscopy [36,37] to study the AC conductivity (σ_{ac}) and the mechanisms of relaxation in PDCs. However, these studies did not emphasize the importance of the nanodomain structure. To date, no report has yet distinguished the σ_{ac} contribution from individual types of nanodomains in the structure of PDCs. Based on the results from IS, the contribution of the different phases on the electrochemical behavior of PDCs is interpreted and discussed.

PDCs are also promising as anode materials for lithium-ion batteries. Their capacities exceed that of graphite, and they also exhibit stable cycling behavior. Ahn et al. [38] claimed that it is necessary for the nitrogen to oxygen (N/O) ratio to be below 1 to achieve high capacities of ca. 600 mA h g^{-1}. In this work, four SiC(O)N ceramics with a N/O ratio of 6 to 9.5 show outstanding electrochemical properties. These four ceramics were derived from polymers with different molecular structures and degrees of branching, namely linear and branched polysilylcarbodiimides and polysilazanes. The focus of this study is the relationship between the molecular structure of the precursor on the microstructure of the derived ceramics, and thus on the electrochemical properties of the materials.

In summary, this Ph.D. work demonstrates that the structures of polymer-derived ceramics can be widely varied by tailoring the precursors in terms of molecular architecture, boron modification, and carbon contents. It also demonstrates that the behavior of the obtained materials can be strongly affected by processing route (i.e., for powder vs. bulk). It was found that polymer-derived ceramics are thermodynamically more stable than their crystalline constituting phases. The origin of the thermal stability was attributed to the nanodomain structure of the amorphous PDCs. Models of the nanodomain structures were constructed for all systems, taking into account nanodomain types, nanodomain size and bonding environment at the interdomain regions. The effect of this unique nanodomain structure on the electrical properties of PDCs was studied, and impedance spectroscopy was employed to distinguish the contribution of different phases to the electrical behavior. The electrochemical study demonstrates that certain SiCN ceramics with a N/O ratio of about 6-

9.5 show outstanding behavior in light of their potential application as lithium-ion batteries anodes.

2. Literature review

Polymer-derived ternary SiCN and quaternary SiBCN ceramics are refractory materials exhibiting a great resistance to crystallization and decomposition at high temperatures [1,39,40]. Unlike conventional polycrystalline ceramics made by sintering of corresponding powders, polymer-derived ceramics possess a unique structure that contains a Si-based amorphous phase, and in some cases, a highly-disordered "free" carbon phase. While PDCs are X-ray amorphous, they are nanoscopically heterogeneous, containing intrinsically complex nanodomains, which can be varied in a large range by tailoring the precursor chemistry and processing conditions. The properties of PDCs also strongly depend on precursor chemistry and processing conditions [1,20,40,41]. For example, compared to low carbon SiCN systems, previous studies showed that carbon-rich SiCN ceramics have much higher stability against crystallization and remain amorphous up to higher temperatures [2,5,10]. This phenomenon was attributed to the finely dispersed "free" carbon phase which acts as a diffusion barrier in the structure. The presence of "free" carbon and boron dramatically influences the properties of the ceramics with respect to their microstructure. Carbon-rich polymer-derived SiBCNs are defined as complex nanostructured systems which have remarkably high thermal, chemical, and mechanical stability (i.e., creep resistance) even at temperatures up to 2000-2200 °C in inert atmospheres [17,42].

The best-known precursors for silicon carbonitride (SiCN) ceramics are polysilazanes $-[R^1R^2Si\text{-}NR^3]_n-$ and polysilylcarbodiimides $-[R^1R^2Si\text{-}N{=}C{=}N]_n-$, where R^1, R^2 and R^3 are organic groups such as methyl, phenyl, etc. As demonstrated by solid-state NMR studies [1,20,40], ceramics derived from polysilazanes contain mixed bonding environments about the Si atoms forming SiC_xN_{4-x} ($x = 0\text{-}4$) tetrahedra. Meanwhile, the ceramics derived from polysilylcarbodiimides contain two amorphous phases, namely, amorphous Si_3N_4 (a-Si_3N_4) and amorphous carbon (a-C). The pyrolysis of highly carbon-rich polysilylcarbodiimides produces a microstructure composed of three amorphous phases— a-Si_3N_4, a-SiC and a-C [2,5].

Polymer chemistry and processing routes play important roles on the nanodomain structure, thereby, the performance of SiCN and SiBCN ceramics. Here, SiCN and SiBCN PDCs were studied based on previous findings. This chapter addresses previous accomplishments in polymer synthesis, bulk processing, energetic stability, nanodomain structure, and the electrochemical study of SiCN and SiBCN PDCs. This review offers a general understanding of the field, and highlights the contributions of this work to the current understanding of PDCs.

2.1 Synthesis of Si-based preceramic polymers

Polysilylcarbodiimides are an important class of precursors for SiCN ceramics. The popularity of these precursors grew after many previous studies revealed that polysilylcarbodiimides-derived ceramics were more thermally stable than analogous ceramics derived from polysilazanes [6,39,43–48]. Bis(trimethylsilyl)carbodiimide and cyanamide are typical starting materials for the synthesis these polymers, as shown in Scheme1 [1]. They are reacted with organo element halides or pure element halides to form polysilylcarbodiimides.

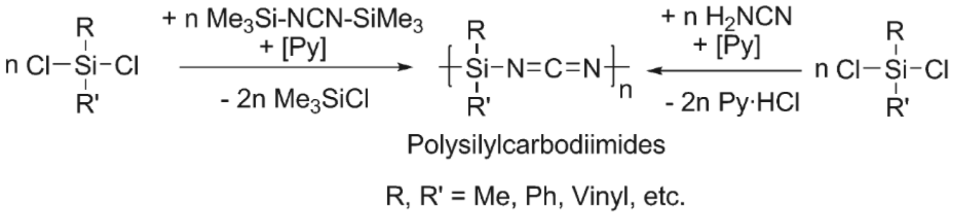

Scheme1 carbodiimidolysis and cyanamidolysis of chlorosilanes with bis(trimethylsilyl)carbodiimide and cyanamide [40]

It was found that bis(trimethylsilyl)carbodiimide was an efficient starting material for synthesizing other element carbodiimides [49–53]. These days, the synthesis of polysilylcarbodiimides is commonly accomplished by the reaction of chlorosilanes and bis(trimethylsilyl)carbodiimide with pyridine as a catalyst, following the work of Riedel et al. [20]. The by-product, trimethylchlorosilane, was removed by vacuum drying. Depending on the chlorosilanes used, cyclic, linear, or highly-branched poly(silsesquicarbodiimides) can be obtained [43,44,46,54,55]. Recently, Mera et al. [5] reported a group of linear carbon-rich polysilylcarbodiimides which contain phenyl functional organic groups, and another alternative group in the form of hydrogen, vinyl, or methyl. It was found that highly carbon-rich polysilylcarbodiimide-derived ceramics exhibited even greater thermal stability against crystallization.

The synthesis of polysilazane precursors could be achieved from chlorosilanes, by means of ammololysis reactions with ammonia, or aminolysis with different amines. Scheme2 shows the ammonolysis and aminolysis reactions of dichlorosilanes resulting in the synthesis of polysilazanes. Numerous studies on polysilazanes as ceramic precursor have been carried out since the 1960s [56–65]. The main disadvantage of these routes is the difficulty of separating the by-products, NH_4Cl or H_3NRCl. In the routes shown in Scheme2, chlorosilane could also be replaced by various silanes which have Si-H groups, and these Si-H groups could react with N-H groups [58,66–68]. This alternative reaction avoids producing the chlorine-containing salt by-product. However, silanes cost much more than chlorosilanes, and silanes are more dangerous to handle. Therefore, silanes are not preferred for obtaining polysilazanes.

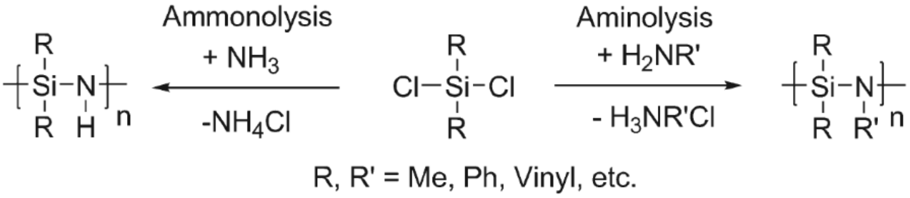

Scheme2 Synthesis routes to polysilazanes starting from chlorosilanes [40]

In contrast to the typical ammonolysis or aminolysis way for synthesizing polysilazane precursors, a reflux method was also reported for the synthesis of polysilazanes using hexamethyldisilazane and chlorosilane as starters, either without catalyst [69,70] or with $AlCl_3$ [70] as the catalyst.

In this work, a new method using hexamethyldisilazane and chlorosilane as starting materials and pyridine as catalyst was performed, and polysilazanes with different substitutes were acquired. This new route has not yet been reported.

2.2 Processing of polymer-derived ceramic bulks

The polymer-derived ceramic route can be used to produce complex-shaped bulk ceramics using the advantages of plastic technologies [1,20,40]. However, precursor pyrolysis is always accompanied by the evolution of gaseous by-products, pore formation, and significant shrinkage which can introduce stresses and deformation. Many efforts were made to obtain dense bulk ceramics, including pressing, extrusion, and injection molding. Among these techniques, pressing was most performed and studied. Pressing techniques includes cold isostatic pressing, cold uniaxial pressing, warm uniaxial pressing, hot isostatic pressing, etc. These works have been previously summarized elsewhere [40].

Uniaxial warm press is an effective technique for bulk shaping, and is correlated to the polymer crosslinking process. During warm-pressing and the accompanied crosslinking process, the shaping of greenbody compacts is achieved by producing duroplastic materials. The other benefit of crosslinking is that it helps to avoid the loss of oligomers during pyrolysis, and increases the ceramic yield. Warm presssing is proved to be practical in a variety of precursor systems [21,23–32,71] when the parameters applied, including temperature, pressure, presssing time, etc. were optimized. Optimal processing parameters of course depend on the type of precursor. Pressing temperatures usually vary from 120°C to 320°C, and applied pressure range from 20 to 710 MPa. For liquid polymers, a pre-crosslinking step is essential in order to obtain dense materials. Pre-crosslinking is considered as a partial crosslinking, which is to say, the polymers are solidified, but reactive groups remain for further crosslinking during shaping.

Fillers are often introduced for monolith forming in order to minimize shrinkage of the whole composite. Passive fillers include metal oxides, carbides or nitrides that occupy space, but do not react during pyrolysis, and reduce the volume fraction of polymer. Active fillers are usually metals or intermetallics, e.g. Al, Ti, Zr, B, Si, which react with decomposition products or in the pyrolysis atmosphere to form a new phase that expends in volume [72–75]. Self-fillers are thermolyzed from the same precursor as the matrix material, and are heat treated to an intermediate state between the precursor polymer and the final ceramic. Self-fillers play the same role as normal fillers, but still generate a “pure” system. Fillers can constitute the volume fraction majority of the final ceramic part, and assist in achieving higher densities.

A flow chart of the pressing technique for polymer-derived ceramic processing is given in Figure 1. The alternative to using fillers is also shown [40].

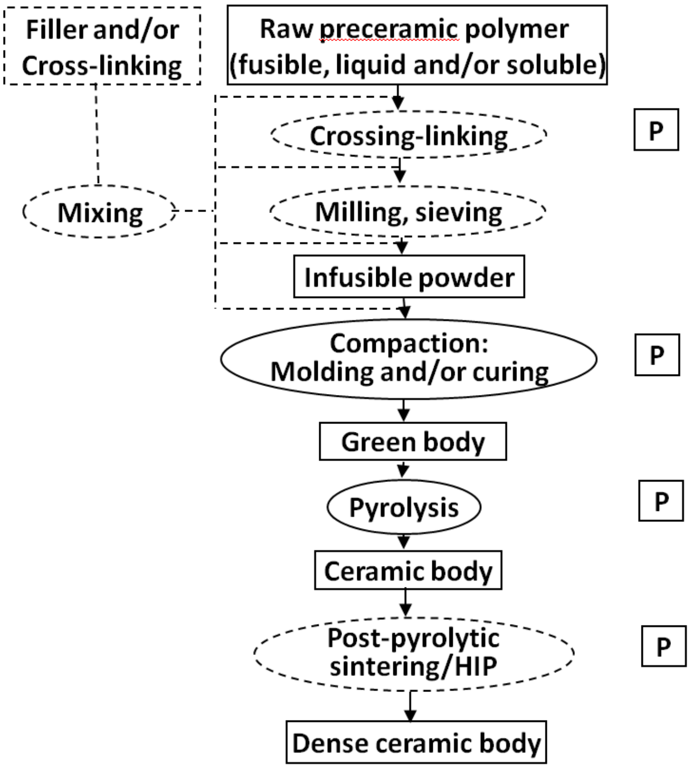

Figure 1 Pressing technique used in shaping polymer-derived ceramics, “P” marked when pressure is applied. Reprinted with permission of DEStech Publications, Inc., from *Polymer Derived Ceramics*, Eds. P. Colombo et al. Copyright 2010 [40].

2.3 Energetics of PDCs from calorimetry

The most remarkable property of Si(B)CN PDCs is their extraordinary thermal stability against crystallization and decomposition. Observations of some SiBCN PDCs reveal that no significant mass loss occurs at 1600°C, and no tremendous decomposition occurs up to 2000°C when the Si_3N_4 phase, which decomposes at 1841°C, is present [42,76–80]. Both SiCN and SiBCN PDCs have crystallization temperatures above 1400°C. This is a substantial improvement considering that the crystallization temperature of amorphous SiC is about 1000°C, and that of Si_3N_4 is about 1200°C [81,82].

Due to the outstanding thermal stability of PDCs, numerous studies have been conducted to sought out an explanation for why these ternary and quaternary systems possess such strong resistance to thermal treatment [8,42,80,83–91]. Calorimetry may paint the real thermodynamic landscape of these materials. High temperature oxidative drop solution calorimetry is well established [92,93], and has been used to study polysiloxanes-derived silicon oxycarbide ceramics (SiOC PDCs) [12,14], polysilylcarbodiimides-derived SiCN ceramics [10,11], and polyborosilazane-derived SiBCN ceramics [13]. Using this method, a pellet of pressed powder a few mg in mass is dropped from room temperature into a molten oxide solvent at high temperature in a Tian-Calvet twin microcalorimeter under oxidizing conditions (Figure 2). When the pellet is dissolved in sodium molybdate ($3Na_2O{\cdot}4MoO_3$) solvent, the final state of the sample is SiO_2 (cristobalite) and evolved gases (CO_2 and N_2) [11,94]. In order to accelerate sample dissolution and maintain an oxidizing environment, oxygen gas is bubbled through the melt. The evolved CO_2 and N_2 gases produced by the dissolution of the sample in the oxide melt are removed by continuously flushing oxygen gas in the headspace above the solvent. The calorimeter is calibrated using the heat content of Pt wire [92,93,95].

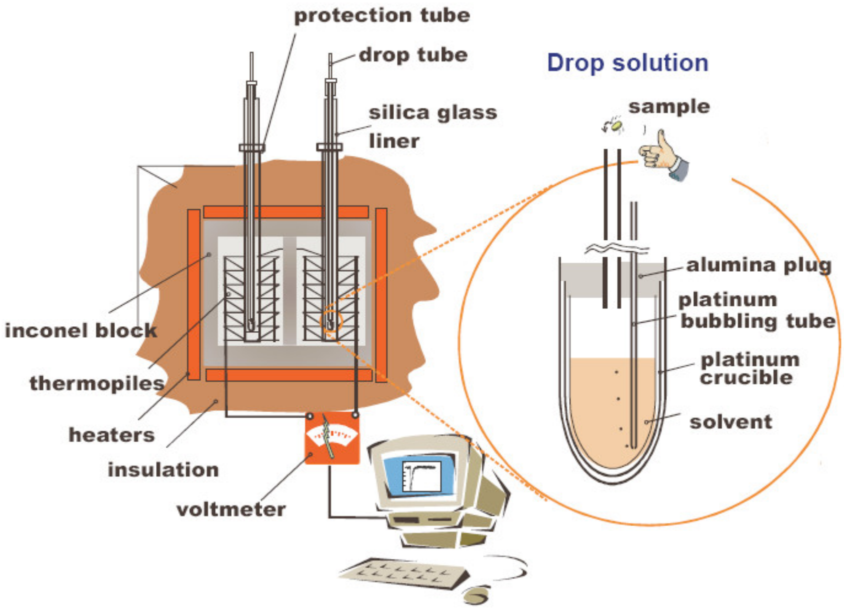

Figure 2 schematic of high temperature drop solution calorimetry

The results of high-temperature drop solution calorimetry showed that SiOC ceramics are thermodynamically stable with respect to the crystalline components, namely cristobalite, graphite and silicon carbide of the same composition. The interfacial region between nanodomains was claimed to be the source of the negative enthalpy. Mixed bonds in the interfacial region are far less strained in an amorphous structure than in a crystalline one [14]. Further study of SiOC PDCs produced at different pyrolysis temperatures revealed that, at lower temperatures, hydrogen releases some strain in the structure, leading to a lower energy state. At much higher temperatures, the carbon nanodomains gain stability due to phase separation. The carbon domains grow from single graphene sheets into stacks of graphite-like layers [12]. Similar interpretations have been made in previous studies of SiOC PDCs based on ab initio calculations that indicate that the presence of mixed Si−C−O bonds energetically stabilized the structures of these materials [96].

Studies of carbon-rich polysilylcarbodiimides-derived SiCN PDCs show that these SiCN PDCs are less stable than the SiOC ceramics studied previously. They have slightly positive heats of formation from the binary crystalline components Si_3N_4, SiC, and C [10]. Microstructural studies revealed that significant mixed bonds did not exist in these ceramics, but separate Si_3N_4, SiC and amorphous carbon nanodomains did [2,5]. Tavakoli et al. studied a series of amorphous Si(B)CN PDCs and demonstrated that thermodynamic stability diminished with an increase in boron content, meaning the hindering effect of boron on Si_3N_4 crystallization is kinetic [13,97]. In this work, we study the effect of (i) branched and linear polymer, (ii) different pyrolysis temperatures, on the the structure and energetics of selected ceramics.

2.4 Nanodomain structure of Si(B)CN ceramics

Compared to the conventionally processed SiC and Si_3N_4 ceramics, PDCs can be synthesized with highly tunable compositions to produce unique amorphous nanodomain structures. While distinct compositions show very different properties, similar compositions derived from different precursors or pyrolyzed at different temperatures may also have dramatically different properties due to variations in the size and nature of their nanodomains and interdomain regions [6,20,98].

The constitution of nanodomains in these amorphous PDCs depends on the materials system. Carbon-rich Si-C-N PDCs with compositions located within the limit of the SiC-Si_3N_4-C three phase region of the ternary Si-C-N system generally consist of sp^2 C nanodomains and silicon carbonitride domains, the latter composed of SiC_xN_{4-x} ($x = 0$– 4) tetrahedral units [99–103]. Si-B-C-N PDCs with compositions located in the SiC-Si_3N_4-C-BN four phase region of the quaternary Si-B-C-N system generally consist of sp^2 C nanodomains, domains of SiC_xN_{4-x} ($x = 0$–4) tetrahedra, and nanosized features containing B, N and C [104–106]. During pyrolysis, the covalent bonds in PDCs can rearrange and redistribute. Accordingly, two phenomena are usually observed, namely coarsening and demixing. Solid-state NMR investigations of Si-C-N and Si-B-C-N PDCs pyrolyzed at temperatures above 1000 °C show that demixing of tetrahedral environments in SiC_xN_{4-x} matrices occurs [99,104,106].

In small angle X-ray scattering (SAXS), X-rays are used to investigate the structural properties of solids, liquids or gels. Photons interact with electrons, and provide information about the fluctuations of electronic densities in heterogeneous matter. A typical experimental set-up is shown in Figure 3. The scattered intensity is collected as a function of the so-called scattering angle 2θ. Elastic interactions are characterised by zero energy transfers, such that the final wave vector k_f is equal in modulus to k_i. The relevant parameter to analyse the interaction is the momentum transfer or scattering vector $q=k_i-k_f$, defined by $q=(4\pi/\lambda)\sin\theta$. The standard unit for q is $Å^{-1}$.

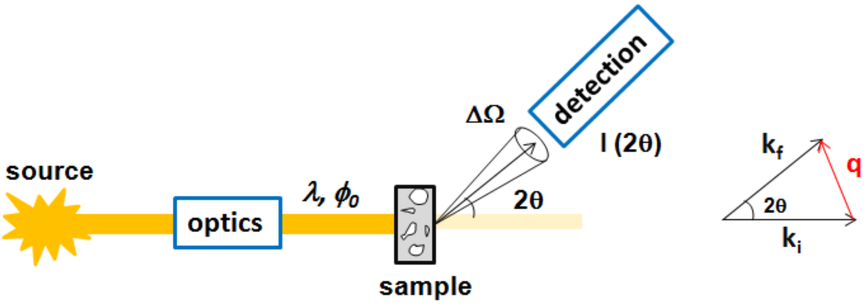

Figure 3 Schematic view of a typical scattering experiment

The number of photons scattered by a sample is proportional to its total volume V and to its electronic contrast. The higher the contrast between particles and solvent, the more intense the scattered signal. Figure 4 shows a binary sample and "q-window" corresponding to a measurement at a given q_0. The contrast is equal to zero in Cases 3 and 4, and non-zero in Cases 1 and 2.

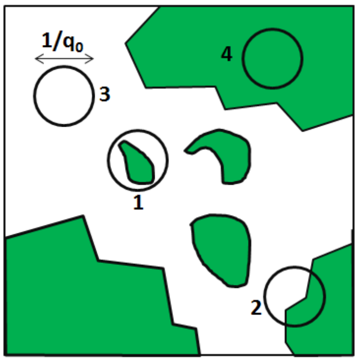

Figure 4 An example for binary system

Intuitively, a measurement made at a given q_0 allows one to investigate the density fluctuations in a sample based on a distance scale $D_0=2\pi/q_0$. It is equivalent to observing the system through a $2p/q_0$ diameter "window" in real space, as shown in Figure 4, with the circle being the observation window. A scattering signal is observed if the contrast Δρ inside the circle is non-zero. To study objects much smaller or much larger than $D_0=2\pi/q_0$, another "window" must be selected. The q-range of small angle experiments is usually divided into three main domains, as shown in Figure 5.

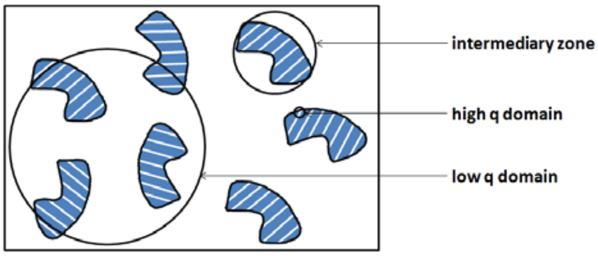

Figure 5 q-range of small angle experiments

At a high q domain, the window is very small, and there exists contrast only at the interface between two media. This domain, called the Porod's region, gives information about the interfaces present in the sample. In the intermediary zone, the window is of the order of the "elementary bricks" in the systems. The form factor P(q) can be measured, as it relates to the size, shape and internal structure of one particle. At a low q domain, the observation window is very large and the structural order can be obtained through the so-called structure factor S(q), which allows one to calculate the interactions within the system.

Guinier plots of small angle X-ray scattering (SAXS) data show that the domain size in Si-(B-)-C-N PDCs increases in the range of ~ 0.5 nm to 4 nm with increasing pyrolysis temperature and time [107–110].

2.5 Impedance spectroscopy and its use in PDCs

Polymer-derived ceramics thermolyzed possess amorphous structures and outstanding properties, such as thermal stability against decomposition and crystallization, as well as interesting optical and electrical properties. Previous studies of electrical properties were carried out basically focusing on the DC conductivity (σ_{dc}) of the materials. Studies of some polysilazane-derived ceramics [36] found that, for PDCs pyrolyzed/annealed from 1000 ºC to 1400 ºC, σ_{dc} increased by as much as 3 orders of magnitude with increasing temperature. This may due to the loss of residual hydrogen accompanied by an increase of the sp^2/sp^3-carbon ratio. At higher temperatures (T > 1400ºC), the pronounced increase in conductivity was attributed to both the formation of nano-crystalline SiC, and to a reduction in the nitrogen content of the amorphous matrix. At even higher temperature T > 1600ºC, the SiC particles formed percolation paths throughout the sample. At annealing temperature above 1300 ºC, the formation of crystalline SiC and Si_3N_4, and hence the increase in conductivity, cannot be considered an intrinsic property of the SiCN ceramics. Other studies found that at pyrolysis temperature above 1000 ºC, graphitic-like carbon was shown to be the main conductive phase [101,103].

Despite identifying the main conductive phases in the SiCN system, all experimental data showed an increase of σ_{dc} with increasing annealing temperature. This may be correlated to the growth of dehydrogenated aromatic carbon and its local arrangement as cage-like structures around SiC-crystallites [37], as well as with an enhanced sp^2/sp^3-carbon ratio [36]. A number of experimental investigations [3] and theoretic calculations [111] showed the existence of cross-linked graphitic carbon networks in the SiCN system. If the content of the graphitic carbon phase reached the percolation threshold, the electrical properties of the material are dominated by this phase. This phase may be assumed to be in the form of carbon clusters, or a network of graphitic-like lamellae a few atom layers in size. In the case of carbon clusters, about 16 vol% was the threshold for percolation [37], and in the case of graphitic-like carbon layers, high conductivity could be achieved by a very small volume fraction (less than 1 vol%) [112]. Samples with high carbon contents obtained at high temperatures showed Arrhenius dependence [113–115], behaved as if containing graphitic-like amorphous carbon [116].

Impedance spectroscopy (IS) allows one to simply treat carrier transport processes and reactions in complex situations, such as in intrinsically disordered material components [35]. Some investigations using impedance spectroscopy [36,37] studied the σ_{ac} of PDCs, and the mechanism of relaxation. Impedance spectroscopy is very sensitive to every phase in the structure, and thus gives the σ_{ac} of each individual type of nanodomain.

Impedance spectroscopy studies the properties that influence the conductivity of materials systems intrinsically and/or under external stimulus. The parameters derived from IS spectrum fall generally into two categories: (a) those pertinent only to the material itself, such as conductivity, dielectric constant, mobility of charge carriers, equilibrium concentrations of the charged species, and bulk generation–recombination rates; and (b) those pertinent to an electrode–material interface, such as absorption-reaction rate constants, capacitance of the interface region, and diffusion coefficient of neutral species in the electrode itself [35].

Generally, the experimental impedance data may be approximately simulated by an equivalent circuit made up of resistors, capacitors, inductors and other circuit elements. A resistance (R) represents a conductive path for the bulk conductivity, a dissipative component of the dielectric response, or a chemical step associated with an electrode reaction. In the same way, capacitors (C) and inductors (L) model space charge polarization and electrocrystallization processes at an electrode. The complex impedance of a series circuit RC (Formula 1, Figure 6(a)) and of a parallel circuit (RC) (Formula 2, Figure 6(b)) are given by:

$$\mathbf{Z = R + 1/j\omega C}$$

Formula 1

$$\mathbf{Z = \frac{R}{1 + (\omega RC)^2} - j\frac{\omega R^2 C}{1 + (\omega RC)^2}}$$

Formula 2


(a) RC

(b) (RC)

Figure 6: Circuit diagram of serial (a) and parallel (b) R and C

S. Wansom et al. [117] developed a “universal equivalent circuit model” to describe the impedance behavior of composites with conduction particles as shown in Figure 7. Each box represents a parallel resistor and capacitor. Basically, below the percolation point of the particles, the upper two paths agree between the simulated and measured spectra. The uppermost path is the matrix path, where the first element represents the unreinforced matrix. The second element only exists with the addition of insulating particles in the matrix. The middle path accounts for particle path, with the first element representing the electrical properties of the particle. The second element corresponds to the inter-particle current flow at high frequencies, which is usually responsible for the low resistance at high-frequency cusp.

The third element of the middle path and the rightmost element in Figure 7 account for the double layer, respectively, of the particle and external electrode surfaces. The bottom-most path is required to describe the composite beyond the percolation threshold of the particles.

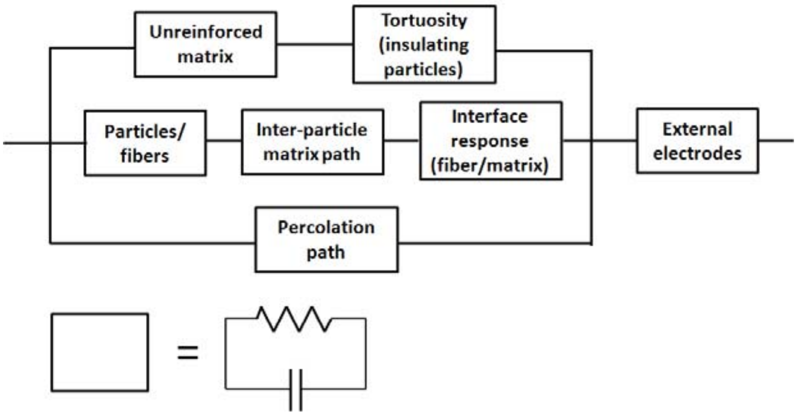

Figure 7: A universal equivalent circuit model for composite with particles/fibers distribution. Reprinted from Cement and Concrete Composites, Vol 28, S. Wansom, N. J. Kidner, L. Y. Woo, and T. O. Mason, AC-impedance response of multi-walled carbon nanotube/cement composites, 509-519, Copyright (2006), with the permission from Elsevier [117].

2.6 Electrochemistry of SiCN ceramics as anode material in lithium-ion batteries

Recently polymer-derived ceramics were also applied as anode materials in lithium-ion batteries. PDCs exhibit capacities exceeding that of graphite and furthermore show stable cycling behavior, even at elevated charge/discharge rates. There exists a clash of opinions with respect to the lithium storage sites in PDCs. Ahn et al. claim that the mixed bonding configuration (tetrahedrally coordinated silicon from SiC_4 via SiC_3O, SiC_2O_2 and $SiCO_3$ to SiO_4) of SiOC ceramics acts as a major lithiation site [38], while Fukui et al. found that the “free” carbon phase within these materials to provide the major hosting sites for Li ions [118]. So far, considering pure PDCs, most existing publications related to the electrochemical performance of PDCs have been focused on SiOC ceramics [38,118–121]. Even though Dahn et al. have already patented the use of silazane-derived SiCN ceramics showing reversible discharge capacities up to 560 mA h g^{-1} in 1997 [122], little research has been done on the application of these materials to lithium-ion batteries since that time. Pure PDC-based SiCN materials derived from polysilylethylenediamine have been investigated by Su et al. [123] and Feng [124]. The work of Su et al. showed a first discharge cycle capacity of 456 mA h g^{-1}, but the material suffered strong fading with cycling. The problem of capacity fading was solved by Feng, who achieved capacities higher than 300 mA h g^{-1} after 30 cycles for a current rate of 160 mA g^{-1}, after an additional heat treatment was applied to the polymer-derived SiCN material. Promising electrochemical results (capacity and stability) for SiCN derived from high-carbon containing polysilylcarbodiimides have been reported by Kaspar et al. [125] and Graczyk-Zajac et al. [126]. Recently, it has been found that composite anode materials composed of SiCN and graphite [127] and SiCN and silicon [128] demonstrate better electrochemical properties than that of pure graphite and silicon, respectively. In parallel, Ahn et al. [129] suggested that the presence of nitrogen in SiOC ceramics strongly diminishes capacity reversibility. In the above report, it is claimed that high capacities of 600 mA h g^{-1} can only be found in materials with a nitrogen to oxygen (N/O) ratio below 1. The results are discussed in relation to the degree of bond covalency, with Si-N bonds being more covalent than Si-O bonds. It is suggested that lithium is sequestered in Si-O-C mixed bond environments. Accordingly, the replacement of oxygen by nitrogen within the amorphous network leads to a loss in the ability of these mixed bonds to reversibly bind lithium. In the present, work we demonstrate that SiC(O)N materials with a N/O ratio of about 6-9.5 show outstanding electrochemical properties in view of their potential application as lithium-ion battery anodes. Furthermore, the molecular structure of the polymer precursors and the nanostructure of the final ceramics play important roles in the electrochemical behavior of these polymer-derived ceramics.

3. Experimental

3.1 Chemicals

The chemicals used here are phenylvinyldichlorosilane, methylvinyldichlorosilane, phenyltrichlorosilane, hexamethyldisilazane, borane dimethylsulphide, dicyandiamide, cyanamide, $^{13}C/^{15}N$-isotope cyanamide and pyridine. They were purchased from Sigma-Aldrich Chemie GmbH, Germany. All chemicals were used as-received without further purification.

3.2 Synthesis of Si-based preceramic polymers

All polymers in this study were house-synthesized at TU Darmstadt. The structures of the different polymers are shown in Figure 8. Synthesis was performed using the Schlenk technique in protective argon. All glassware involved was dried under vacuum heating, and then filled with argon. The precursors and derived ceramics were handled, stored, and prepared for characterization in a glovebox.

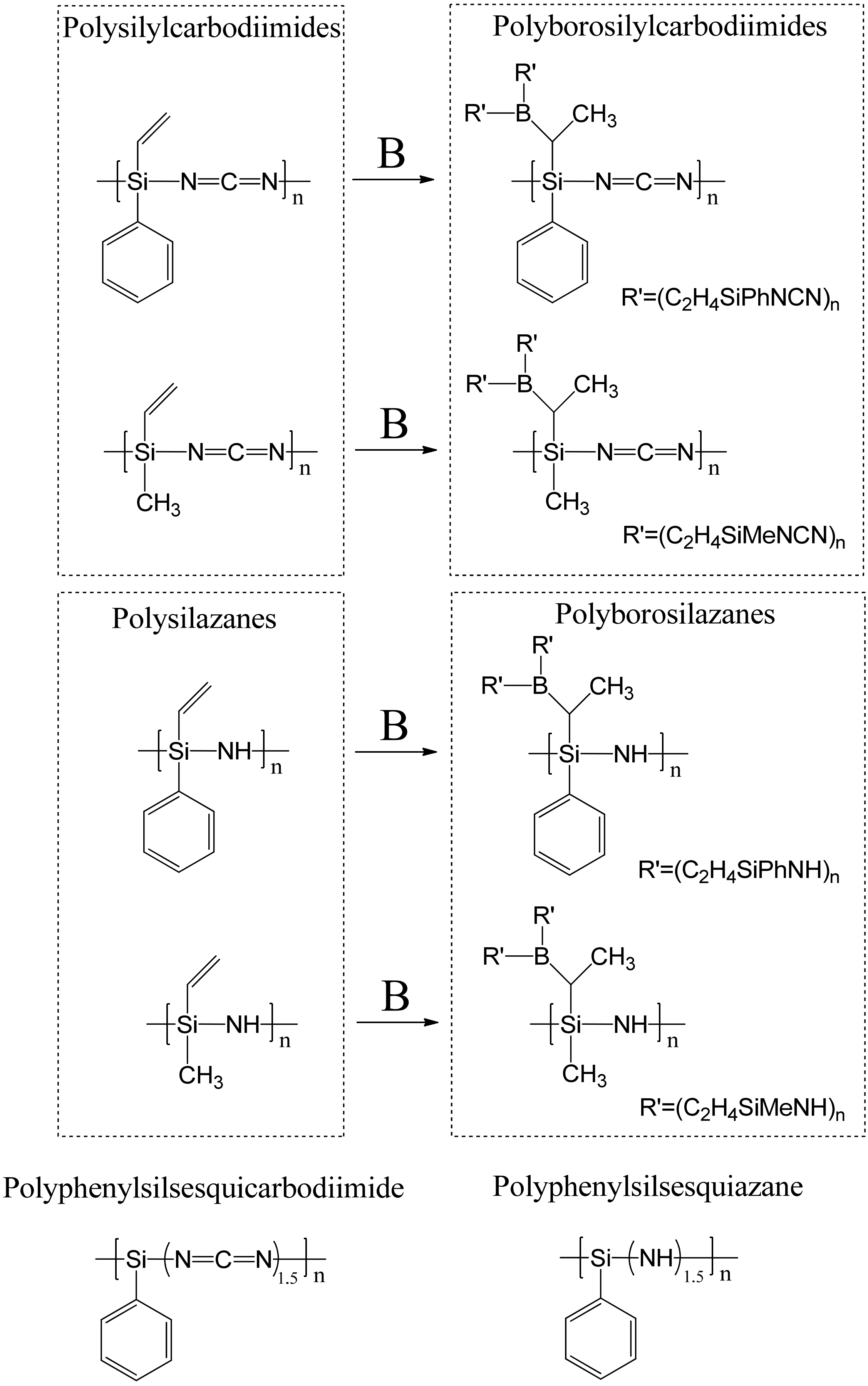

Figure 8 Description of the preceramic polymers synthesized in this work

3.2.1 Synthesis of polysilylcarbodiimides

The synthesis of polysilylcarbodiimide was completed using self-made bis(trimethylsilyl)carbodiimide and pyridine as the catalyst. Dichlorosilane with the vinyl substituent was used for the synthesis. To vary the carbon content of the precursors, a phenyl substituent ($-C_6H_5$) was used for higher carbon content precursors and a methyl group substituent ($-CH_3$) was used for lower carbon content precursors. The production of polysilylcarbodiimide using bis(trimethylsilyl)carbodiimide and chlorosilanes has the advantage that the byproduct Me_3SiCl is easy to remove under vacuum. The syntheses are described in detail as following.

Bis(trimethylsilyl)carbodiimide was synthesized according to the literature [130], as shown in Scheme 3. First, dicyandiamide (42 g) was mixed with an excess of hexamethyldisilazane (177g), and the catalyst ammonium sulfate (0.2 g). The mixture was constantly stirred at 170°C under refluxing. The created by-product was NH_3, which is released as gas. The mixture was then distilled by a Vigreux column and the phase bis(trimethylsilyl)carbodiimide was separated from the mixture.

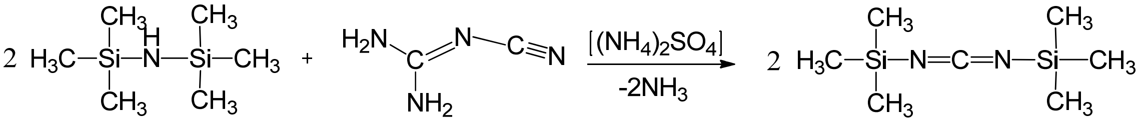

Scheme 3 Reaction of Bis(trimethylsilyl)carbodiimide

Polyphenylvinylsilylcarbodiimide was synthesized using phenylvinyldichlorosilane and bis(trimethylsilyl)carbodiimide with pyridine as a catalyst (Scheme 4). The synthesis was performed in inert argon atmosphere. First, bis (trimethylsilyl)carbodiimide (0.24 mol) and pyridine (0.12 mol) were added into a flask under constant stirring. Then, dichlorovinylphenylsilane (0.24 mol) was added to the mixture. The mixture was first refluxed at 66 °C for 7 hours in order to prevent the evaporation of phenylvinyldichlorosilane, which has a boiling point of 84-87°C. A secondary refluxing was carried out at 120 °C for additional 11 hours. NMR investigations were carried out to check the reactions. The by-product, Me_3SiCl, was removed under vacuum while heating the mixture at 120 °C. Polyphenylvinylsilylcarbodiimide was obtained after the separation of the by-product. The yield of dried polymer was about 85%.

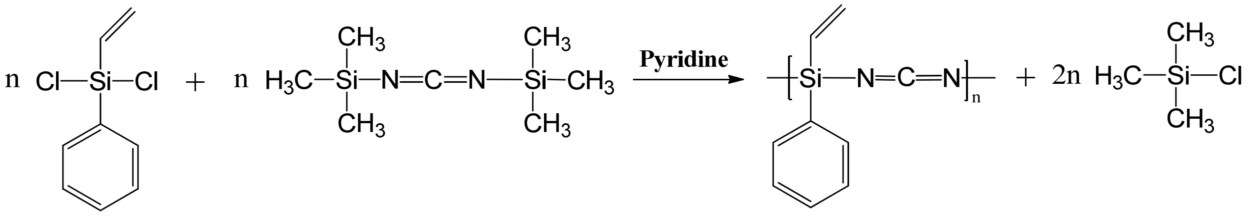

Scheme 4 Synthesis of polyphenylvinylsilylcarbodiimide

The reaction of polymethylvinylsilylcarbodiimide was performed under the same conditions as polyphenylvinylsilylcarbodiimide. The reaction is shown in Scheme 5. The removal of the by-product was carried out at room temperature. NMR measurements were performed to check the formation of the polymer and the complete removal of the by-product. The yield of polymer was about 70%.

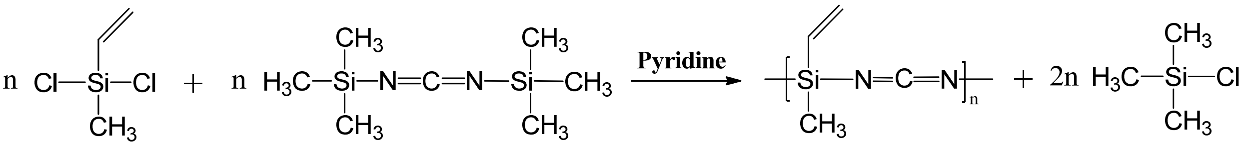

Scheme 5 Synthesis of Polymethylvinylsilylcarbodiimide

3.2.2 Synthesis of polyborosilylcarbodiimides

Polyborosilylcarbodiimides were synthesized using the polysilylcarbodiimides prepared above and boranedimethylsulfide ($BH_3 \cdot SMe_2$). Toluene was used as the solvent and was removed after reaction.

Polyphenylvinylsilylcarbodiimide (0.24 mol) and toluene (100 ml) were mixed in a flask in a cold bath consisting of dry ice and isopropanol. After one hour of cooling in the cold environment under stirring, 0.082 mol boranedimethylsulfide ($BH_3 \cdot SMe_2$) dissolved in 50 ml toluene was dropped into the mixture from a dropping funnel. When the dropping finished, the cold bath was removed and the mixture was slowly warmed up to room temperature. The mixture was then solidified. This hydroboration reaction is shown in Scheme 6. To remove the toluene, the polymer was dried under vacuum for 3 hours at room temperature, followed by 9 hours at 66 °C and 7 hours at 120 °C. The reaction had a yield of 100% and the obtained polymer was free from residual toluene.

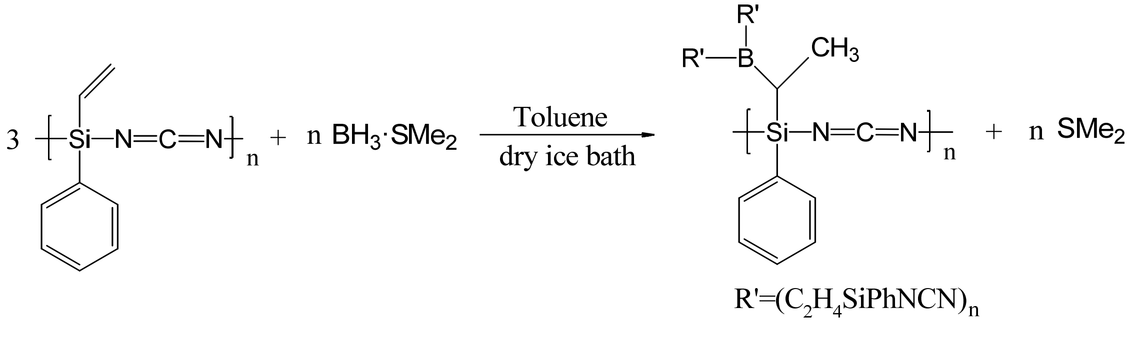

Scheme 6 Synthesis of polyborophenylvinylsilylcarbodiimide

The synthesis of polyboromethylvinylsilylcarbodiimide was performed using the same conditions as the polyborophenylvinylsilylcarbodiimide. Polymethylvinylsilylcarbodiimide was reacted with $BH_3 \cdot SMe_2$. The synthesis route is shown in Scheme 7.

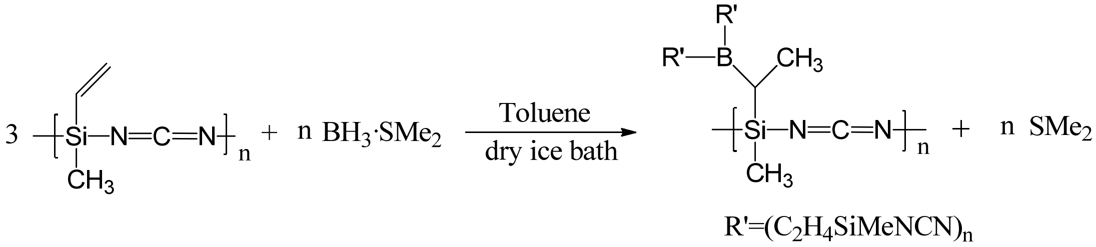

Scheme 7 Synthesis of polyboromethylvinylsilylcarbodiimide

3.2.3 Synthesis of polysilazanes

The synthesis of polyphenylvinylsilazane was performed by reacting 1 mol hexamethyldisilazane (HMDS) and 1 mol phenylvinyldichlorosilane with pyridine (0.5 mol) as the catalyst, as shown in Scheme 8. The mixture was refluxed at 60°C for 21 hours followed by a distillation under 120 °C to remove the by-product, trimethylchlorosilane. In order to further remove trimethylchlorosilane, the product was dried under vacuum at room temperature for another 5 hours. NMR confirmed that the polymer formed and was free from the by-product.

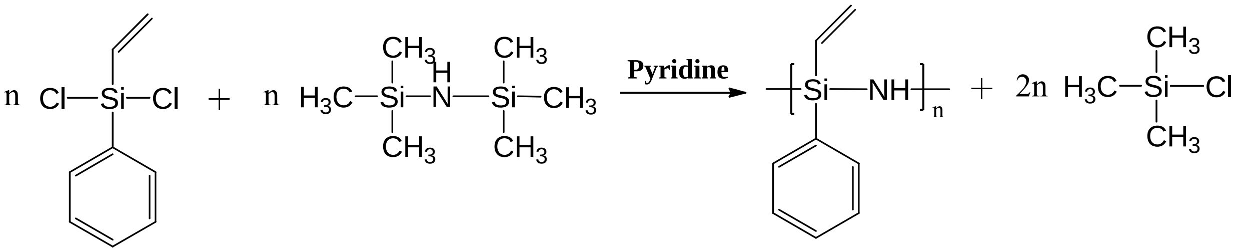

Scheme 8 Synthesis of polyphenylvinylsilazane

Similarly, the synthesis of polymethylvinylsilazane was carried out by using methylvinyldichlorosilane and hexamethyldisilazane (HMDS) as the starting materials, and pyridine as the catalyst, as shown in Scheme 9. The mixture was refluxed at 60°C for 7 h, 120°C for 7h and 180°C for 7h. To remove trimethylchlorosilane, the product was dried under vacuum at 60°C for 5 hours.

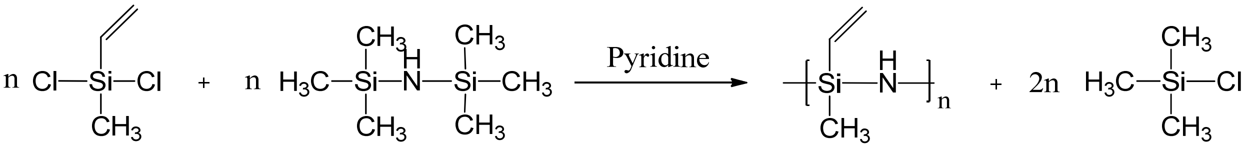

Scheme 9 Synthesis of polymethylvinylsilazane

3.2.4 Synthesis of polyborosilazanes

Polyborosilazanes were synthesized through the hydroboration of corresponding polysilazanes. The conditions used were the same as in the case of polyborophenylvinylsilylcarbodiimide and polyboromethylvinylsilylcarbodiimide. The reactions for forming {B[-

$(C_2H_4)Si(Ph)\text{-}NH\text{-}]_3\}_n$ and $\{B[\text{-}(C_2H_4)Si(Me)\text{-}NH\text{-}]_3\}_n$ are shown in Scheme 10 and Scheme 11, respectively.

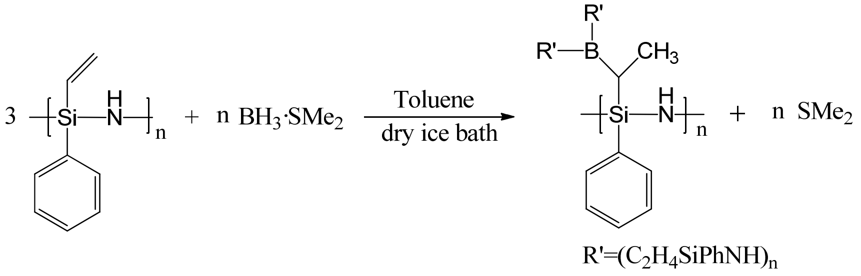

Scheme 10 Synthesis of polyborophenylvinylsilazane

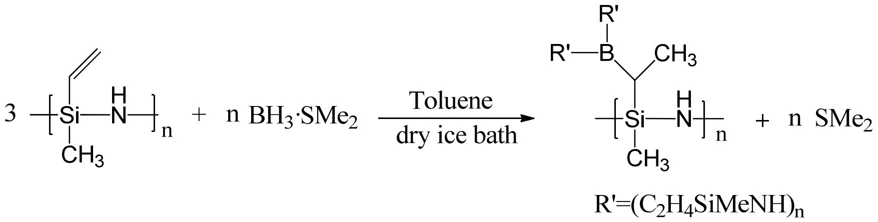

Scheme 11 Synthesis of polyboromethylvinylsilazane

3.2.5 Synthesis of polyphenylsilsesquicarbodiimides

A branched polyphenylsilsesquicarbodiimide was synthesized using bis(trimethylsilyl)carbodiimide and trichlorophenylsilane. Pyridine was used as the catalyst. The reaction is shown in Scheme 12.

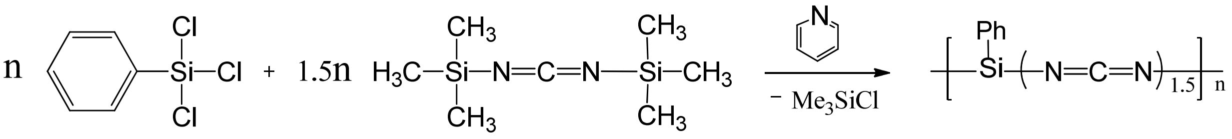

Scheme 12 Synthesis of polyphenylsilsesquicarbodiimide

$^{13}C/^{15}N$ isotope-enriched polyphenylsilsesquicarbodiimide was synthesized from trichlorophenylsilane and cyanamide with pyridine as the catalyst. 10 % of the cyanamide was labeled with ^{15}N and ^{13}C isotopes. Cyanamide and pyridine were mixed with the solvent THF. The mixture was first stirred in an ice bath for one hour. Trichlorophenylsilane was diluted by THF and then dropped into the mixture of cyanamide and pyridine. After the dropping finished, the mixture was further stirred for one hour in the ice bath. Then, the ice bath was removed and the mixture was warmed up to room temperature and kept under stirring for 12 hours. After removing the THF by vacuum drying, the by-product, pyridine·HCl, was removed by washing the polymer with pyridine. More THF was used to wash away the residual pyridine, and at last, THF was removed by performing vacuum dring. The ^{15}N and ^{13}C isotopes go into the carbodiimide groups forming the structure $[\text{-}(Ph)Si\text{-}(^{15}N{=}^{13}C{=}^{15}N)_{1.5}\text{-}]_n$. The reaction is shown in Scheme 13.

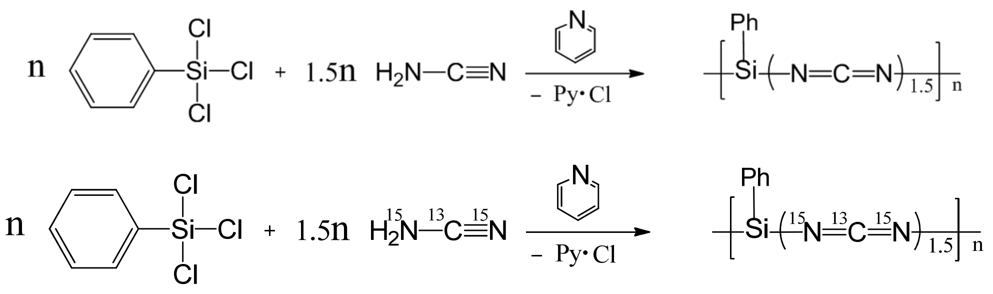

Scheme 13 Synthesis of $^{13}C/^{15}N$-isotopes enriched polyphenylsilsesquicarbodiimide

3.2.6 Synthesis of polyphenylsilsesquiazane

Polyphenylsilsesquiazane was synthesized from the reaction of hexamethyldisilazane and trichlorophenylsilane with pyridine as catalyst. The reaction was carried out at room temperature for 0.5 hour, and then at 120°C for another 10.5 hours. The by-product, trimethylchlorosilane, was removed by vacuum drying. The final state of the polymer is a white powder. The reaction is shown in Scheme 14.

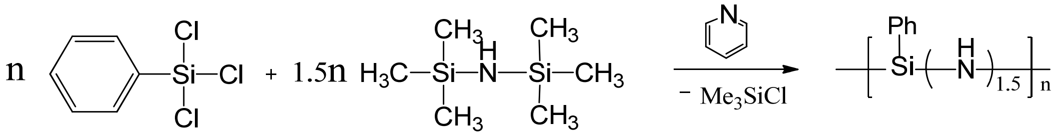

Scheme 14 Synthesis of polyphenylsilsesquiazane

3.3 Pyrolysis of polymers

The samples studied in this work included both ceramic powders and bulk ceramics. Ceramic powders were obtained from a direct pyrolysis of the polymers, while bulk ceramics were synthesized using the procedure described in Section 3.4.

To obtain ceramic powders, the precursors were pyrolyzed in a horizontal tube furnace (Gero GmbH & Co., Neuhausen, Germany). The polymer was put into a quartz boat, which was kept in a quartz Schlenk tube. The polymers were pyrolyzed at a heating rate of 100 °C/h to the target temperature under constant argon flow. At the desired temperature, the material was held for 2 hours. The furnace was then cooled to room temperature at a cooling rate of 100 °C/h to 700°C, followed by furnace cooling. The yields of ceramics at 1100°C are given in Table 1.

The green bodies of bulk ceramic were put in a SiC boat, and kept in quartz Schlenk tube. The pyrolysis schedule differed with the precursors according to their mass loss features — details can be found in Section 3.4.

The pyrolyzed ceramic samples are identified hereon as “Si(B)CNX-pyrolysis temperature,” in which X represents a sequence number given in Table 1. For instance, SiBCN4-1400 stands for the ceramic sample derived from polyboromethylvinylsilazane pyrolyzed at 1400°C.

Table 1 Ceramic yields and identification

Preceramic polymer	Polymer formula	Ceramic yield (1100°C)	Ceramic sample
polyphenylvinylsilylcarbodiimide	$[-(PhVi)Si-NCN-]_n$	61.5%	SiCN1
polymethylvinylsilylcarbodiimide	$[-(MeVi)Si-NCN-]_n$	32.7%	SiCN2
polyborophenylvinylsilylcarbodiimide	$\{B[-(C_2H_4)Si(Ph)-NCN-]_3\}_n$	59.3%	SiBCN1
polyboromethylvinylsilylcarbodiimide	$\{B[-(C_2H_4)Si(Me)-NCN-]_3\}_n$	55.7%	SiBCN2
polyphenylvinylsilazane	$[-(PhVi)Si-NH-]_n$	59.1%	SiCN3
polymethylvinylsilazane	$[-(MeVi)Si-NH-]_n$	35.3%	SiCN4
polyborophenylvinylsilazane	$\{B[-(C_2H_4)Si(Ph)-NH-]_3\}_n$	46.6%	SiBCN3
polyboromethylvinylsilazane	$\{B[-(C_2H_4)Si(Me)-NH-]_3\}_n$	35.6%	SiBCN4
polyphenylsilsesquicarbodiimide	$[-(Ph)Si-(NCN)_{1.5}-]_n$	—	SiCN5
$^{13}C/^{15}N$ isotope-enriched polyphenylsilsesquicarbodiimide	$^{13}C/^{15}N$ isotope-enriched $[-(Ph)Si-(NCN)_{1.5}-]_n$	48.1%	Iso_SiCN5
polyphenylsilsesquiazane	$[-(Ph)Si-(NH)_{1.5}-]_n$	49.3%	SiCN6

3.4 Bulk ceramic processing

Bulk ceramics were produced from all linear polymers. Figure 9 shows the processing route for producing bulk ceramics, together with that for preparing ceramic powders. The bulk ceramics were synthesized using a uniaxial warm-pressing, followed by pyrolysis of the green bodies. All liquid (honey-like) polymers, namely $[-(PhVi)Si-NCN-]_n$, $[-(MeVi)Si-NCN-]_n$, $[-(PhVi)Si-NH-]_n$, $[-(MeVi)Si-NH-]_n$, required a pre-crosslinking step. The required temperatures and dwelling times varied, as shown in Table 2. After pre-crosslinking, the products obtained were milled into a powder, followed by warm-pressing. The parameters used for warm-pressing are shown in Table 2. Compacts and mechanically-stable green bodies were then produced.

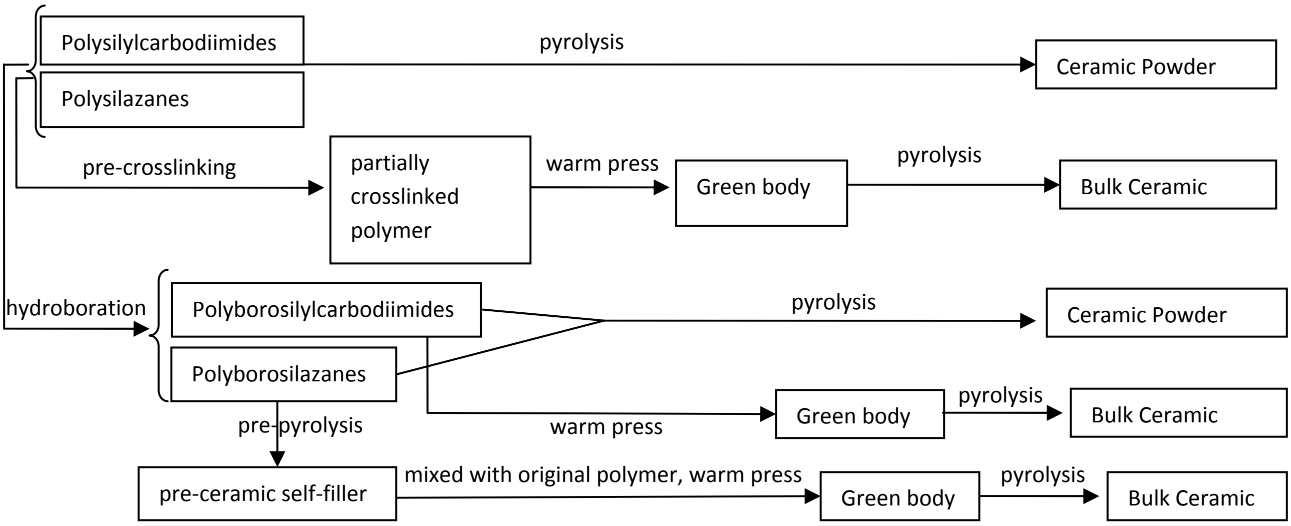

Figure 9 The main procedure utilized for the synthesis of ceramic powder and bulk ceramic

Polyborophenylvinylsilazane and polyboromethylvinylsilazane are thermoplastic with similar melting points around 85°C. In order to obtain bulk samples, the polymers were first pyrolyzed at 500 °C for 2 hours. The pre-pyrolyzed powder and the original polymer were then mixed for warm-pressing. The optimized ratio of pre-pyrolysis powder to polymer was 65:35 for $\{B[-(C_2H_4)Si(Ph)\text{-}NH\text{-}]_3\}_n$, and 50:50 for $\{B[-(C_2H_4)Si(Me)\text{-}NH\text{-}]_3\}_n$.

The processing parameters, including pre-crosslinking/pre-pyrolysis temperature and dwelling time, warm-pressing temperature, pressing time, and applied pressure are listed in Table 2.

Table 2 Optimized parameters for processing bulk ceramics

Preceramic polymer	Pre-crosslink/pre-pyrolysis	Warm-pressing	Pyrolysis schedule
	temperature, time	temperature, holding time, pressure	
$[-(PhVi)Si\text{-}NCN\text{-}]_n$	255°C, 5h	250°C, 2h, 16MPa	r.t.→ (100°C/h)→400°C → (50°C/h)→500°C→ (2h)→500°C→ (50°C/h)→600°C→ (2h)→600°C → (100°C/h)→1100°C→ (2h)→1100°C
$[-(MeVi)Si\text{-}NCN\text{-}]_n$	320°C, 5h	200°C, 2h, 16MPa	r.t.→ (100°C/h)→450°C → (50°C/h)→500°C→ (2h)→500°C→ (50°C/h)→700°C→ (100°C/h)→1100°C→ (2h)→1100°C
$\{B[-(C_2H_4)Si(Ph)\text{-}NCN\text{-}]_3\}_n$	—	250°C, 2h, 16MPa	r.t.→ (100°C/h)→200°C→ (50°C/h)→600°C→ (100°C/h)→1100°C→ (2h)→1100°C
$\{B[-(C_2H_4)Si(Me)\text{-}NCN\text{-}]_3\}_n$	—	250°C, 2h, 16MPa	r.t.→ (100°C/h)→300°C→ (50°C/h)→700°C→ (100°C/h)→1100°C→ (2h)→1100°C
$[-(PhVi)Si\text{-}NH\text{-}]_n$	300°C, 5h	250°C, 2h, 16MPa	r.t.→ (100°C/h)→200°C→ (50°C/h)→ 300°C (1h)→300°C → (50°C/h) → 450°C →(1h)→450°C→ (50°C/h)→ 600°C → (100°C/h)→1100°C→ (2h)→1100°C
$[-(MeVi)Si\text{-}NH\text{-}]_n$	320°C, 5h	300°C, 2h, 16MPa	r.t.→ (50°C/h)→160°C→ (2h)→160°C → (50°C/h)→ 450°C →(1h)→450°C→ (50°C/h)→ 600°C → (100°C/h)→1100°C→ (2h)→1100°C
$\{B[-(C_2H_4)Si(Ph)\text{-}NH\text{-}]_3\}_n$	500°C, 2h	85°C, 1.5h, 16MPa (pre-pyrolyzed powder: original polymer = 65:35 by weight)	r.t.→ (100°C/h)→200°C→ (25°C/h)→600°C→ (100°C/h)→1100°C→(2h)→1100°C
$\{B[-(C_2H_4)Si(Me)\text{-}NH\text{-}]_3\}_n$	500°C, 2h	85°C, 1.5h, 16MPa (pre-pyrolyzed powder: original polymer = 50:50 by weight)	r.t.→ (100°C/h)→200°C→ (25°C/h)→ 300°C (1h)→300°C → (25°C/h) → 400°C →(1h)→400°C→ (25°C/h)→ 500°C→(1h)→500°C → (25°C/h) → 600°C→(1h)→600°C→ (100°C/h)→1100°C→ (2h)→1100°C

3.5 Annealing of ceramics

The post-annealing experiments at 1400 °C, 1700 °C and 2000 °C were performed in an Astro furnace (Thermal Technology Inc., CA, USA) in argon atmosphere. Ceramics obtained at 1100 °C were placed in a silicon carbide crucible and pyrolyzed at a heating ramp of 5 °C/min to target temperatures, and held for 2 hours. The thermolysis was completed by cooling the samples to room temperature at a cooling ramp of 10 °C/min.

3.6 Characterization techniques

Micro-Raman spectra (10 scans, each lasting 3s) were recorded using a Horiba HR800 micro-Raman spectrometer (Horiba Jobin Yvon, Bensheim, Germany) equipped with an Ar laser (irradiation wavelength of 514.5nm). The excitation line has its own interference filter (to filter out the plasma emission) and a Raman notch filter (for laser light rejection). The measurements were performed with a grating of 1800 gmm^{-1} and a confocal microscope (magnification 50×, NA0.5) with a 100 μm aperture, giving a resolution of 2–4 μm. The laser power (ca. 20 mW) on the sample was attenuated in the range of 2mW–20μW using neutral density (ND) filters. For the evaluation of graphitic carbon in ceramics, Gaussian/Lorentz curve fitting of the Raman bands (OriginPro 8.1 Software) was applied.

All-reflecting objective (ARO) IR micro-spectroscopy was done on a confocal Illuminat IR™ FTIR spectrometer using reflection absorption spectroscopy (RAS) for quick analysis. The spectrum of the microscopic specimen is recorded by simply focusing on the specimen.

Scanning electron microscopy (SEM) micrographs were obtained using an FEI Quanta 600 instrument (FEI, Eindhoven, The Netherlands). The samples were sputtered with a conductive gold layer prior to investigation.

For the chemical composition analysis, the carbon content of the samples was determined with a carbon analyzer, CS 800 (Eltra GmbH, Neuss) while the oxygen and nitrogen content was measured with a N/O analyzer, Leco TC-436 (Leco Corporation, Michigan). Hydrogen, boron and chlorine contents of the ceramic pyrolyzed at 1100 °C were carried out at Mikroanalytisches Labor Pascher (Remagen, Germany). The silicon content of the samples was calculated by mass balance.

Transmission electron microscopy (TEM) of the bulk and powder ceramics was performed using an FEI CM20 STEM (FEI, Eindhoven, the Netherlands) operating at an accelerating voltage of 200 kV (wavelength λ=2.51 pm). For the TEM sample preparation, ceramic powders were dispersed in an ultrasonic bath of high purity (99.8%) methanol (Sigma-Aldrich Co.), and a small droplet of the suspension was drop-casted onto a holey carbon (Cu) grid. Upon drying, the samples were lightly coated with carbon to avoid charging under the electron beam. TEM samples of the bulk materials were prepared via conventional preparation techniques involving cutting, grinding and polishing, followed by Ar-ion milling and light carbon coating.

Powder X-ray diffraction (XRD) measurements were performed on a STOE X-ray diffractometer using Ni-filtered Mo Kα radiation at a scan speed of 1^{o} min^{-1}. For the bulk ceramics, XRD measurements were performed on a modified 4 circle X-ray diffractometer (STOE STADI 4). The system was equipped with new FOX X-ray optics with a curved mirror with graded multilayer coating from XENOCS, and a collimator with a divergence of 0.06° primary to the samples. A Cu Kα anode (Seifert) was applied. The step size was 0.05°, and each step was measured for 60 or 90 seconds. The surface of the bulk ceramics were polished prior to the measurements.

Thermogravimetry coupled with mass spectrometry (TG/MS) was used to characterize the pyrolysis behavior of the polymers. The TGA signal was recorded using a Netzsch STA 449 F1 Jupiter. Gases evolved during thermolysis were analyzed by a quadrupole mass spectrometer (Netzsch QMS 403 C Aeolos). The polymers were heated under an argon atmosphere from room temperature to 1400 ºC at a rate of 100 ºC/h.

High temperature TG was carried out at UC Davis using a Setaram SetSys 2400 in helium atmosphere. About 20-30 mg of powders previously pyrolyzed at 1100 ºC was placed into a lidded graphite crucible. The samples were heated at 10 °C/min from 1100 to 2100 °C. After the first run of each sample, a second, identical run was completed in order to obtain a background signal that was subtracted from the initial raw data.

Nuclear magnetic resonance (NMR) spectroscopy was conducted at room temperature on liquid state polymers using a 500 MHz Bruker DRX 500 spectrometer. The chemical environments of ^{1}H, ^{13}C and ^{29}Si were characterized. Tetramethylsilane was used as an external reference. Measurements were performed on 0.4 ml of sample mixed with 0.2 ml of deuterated C_6D_6 solvent.

Multinuclear MAS NMR spectra were collected at UC Davis on SiCN1-800, SiCN1-1100, SiBCN1-1100, SiBCN3-1100, SiCN4-1100, SiCN4-1400, SiBCN4-1100, SiBCN4-1400, Iso_SiCN5-800, and Iso_SiCN5-1100 using a Bruker Avance solid-state spectrometer operating at the Larmor frequencies of 99.3, 125.7, and 160.4 MHz, respectively, for the ^{29}Si, ^{13}C and ^{11}B nuclides. The ceramics were ground and then loaded into ZrO_2 rotors under argon atmosphere. Samples were spun at a rate of 14 kHz using a 4 mm Bruker CPMAS probe. All NMR spectra were externally referenced to tetramethylsilane for ^{29}Si and ^{13}C, and to a 0.1 M $Na_2B_4O_7$ solution for ^{11}B. Specific experimental parameters have been reported previously [131].

Solid state MAS NMR was performed on $[-(PhVi)Si-NH-]_n$ pre-crosslinked material, $[-(MeVi)Si-NH-]_n$ pre-crosslinked material; $\{B[-(C_2H_4)Si(Ph)-NH-]_3\}_n$ and $\{B[-(C_2H_4)Si(Me)-NH-]_3\}_n$ polymers; SiCN1-1400, SiBCN1-1400, SiCN2-1100, SiCN2-1400, SiBCN2-1100, SiBCN2-1400, SiCN3-1100, SiCN3-1400 and SiBCN3-1400 ceramics. The device used was a house-built 11.7 Tesla spectrometer with a 4 mm rotor probehead and with the frequencies of proton at 500.144 MHz, carbon at 125.777 MHz, and silicon at 99.355 MHz. The samples were spun at 6 kHz.

Small Angle X-ray scattering (SAXS) measurements on SiCN1 and SiBCN1 ceramics were completed using a SAXS device equipped with a Cu anode operating at 40 kv and 55 mA. Other equipment details include a 3-pinhole point focus, a 2-dimensional detector, and a designed q-range of 0.08 – 2.8 nm^{-1}. The usable q-range is between 0.014 and 0.5 1 $Å^{-1}$. Measurements were taken at room temperature. Samples were affixed to the sample chamber using office tape, and no sample holder was used.

SAXS measurements on SiCN2, SiBCN2, SiCN3, SiBCN3, SiCN4 and SiBCN4 ceramics prepared at 1100°C and 1400°C were measured at the Hamburger Synchrotronstrahlungslabor (HASYLAB) at the Deutsches Elektronen-Synchrotron (DESY) Research Centre of the Helmholtz Association, in Hamburg, Germany. Beamline A2 of the DORIS III storage ring was used. The wavelength was 0.15 nm, and the sample-detector distance was 1200 mm. The samples were loaded into 0.5 mm capillaries.

High temperature oxidative drop solution calorimetry in molten sodium molybdate solvent, as previously described in detail by Navrotsky [92,93], was conducted at UC Davis in order to determine the enthalpies of structural evolution. Pressed powder pellets (1-2 mg) were dropped from room temperature into molten sodium molybdate ($3Na_2O \cdot 4MoO_3$) solvent at about 800 °C in a custom-built Tian-Calvet twin microcalorimeter (Davis, CA). In order to maintain a oxidizing atmosphere, and to encourage rapid sample dissolution by solvent agitation, oxygen gas was bubbled through the solvent at 5 $ml \cdot min^{-1}$. All pellets dissolved within 1 hour, and were converted to dissolved oxides with the evolution of CO_2, N_2, and H_2O gases. To remove the evolved gases, and to maintain a constant atmosphere, oxygen gas was used to flush the headspace above the solvent at a rate of 90 $ml \cdot min^{-1}$. At least 8 experiments were carried out for each sample in order to obtain acceptable statistics. To determine the enthalpies of drop solution, ΔH_{ds}, the calorimeter was calibrated using the heat capacity of platinum. Additional details regarding calorimeter calibration can be found in the literature [95,132].

Impedance spectroscopy measurements were taken using a Broadband Dielectric/Impedance Spectrometer from Novocontrol Technologies. The system was equipped with a Alpha-A high performance frequency analyzer. Frequencies from 0.1Hz to 10^7 Hz were applied. The ceramic samples were polished and covered with silver paste prior to the measurements. Simulations of the results were carried out using Zview2 Software.

The ceramics used for the electrochemical studies were ground and sieved using a 40 µm mesh. For the electrode preparation, a mixture of 85 wt% of the ceramic, 5 wt% of Carbon Black Super P® (Timcal Ltd., Switzerland) and 10 wt% of polyvinylidenefluoride (PVdF, SOLEF, Germany) was dissolved into N-methyl-2-pyrrolidone (NMP, BASF, Germany). Additional NMP was added to adjust the viscosity of the mixture. The slurry was printed onto the rough side of a copper foil (10 µm, Copper SE-Cu58 (C103), Schlenk Metallfolien, Germany) by hand, and dried at 80°C for 24 h. Electrodes (7mm diameter) were cut from the coated copper foil and dried at 80°C under vacuum in a Buchi oven for 24 h. The dried electrodes were transferred to a glove box (MBraun, Germany) without further contact to air for the cell assembly. For electrochemical testing a Swagelok® type cell set up was chosen. The counter/reference electrode was cut out of metallic lithium foil (99.9% purity, 0.75 mm thickness, Alfa Aesar, Germany) to have a diameter of 10 mm. QMA (Whatmann™, UK) was used as a separator and 180 µl of LP30 (Merck, Germany) was added as the electrolyte. Electrochemical testing was performed using a VMP multipotentiostat (BioLogic Science Instruments). The same rate was used for the charge (C) and discharge (D) processes, with C = D at C/20 = 18 $mA \cdot g^{-1}$, C/10 = 36 $mA \cdot g^{-1}$, C/5 = 72 $mA \cdot g^{-1}$, C/ 2 = 180 $mA \cdot g^{-1}$, and C/1 = 360 $mA \cdot g^{-1}$. Charge is considered to be lithium insertion, while discharge is considered to be lithium extraction. All capacity calculations were completed taking into account that the active material only made up 85 wt % of the electrode.

3.7 Characterization of ceramics prepared at selected temperatures

Several pyrolysis temperatures have been chosen. 800ºC is the temperature at which the precursor begins to transform from polymer to ceramic, thus considerable hydrogen remains in the structure. 1100°C was selected since it is the standard temperature for producing amorphous PDCs. In most SiCN and SiBCN PDCs, 1400°C is considered the temperature at which phase separation begins, but no deleterious crystallization initiates.

Table 3 gives the chemical compositions of the ceramics. The chemical formulas were calculated by considering one Si atom per formula unit. The stoichiometric binary phases were also obtained based on elemental content.

Table 3 Chemical compositions of the synthesized ceramics

Preceramic polymer	Ceramic sample	Si wt% atom%	C wt% atom%	N wt% atom%	B wt% atom%	O wt% atom%	H wt% atom%	Cl wt% atom%	Empirical formula	Calculated phases (Mol%)				
										Free C	Si_3N_4	SiC	BN	SiO_2
[-(PhVi)Si-NCN-]$_n$	SiCN1-800	26.10 12.14	54.61 59.40	15.93 14.88	—	2.46 1.96	0.89 11.62	—	$SiC_{4.88}N_{1.22}O_{0.16}$	92.61	5.79	0.04	—	1.56
	SiCN1-1100	24.80 12.53	56.50 66.61	14.80 14.95	—	2.14 1.89	0.24 3.40	1.55 0.62	$SiC_{5.32}N_{1.19}O_{0.15}$	92.91	5.24	0.52	—	1.33
	SiCN1-1400	29.24 15.36	59.21 72.57	11.03 11.59	—	0.52 0.48	—	—	$SiC_{4.72}N_{0.75}O_{0.03}$	87.37	3.83	8.49	—	0.32
{B[-(C_2H_4)Si(Ph)-NCN-]$_3$}$_n$	SiBCN1-1100	23.79 12.62	51.32 63.54	16.58 17.59	3.05 4.20	2.21 2.05	—	—	$SiC_{5.03}N_{1.39}B_{0.33}O_{0.16}$	85.97	4.65	2.15	5.82	1.42
	SiBCN1-1400	28.21 14.83	51.08 62.64	16.19 17.02	3.06 4.17	1.46 1.34	—	—	$SiC_{4.22}N_{1.15}B_{0.28}O_{0.09}$	82.22	4.54	6.39	5.90	0.95
[-(MeVi)Si-NCN-]$_n$	SiCN2-1100	39.95 23.49	32.37 44.42	24.53 28.85	—	3.15 3.24	—	—	$SiC_{1.89}N_{1.23}O_{0.14}$	82.97	13.54	0.44	—	3.04
	SiCN2-1400	40.05 23.51	33.65 46.09	22.98 26.98	—	3.32 3.41	—	—	$SiC_{1.96}N_{1.15}O_{0.14}$	81.63	12.37	2.88	—	3.13
{B[-(C_2H_4)Si(Me)-NCN-]$_3$}$_n$	SiBCN2-1100	37.71 21.78	30.41 40.98	24.67 28.50	3.00* 4.49*	4.21 4.25	—	—	$SiC_{1.88}N_{1.31}B_{0.21}O_{0.20}$	73.38	11.20	3.08	8.38	3.97
	SiBCN2-1400	39.94 23.34	30.31 41.33	23.43 27.39	3.00* 4.55*	3.32 3.40	—	—	$SiC_{1.77}N_{1.17}B_{0.19}O_{0.15}$	69.10	10.72	8.47	8.53	3.19
[-(PhVi)Si-NH-]$_n$	SiCN3-1100	31.31 16.53	52.52 64.68	13.01 13.73	—	2.41 2.23	0,18 2.59	0.57 0.24	$SiC_{3.91}N_{0.83}O_{0.13}$	86.0	5.0	7.4	—	1.6
	SiCN3-1400	33.23 18.05	51.83 65.71	13.76 14.95	—	0.64 0.61	0.03 0.46	0.51 0.22	$SiC_{3.64}N_{0.83}O_{0.03}$	84.8	5.4	9.4	—	0.4
{B[-(C_2H_4)Si(Ph)-NH-]$_3$}$_n$	SiBCN3-1100	27.71 14.28	55.18 66.37	11.85 12.22	2,57 3.37	2.27 2.05	0,11 1.59	0.305 0.12	$SiC_{4.65}N_{0.86}B_{0.24}O_{0.14}$	81.9	3.0	9.1	4.6	1.4
	SiBCN3-1400	27.77 14.49	55.44 67.50	12.20 12.52	2.55 3.39	1.94 1.77	0.02 0.22	0.28 0.12	$SiC_{4.66}N_{0.86}B_{0.23}O_{0.12}$	82.0	3.1	9.1	4.6	1.2

Preceramic polymer	Ceramic sample	Si wt% atom%	C wt% atom%	N wt% atom%	B wt% atom%	O wt% atom%	H wt% atom%	Cl wt% atom%	Empirical formula	Calculated phases (Mol%)				
										Free C	Si_3N_4	SiC	BN	SiO_2
[-(MeVi)Si-NH-]$_n$	SiCN4-1100	51.75 31.01	29.19 40.81	17.10 20.49	—	1.56 1.64	0.36 6.04	0.04 0.02	$SiC_{1.32}N_{0.66}O_{0.05}$	55.6	11.0	31.7	—	1.8
	SiCN4-1400	51.283 31.55	29.84 42.84	17.23 21.20	—	1.44 1.55	0.165 2.84	0.042 0.02	$SiC_{1.36}N_{0.67}O_{0.05}$	57.2	10.8	30.4	—	1.6
{B[-(C_2H_4)Si(Me)-NH-]$_3$}$_n$	SiBCN4-1100	48.36 29.70	28.85 41.35	13.60 16.71	4.52 7.07	4.63 4.98	0.01 0.17	0.03 0.01	$SiC_{1.39}N_{0.56}B_{0.24}O_{0.17}$	40.1	4.5	37.5	13.3	4.7
	SiBCN4-1400	48.20 29.55	28.39 40.62	14.09 17.28	4.68 7.44	4.59 4.93	0.01 0.17	0.04 0.02	$SiC_{1.37}N_{0.58}B_{0.25}O_{0.17}$	39.5	4.6	37.2	14.0	4.7
$^{13}C/^{15}N$ isotope-enriched [-Si(Ph)-(NCN)$_{1.5}$-]$_n$	Iso_SiCN5-800	24.03 9.59	37.08 34.53	30.54 24.38	—	5.90 4.12	2.45 27.38	—	$SiC_{3.60}N_{2.54}O_{0.43}$	74.5	7.9	C_3N_4 11.2	—	6.5
	Iso_SiCN5-1100	28.11 13.39	39.16 43.52	29.94 28.52	—	1.81 1.51	0.98 13.07	—	$SiC_{3.25}N_{2.13}O_{0.11}$	81.5	9.9	C_3N_4 6.8	—	1.8
[-Si(Ph)-(NH)$_{1.5}$-]$_n$	SiCN6-1100	34.59 18.43	46.86 58.25	16.04 17.09	—	2.13 0.99	0.35 5.22	0.03 0.01	$SiC_{3.16}N_{0.93}O_{0.11}$	84.4	6.7	7.3	—	1.6

* samples have not been measured, the values are estimated from the ratio of starters in polymer reactions and the ceramic yield.

Figure 10 reveals that in a composition diagram, the compositions of all ceramics pyrolyzed at 1100 ºC lie within the triangular region constituted by Si_3N_4, SiC and "free" carbon. The compositions of SiCN1-1100, SiBCN1-1100, SiCN2-1100 and SiBCN2-1100 ceramics, which are derived from poly(boro)silylcarbodiimides, are near the Si_3N_4-carbon tie-line. Meanwhile, ceramics derived from poly(boro)silazanes, by calculation, have a greater SiC component.

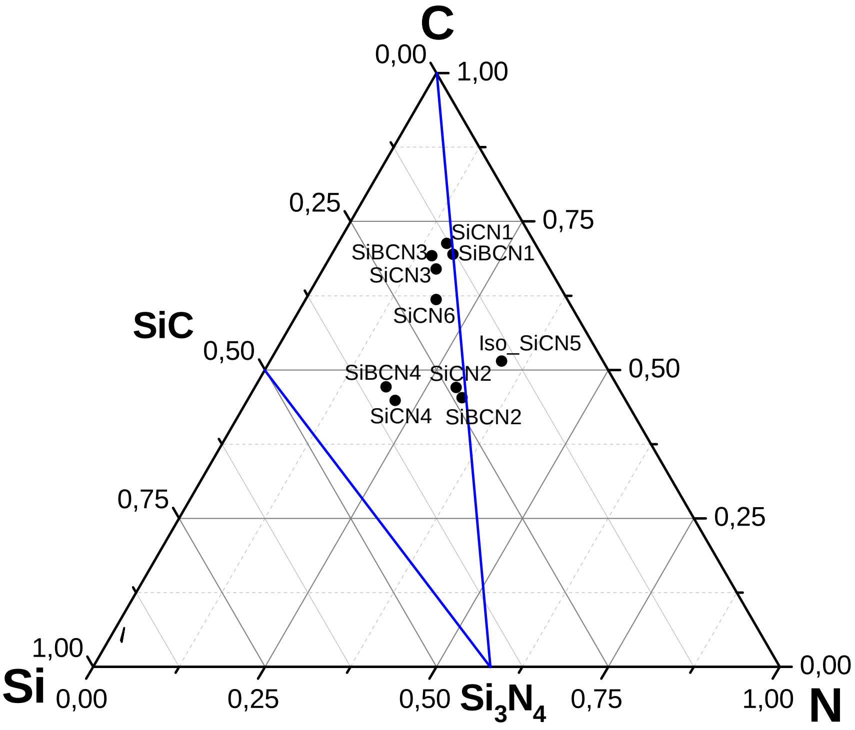

Figure 10 The compositions of the ceramics pyrolyzed at 1100 ºC marked in a Si-C-N ternary composition diagram

Disregarding hydrogen and boron contents, the compositions of Si, C, N elements in the synthesized poly(boro)phenylvinylsilylcarbodiimide, poly(boro)methylvinylsilylcarbodiimide, poly(boro)phenylvinylsilazane, poly(boro)methylvinylsilazane and ^{13}C/ ^{15}N isotope-enriched polyphenylsilsesquicarbodiimide have the formulas SiN_2C_9, SiN_2C_4, $SiNC_8$, $SiNC_3$, $SiN_3C_{7.5}$ and $SiN_{1.5}C_6$, respectively. From the locations of their compositions in the diagram, Si atoms prefer to bond to N to form Si_3N_4, and extra Si bonds to C to form SiC. In the Iso_SiCN5 ceramics, which contain considerably more N than the other ceramics, after bonding to Si, residual N bonds to C. The existence of "free" carbon is a common characteristic in all of these ceramics.

4. Results and discussion

4.1 Polymer synthesis and processing

The procedures for polymer synthesis were given in Chapter 3. In this Section, important characterization results for the obtained polymers are presented. The critical processing steps for producing bulk ceramics, namely polysilylcarbodiimides and polysilazanes pre-crosslinking and polyborosilazanes pre-pyrolysis, are discussed in Sections 4.1.1 and 4.1.2, respectively. The formation of branched polysilylsesquicarbodiimide is discussed in Section 4.1.3, followed by the synthesis of its ^{15}N/ ^{13}C isotope-enriched counterpart. More details of the polymer synthesis can be found in the references [131,133–137].

4.1.1 Synthesis of poly(boro)silylcarbodiimides and bulk ceramic processing

The polymer precursors were characterized by NMR spectroscopy. Figure 11(a) shows the ^{29}Si NMR DEPT spectra for both polyphenylvinylsilylcarbodiimide and polymethylvinylsilylcarbodiimide after by-product removal. The signal at -46 ppm represents the Si environment in -(NCN)-(PhVi)Si-(NCN)- and the peak at -34 ppm is from the end group -(NCN)-(PhVi)Si-Cl. The strong peak at -46 ppm indicates that the linear $[-(PhVi)Si-NCN-]_n$ is obtained through the designed route. The reaction products of $[-(MeVi)Si-NCN-]_n$ are shown by three significant peaks. A shift at -37 ppm is from the basic polymer structure, -(NCN)-(MeVi)Si-(NCN)-. This result verifies that $[-(MeVi)Si-NCN-]_n$ was successfully synthesized. Two kinds of end groups, $-SiMe_3$ and -(NCN)-(MeVi)Si-Cl, are found located at ca. 0 ppm and -12 ppm, respectively.

Figure 11 (b) compares the ^1H NMR spectra of $[-(PhVi)Si-NCN-]_n$ and $[-(MeVi)Si-NCN-]_n$. $[-(PhVi)Si-NCN-]_n$ shows peaks between 7 ppm and 8 ppm, which is typical for phenyl groups. The multiple peaks between 5.5 ppm and 6 ppm in both polymers result from vinyl groups. The polymer, $[-(MeVi)Si-NCN-]_n$, shows strong peaks around 0 ppm due to the methyl groups—the functional methyl groups, and the methyl groups from the end-group $-SiMe_3$. $[-(PhVi)Si-NCN-]_n$ also has methyl groups which are end-groups in the same chemical shift range. There are two additional small peaks in the $[-(PhVi)Si-NCN-]_n$ spectra at ca. 0.9 ppm and 1.5 ppm, which represent the $-CH_2-$ and -CH- groups. These signals may be from the small amount of saturated vinyl groups from the polymer synthesis.

Figure 11(c) shows the ^{13}C NMR spectra of $[-(PhVi)Si-NCN-]_n$ and $[-(MeVi)Si-NCN-]_n$. The peaks belonging to the -N=C=N- groups and the benzene solvent C_6D_6 are at ca. 120 ppm. Phenyl groups have chemical shifts between 126 ppm and 131 ppm. Signals for the vinyl groups are located at about 136 ppm. In addition to these peaks, $[-(MeVi)Si-NCN-]_n$ is also characterized by the peak around 0 ppm, which is again the signal for the methyl substituents and methyl end-groups. The ^{13}C NMR DEPT spectra (Figure 11 (d)) differ between the odd and even protons bonded to carbon atoms. The signals from the -N=C=N-groups and C_6D_6 are not detectable in the ^{13}C DEPT NMR spectra. The difference between the carbons in the phenyl and vinyl groups can be distinguished with the help of ^{13}C NMR. Carbon atoms with an even number of protons have negative intensities, as shown by the signal at 136 ppm for the vinyl group in Figure 11(d). Signals from phenyl groups have positive intensity.

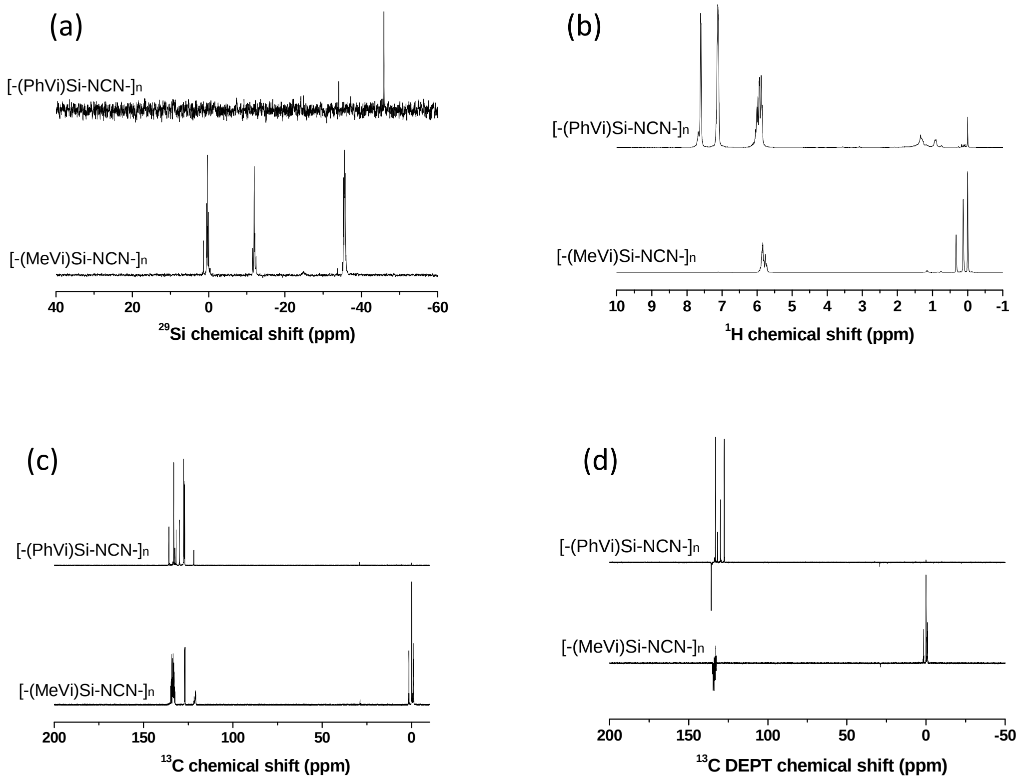

Figure 11 (a) ^{29}Si, (b)^{1}H, (c)^{13}C, (d)^{13}C DEPT NMR spectra of [-(PhVi)Si-NCN-]$_n$ and [-(MeVi)Si-NCN-]$_n$

As previously discussed, the ^{29}Si NMR spectra show that [-(PhVi)Si-NCN-]$_n$ and [-(MeVi)Si-NCN-]$_n$ are linear polymers. Since they are liquid (honey-like) after synthesis, in order to accomplish bulk ceramic shaping, a pre-crosslinking process is needed. This is the most critical step, since polymer solidification is needed through the polymerization of vinyl groups. Meanwhile, some of the C=C bonds must remain active for the warm pressing step (Figure 12, [-(PhVi)Si-NCN-]$_n$ as an example). Partial pre-crosslinking, as opposed to full crosslinking, is essential. This step was optimized after a systematic study of varied temperatures and heat treatment times.

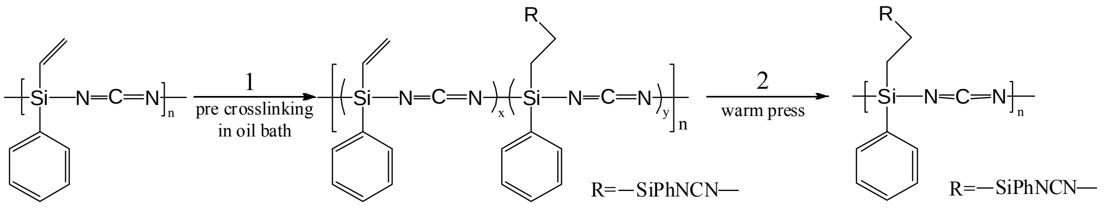

Figure 12 partially pre-crosslinking step of [-(PhVi)Si-NCN-]$_n$

For [-(PhVi)Si-NCN-]$_n$, heat treating at 255°C for 5 h is optimal, while for [-(MeVi)Si-NCN-]$_n$, 320°C for 5 h is optimal. From ^{1}H NMR (Figure 13), some vinyl groups remain after pre-crosslinking, and the signal intensity of the saturated -CH$_2$- and -CH- increased. The partially saturated vinyl groups meet the needs of warm-pressing.

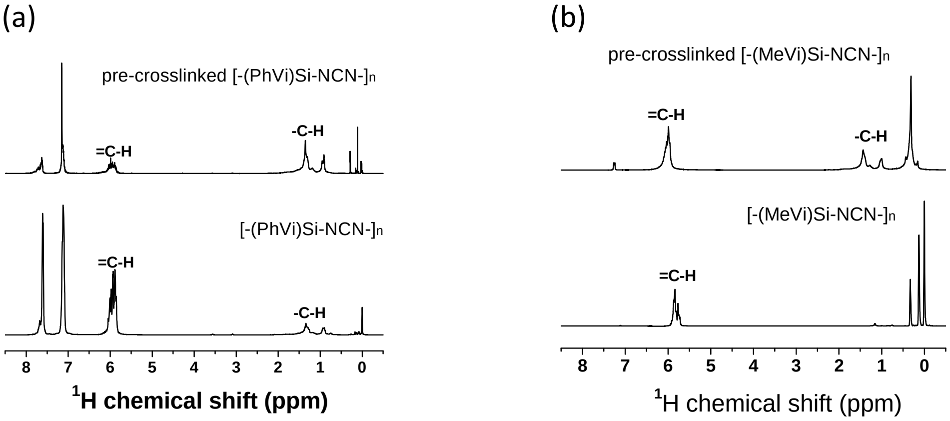

Figure 13 ^{1}H NMR of the comparison of polymer and pre-crosslinked material for (a) [-(PhVi)Si-NCN-]$_n$ and (b) [-(MeVi)Si-NCN-]$_n$

Boron-modified polyborophenylvinylsilylcarbodiimide and polyboromethylvinylsilylcarbodiimide are synthesized via hydroboration of polyphenylvinylsilylcarbodiimide and polymethylvinylsilylcarbodiimide, respectively. Vinyl groups were mostly saturated by reaction with BH$_3$. The obtained polyborophenylvinylsilylcarbodiimide and polyboromethylvinylsilylcarbodiimide have crosslinked network structures. No extra pre-crosslinking process is needed for warm-pressing.

Green body compacts were produced via the warm presssing of polyborosilylcarbodiimides and pre-crosslinked polysilylcarbodiimides. Figure 14 shows the warm-pressed green bodies.

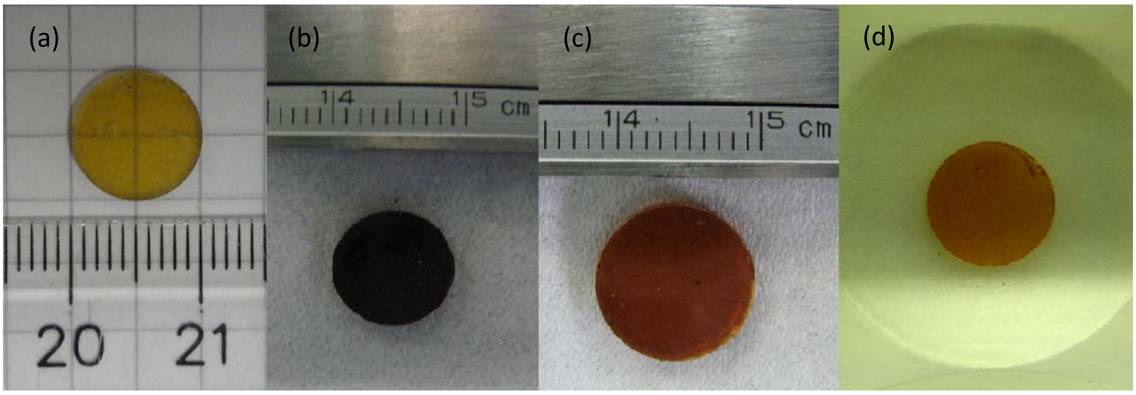

Figure 14 Warm pressed greenbodies derived from (a) [-(PhVi)Si-NCN-]$_n$, (b) [-(MeVi)Si-NCN-]$_n$, (c) {B[-(C$_2$H$_4$)Si(Ph)-NCN-]$_3$}$_n$, (d) {B[-(C$_2$H$_4$)Si(Me)-NCN-]$_3$}$_n$

4.1.2 Synthesis of poly(boro)silazanes and bulk ceramic processing

Polysilazanes as polymer precursors were traditionally sythesized by ammonolysis or aminolysis reactions of chlorosilane [56]. Polyborosilazanes are usually synthesized through the hydroboration of vinyl-containing polysilazanes. In this reaction, borane reacts with the vinyl groups, and the saturation of the vinyl groups leads to cross-linking and the formation of a 3D network structure.

The newly obtained polysilazane polymers were synthesized using a reflux method. Polyborosilazanes are the hydroboration products of polysilazanes. The synthesis route is described in Chapter 3. The resultant polyborosilazanes are solid at room temperature, but can be melted at temperatures greater than 85°C. This offers a good opportunity to employ various plastic forming techniques to produce polymer-derived SiBCN ceramic parts.

Another advantage of this reflux synthesis route of polysilazanes is that it avoids the filtration of NH_4Cl, which was formed as a solid by-product, and is not easily separated from the mixture in the traditional synthesis of polysilazanes. In this work, the by-product, which was formed during the synthesis of $[-(PhVi)Si-NH-]_n$ and $[-(MeVi)Si-NH-]_n$, namely Me_3SiCl, was liquid and could be easily removed by vacuum drying. There also have been studies on using a reflux method for the synthesis of polysilazane, without a catalyst [69,70], or with $AlCl_3$ as the catalyst [70]. However, the properties of the polymers produced by these methods have not been reported.

^{29}Si and ^{13}C DEPT NMR measurements were completed on the as-synthesized polysilazanes (Figure 15). Two bands at ca. -25 ppm for $[-(PhVi)Si-NH-]_n$ (Figure 15(a)) indicate the Si environment in the -NH-Si(PhVi)-NH- group. The peaks between 0 and 10ppm are from the intermediate product, $Cl-(PhVi)Si-NH-SiMe_3$, and the residual monomer, phenylvinyldichlorosilane, respectively. The residual by-product, Me_3SiCl, shows a weak peak at 30ppm. The spectrum of $[-(MeVi)Si-NH-]_n$ shows peaks at ca.-12 to -22ppm which indicate -NH-(MeVi)Si-NH-. The signal for the end group, -(MeVi)Si-Cl, appears at ca. -10ppm. A signal at 2ppm is the residual starter HMDS. The ^{13}C DEPT NMR spectrum (Figure 15(b)) contains two peaks between 130 ppm and 140 ppm corresponding to =CH- and $=CH_2$, as observed for both $[-(PhVi)Si-NH-]_n$ and $[-(MeVi)Si-NH-]_n$. In addition, $[-(PhVi)Si-NH-]_n$ also has a signal at 125 ppm, which represents phenyl groups. These spectra confirm the formation of expected polymer structures.

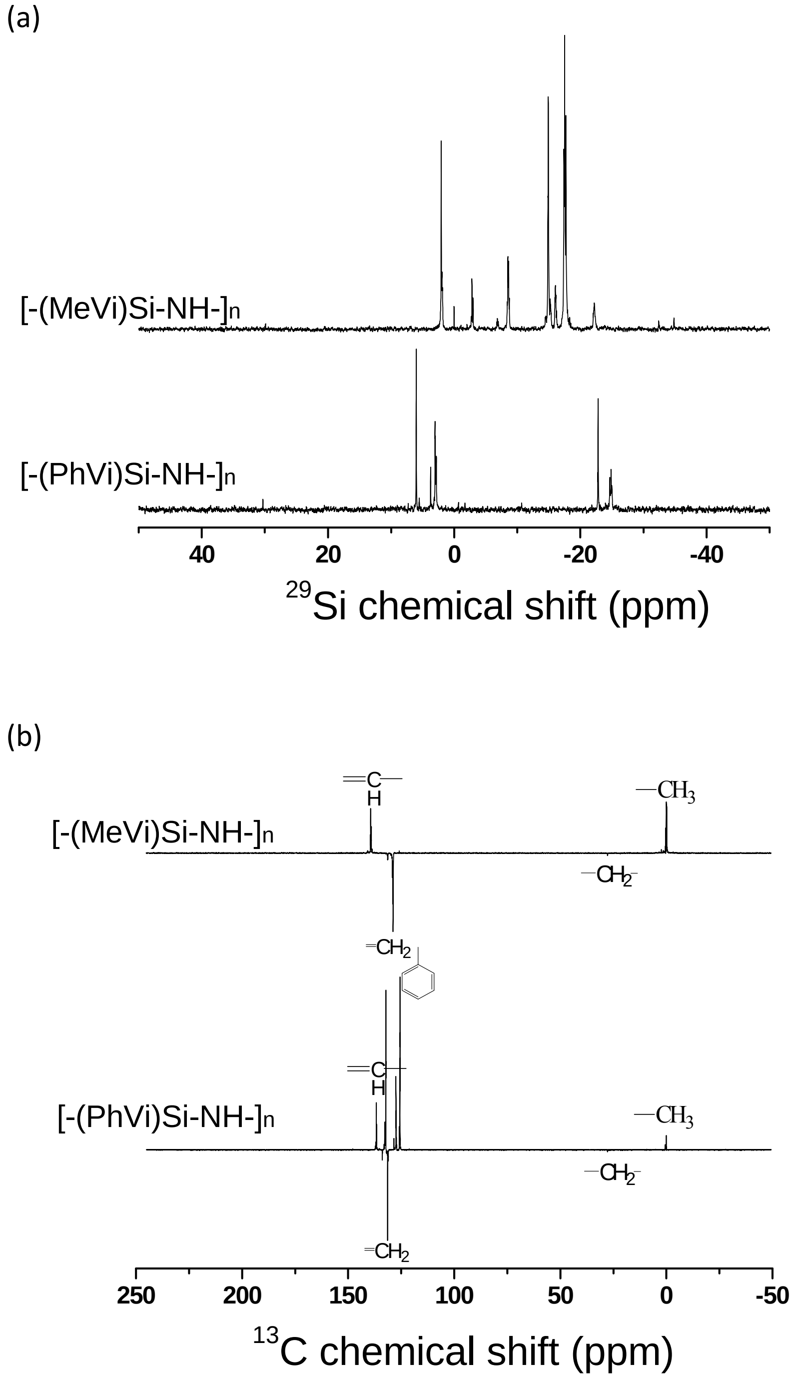

Figure 15 (a) ^{29}Si DEPT NMR (b) ^{13}C DEPT NMR spectra of [-(PhVi)Si-NH-]$_n$ and [-(MeVi)Si-NH-]$_n$

Similar to polysilylcarbodiimides, polysilazanes need a pre-crosslinking process (by heating) before warm pressing. The optimized heating temperature and treatment time are 300ºC for 5 hours for [-(PhVi)Si-NH-]$_n$, and 320ºC for 5 hours for [-(MeVi)Si-NH-]$_n$. ^{29}Si and ^{13}C MAS NMR were measured on pre-crosslinked polymers. The ^{29}Si MAS NMR of pre-crosslinked [-(PhVi)Si-NH-]$_n$ (Figure 16(a)) mainly has two peaks around -26 and -15 ppm, which represent -N-(PhVi)Si-N- cites and -N-Si(PhC^{sp3})-N- sites. Sp^3 C in -N-Si(PhC^{sp3})-N-sites are from the polymerisation of vinyl groups. The bands of [-(MeVi)Si-NH-]$_n$ are mainly centered at -18 and -5 ppm signify -N-(MeVi)Si-N- cites and -N-Si(MeC^{sp3})-N- sites. The positions of these Si environments are reported in reference [102]. Similarly, sp^3 C in -N-Si(MeC^{sp3})-N- sites are from vinyl saturation. These results demonstrate that vinyl groups are partially saturated in the pre-crosslinking step. The unsaturated vinyl groups are essential for the following warm pressing process.

^{13}C MAS NMR (Figure 16(b)) also demonstrates that the pre-crosslinked [-(PhVi)Si-NH-]$_n$ and [-(MeVi)Si-NH-]$_n$ still have unsaturated vinyl bonds. The two peaks of =CH- and =CH$_2$ appear between 130ppm and 140ppm for both the [-(PhVi)Si-NH-]$_n$ and [-(MeVi)Si-NH-]$_n$ pre-crosslinked materials. They are located in the same region as in the liquid state NMR spectra (Figure 15(b)), which were collected on as-synthesized polymers. The residual unsaturated bonds are important because they help the monolith shaping via warm-presssing. The peaks at ca. 126 ppm in the ^{13}C solid state MAS NMR spectra of [-(PhVi)Si-NH-]$_n$ pre-crosslinked material are from phenyl groups, and that at 0 ppm are from methyl groups for both [-(PhVi)Si-NH-]$_n$ and [-(MeVi)Si-NH-]$_n$ pre-crosslinked materials. The signal is not intense in the case of [-(PhVi)Si-NH-]$_n$ pre-crosslinked material, because the methyl groups only come from the saturated vinyl groups. The peak is very strong in the spectrum of pre-crosslinked [-(MeVi)Si-NH-]$_n$ since this precursor has a methyl group attached to silicon.

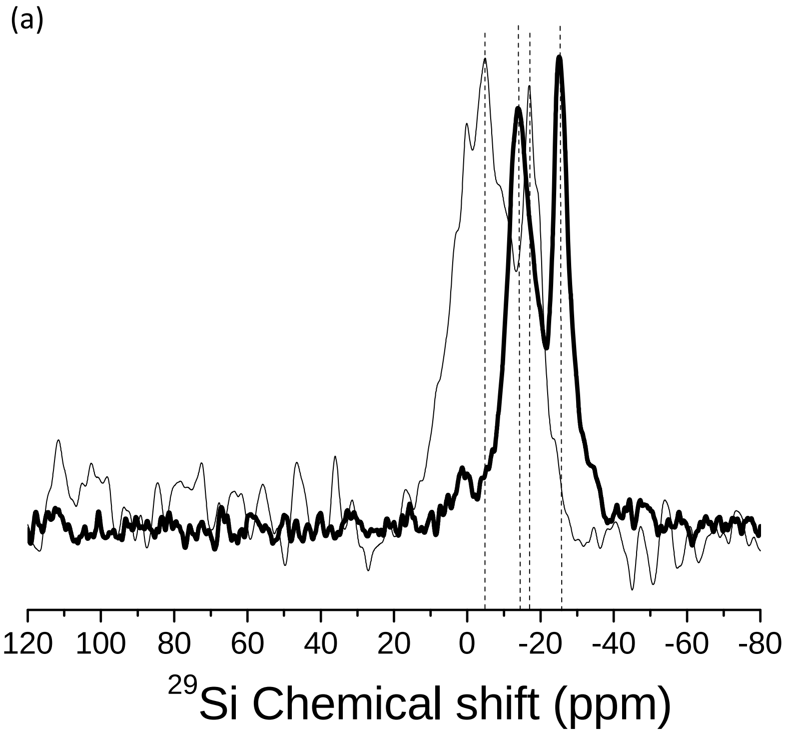

(b)

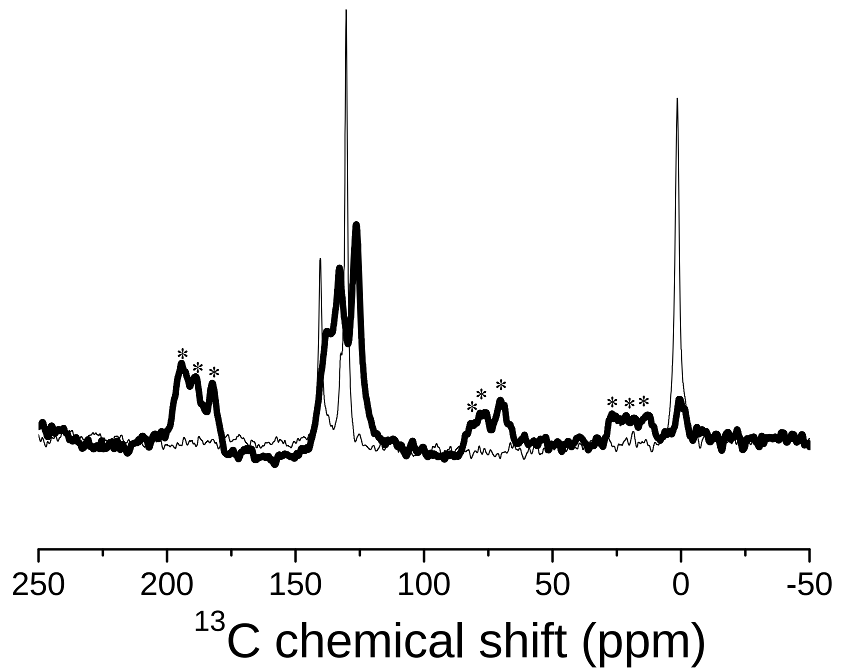

Figure 16 (a) ^{29}Si and (b) ^{13}C MAS NMR of pre-crosslinked [-(PhVi)Si-NH-]$_n$ (bold line) and [-(MeVi)Si-NH-]$_n$ (thin line). The asterisks in ^{13}C MAS NMR spectra represent spinning side bands

^{29}Si, ^{13}C and ^{11}B MAS NMR (Figure 17) spectra of the boron modified polyborosilazanes were measured. The peaks at ca. -31 and -19 ppm in the ^{29}Si MAS NMR spectrum of {B[-(C_2H_4)Si(Ph)-NH-]$_3$}$_n$ are due to -N-(PhVi)Si-N- cites and -N-Si(PhC^{sp3})-N- sites, respectively. Similarly, the peaks at ca. -20 and -7 ppm in the ^{29}Si MAS NMR spectrum of {B[-(C_2H_4)Si(Me)-NH-]$_3$}$_n$ are due to -N-(MeVi)Si-N- cites and -N-Si(MeC^{sp3})-N- sites, respectively. The signal at ca. -1 ppm for both polymers is due to -N-Si(C^{sp3})$_3$ cites which indicate the end groups. The presence of big amount end groups reveals the existence of low molecular weight borosilazane oligomers in the samples.The ^{13}C MAS NMR spectra of boron-containing polymers are similar to the pre-crosslinked boron-free polymers. Through the reaction with borane, vinyl groups are partially saturated. Signals at ~130 and ~140 ppm are due to the unsaturated carbon double bonds. The saturated –CH_2– are manifested as peaks at ca. 10 ppm. The band near 28ppm is a signal of the saturated —CH– bonds, and that at about 0 ppm is from the –CH_3bonds. The appearance of saturated vinyl groups confirms the hydroboration reaction. The most intense bands in the ^{11}B MAS NMR spectra are at ~50 and 0 ppm, which are signals of the C_2B-N bonds and $C_3B \leftarrow N$ environments, respectively. BC_3 bonds are manifested as bumps at ca. 70 ppm. From the difference in the integrated intensity beneath these bands, {B[-(C_2H_4)Si(Me)-NH-]$_3$}$_n$ has more B-C and less B-N bondingthan {B[-(C_2H_4)Si(Ph)-NH-]$_3$}$_n$.

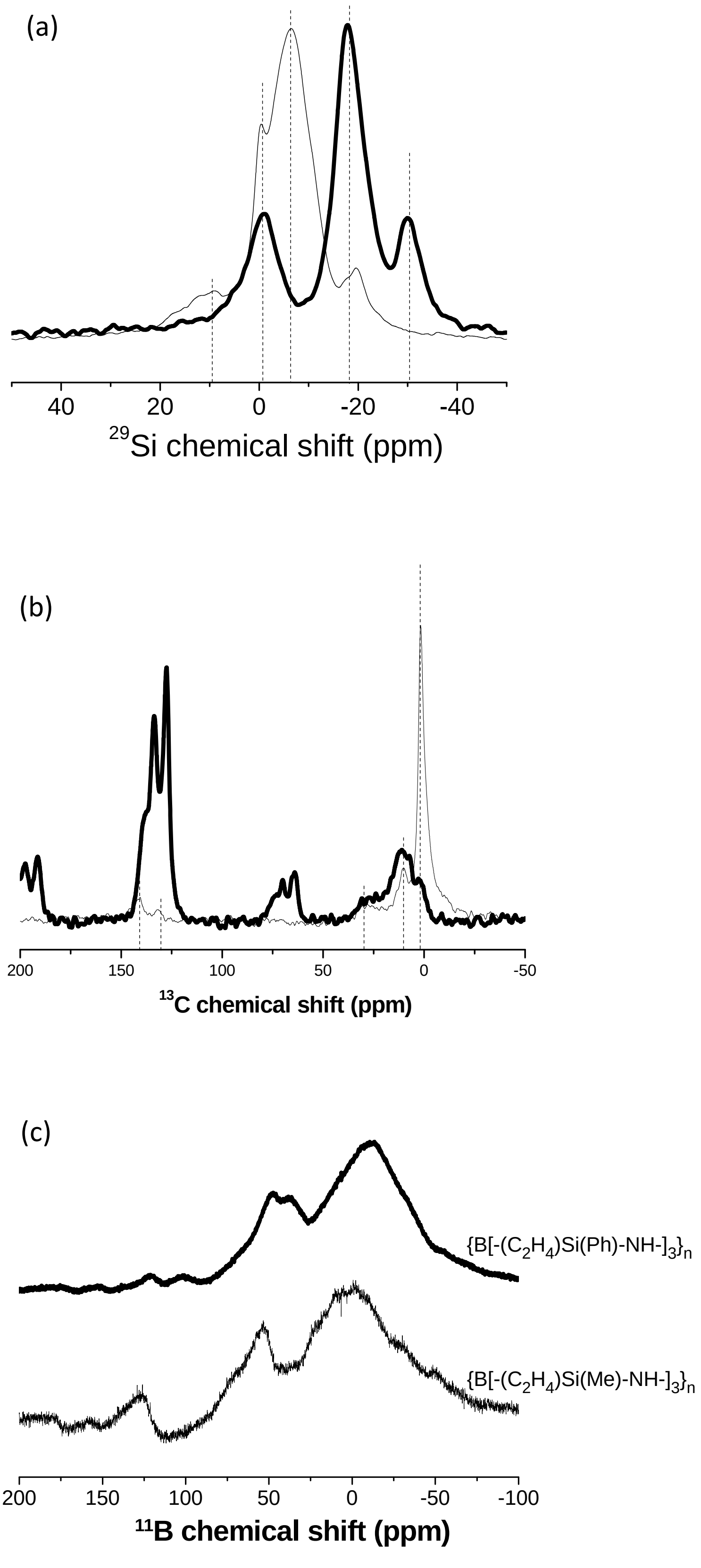

Figure 17 (a) ^{29}Si, (b) ^{13}C and (c) ^{11}B MAS NMR of polyborosilazanes

There are two kinds of bonds connecting B and N. The formation of C_2B-N bonds suggests dehydrocoupling of B-H and N-H (Figure 18(a)). The appearance of $C_3B{\leftarrow}N$ environments suggests that boron atoms bond to nitrogen atoms via coordinate covalent bonds (Figure 18(b)). The B-N bonding may impede the formation of branched polymer with big molecular weight. This explains the low melting point of these boron-containing samples.

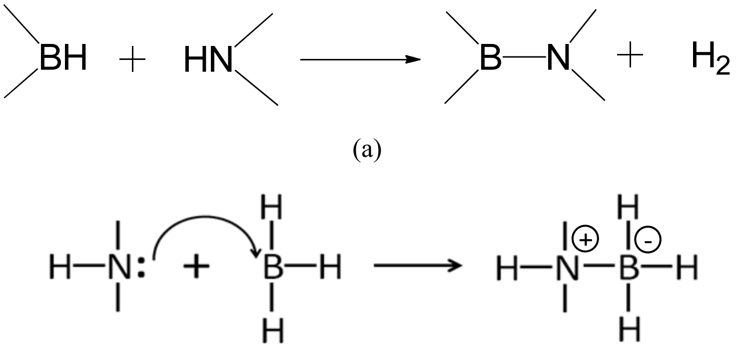

(a)

(b)

Figure 18 (a) dehydrocoupling of B-H and N-H, (b) boron bonds to nitrogen via formation of adducts

Similar results of B-N bonding can also be observed in the FT-IR measurements (Figure 19). The peaks found around 1380 cm^{-1}, 1100 cm^{-1} and 780 cm^{-1} are from B-N bonds. B-C bonds are found at ca. 1270 cm^{-1} and 1020 cm^{-1}. At the same time, N-H bonds, which are located at about 3400cm^{-1}, are also found, meaning N-H groups obviously still exist in the structure. Some of these take part in the reaction with borane. =C-H bonds and C=C bonds, which were found at about 2930 cm^{-1} and 1600 cm^{-1}, respectively, represented the remaining vinyl groups which did not react with borane.

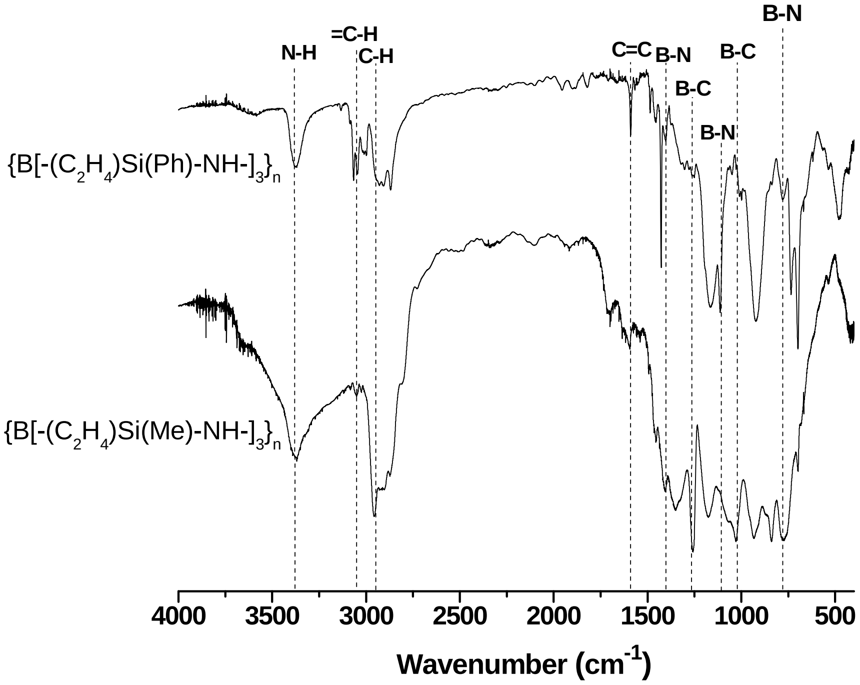

Figure 19 FT-IR of polyborosilazanes

As discussed, pre-pyrolysis is necessary for shaping thermoplastic {B[-(C_2H_4)Si(Ph)-NH-]$_3$}$_n$ and {B[-(C_2H_4)Si(Me)-NH-]$_3$}$_n$. The pre-pyrolyzed materials act as self-fillers in warm-pressing. Thermalgravimetry was studied from room temperature to 1400°C (Figure 20). The mass loss of the polymers due to gas evolution basically occurred in two steps. {B[-(C_2H_4)Si(Ph)-NH-]$_3$}$_n$ has a first mass loss step above 200°C, while {B[-(C_2H_4)Si(Me)-NH-]$_3$}$_n$ begins to lose mass at a much lower temperature. This mass loss is likely due to the oligomers, which are easily removed during thermolysis. Both {B[-(C_2H_4)Si(Ph)-NH-]$_3$}$_n$ and {B[-(C_2H_4)Si(Me)-NH-]$_3$}$_n$ have a second gas-release step from 400°C to 700°C. Mass spectra were measured, as shown in Figure 21, the mass-to-charge ratios (i.e., m/z values) of these gasses are 78 for C_6H_6, 52 for C_2N_2, 41 for CH_3-CN, 27 for HCN, 17 for NH_3, 16 for CH_4, and 2 for H_2. N_2 (28) is also detected, but is not given in the figure, because during the measurements the purge gas (air) was also detected. Thus, the "detected" amount of evolved N_2, which has a mass fragment of m/z=28, was partially from N_2 in the purge gas.Self-fillers were produced by the thermolysis of both polymers at 500°C. According to the TG analysis, at this temperature, a significant amount of gas is released, but the decomposition of the polymers is not yet complete. Gasses, including H_2, CH_4 and NH_3, keep releasing above 500 °C.

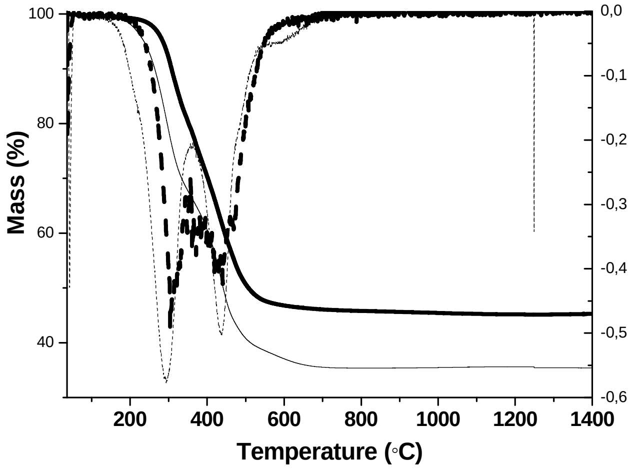

Figure 20 TG (solid line) and DTG (dash line) of {B[-(C_2H_4)Si(Ph)-NH-]$_3$}$_n$ (bold line) and {B[-(C_2H_4)Si(Me)-NH-]$_3$}$_n$ (thin line)

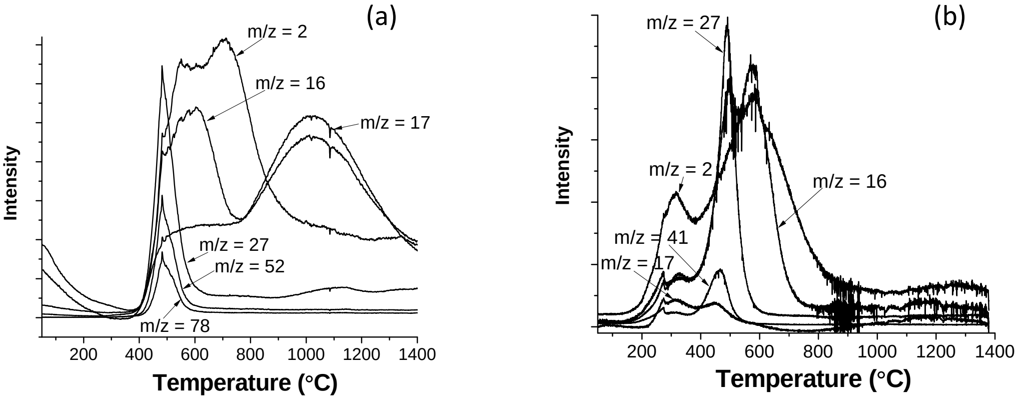

Figure 21 Mass loss of (a) $\{B[-(C_2H_4)Si(Ph)-NH-]_3\}_n$ and (b) $\{B[-(C_2H_4)Si(Me)-NH-]_3\}_n$ during second gas-releasing step

MS spectra confirm that the pre-pyrolyzed samples are intermediate materials between polymer and ceramic—they still maintain a certain amount of organic groups. The remaining organic groups in pre-pyrolyzed powders, e.g. N-H and C=C-H, offer the opportunity to react further with as-synthesized polymer. This process helps the achievement of warm-pressing. FT-IR spectra measured on the 500°C pre-pyrolyzed samples are shown in Figure 22. Organic groups including =C-H, -C-H and N-H can still be detected in the structure. This result is constant with MS spectra.

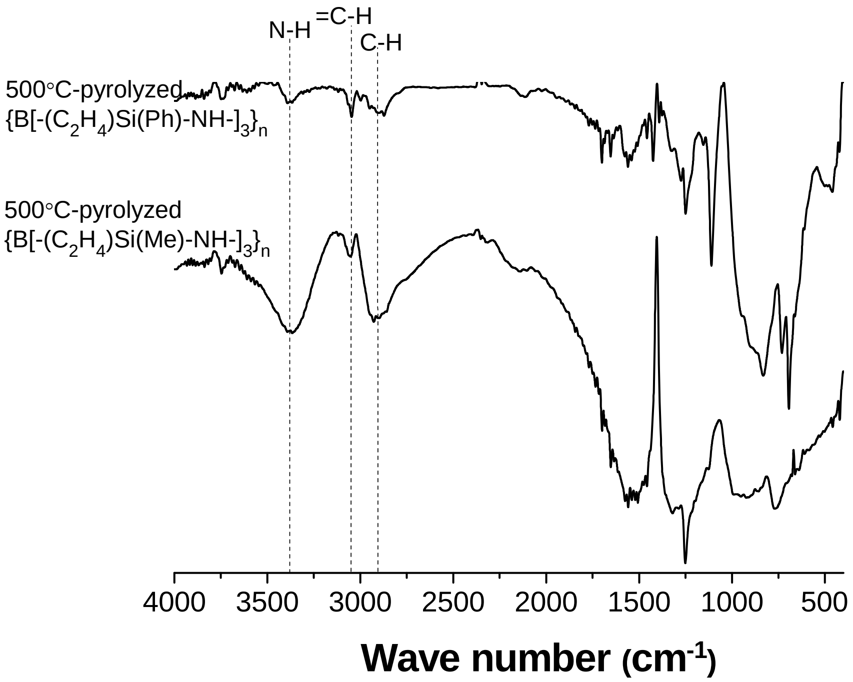

Figure 22 FT-IR spectra of 500 °C pre-pyrolyzed $\{B[-(C_2H_4)Si(Ph)-NH-]_3\}_n$ and $\{B[-(C_2H_4)Si(Me)-NH-]_3\}_n$

Monoliths from boron-free $[-(PhVi)Si-NH-]_n$ and $[-(MeVi)Si-NH-]_n$ were warm-pressed using pre-crosslinked materials (as discussed before). Boron-containing $\{B[-(C_2H_4)Si(Ph)-NH-]_3\}_n$ and $\{B[-(C_2H_4)Si(Me)-NH-]_3\}_n$ were warm-pressed using a mixture of the pre-pyrolyzed powder and the original polymers. The original polymers offer the fluidity needed for shaping, while the pre-pyrolyzed powder acted as fillers to form the skeleton of the compacts. The ratio of the pre-pyrolyzed powder to the polymer was adjusted in order to obtain a dense greenbody compact without signficant defects. As shown in Figure 23, essentially defect-free green bodies and pyrolyzed ceramics (at 1100^{0}C, Figure 24) were obtained from all precursors.

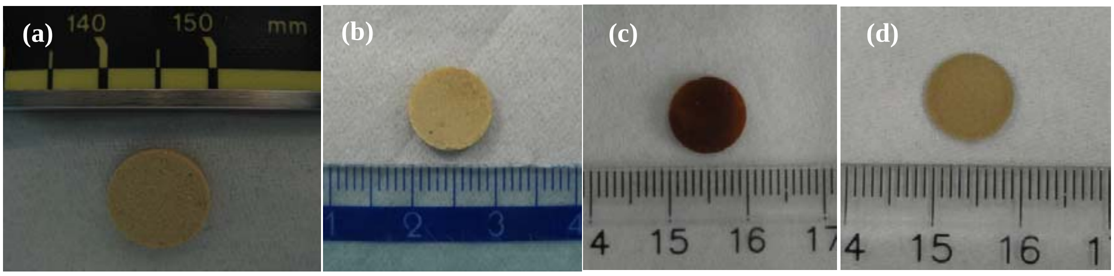

Figure 23 warm-pressed greenbodies from the precursors: (a) $[-(PhVi)Si-NH-]_n$, (b) $[-(MeVi)Si-NH-]_n$, (c) $\{B[-(C_2H_4)Si(Ph)-NH-]_3\}_n$ and (d) $\{B[-(C_2H_4)Si(Me)-NH-]_3\}_n$

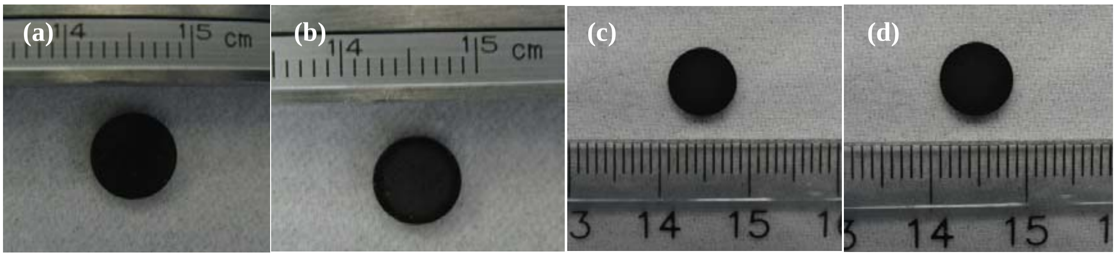

Figure 24 (a) SiCN3, (b) SiCN4, (c) SiBCN3 and (d) SiBCN4 bulk ceramics pyrolyzed at 1100^{0}C

SEM of the ceramics pyrolyzed at 1100^{0}C reveal an essentially defect-free, homogeneous structure. The corresponding crosssections are shown in Figure 25.

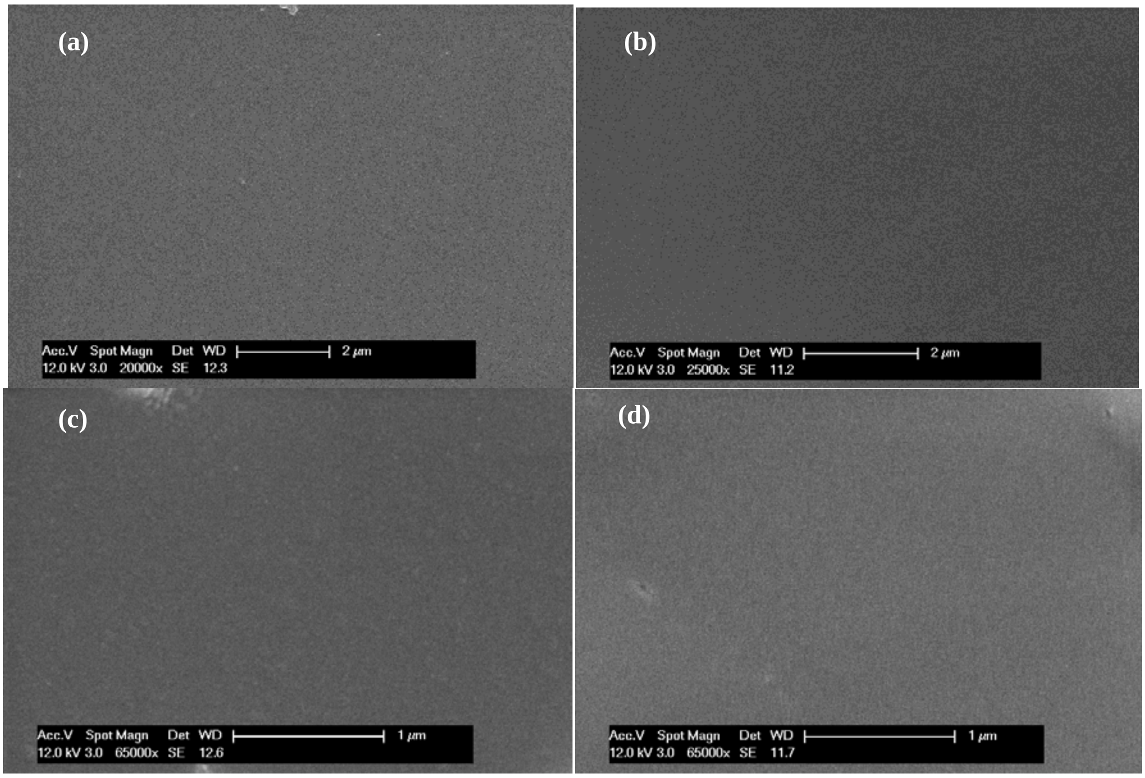

Figure 25 SEM of crosssections of (a) SiCN3, (b) SiCN4, (c) SiBCN3 and (d) SiBCN4 monoliths pyrolyzed at 1100 ^oC

As a short summary, in order to produce ceramic monoliths, the polysilazanes are pre-crosslinked and warm-pressed. the polyborosilazanes are good binders in plastic forming, using the pre-pyrolyzed powder as self-fillers. The optimized ratio between original polymer and pre-pyrolyzed powder was found. Bulk green bodies were formed, and finally, compact ceramic monoliths were produced after pyrolysis at 1100 °C.

4.1.3 Polysilsesquicarbodiimide and $^{13}C/^{15}N$ isotope-enriched polysilsesquicarbodiimide

Due to the low natural abundance of ^{15}N (0.37%), it is very difficult to detect the ^{15}N nucleus by NMR Therefore the nitrogen environments in polymer-derived SiCN ceramics was previously not well understood. In this work, by enriching the reactant chemicals with the ^{15}N isotope, it was possible to investigate nitrogen cites in the synthesized polymers and the derived ceramics.

As shown in Chapter 3, unenriched polyphenylsilsesquicarbodiimide was synthesized from bis(trimethylsilyl)carbodiimide and trichlorophenylsilane. The $^{13}C/^{15}N$ isotope-enriched polyphenylsilsesquicarbodiimide was synthesized from isotope enriched-cyanamide and trichlorophenylsilane. $^{13}C/^{15}N$ isotope-enriched polyphenylsilsesquicarbodiimide was obtained by adding 10% ^{15}N and ^{13}C isotope-labeled cyanamide. The synthesis of the polymer from the labeled cyanamide is shown in Scheme 15.

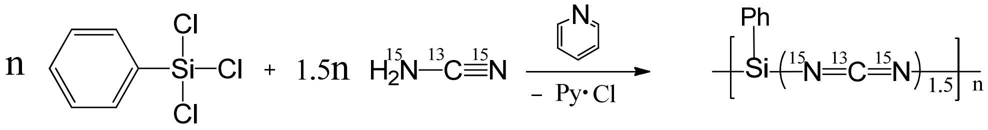

Scheme 15 Synthesis of $^{13}C/^{15}N$ isotope-enriched polyphenylsilsesquicarbodiimide

^{29}Si and ^{13}C MAS NMR (Figure 26) measurements were made on the as-synthesized polymers. For both the $^{13}C/^{15}N$-isotope-enriched and -unenriched $[-(Ph)Si-(NCN)_{1.5}-]_n$ polymer, the ^{29}Si MAS NMR spectra show a main band at -75ppm, which represents the Si sites in $Ph-Si-(NCN)_3$, confirming the formation of the expected structure. Additionally, $[-(Ph)Si-(NCN)_{1.5}-]_n$ shows two other bands at ca. 0 ppm and -60 ppm. The former band represents the silicon environments in the starting materials, $(CH_3)_3-Si-NCN-Si-(CH_3)_3$ or ph-Si-Cl_3. The latter band at -60 ppm is assumed to be from the end group $Ph-Si(NCN)_2-Cl$. This difference in the Si environments between the enriched and unenriched $[-(Ph)Si-(NCN)_{1.5}-]_n$ polymers is due to their different synthesis routes. There is reactant residue of bis(trimethylsilyl)carbodiimide or trichlorophenylsilane in the unenriched $[-(Ph)Si-(NCN)_{1.5}-]_n$, while the $^{13}C/^{15}N$ isotope-enriched $[-(Ph)Si-(NCN)_{1.5}-]_n$ from the reaction of cynamide and trichlorophenylsilane has no such residue. The endgroup $Ph-Si(NCN)_2-Cl$ is only observed in the unenriched polymer. There is no considerable amount of $Ph-Si(NCN)_2-Cl$ endgroup in the $^{13}C/^{15}N$ isotope-enriched polymer. This means that the $^{13}C/^{15}N$ isotope-enriched polymer may have a larger average molecular weight.

^{13}C MAS NMR spectra (Figure 26(b)) show that the main bands for both the unlabeled and labeled polymers lie between 125 and 130 ppm, which represents aromatic carbon rings.

The bands at ca. 120ppm represent carbon in the -N=C=N- environments. This band is much more enhanced in the $^{13}C/^{15}N$ isotope-enriched polymer, $[-(Ph)Si-(NCN)_{1.5}-]_n$, because the ^{13}C isotope is only in the -N=C=N- groups, not in the phenyl groups. The band at ~25ppm in the isotope-enriched polymer $[-(Ph)Si-(NCN)_{1.5}-]_n$ may come from the solvent THF.

^{15}N enrichment of the material offers the opportunity to observe the chemical bonding environments of nitrogen. Large chemical shifts in nitrogen NMR are attractive from the point of view of molecular structural investegations. The chemical shifts are very sensitive to changes in the N environments. ^{15}N MAS NMR of $^{13}C/^{15}N$ isotope-enriched $[-(Ph)Si-(NCN)_{1.5}-]_n$ is shown in Figure 26 (c). Only one peak at ca. 20ppm is observed in the whole measuring range. This peak represents N in Si-N=C=N-Si sites.

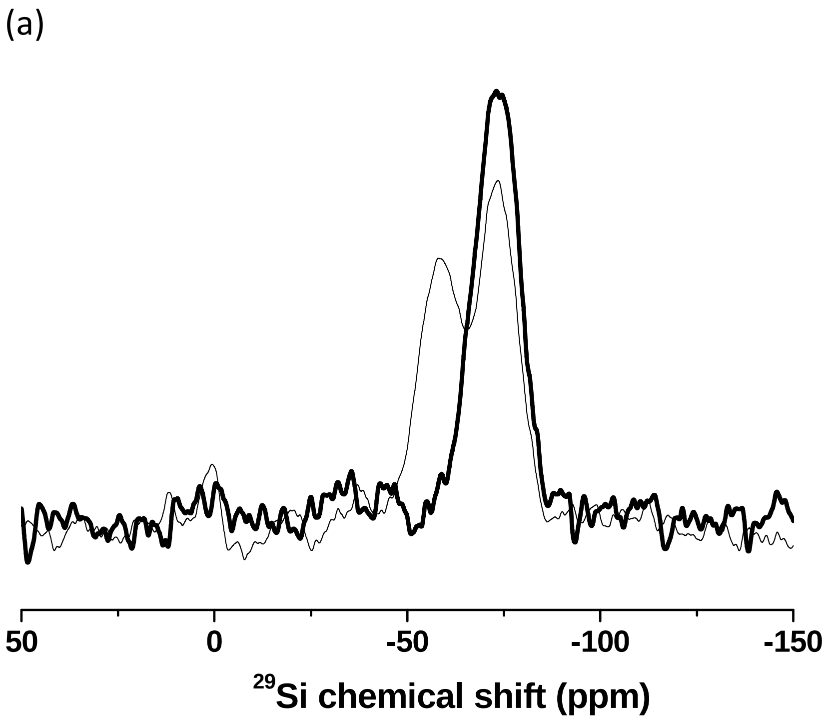

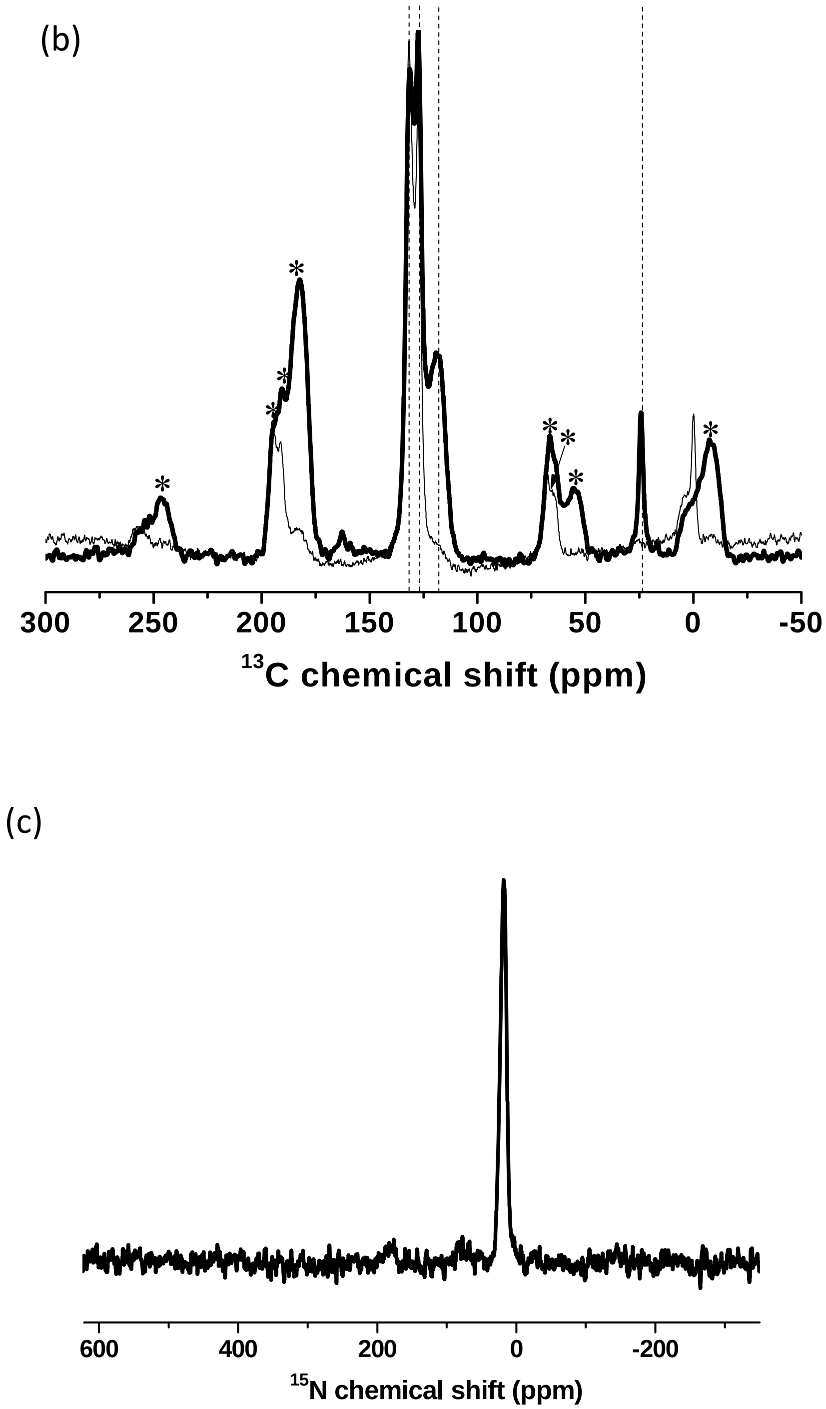

Figure 26 (a) ^{29}Si and (b) ^{13}C MAS NMR of $[-(Ph)Si-(NCN)_{1.5}-]_n$(thin line) and ^{13}C/^{15}Nisotope-enriched $[-(Ph)Si-(NCN)_{1.5}-]_n$ (bold line); (c) ^{15}N MAS NMR of ^{13}C/^{15}N isotope-enriched $[-(Ph)Si-(NCN)_{1.5}-]_n$. The asterisks in ^{13}C MAS NMR spectra represent spinning side bands

^{13}C/^{15}N isotope-enriched $[-(Ph)Si-(NCN)_{1.5}-]_n$ polymer-derived ceramics pyrolyzed at 800 and 1100 ºC have one main band at ca. -47ppm (Figure 27), which represents the $Si-N_4$ tetrahedral environment of Si. The lack of any SiC_xN_{4-x} (x=0-4) mixed units is characteristic of polysilylcarbodiimide-derived ceramics.

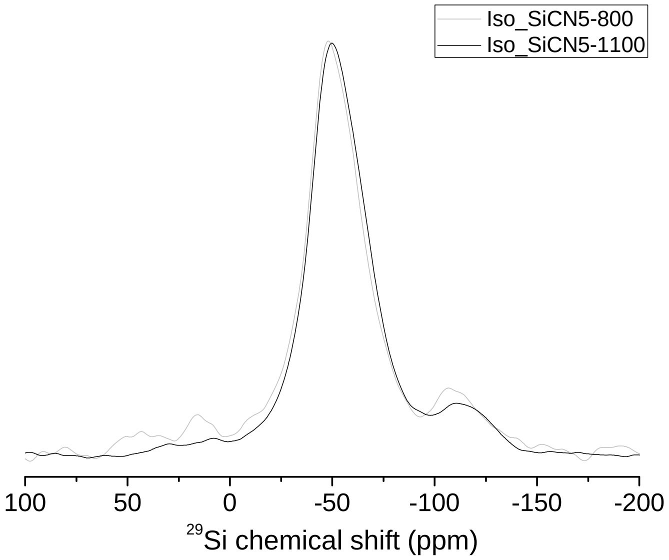

Figure 27 ^{29}Si MAS NMR of Iso_SiCN5 ceramics prepared at 800 ºC(grey line) and 1100 ºC(black line)

The ^{13}C MAS NMR spectra (Figure 28) show a significant difference between the ceramics derived from the labeled and unlabeled polymers. The carbon atoms in SiCN5 ceramics basically assume only one type of environment, which is graphitic carbon with a signal centered at ~ 110 ppm. Iso_SiCN5 ceramics show two additional bands at ~125 ppm and ~150 ppm in the ^{13}C MAS NMR spectra. The band at ~150 ppm represents the sp^{2}C-N bonding and the one at ~125 ppm is from amorphous sp^2 C. It is belived that these two kinds of carbon environments also exsist in the SiCN5 ceramics which are derived from unenriched polymer. They do not appear in the spectra because of their relatively low intensity compared to that of graphitic carbon. However, in the spectra of Iso_SiCN5 ceramics, which are enriched with ^{13}C, the intensity of the sp^{2}C-N and sp^{2}C bands are relatively enhanced. This means that the graphitic carbon in the ceramics is mainly derived from the phenyl groups, while carbon in the sp^{2}C-N and amorphous sp^{2}C environments are mainly derived from N=C=N groups in the preceramic polymer.

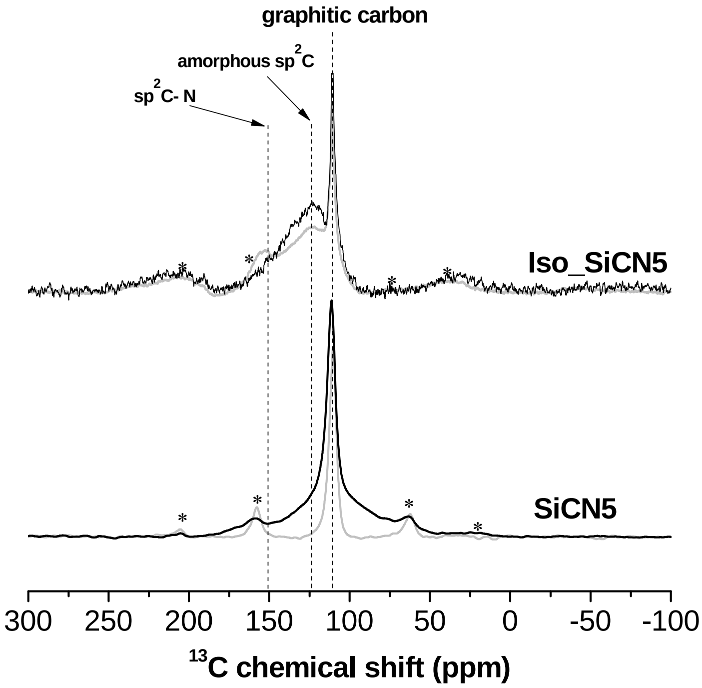

Figure 28 ^{29}Si MAS NMR of SiCN5 and Iso_SiCN5 ceramics prepared at 800 ºC (grey line) and 1100 ºC (black line)

For the isotope-enriched ceramic prepared at 800 ºC, there are two bands in the ^{15}N MAS NMR spectrum (Figure 29) at 21ppm and 49 ppm, representing N-Si_2C and N-Si_3, respectively. When heated to 1100 ºC, a dominant band appears at 49 ppm, which suggests the formation of N-Si_3. For both pyrolysis temperatures (800 and 1100 ºC), ^{15}N CPMAS NMR shows an intense band at 21ppm, which represents N-Si_2C. Thus, a greater amount of hydrogen atoms are located in the N-Si_2C environment. More interestingly, an energetic investigation reveals that the presence of hydrogen near the N mixed-bond environment stabilizes the structure of this branched polymer-derived ceramic. Details will be discussed in Section 4.3.

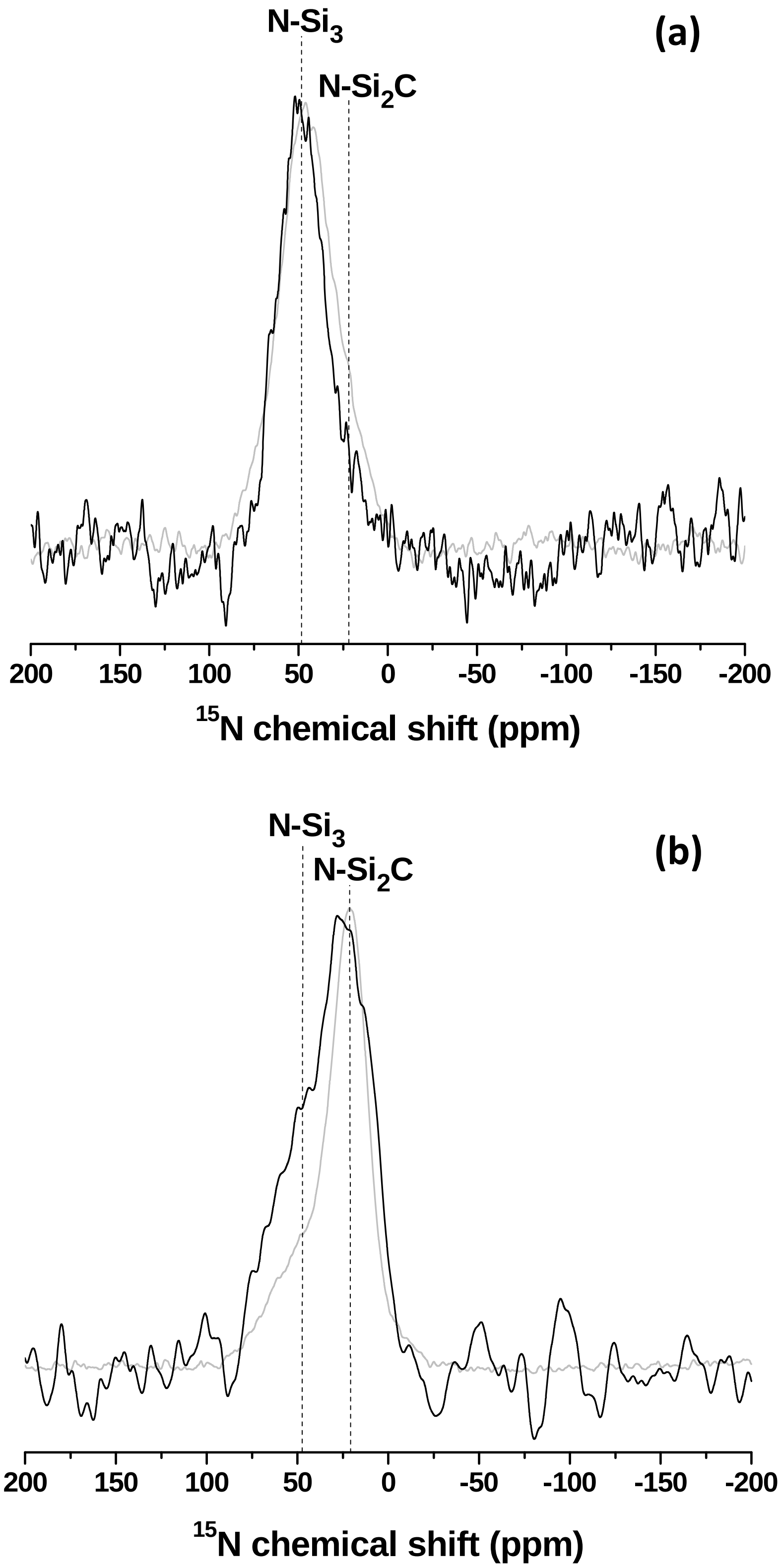

Figure 29 ^{15}N (a) MAS and (b) CPMAS NMR spectra of Iso_SiCN5-800(grey line) and Iso_SiCN5-1100(black line) ceramics

4.1.4 Summary

Two classes of preceramic polymers have been synthesized: polysilylcarbodiimide and polysilazane. Polymers with phenyl groups in the structure had higher carbon contents, while those with methyl group had lower carbon contents. The formation of these polymers was confirmed by NMR spectroscopy. Borane was reacted with all obtained polymers to produce boron-modified counterparts, namely polyborosilylcarbodiimide and polyborosilazane. The pre-crosslinking process is considered to be the most critical step in shaping the polysilylcarbodiimides and polysilazanes to manufacture bulk ceramics. Meanwhile, for polyborosilazanes, it is important to have a pre-pyrolysis procedure. The pre-pyrolyzed material acts as self-filler, and the original thermoplastic polymers acts as binders. Final bulk ceramic compacts were successfully produced from all of the precursors. In addition to the linear polymers, branched polysilsesquicarbodiimide was synthesized, as well as its ^{13}C and ^{15}N isotope-enriched analogue. ^{15}N enrichment of the polymer enables the measurement of ^{15}N MAS NMR and ^{15}N CPMAS NMR spectra which provides more detailed information related to structural features.

4.2 Effect of processing route

The polymer-derived ceramic technique is an efficient and promising method to produce complex-shaped bulk ceramics by taking advantage of plastic technologies [1,39,40]. Uniaxial warm pressing is one of the most frequently used processes in the fabrication of bulk ceramics from precursors. In this work, we investigated the effect of processing route, namely to produce powders or bulk ceramics, on the nanostructure of carbon-rich SiCN and SiBCN polymer-derived ceramics. These ceramics were also characterized by elemental analysis, SEM, and local analysis by high resolution TEM (HRTEM). The final microstructures are discussed with respect to the precursor chemistry, processing route (powder and bulk synthesis), temperature, and presence of boron and "free" carbon.

4.2.1 Effect of processing route on the nanostructure — Low temperature thermal transformation

The synthesis and processing of the polyphenylvinylsilylcarbodiimide and polyborophenylsilylcarbodiimide were carried out as described in the Experimental Section, and are summarized in Figure 30. As discussed in Section 4.1, a pre-crosslinking step is essential for [-(PhVi)Si-NCN-]$_n$, and after that, green body compacts were produced.

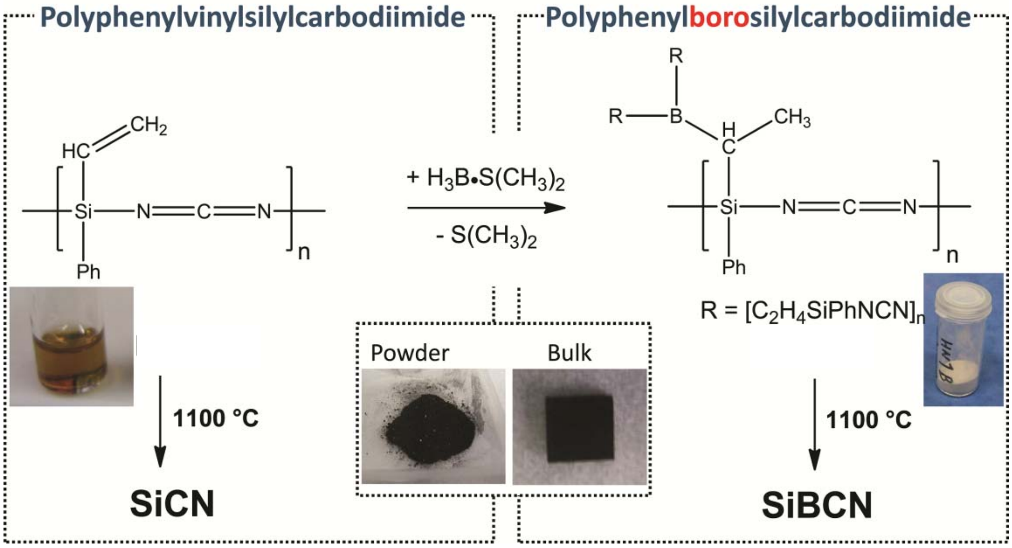

Figure 30 Synthesis and processing of polyphenylvinylsilylcarbodiimide and polyborophenylsilylcarbodiimide. Reprinted from Journal of the European Ceramic Society, V 32, Y. Gao, G. Mera, H. Nguyen, K. Morita, H.-J. Kleebe, and R. Riedel, Processing route dramatically influencing the nanostructure of carbon-rich SiCN and SiBCN polymer-derived ceramics Part I: Low temperature thermal transformation, 1857, copyright (2012), with permission from Elsevier [134].

Two pyrolysis temperatures were selected. 1100 °C, the standard temperature for amorphous PDC fabrication, was selected since it is the temperature at which the polymer-to-ceramic transformation has basically completed. 1400°C was selected as the temperature at which the PDCs just begin to undergo nano-crystallization and show a difference from the amorphous architecture.

The microstructure of the green bodies and of the pyrolyzed bulk ceramics were observed and studied by SEM. A SiCN(O) surface layer, which contains cracks and pores, was found on the surface of bulk SiCN1-1100 and SiBCN1-1100 ceramics. Figure 31 shows the presence of this ~3 µm layer on SiCN1-1100. Beneath the SiCN(O) layer, the ceramic is very dense, showing no defects. The same microstructural characteristics were found also in the SiBCN1-1100 sample. The formation of the SiCN(O) layer is due to the handling of green body in air. Samples were polished prior to annealing at 1400 °C in order to avoid the influence of the SiCN(O) layer on the microstructure of the bulk ceramics.

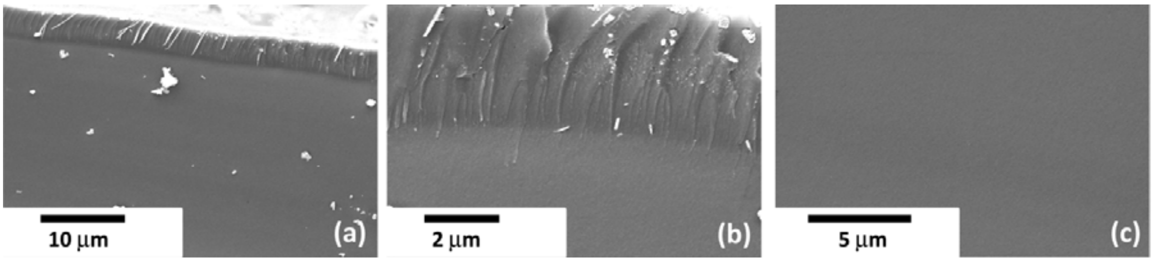

Figure 31. SiCN1-1100 cross-section: a) and b) thin SiCN(O) layer on the surface; c) defect-free bulk SiCN1-1100 ceramic under the SiCN(O) layer. Reprinted from Journal of the European Ceramic Society, V 32, Y. Gao, G. Mera, H. Nguyen, K. Morita, H.-J. Kleebe, and R. Riedel, Processing route dramatically influencing the nanostructure of carbon-rich SiCN and SiBCN polymer-derived ceramics Part I: Low temperature thermal transformation, 1857, copyright (2012), with permission from Elsevier [134].

FTIR is an important integral method for the characterization of bonding, and furthermore, the microstructure of the ceramics. Figure 32 presents the ARO FTIR (all-reflecting objective FTIR) of $[\text{-(PhVi)Si-NCN-}]_n$- and $\{B[\text{-}(C_2H_4)Si(Ph)\text{-NCN-}]_3\}_n$-derived SiCN1 and SiBCN1 bulk and powder samples.

As shown by FTIR, the majority of the bands correspond to the “free” carbon phase (1652, 1583, 1503, 1447, 1378 cm^{-1}). All ceramics still contain $C(sp^3)$-H bands (C-H asymmetric and symmetric stretching vibrations at 2924 and 2860 cm^{-1}, respectively) probably as terminally saturated groups in the graphene-like carbon phase. The most important bands are related to the presence of the Si_3N_4 and SiC phases (Si-N stretching vibration at 970 cm^{-1}, and Si-C stretching at 812 cm^{-1}). Remarkably, the FTIR of all samples contain C=N (stretching vibration at 1720 cm^{-1}) and C-N (stretching at 1253 and 1188 cm^{-1}). Moreover, the FTIR spectrum of SiCN1-1400 powder shows an intense band for Si-C due to the crystallization of SiC (812 cm^{-1}). The intensity of the Si_3N_4 band also varies depending on the temperature and processing route. For the bulk ceramics, the silicon nitride band is strong, independent of the annealing temperature. In the case of the powder ceramics, at 1400 °C, the Si-N band is less intense than in the 1100 °C analogue. This observation corroborates very well with the increase in the intensity of the SiC band. The ceramics are losing nitrogen by the carbothermal reaction of Si_3N_4 with carbon to form SiC and nitrogen gas according to $\text{a-}Si_3N_4 + 3\ \text{a-C} \rightarrow 3\ \alpha/\beta\text{-SiC} + 2\ N_2\uparrow$.

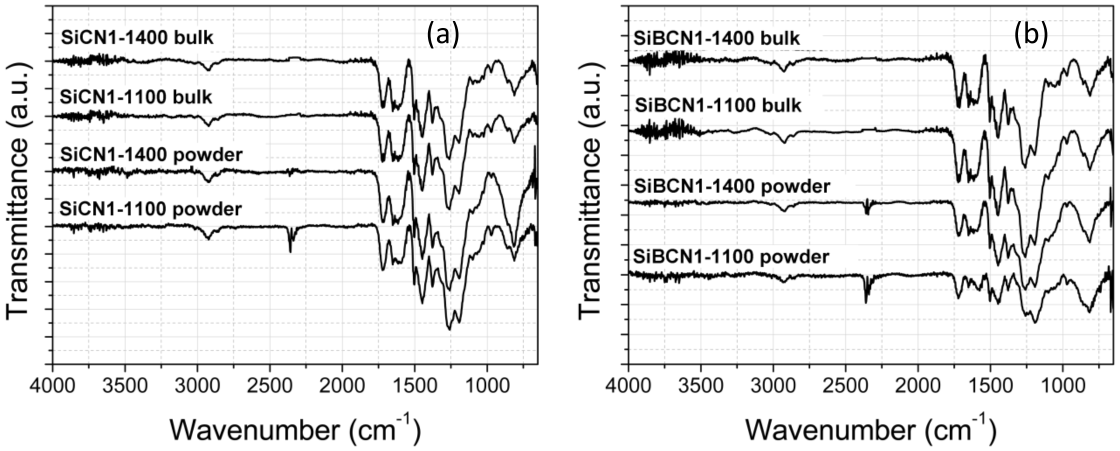

Figure 32 ARO FTIR spectroscopy of (a) SiCN1 ceramics and (b) SiBCN1 ceramics at 1100 and 1400 °C. Reprinted from Journal of the European Ceramic Society, V 32, Y. Gao, G. Mera, H. Nguyen, K. Morita, H.-J. Kleebe, and R. Riedel, Processing route dramatically influencing the nanostructure of carbon-rich SiCN and SiBCN polymer-derived ceramics Part I: Low temperature thermal transformation, 1857, copyright (2012), with permission from Elsevier [134].

Raman spectroscopy is a key nondestructive tool for the examination of the structural evolution of the “free” carbon phase in PDCs. [138–142] The representative features of “free” carbon in the Raman spectra of PDCs are (1) the so-called disorder-induced D-band at approx. 1350 cm^{-1}, and (2) the G band at approximately 1582 cm^{-1} due to in-plane bond stretching of sp^2 carbon, and (3) the G′-band (the overtone of the D-band which is always observed in defect-free samples) at 2700 cm^{-1}. The D and G bands can vary in intensity, position, and width, depending on the structural organization of the sample under investigation. The intensity ratio of the D and G modes, I_D/I_G, enables the evaluation of the lateral size of graphitic carbon using the formula (Formula 3) reported by Ferrari and Robertson: [138]

$$\frac{I_D}{I_G} = C'(\lambda) L_a^{\,2}$$

Formula 3

where, L_a is the size of graphitic carbon along the six fold ring plane (lateral size), and C′ is a coefficient that depends on the excitation wavelength of the laser. The value of the coefficient, C′, for the wavelength of the Ar-ion laser employed (514.5 nm) is 0.0055 $Å^{-2}$. Gaussian curve fitting of the Raman bands was performed in order to extract the I_D/I_G intensity ratios, and to determine the lateral size of the graphitic carbon. Peak fitting was completed including the minor T bands (shoulder at ~1200 cm^{-1}), which are attributed to sp^2-sp^3 C-C and C=C bonds, and the D′′ at ~1500 cm^{-1} corresponding to the fraction of amorphous carbon contained in the samples [143]. These additional bands were present due to the structural disorder that activates otherwise forbidden vibrational modes [144,145].

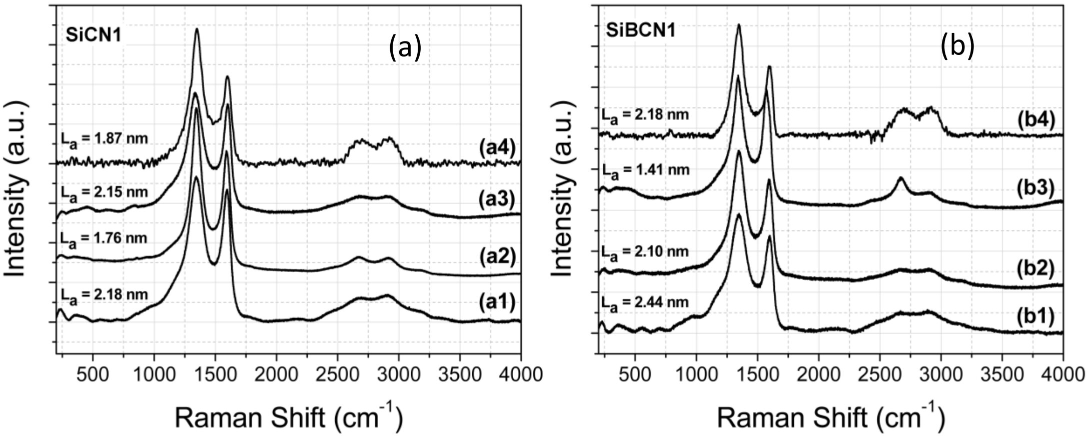

Figure 33 Micro-Raman spectroscopy of a) SiCN ceramics (a1) SiCN1-1100 powder; (a2) SiCN1-1400 powder; (a3) SiCN1-1100 bulk; (a4) SiCN1-1400 bulk; and b) SiBCN ceramics: (b1) SiBCN1-1100 powder; (b2) SiBCN1-1400 powder; (b3) SiBCN1-1100 bulk; (b4) SiBCN1-1400 bulk. The corresponding cluster size of carbon (L_a) for each measurement is provided in the graphs. Reprinted from Journal of the European Ceramic Society, V 32, Y. Gao, G. Mera, H. Nguyen, K. Morita, H.-J. Kleebe, and R. Riedel, Processing route dramatically influencing the nanostructure of carbon-rich SiCN and SiBCN polymer-derived ceramics Part I: Low temperature thermal transformation, 1857, copyright (2012), with permission from Elsevier [134].

The micro-Raman spectra of all samples are characterized by broad and overlapped D and G bands, indicating a strongly disordered state (Figure 33). The disorder in the carbon phase can primarily be induced by the presence of edges in the graphene layers, by the deviation from planarity of the graphene layers, and also by the presence of carbon atoms in the sp^3 hybridization state. Recently, the dependence of the I_D/I_G ratio on the degree of disorder in graphene-like materials was reported [146–148]. The disorder was quantified as depending on point-like defects. Assuming that we have a low defect density, the typical interdefect distance, L_D, can be calculated with the formula: $I_D/I_G = C(\lambda)/L_D^2$, which is valid when $L_D > 6$ nm ($C(514.5 \text{ nm}) \approx 107 \text{ nm}^2$) [146–148]. Unfortunately, the equation is not valid for high defect densities, but despite this, it can help qualitatively compare the samples prepared by different processing routes. The processing of bulk ceramics is expected to result in a decreased defect densitiy in the carbon phase. The interdefect distances, L_D, together with the I_D/I_G ratio and the lateral cluster size L_a are summarized in Table 4. Except for the SiBCN1-1100 powder sample, all other ceramics show valid L_D distances. For the SiBCN1-1100 powder sample, the distance between defects ($L_D = 5.71$ nm) is lower than the limit of validity of the equation ($L_D > 6$ nm), and is therefore omitted from discussion. As observed in Table 1, the bulk samples show a lower defect density than the powder samples. Moreover, at 1400 °C, the carbon phase is more organized than at 1100 °C, and also shows fewer defects. Furthermore, the presence of boron decreases the defect density and enhances the organization of the carbon. Especially at 1100 °C, the SiBCN1-1100 bulk sample shows decreases in the lateral size of the carbon (1.41 nm) and in the I_D/I_G ratio due to the high organization of the graphene layers. This fact is underlined also by the presence of a sharp single Gaussian peak for the G′ band at 2672.62 cm^{-1}. Regarding the lateral size of the graphitic carbon in the SiCN ceramics, a decrease is observed when comparing the 1400 °C samples to the 1100 °C ones. This trend is observed in both the powder and bulk ceramics cases.

Table 4 The Raman parameters of the "free" carbon phase in powder and bulk SiCN1 and SiBCN1 ceramics.

Sample	I_D/I_G	L_a [nm]	L_D [nm]
SiCN1-1100 powder	2.61	2.18	6.40
SiCN1-1400 powder	1.71	1.76	7.91
SiCN1-1100 bulk	2.54	2.15	6.49
SiCN1-1400 bulk	1.92	1.87	7.47
SiBCN1-1100 powder	3.28	2.44	5.71
SiBCN1-1400 powder	2.43	2.10	6.64
SiBCN1-1100 bulk	1.09	1.41	9.90
SiBCN1-1400 bulk	2.61	2.18	6.40

The compositions of the SiCN1 and SiBCN1 bulk and powder samples were determined by elemental analysis (Table 5).

Table 5 Chemical composition of the powder and bulk SiCN1 and SiBCN1 ceramics.

Sample	Chemical composition							Empirical formula
	Si %	C %	N %	B %	O %	H %	Cl %	
SiCN1-1100 Powder	24.80	56.50	14.80	-	2.14	0.24	1.55	$SiC_{5.32}N_{1.19}H_{0.27}Cl_{0.05}O_{0.15}$
SiCN1-1100 Bulk	28.45	51.42	10.98	-	9.15	-	-	$SiC_{4.22}N_{0.77}O_{0.56}$
SiBCN1-1100 Powder	23.79	51.32	16.58	3.05	2.21	0.30	2.75	$SiB_{0.33}C_{5.04}N_{1.40}H_{0.35}Cl_{0.09}O_{0.16}$
SiBCN1-1100 Bulk	28.81	42.31	13.63	3.41	11.84	-	-	$Si_1B_{0.30}C_{3.43}N_{0.88}O_{0.72}$
SiCN1-1400 Powder	29,24	59.21	11.03	-	0.52	-	-	$SiC_{5.47}N_{0.87}O_{0.04}$
SiCN1-1400 Bulk	28.65	57.06	11.66	-	2.63	-	-	$SiC_{4.65}N_{0.81}O_{0.16}$
SiBCN1-1400 Powder	28.21	51.08	16.19	3.06	1.46	-	-	$SiB_{0.28}C_{4.23}N_{1.07}O_{0.09}$
SiBCN1-1400 Bulk	29.15	48.62	14.62	3.45	4.16	-	-	$SiB_{0.30}C_{3.89}N_{0.94}O_{0.25}$

Regarding the compositions of the powder samples compared to their bulk analogues, it was observed that the powder ceramics at 1100 °C and 1400 °C contain a higher content of carbon and nitrogen. At the same time, the silicon content is higher in the bulk ceramics. Another interesting observation is that the hydrogen and chlorine contents registered in the powder ceramics at 1100 °C are not present in the bulk ceramics pyrolyzed at the same temperature. Even though the FTIR study showed the presence of C-H bonds in bulk ceramics, the amount of hydrogen is less than the detection limit for elemental analysis. Differences in the Si, C, N, H and Cl contents are attributed to changes in the chemistry and architecture of precursors using different processing routes. The processing of bulk ceramics includes a crosslinking and shaping step, which allows the formation of a 3D structure, and the elimination of the chlorine-containing end-group from the precursor. The boron content in all SiBCN samples is constant, with no difference measured between the bulk and powder ceramics. As presented in Figure 31, the bulk SiCN1 and SiBCN1 samples pyrolyzed at 1100 °C show a 3 μm thick SiCN(O) surface layer. In order to understand how the presence of this layer can change the composition of the samples, elemental analysis was completed without polishing. As expected, the SiCN1 1100 °C bulk and SiBCN1-1100 bulk contain a high amount of oxygen contamination—9.15 and 11.84 %, respectively. The oxygen-containing surface layer was removed from the 1400 ºC bulk analogues prior to elemental analysis, and thus these samples showed less oxygen contamination.

High-resolution TEM microscopy (HRTEM) is a powerful method for locally investigating the nanostructural evolution of polymer-derived ceramics at different temperatures of annealing. Even if the PDCs are X-ray amorphous after pyrolysis at low temperatures ($T < 1400$ °C), they are typically heterogeneous as shown by several TEM studies [149–151]. Until now, there existed a lack of information regarding the TEM investigations of polysilylcarbodiimides-derived ceramics. Due to the complicated, and until now, never-before successful processing of these precursors into bulk monoliths, no nanostructure investigation of these ceramics has been reported. This study presents an easy route to produce bulk carbon-rich polysilylcarbodiimides-derived ceramics, and their nanostructural analysis by TEM. By comparing bulk and powder SiCN ceramics, the effects of the crosslinking and shaping processes on the thermal stability of PDCs can be indirectly assessed. Moreover, the low boron content of these samples is discussed in light of the resultant nanostructure.

Figure 34 presents the HRTEM images of the powder and bulk SiCN and SiBCN ceramics at 1100 °C. The selected area electron diffraction (SAED) patterns of the SiCN and SiBCN ceramics synthesized at 1100 °C are displayed as insets in the figures. All four ceramics, independent of composition or processing route, show a diffuse, elastically scattered ring pattern typical of amorphous samples. No major contrast variations were observed for the samples annealed at 1100 °C, indicating the amorphous nature of the samples. At even higher magnifications, no indication of any crystalline phases could be imaged. At this low pyrolysis temperature, no difference can be observed between the nanostructures of the powder and bulk SiCN ceramics, with or without boron.

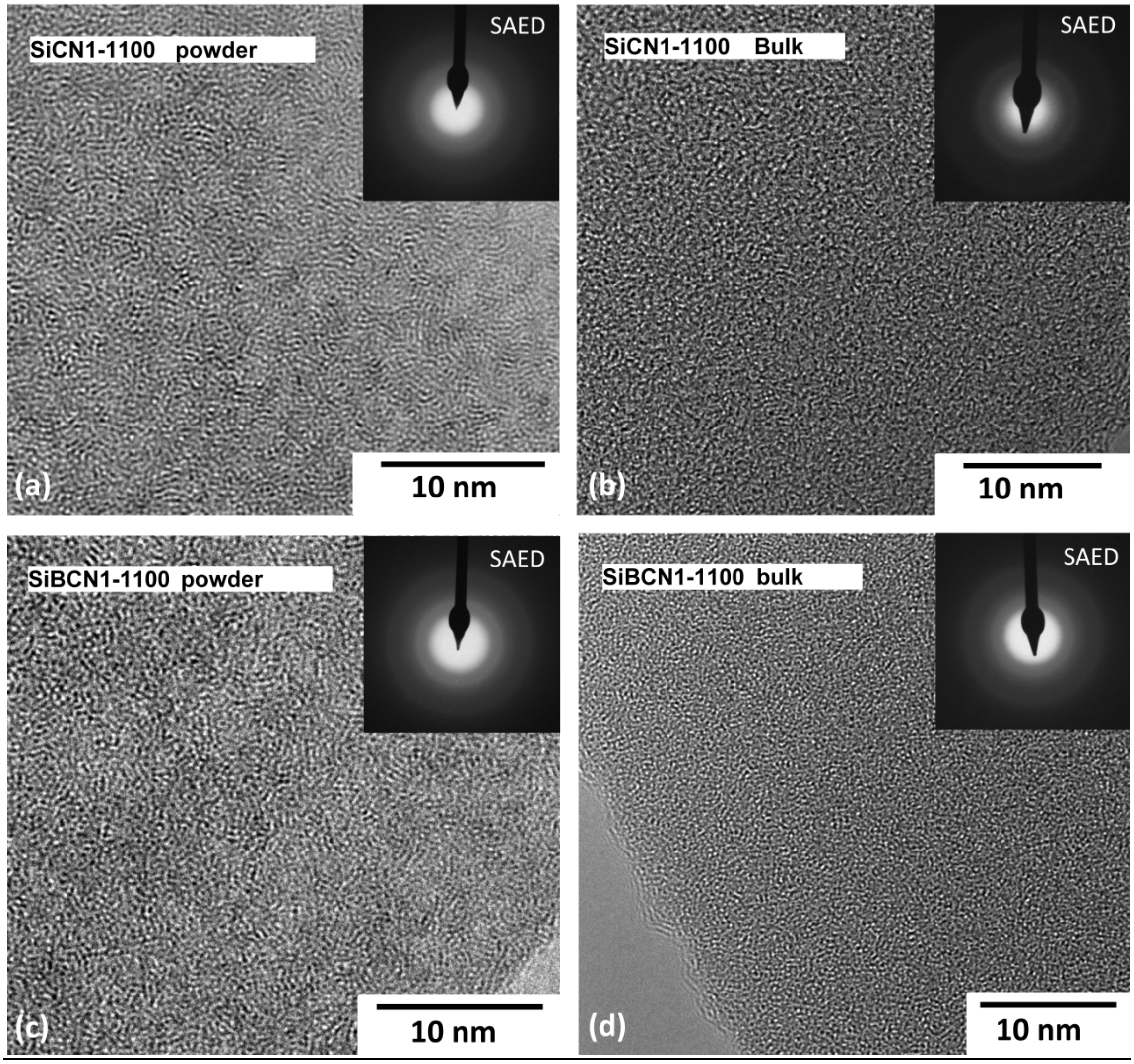

Figure 34. HRTEM images of powder and bulk SiCN and SiBCN ceramics at 1100 °C (the insets present the selected area electron diffraction): (a) SiCN1-1100 powder; (b) SiCN1-1100 bulk; (c) SiBCN1-1100 powder; (d) SiBCN1-1100 bulk. Reprinted from Journal of the European Ceramic Society, V 32, Y. Gao, G. Mera, H. Nguyen, K. Morita, H.-J. Kleebe, and R. Riedel, Processing route dramatically influencing the nanostructure of carbon-rich SiCN and SiBCN polymer-derived ceramics Part I: Low temperature thermal transformation, 1857, copyright (2012), with permission from Elsevier [134].

In the case of powder SiCN1 and SiBCN1 ceramics pyrolyzed at 1400 °C, high-resolution TEM imaging shows that crystallization has initiated in the samples. Figure 35 displays the nanostructural characteristics of these ceramics, in which crystallites of α/ß-SiC are embedded in a graphene-like carbon matrix. In addition, as indicated by the elemental analysis, amorphous Si_3N_4 is still present in the amorphous network (Table 5). As previously reported for carbon-rich SiCN ceramics obtained from polysilylcarbodiimides, no Si_3N_4 crystallization was detectable [98]. As observed in the SAED insets in Figure 35, the SiBCN1 sample (Figure 35b) shows enhanced crystallization compared to the SiCN1 (Figure 35a) analogue. Thermodynamic modeling studies as well as experimental work demonstrate that the presence of boron in SiCN is the driving force for SiC crystallization [15,152]. Indeed, also in the case of the polyborophenylvinylsilylcarbodiimide-derived SiBCN1 ceramic, the same enhancement in SiC crystallization due to the presence of boron was observed.

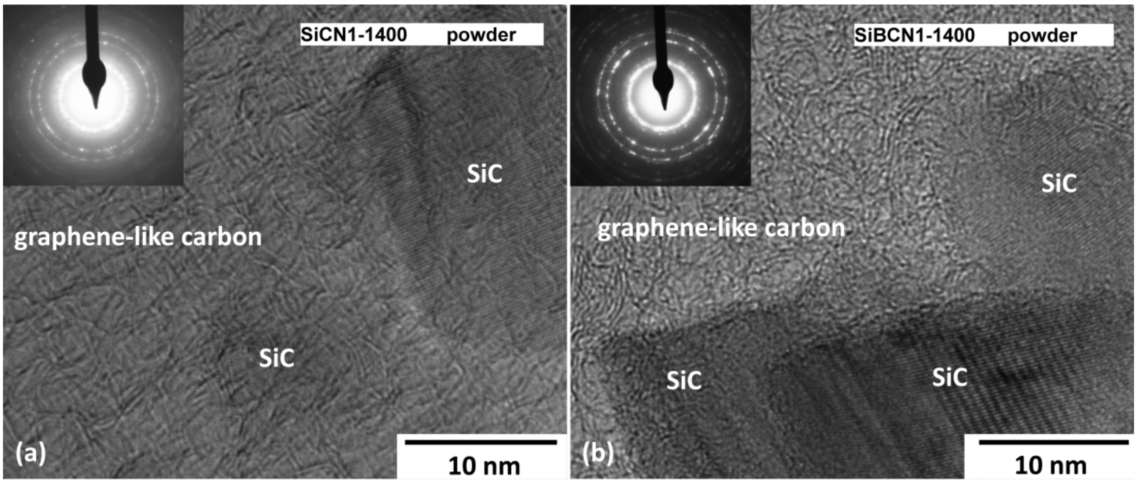

Figure 35. HRTEM images of powder SiCN and SiBCN ceramics annealed at 1400 °C. The SAED patterns (insets) show the presence of α/ß-SiC. Reprinted from Journal of the European Ceramic Society, V 32, Y. Gao, G. Mera, H. Nguyen, K. Morita, H.-J. Kleebe, and R. Riedel, Processing route dramatically influencing the nanostructure of carbon-rich SiCN and SiBCN polymer-derived ceramics Part I: Low temperature thermal transformation, 1857, copyright (2012), with permission from Elsevier [134].

In contrast to the nanostructures of the SiCN and SiBCN powder ceramics, the TEM investigation of the bulk analogues revealed *no* α/ß-SiC crystallization. Even at higher magnifications, no SiC nuclei were detectable. In order to confirm the amorphous nature of the bulk samples, several TEM micrographs at different defocus settings of the objective lens were taken.

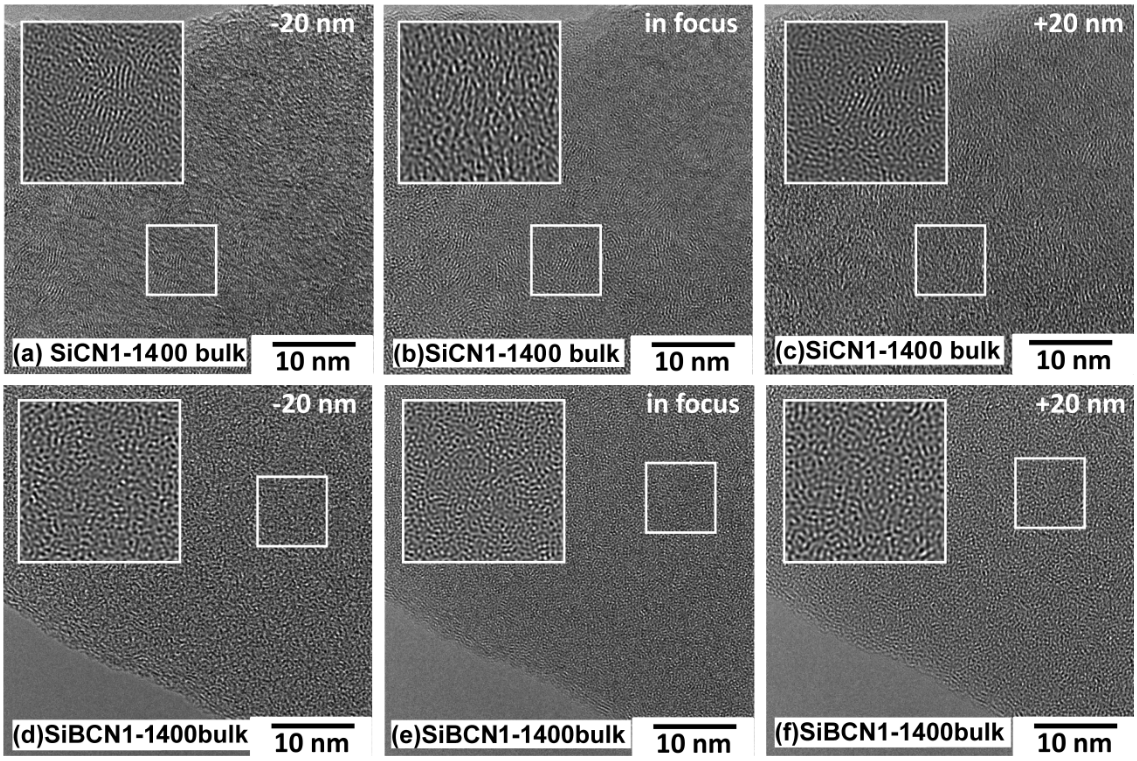

Figure 36 HRTEM images of bulk SiCN and SiBCN ceramics pyrolyzed at 1400 °C. Different defocus setting of the objective lens were chosen since carbon and SiC can better be imaged at slight over- and underfocus conditions [153], respectively; (a), (b), (c) SiCN 1400 °C bulk and (d), (e), (f) SiBCN 1400 °C bulk. The insets represent the inverse FFT images of the selected areas (boxed regions). Reprinted from Journal of the European Ceramic Society, V 32, Y. Gao, G. Mera, H. Nguyen, K. Morita, H.-J. Kleebe, and R. Riedel, Processing route dramatically influencing the nanostructure of carbon-rich SiCN and SiBCN polymer-derived ceramics Part I: Low temperature thermal transformation, 1857, copyright (2012), with permission from Elsevier [134].

For polysilazanes-derived ceramics, with increasing temperature, the first crystallization event is the formation of basic structural units (BSU) of carbon, followed by the nucleation of SiC. In the SiCN bulk ceramic annealed at 1400 °C, depending on the defocus setting of the objective lens, slight contrast variations are seen in the HRTEM image. At an under- (-20 nm) and an overfocus (+20nm) setting (Figure 36), the inverse fast Fourier transform (FFT) images show variations in phase contrast, indicating a fine organization of the carbon phase. The FFT inset clearly shows the presence of a carbon phase (Figure 37a), as also indicated in the inverse FFT image of a thicker region (Figure 37b).

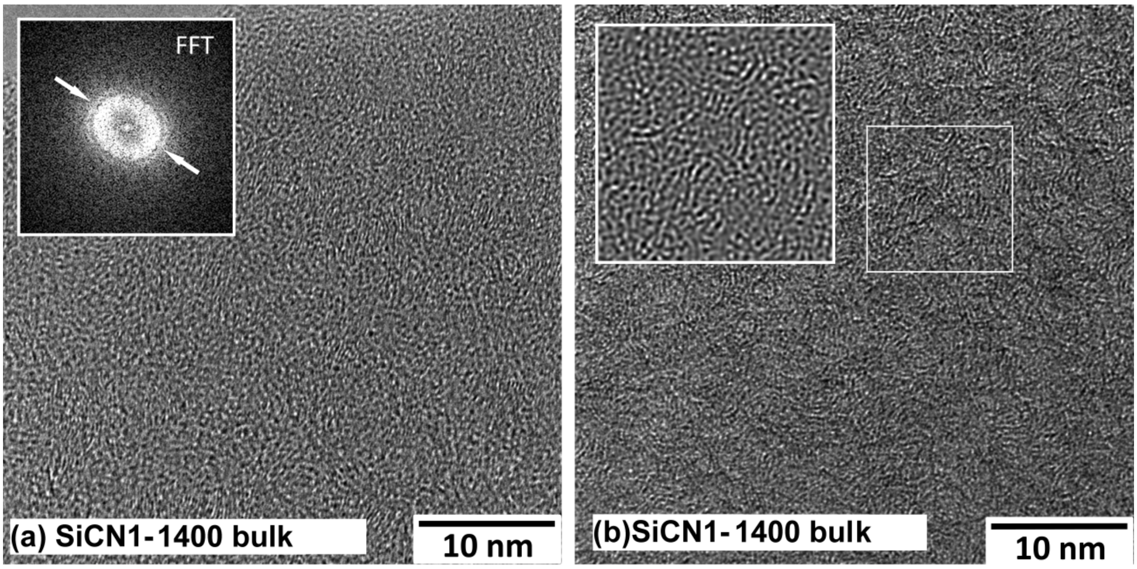

Figure 37 (a) HRTEM micrographs of SiCN1-1400 bulk (the inset shows the FFT image corresponding to carbon phase); (b) inverse FFT image of the thick region of SiCN1-1400 bulk. Reprinted from Journal of the European Ceramic Society, V 32, Y. Gao, G. Mera, H. Nguyen, K. Morita, H.-J. Kleebe, and R. Riedel, Processing route dramatically influencing the nanostructure of carbon-rich SiCN and SiBCN polymer-derived ceramics Part I: Low temperature thermal transformation, 1857, copyright (2012), with permission from Elsevier [134].

In the case of bulk SiBCN pyrolyzed at 1400 °C (Figure 36d-f), depending on the defocus value of the objective lens, no phase contrast variations can be seen in the HRTEM images, with the sample being fully amorphous. This fact can be due to the higher thermal stability of the SiBCN ceramics. It has been assumed that the boron-containing carbon matrix, similar to a graphene-like phase, acts as an effective diffusion barrier in preventing SiC nucleation. As presented in Table 5, the SiBCN ceramics, both powder and bulk, contain only up to 3-3.4 wt% of boron—an amount obviously not sufficient to prevent SiC crystallization in higher surface area powder samples.

Differences in thermal stability against crystallization between the powder and bulk samples are due to surface nucleation and increased nanoporosity in the powders. The greater specific surface area of powder samples increases the “reactivity” of the materials with regard to the carbothermal reaction. Thus, the powders begin to crystallize at lower temperatures and at higher rates. A confirming trend was previously observed for SiBCN ceramics of different particle sizes as investigated with respect to thermal decomposition and crystallization [33]. The skin-core effect reported for polyborosilazanes-derived ceramics [34] was not observed in our study.

It has been reported that, in the case of SiBCN ceramics composed of Si_3N_4, SiC, BN and C, thermal stability strongly depends on the boron content [154,155]. In our case, a low boron concentration is expected to decrease the thermal stability of the ceramics against crystallization. However, at the same time, a high “free” carbon concentration is assumed to improve the thermal stability of these materials, counterbalancing the boron effect [17–19]. Furthermore, surfaces provide active reaction sites for decomposition and crystallization.

4.2.2 Effect of processing route on the nanostructure — Thermal transformation up to 2100°C

Thermal transformation of SiCN1 and SiBCN1 ceramics (powder and bulk) are further studied at high temperatures. Figure 38 compares the TG curves of powder and bulk SiCN1-1100 and SiBCN1-1100 samples as heated up to 2100°C. Several interesting features can be seen from the curves. For the SiCN1 material, the weight loss of the powder sample is drastically different from that of the bulk sample. At up to 2100^{o}C, the bulk sample only loses about 16.0 % of its original weight, while the powder sample loses 26.1 wt% (Figure 38 a). On the other hand, the SiBCN1 powder and bulk samples exhibited similar amounts of total weight loss at 2100^{o}C (~ 26.5 % of their original weight) (Figure 38 b), even though the bulk sample loses less weight than the powder one at temperatures below 1900^{o}C. The SiCN1 and SiBCN1 powder samples exhibited similar weight loss behavior: both of them lose weight significantly between 1400 and 1650^{o}C, and almost no weight change occurs at higher temperatures. The total amount of weight loss at 2100^{o}C is also similar for these samples. However, the weight loss of bulk SiCN1 is much less than that of bulk SiBCN1. Closer comparison between the two curves reveals that both SiCN1 and SiBCN1 samples exhibit similar weight loss below 1400^{o}C. At higher temperatures, both samples exhibit two weight loss stages at 1400-1600^{o}C, and at 1600-1900^{o}C, respectively. During both stages (particularly, during the second stage), SiBCN1 exhibited more weight loss than SiCN1. These results clearly show that bulk samples have improved thermal stability against weight loss, which is more obvious for SiCN1 than for the SiBCN1, and that boron likely decreases the thermal stability of bulk samples. However, boron has no noticeable effect on the weight loss of powder samples.

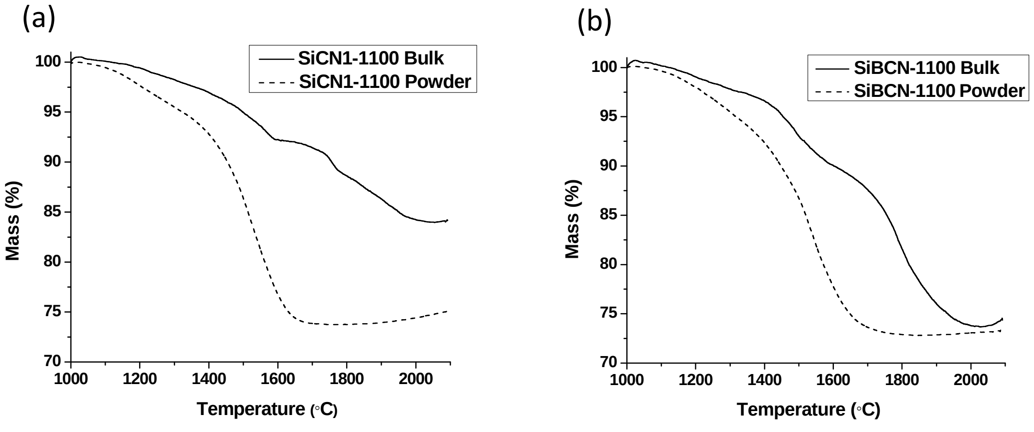

Figure 38: TG cures of a) SiCN1-1100 and b) SiBCN1-1100 bulk (solid line) and powder (dash line) samples.

The thermal transform behavior of the SiCN1 and SiBCN1 ceramics were further analyzed by comparing their differential TG (DTG) curves (Figure 39). It is seen that the DTG curves for the SiCN1 and SiBCN1 powder samples exhibit one peak centered at ~ 1540^{o}C, while the DTG curves for the bulk SiCN1 and SiBCN1 ceramics showed two peaks centered at ~ 1540 and 1750^{o}C, respectively. For the bulk samples, the first peak occurs at the same temperature as the single peak for the powder samples, indicating they arise from the same reaction. The additional peak of the bulk samples occurs at higher temperature, suggesting the occurance of an additional degradation reaction in the bulk samples.

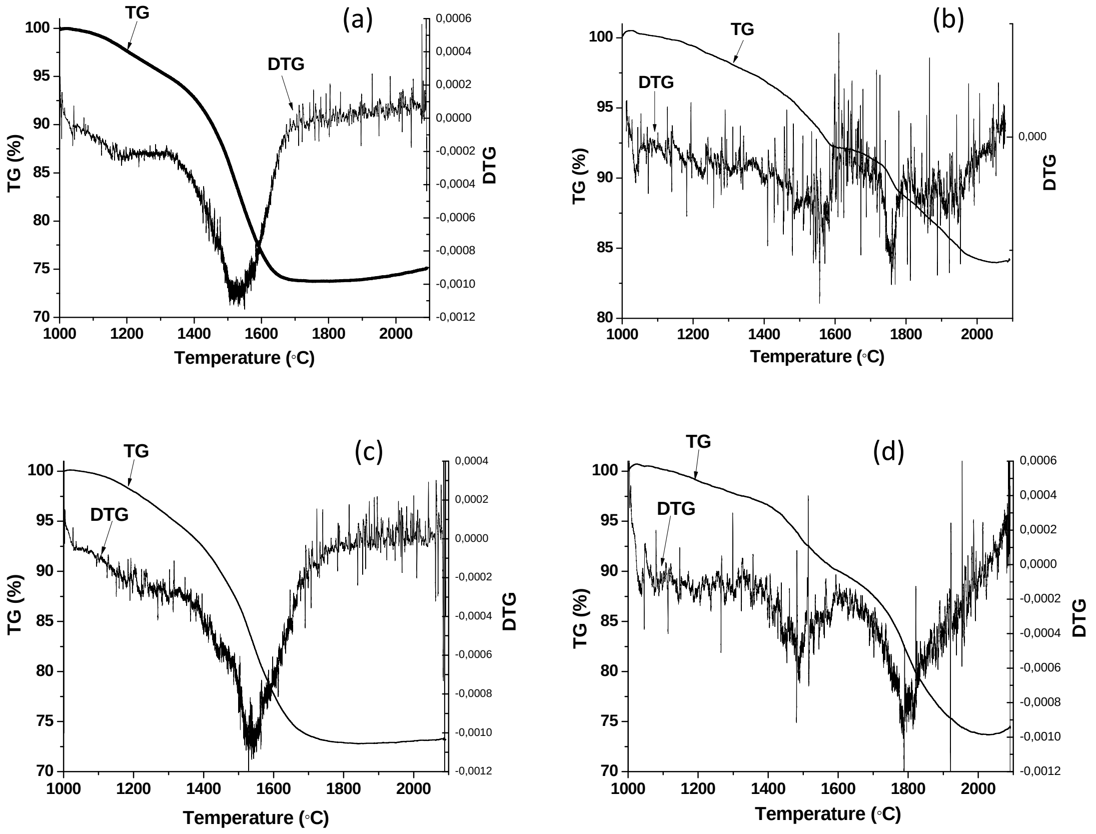

Figure 39: HT-TG and DTG curves of a) SiCN1-1100 powder, b) SiCN1-1100 bulk, c) SiBCN1-1100 powder and d) SiBCN1-1100 bulk samples.

Two annealing temperatures were selected: 1700°C, which is a temperature between the two peaks of the DTG curves of the bulk samples, and 2000°C, which is a temperature above both peaks. The compositions of the SiCN and SiBCN ceramics were measured by elemental analysis on both powder and bulk samples annealed at various temperatures (Table 6). It is interesting to see that, for the SiCN materials, the powder samples always contained higher carbon and silicon contents, while the nitrogen and oxygen contents are lower than bulk samples annealed at the same temperature. In contrast, for the SiBCN materials, the powder samples always contained higher carbon contents, while the silicon, nitrogen and oxygen contents were lower than in the bulk samples. Boron content remains the same for all samples, regardless of form and annealing temperature.

Table 6: Chemical composition of the powder and bulk SiCN1 and SiBCN1 ceramics pyrolyzed at 1700 and 2000 ^{o}C

Sample	Chemical composition (at. %)					Empirical formula	Calculated phases (Mol%)				
	Si	C	O	N	B		Free C	Si_3N_4	SiC	BN	SiO_2
SiCN1-1700 powder	33.31	65.38	0.71	0.60	/	$SiC_{4.59}N_{0.04}O_{0.04}$	78.69	0.20	20.71	/	0.40
SiCN1-2000 powder	32.25	67.75	0	0	/	$SiC_{4.91}$	79.60	0	20.40	/	0
SiCN1-1700 bulk	26.14	62.19	1.68	9.99	/	$SiC_{5.56}N_{0.76}O_{0.11}$	89.35	3.30	6.39	/	0.97
SiCN1-2000 bulk	31.12	63.18	0.42	5.29	/	$SiC_{4.75}N_{0.34}O_{0.02}$	82.83	1.76	15.17	/	0.24
SiBCN1-1700 powder	29.53	61.54	1.03	7.91	3.36	$SiB_{0.30}C_{4.87}N_{0.54}O_{0.06}$	77.62	1.15	15.03	5.62	0.58
SiBCN1-2000 powder	31.08	62.03	0	6.89	3.83	$SiB_{0.32}C_{4.67}N_{0.44}$	74.89	0.62	18.12	6.38	0
SiBCN1-1700 bulk	31.81	54.33	2.91	10.95	3.54	$SiB_{0.30}C_{3.99}N_{0.69}O_{0.16}$	75.56	2.24	13.92	6.48	1.80
SiBCN1-2000 bulk	31.17	58.64	1.27	8.92	3.83	$SiB_{0.32}C_{4.40}N_{0.57}O_{0.07}$	75.21	1.32	16.10	6.63	0.74

It is well-accepted that the transformation of polymer-derived amorphous ceramics at high annealing temperatures involves several reactions, including:

$$Si_{3+x}N_4C_{x+y} \rightarrow Si_3N_4 + xSiC + yC \tag{1}$$

$$2Si\text{-}N + 2C \rightarrow 2Si\text{-}C + N_2\uparrow \tag{2}$$

$$2Si\text{-}N \rightarrow 2Si + N_2\uparrow \tag{3}$$

$$Si + C \rightarrow SiC \tag{4}$$

The first reaction starts at low temperatures, and leads to phase seperation. The carbothermal reaction (Reaction (2)) and decomposition of Si_3N_4 (Reaction (3)) occur at 1484 and 1841^{o}C under 1 atm N_2 atmosphere, respectively. The product Si from Reaction (3) may react with carbon again and produce SiC(Reaction (4)).

Previous studies revealed that the carbothermal reaction (Reaction (2)) and the following crystallization of SiC in polymer-derived amorphous ceramics preferentially initiates at surfaces. We tested this theory by annealing polished bulk samples at 1400^{o}C. Figure 40 compares the XRD patterns of the SiCN1 and SiBCN1 ceramics before and after surface polishing. SiCN1 and SiBCN1 bulk ceramics without surface polishing are marked as SiCN1_S and SiBCN1_S. It is clearly seen that, for both SiCN1 and SiBCN1 ceramics, crystallization iniates at 1400^{o}C, and is only observed at the surface.

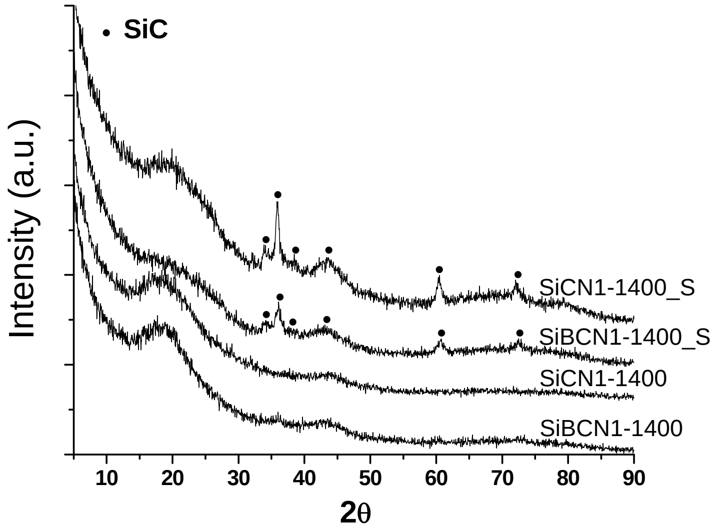

Figure 40: XRD patterns of bulk ceramics prepared at 1400°C before and after polishing

It is seen that Reaction (1) does not lead to any weight change; while both Reactions (2) and (3) result in weight loss. Thereby, we can conclude that the weight loss exhibited by the current materials is mainly due to the evolution of N_2. Indeed, the nitrogen content within the materials significantly decreased with increasing annealing temperature, which can be seen more clearly by comparing the nitrogen content in the samples annealed at 1700°C with their analogues annealed at 1400°C, as discussed in Section 4.2.1 [134]. Since the TG analyses in this study were carried out in a pure argon atmosphere, the reaction (2) and (3) are encouraged and their respective starting temperatures may shift to lower temperatures. Starting temperatures of Reaction (2) and Reaction (3) shift to below 1400 °C and 1800 °C, respectively. For the powder samples, due to the high surface-to-volume ratio, reaction (2) can quickly occur on the surface of the powders at relative low temperature (~1400-1700 °C), leading to a single peak in the corresponding DTG curves (Figure 39 a and c). The boron effect is not obvious. For the bulk samples, Reaction (2) occurs on the surface. Si_3N_4 in the inner part of bulks remains unreacted. Plateaus are shown in temperature range ~ 1600-1700 °C in the TG curves of bulks. This means that there is no significant N_2 revolution in this temperature range. With increasing temperature, Reaction (3) occurs and the bulks lose weight again. Consequently, they exhibit two weight loss peaks (Figure 39 b and d). The build-up of N_2 pressure within the sample may impede the decomposition of Si_3N_4 (Reaction (3)). This explains the lesser weight loss of the bulk samples as compared to the powder samples, especially in the case of SiCN ceramics.

While there is no considerable difference in weight loss between the SiCN1 and SiBCN1 powder samples, the SiCN1 bulk sample showed dramatically greater thermal stability against weight loss as compared to the SiBCN1 analogue. Closer comparison of the TG curves reveals that the weight-loss difference between the SiCN1 and SiBCN1 mainly occurs at the higher temperature range (1600-2100°C), suggesting that Reaction (3) is the dominate source. While Reaction (3) occurres in both bulks, it undergoes faster in SiBCN1 bulk than in SiCN1 bulk. The reason for this is not clear at this moment. One possible explanation is that the boron-containing SiBCN1 bulk sample has more pores than the SiCN1. Therefore, N_2 is released more easily in SiBCN1 bulk and Reaction (3) is enhanced.

The thermal stability of the materials against crystallization was first analyzed using XRD. The results (Figure 41a) reveal that, in SiCN1, the powder sample annealed at 1700°C contains SiC as the main crystalline phase, together with a very small amount of Si_3N_4. For the 2000°C annealed powder sample, SiC is still the dominant crystalline phase, in addition, there is also a small amount of crystalline graphite which is not found in the 1700°C annealed sample. On the other hand, the SiCN1 bulk samples contain more Si_3N_4 phase than the powder sample; and the concentration of the Si_3N_4 phase in the bulk sample increases with increasing annealing temperature. No crystalline carbon was found in bulk samples.

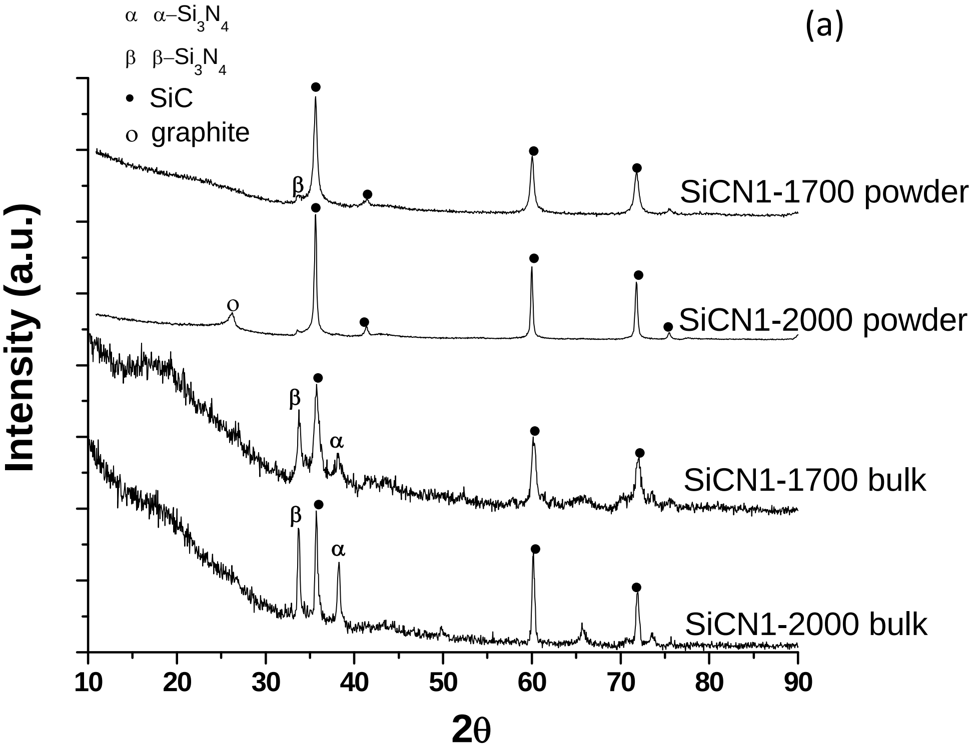

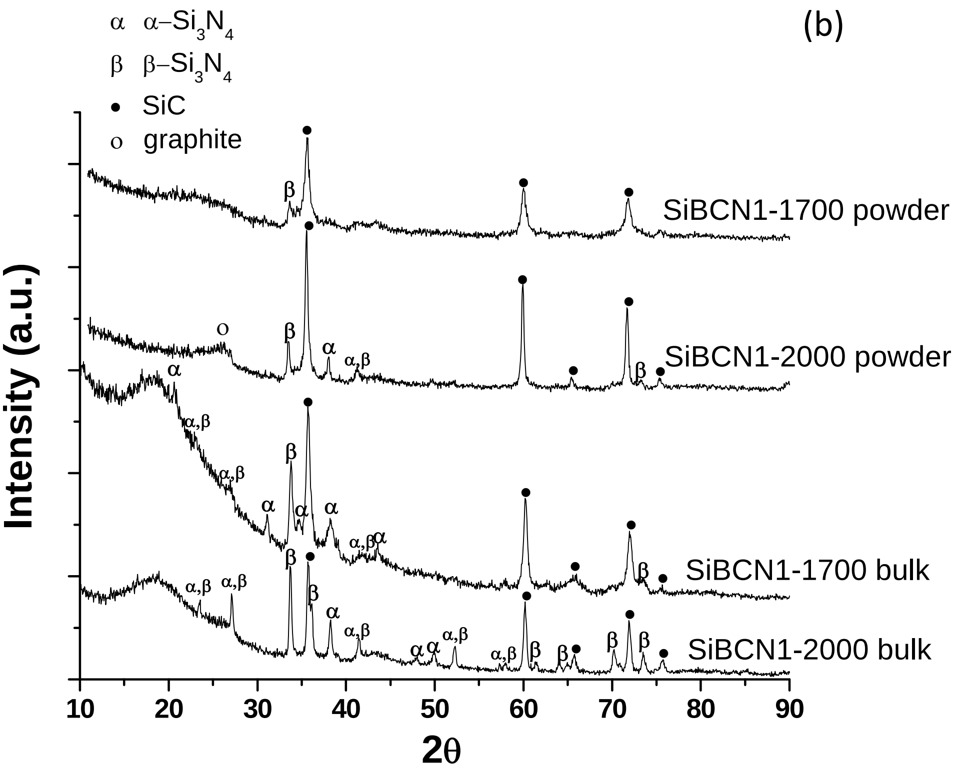

Figure 41: XRD patterns of (a) SiCN1 and (b) SiBCN1 ceramic powder and bulk samples at 1700°C and 2000°C

Figure 41(b) shows the XRD patterns for the SiBCN1 samples. Similar to SiCN1, SiBCN1 powder samples also have a major SiC phase occurring with a very small amount of Si_3N_4. The amount of the Si_3N_4 phase increases with increasing annealing temperature, and a small amount of graphite is found in the 2000°C annealed powder sample. The bulk SiBCN1 samples contain much more Si_3N_4 than the powder analogues, but no crystalline carbon phase exists after annealing at either temperature.

Considering crystalline Si_3N_4 formation, the XRD patterns in Figure 41 reveal that bulk samples always have higher concentrations of Si_3N_4 than their powder analogues, regardless of composition. This could be explained if Reaction (2) occurs more easily in the powder samples. The XRD patterns were measured on polished bulk samples. It demonstrates that relative to powder samples, the inner part of bulk samples contains more crystalline Si_3N_4. Again, this is due to the build-up of N_2 pressure within the bulks, impeding the decompostion of Si_3N_4. The patterns also reveal that, for both the powder and bulk samples, the boron-containing materials have higher Si_3N_4 concentrations than the boron-free samples. This suggests that boron impedes the degradation of Si_3N_4.

Several factors can affect the thermal stability of PDCs against crystallization, including surface area and boron concentration. Surface area effects can be easily seen by XRD. Regardless of the annealing temperature and composition, powder samples have more crystalline phases (evidenced by stronger diffraction peaks) than the bulk counterparts, suggesting that surface area significantly enhances crystallization by providing lower-energy nucleation sites. On the other hand, comparisons between the SiCN1 and SiBCN1 samples reveal that, regardless the sample form, boron-containing samples have more crystalline Si_3N_4, indicating that a low concentration of boron impedes Si_3N_4 degradation.

4.2.3 Summary

Poly(boro)silylcarbodiimide-derived SiCN1 and SiBCN1 ceramics were transformed into bulk materials via a warm pressing process, and into powder materials by simple thermal pyrolysis. The results show that the thermal stability of the ceramics strongly depends on the processing route and on the chemistry of the precursors (i.e., carbon content, precursor type and presence or absence of boron). The microstructures of SiCN1 and SiBCN1 ceramic powders pyrolyzed at 1400 ºC were characterized by the presence of α/β-SiC crystallites embedded in a matrix of amorphous carbon and Si_3N_4 in contrast to the bulk ceramics which remain completely amorphous at this temperature. Moreover, the presence of boron in the SiBCN powder promotes crystallization of SiC. In case of bulk ceramics, SiCN1-1400 shows a fine organization of carbon. The factors influencing the thermal stability against crystallization and decomposition are the chemical composition (especially carbon content and the presence of boron), the architecture of the precursor polymer, and the processing route in terms of its effect on final residual porosity and surface area.

During annealing at temperatures up to 2100 ^{o}C, the crystallization and degradation behaviour were investigated by elemental analysis, TG/DTA and XRD. Compared with their bulk analogues, the powder samples exhibited higher weight loss. The bulk samples exhibited two weight loss events while their powder analogues showed only one, regardless of composition. The degradation of Si_3N_4 in the powder samples is mainly related to the carbothermal reaction, while in the bulk samples both carbothermal reaction and decomposition occur. This difference is likely due to the greater suface-to-volume ratio of the powder samples. We also found that the surface area can enhance the crystallization of ceramics. Samples with larger specific surface areas contain more “easy” sites for the carbothermal reaction to proceed, and for the crystallization of silicon carbide. Meanwhile, the presence of boron impedes the degradation of silicon nitride, indicated by the higher Si_3N_4 concentrations analyzed in boron-containing materials.

4.3 Thermodynamic stability

PDCs exhibit pronounced thermal stability against crystallization and decomposition, making them excellent candidates for high-temperature and ultra-high-temperature applications [2,21,105,107,108,156,157]. Many previous works focused on the nanostructure of these amorphous materials, and furthermore, their thermodynamic stability. It was found that the energetics of this class of ceramics greatly depends on their structures [10–14]. To further understand the effects of structure characteristic on the energetics, following two experiments are designed and carried out in this section:

1) Investigate the effect of the molecular architecture of the precursors, namely linear $[\text{-(PhVi)Si-NCN-}]_n$ and branched $[\text{-(Ph)Si-(NCN)}_{1.5}\text{-}]_n$ polymer, on the structure and energetics of SiCN PDCs. Comprehensive and comparative studies of the structure and energetics of SiCN ceramics were carried out by using multinuclear (^{29}Si, ^{13}C, ^{15}N, and ^{1}H) NMR spectroscopy and oxidative drop solution calorimetry. Special emphasis was given to the previously unexplored aspects of structure and bonding at the interfaces between the constituent nanodomains and their role in controlling the thermodynamic stability of these PDCs.

2) Investigate the effect of pyrolysis temperature (1100°C and 1400°C) on the structural evolution and energetics of amorphous poly(boro)methylvinylsilazane-derived Si(B)CN PDCs. Similarly, the structural and energetic changes were investigated by solid state NMR spectroscopy and oxidative solution calorimetry in molten sodium molybdate.

4.3.1 Structure and energetics of polysilylcarbodiimide-derived SiCN ceramics

The structures of ceramics derived from two polysilylcarbodiimides polymers, namely branched ^{13}C/^{15}N isotope-enriched $[\text{-(Ph)Si-(NCN)}_{1.5}\text{-}]_n$ and linear $[\text{-(PhVi)Si-NCN-}]_n$, were characterized by MAS NMR, and their energetic were measured by high temperature drop solution calorimetry. The chemical compositions are shown in Table 3 of Chapter 3 (Experimental Section). The hydrogen in these ceramics is residual from the precursor polymers due to the relatively low pyrolysis temperature used, and the oxygen is from contamination in air. The nitrogen content is much higher in the Iso_SiCN5 ceramics than in the SiCN1 ceramics because, in branched ^{13}C/^{15}N isotope-enriched $[\text{-(Ph)Si-(NCN)}_{1.5}\text{-}]_n$, each silicon atom connects with a net 1.5 –NCN– group, compared to 1 in $[\text{-(PhVi)Si-NCN-}]_n$. Meanwhile, the carbon content of the SiCN1 ceramics is much higher than the carbon content of the Iso_SiCN5 ceramics. By increasing the pyrolysis temperature, both polymers lose hydrogen in the form of hydrogen gas or other organics; however, there is still a noticeable amount of residual hydrogen in the Iso_SiCN5 ceramic pyrolyzed at 800ºC.

Figure 42 a and b show the ^{29}Si MAS NMR spectra for Iso_SiCN5 and SiCN1 ceramics prepared at 800 and 1100 °C. There is basically only one intense signal at ca. −47 ppm, which is from the SiN_4 tetrahedra similar to that in crystalline Si_3N_4 polymorphs. [158]

Except for SiN_4 tetrahedra, other Si tetrahedral environments with the form SiC_xN_{4-x} (x=0~4) are not significant. However, a minor amount of Si−C bonding from $SiCN_3$ tetrahedra cannot be completely discarded. ^{29}Si nuclides in such environments with 1 C and 3 N nearest neighbors are expected to have a ^{29}Si chemical shift at about −30 ppm [159,160]. Due to the absence of the characteristic band at -110 ppm, there appears to be no SiO_4 tetrahedra.

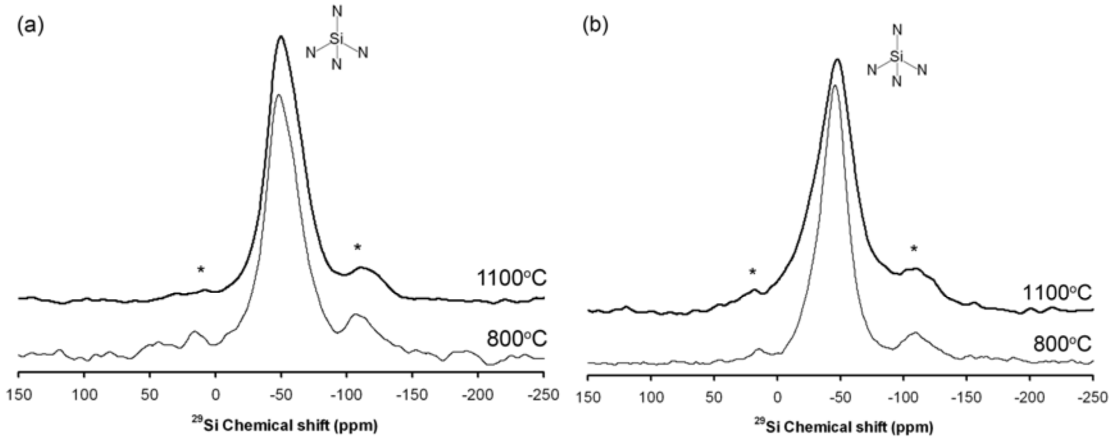

Figure 42: ^{29}Si MAS NMR spectra of (a) Iso_SiCN5-800 and Iso_SiCN5-1100 and (b) SiCN1-800 and SiCN1-1100. Spinning side bands are denoted with asterisks. Reprinted with permission from S. Widgeon, G. Mera, Y. Gao, E. Stoyanov, S. Sen, A. Navrotsky, and R. Riedel, Chem. Mater. 24, 1181 (2012). Copyright © 2012, American Chemical Society [136].

The ^{13}C CPMAS NMR spectra of the Iso_SiCN5 and SiCN1 ceramics are shown in Figure 43. The spectra of the Iso_SiCN5 ceramics prepared at both temperatures (800 and 1100 ºC) indicate two isotropic peaks positioned at approximately 126 and 150 ppm (Figure 43 a,b). The chemical shift at 126 ppm is from turbostratic and amorphous carbon, which lie in the range of 125 to 130 ppm, while the one at ~148 ppm may correspond to sp^2C-N environments [98,161–163]. By carefully fitting the spectra, a calculation was performed to determine the environment around the carbon atoms. The relative fractions of the two carbon sites with chemical shift of 126 and 150 ppm are 62 and 38% for Iso_SiCN5-800, and 76 and 24% for Iso_SiCN5-1100, respectively. It is evident that the content of sp^2C-C increased with increasing pyrolysis temperature, while the fraction of sp^2C-N decreased. The ^{13}C CPMAS NMR spectrum of the SiCN1-800 ceramic (Figure 43 c) shows, predominantly, only one resonance at about 127 ppm. A ^{13}C CPMAS NMR spectrum for the SiCN1-1100 sample was not acquired due to the insufficiency of hydrogen at 1100ºC.

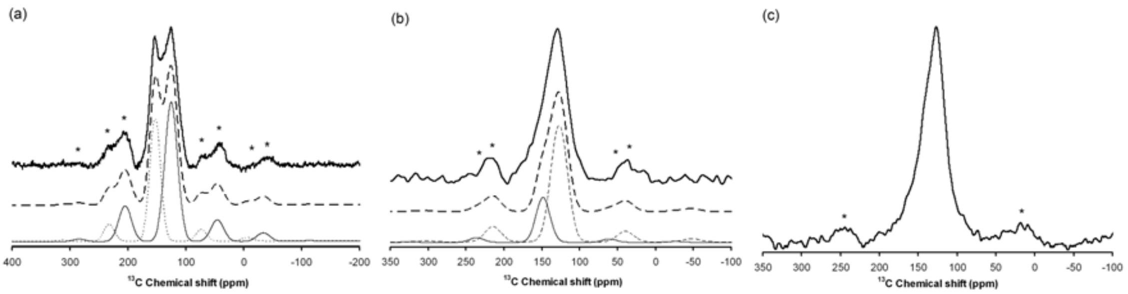

Figure 43: ^{13}C CPMAS NMR spectra of Iso_SiCN5 ceramics prepared at (a) 800 °C and (b) 1100 °C, and (c) SiCN1 ceramics prepared at 800 °C. Experimental spectra are plotted as bold solid lines. Simulations of these spectra are shown with thick dashed lines. Individual simulation components are also shown at the bottom. Spinning side bands are denoted with asterisks. Reprinted with permission from S. Widgeon, G. Mera, Y. Gao, E. Stoyanov, S. Sen, A. Navrotsky, and R. Riedel, Chem. Mater. 24, 1181 (2012). Copyright © 2012, American Chemical Society [136].

The ^{13}C MAS NMR spectra of the Iso_SiCN5 and SiCN1 PDC samples are shown in Figure 44. Besides the dominant resonances at 124 and 150 ppm, there is a third, rather narrow, resonance centered at 111 ppm that likely corresponds to a small fraction of graphite [164]. The fitted bands reveal that there are more relative amounts of sp^{2}C-C and less sp^{2}C-N sites in the Iso_SiCN5-1100 ceramics than in the Iso_SiCN5-800 ceramic. The ^{13}C MAS NMR spectra of the SiCN1 PDC samples pyrolyzed at 800 and 1100 °C (Figure 44 c) display only one broad ^{13}C resonance at about 123 ppm corresponding to an amorphous sp^2 C-C environment.

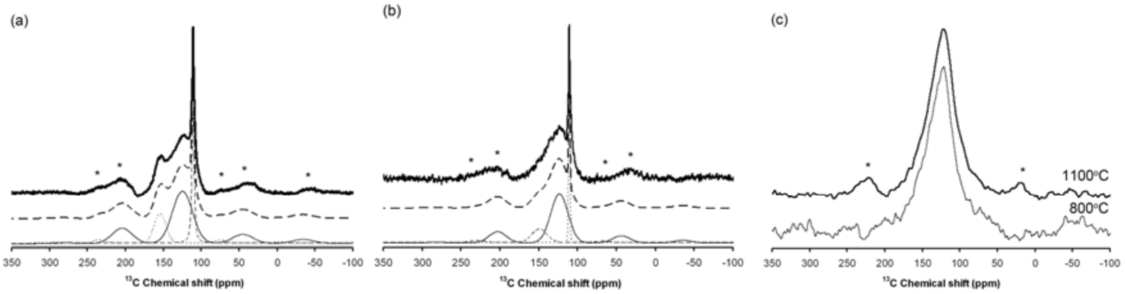

Figure 44: 13C MAS NMR spectra of Iso_SiCN5 PDCs prepared at (a) 800 °C and (b) 1100 °C, and (c) SiCN1 PDCs prepared at 800 °C and at 1100 °C. Experimental spectra are plotted as bold solid lines. Simulations of the Iso_SiCN5 PDCs spectra are shown with thick dashed lines. Individual simulation components are also shown at the bottom. Spinning side bands are denoted with asterisks. Reprinted with permission from S. Widgeon, G. Mera, Y. Gao, E. Stoyanov, S. Sen, A. Navrotsky, and R. Riedel, Chem. Mater. 24, 1181 (2012). Copyright © 2012, American Chemical Society [136].

^{13}C and ^{15}N isotope enrichment of $[\text{-(Ph)Si-(NCN)}_{1.5}\text{-}]_n$ enables one to collect the ^{15}N MAS and ^{15}N CPMAS NMR spectra from derived Iso_SiCN5-800 and Iso_SiCN5-1100 ceramics (Figure 45). Two Gaussian peaks at 21 and 49 ppm can be simulated from the ^{15}N MAS and CPMAS NMR spectra of Iso_SiCN5, although only one resonance exists in the ^{15}N MAS spectrum of Iso_SiCN5-1100. These two bands are assumed to be from the nitrogen environments in $NC_{1/4}Si_{2/4}$ and $NSi_{3/4}$ triangles [162,163,165]. By simulating the direct polariziation ^{15}N MAS NMR spectra (Figure 45c,d), the relative ratios of these environments were found to be 18 % and 82 %, respectively, in Iso_SiCN5-800 (Figure 45c).

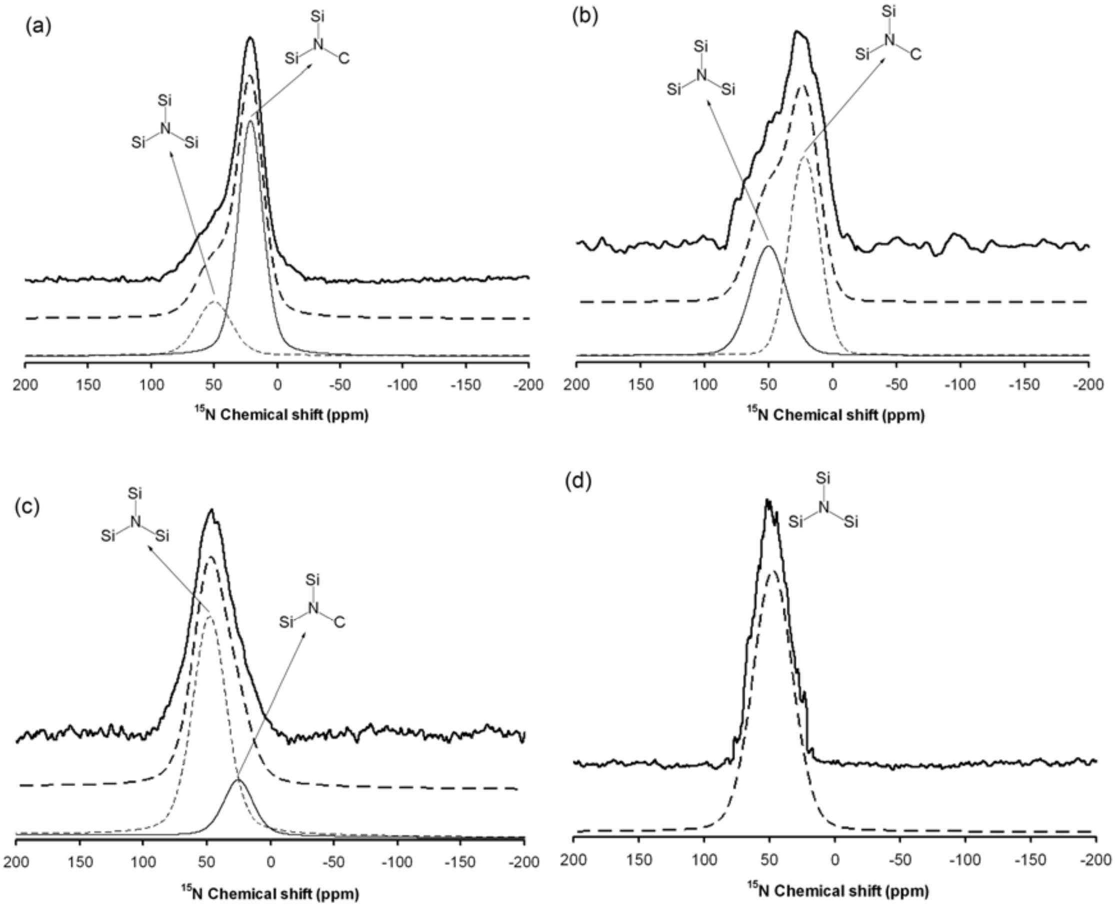

Figure 45: ^{15}N CPMAS NMR spectra of SiCN5 PDCs prepared (a) at 800 °C and (b) at 1100 °C and ^{15}N MAS NMR spectra of SiCN5 PDCs prepared at (c) 800 °C and (d) at 1100 °C. Experimental spectra are plotted as bold solid lines. Simulations of these spectra are shown with thick dashed lines. Individual simulation components are also shown at the bottom. Reprinted with permission from S. Widgeon, G. Mera, Y. Gao, E. Stoyanov, S. Sen, A. Navrotsky, and R. Riedel, Chem. Mater. 24, 1181 (2012). Copyright © 2012, American Chemical Society [136].

The ^{1}H MAS NMR spectra of the Iso_SiCN5 ceramic show two resonances centered at ~1.5 and 6.5 ppm (Figure 46). The broadness of these two bands indicates that these hydrogen atoms are bound to the structure and cannot move freely. The two bands at 1.5 and 6.5 ppm are due to the N-H and sp^{2}C-H chemical bonds, respectively. The line shapes can be simulated using 50% Gaussian - 50% Lorentzian peaks. For ceramics pyrolyzed at either temperature, the relative ratio of N-H and sp^{2}C-H is about 65:35.

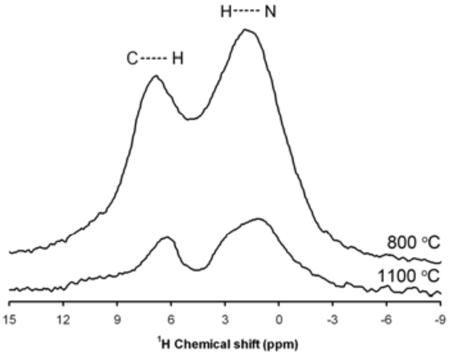

Figure 46: ^{1}H MAS NMR spectra of Iso_SiCN5 PDCs at 800 °C and 1100 °C shown on the same intensity scale. The spectrum of the Iso_SiCN5-800 ceramic has higher intensity than that of the Iso_SiCN5-1100 ceramic indicating loss of hydrogen that occurs during pyrolysis between 800 and 1100 °C. Reprinted with permission from S. Widgeon, G. Mera, Y. Gao, E. Stoyanov, S. Sen, A. Navrotsky, and R. Riedel, Chem. Mater. 24, 1181 (2012). Copyright © 2012, American Chemical Society [136].

Considering all information, these polysilylcarbodiimide-derived SiCN ceramics primarily have only one kind of silicon environment, i.e., the SiN_4 tetrahedra which characterize the Si_3N_4 nanodomains, as indicated by the ^{29}Si MAS NMR spectra. In the SiCN1 ceramics, carbon exists basically as amorphous sp^{2}C-C bonds, based on the ^{13}C MAS and CPMAS NMR spectra. This means that, for the SiCN1 ceramic, the volume fraction of the “free” carbon domains is significantly larger than the interfacial region. The “free” carbon probably forms a continuously interconnected amorphous carbon matrix in the structure, with Si_3N_4 nanodomains embedded in this matrix. The Iso_SiCN5-800 ceramic has sp^{2}C-N bonds in addition to the primary sp^{2}C-C bonds. The sp^{2}C-N bonds are likely positioned at the interface between the Si_3N_4 nanodomains and the “free” carbon regions in the structure. The ^{15}N MAS NMR spectra of the Iso_SiCN5 ceramics also show that the majority of the N atoms are in NSi_3 sites in Si_3N_4 nanodomains, while a relatively minor fraction of the N atoms are bonded to 2 Si and 1 C nearest neighbors, and therefore correspond to the atomic configurations at the interfacial regions between the Si_3N_4 and the C nanodomains. This finding aligns with the ^{13}C MAS NMR results. The C−N−Si linkages are also responsible for the ^{13}C NMR resonance at about 150 ppm, which represents C-N bonds. The intensities of both the ^{13}C NMR resonance at ~150 ppm and the ^{15}N NMR resonance at ~24 ppm are preferentially enhanced upon cross-polarization with ^{1}H (Figure 43 a,b and Figure 45 a,b). These results imply a heterogeneous distribution of protons in the Iso_SiCN5 ceramic. The protons are in much larger abundances near the NC_1Si_2 sites in the interfacial regions than in the interiors of the Si_3N_4 and the “free” C nanodomains. For the Iso_SiCN5-1100 ceramic, there is no observable signal from the NC_1Si_2 environment in the ^{15}N MAS NMR spectrum, which is consistent with the strong drop in intensity of the resonance at 150 ppm in the ^{13}C MAS NMR spectrum. It is believed that the concentration of the NC_1Si environments at the interfacial region between the Si_3N_4 and the “free” C nanodomains decreases with increasing pyrolysis temperature. Concomitantly the hydrogen concentration also decreases. According to the relative fractions of N and H atoms at the interfacial NC_1Si_2 environments, and the total N and H contents in the Iso_SiCN5-800 ceramic (Table 3 in chapter 3), there are nearly 3 H atoms per NC_1Si_2 site. The large loss of hydrogen with an increase pyrolysis temperature leads to a more complete separation of the Si_3N_4 and C nanodomains in Iso_SiCN5-1100 ceramic. This process can be accomplished via bond switching, as shown schematically in Figure 47. Figure 48a shows a schematic of the Iso_SiCN5 ceramic structure with coexisting a-Si_3N_4 and amorphous carbon domains, and an interfacial region constructed by NC_1Si_2 sites. In the case of the SiCN1 PDCs, as discussed above, the carbon domain is possibly continuous, forming a matrix in which the a-Si_3N_4 nanodomains are embedded (Figure 48b).

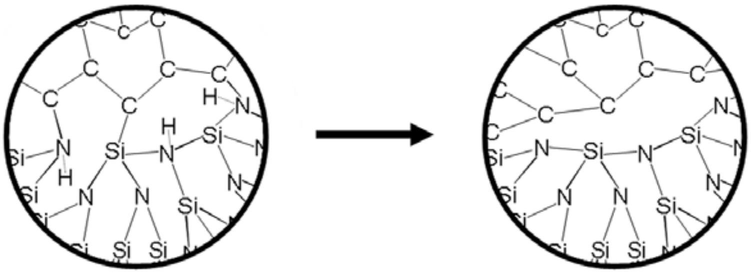

Figure 47: Schematic representation of (left) mixed bonding between Si, C, N and H atoms in the interfacial region between Si_3N_4 and C nanodomains in Iso_SiCN5-800 and (right) loss of hydrogen and of mixed bonding upon pyrolysis at 1100 °C in Iso_SiCN5-1100 facilitated by local bonding switching. Reprinted with permission from S. Widgeon, G. Mera, Y. Gao, E. Stoyanov, S. Sen, A. Navrotsky, and R. Riedel, Chem. Mater. 24, 1181 (2012). Copyright © 2012, American Chemical Society [136].

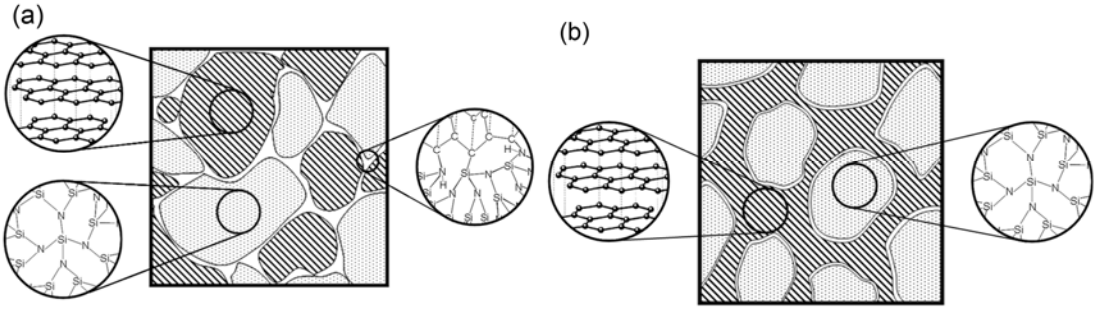

Figure 48: Cartoons of the nanodomain structural models for (a) Iso_SiCN5 and (b) SiCN1 PDCs. The nanometer-scale amorphous/turbostratic carbon and Si_3N_4 domains are shown with stripes and dots, respectively, with the interfacial areas as the white regions. (b) shows a continuous matrix of amorphous/turbostratic carbon with Si_3N_4 clusters embedded in it. The atomic structures within these domains are shown schematically in the insets. Reprinted with permission from S. Widgeon, G. Mera, Y. Gao, E. Stoyanov, S. Sen, A. Navrotsky, and R. Riedel, Chem. Mater. 24, 1181 (2012). Copyright © 2012, American Chemical Society [136].

The high temperature drop solution calorimetry experiments measure the heat of the reaction shown in Scheme 16,

$Si_vC_wN_xO_yH_z$ (solid, 25 °C) + $(v + w - y/2 + z/4)$ O_2 (gas, 809 °C) = $v SiO_2$ (cristobalite, 809 °C) + $w CO_2$ (gas, 809 °C) + $x/2$ N_2 (gas, 809 °C) + $z/2$ H_2O (gas, 809 °C)

Scheme 16

where the values of the coefficients v, w, x, y, and z are given in Table 7.

Table 7 Enthalpies of drop solution (H_{ds}), enthalpies of oxidation at 25 ^{o}C (H_{ox}), enthalpies of formation from the elements ($H^{0}_{f,\ elem}$), and enthalpies of formation from the compounds (see text for details) ($H^{0}_{f,\ comp}$). Uncertainty is two standard deviations of the mean. Numbers in parentheses are numbers of calorimetry drops for each sample.

Sample	g-atom (v + w + x + y + z = 1)					Enthalpies at 25 ^{o}C (kJ/g-atom)			
	Si_v	C_w	N_x	O_y	H_z	H_{ds}	H_{ox}	$H_{f,\ elem}$	$H_{f,\ comp}$
Iso_SiCN5-800	0.096	0.346	0.244	0.041	0.273	-161.1 ± 1.2 (9)	-179.6 ± 1.2	-82.6 ± 1.2	-42.5 ± 1.2
Iso_SiCN5-1100	0.134	0.435	0.285	0.015	0.130	-226.6 ± 1.4 (10)	-243.0 ± 1.4	-68.4 ± 1.4	-25.8 ± 1.5
SiCN1-800	0.121	0.594	0.149	0.020	0.116	-272.0 ± 1.2 (8)	-287.9 ± 1.2	-72.7 ± 1.3	-32.0 ± 1.3
SiCN1-1100	0.126	0.671	0.151	0.019	0.034	-302.0 ± 1.7 (9)	-316.5 ± 1.7	-66.5 ± 1.8	-25.9 ± 1.8

The heat of drop solution, ΔH_{ds}, is the sum of the heat pick-up of the sample from room temperature to the calorimeter temperature, and the heat of the anticipated reaction. From the experimental data (Table 7), the enthalpies of drop solution are strongly negative due to the dominant energetic effect of C and N oxidation. The CO_2 and N_2 gases released after oxidation are swept from the headspace above the solvent using continuously flowing oxygen. Using the thermodynamic data from Table 8, Step 1, the enthalpy of oxidation, ΔH_{ox}, at 25 °C for the two kinds of ceramics can be calculated using the reaction shown in Scheme 17.

$$\Delta H^{0}_{ox} = \Delta H_{ds} - v\Delta H_2 + (v+w-y/2+z/4)\ \Delta H_3 - w\Delta H_4 - x/2\ \Delta H_5 - z/2\ \Delta H_6$$

Scheme 17

The reference heat contents of SiO_2, O_2, CO_2, N_2, and H_2O are marked ΔH_2, ΔH_3, ΔH_4, ΔH_5, and ΔH_6, respectively [166]. The enthalpy of formation from the elements $\Delta H_{f,\ elem}$ at 25 °C for the two ceramics follow from their enthalpy of oxidation ΔH_{ox} (Step 2 in Table 8), and can be generalized by Scheme 18,

$$\Delta H^{0}_{f,\ elem} = -\Delta H_{ox} + v\Delta H_f(SiO_2) + w\Delta H_f(CO_2) + z/2\ \Delta H_f(H_2O)$$

Scheme 18

where the values of ΔH_f are listed in Table 7, and refer to the enthalpies of formation of cristobalite, carbon dioxide, and water from the elements. [167]

In order to calculate the difference in enthalpy between of the amorphous PDCs and an isocompositional mixture of the binary compounds, it is assumed that all of the oxygen in the samples is bonded to silicon forming SiO_2, and the remaining silicon is bonded to nitrogen in form of Si_3N_4. The “free” carbon is assumed to be in form of graphite.

For the Iso_SiCN5 ceramics, “extra” nitrogen is assumed to be N_2 gas in the compositional mixture. In this case, the difference in the enthalpy of formation the PDCs from the binary compounds is calculated using the reaction in Scheme 19.

$$\Delta H_{f,\ SiCNO} = \Delta H_{11} - y/2\ \Delta H_{12} - (v-y/2)/3\ \Delta H_{13}$$

Scheme 19

In the case of the SiCN1 samples, there is sufficient Si to bond to all of the nitrogen, so that nitrogen is not counted as separate component. Thus, the enthalpy differences are calculated using reaction shown in Scheme 20.

$\Delta H_{f,\ SiCNO} = \Delta H_{11} - y/2\ \Delta H_{12} - x/4\ \Delta H_{13}$

Scheme 20

The enthalpies, $\Delta H_{f,\ comp}$, are calculated using the thermodynamic cycles. The measured enthalpies of drop solution, ΔH_{ds}, and the calculated values for ΔH_{ox}, $\Delta H_{f,\ elem}$, and $\Delta H_{f,\ comp}$ are reported in Table 7.

Table 8. Thermodynamic cycles for SiCN1 and Iso_SiCN5 ceramics

Step 1: Enthalpies of oxidation (ΔH^0_{ox}) at 25 °C:	
$Si_vC_wN_xO_yH_z$ (solid, 25 °C) + (v+w-y/2+z/4) O_2 (gas, 809 °C) → v SiO_2 (cristobalite, 809 °C) + w CO_2 (gas, 809 °C) + x/2 N_2 (gas, 809 °C) + z/2 H_2O (gas, 809 °C)	$\Delta H_1 = \Delta H_{ds}$ of SiCN-PDCs
SiO_2 (cristobalite, 25 °C) → SiO_2 (cristobalite, 809 °C)	ΔH_2 = 50.48 kJ/mol [166]
O_2 (gas, 25 °C) → O_2 (gas, 809 °C)	ΔH_3 = 25.51 kJ/mol [166]
CO_2 (gas, 25 °C) → CO_2 (gas, 809 °C)	ΔH_4 = 37.78 kJ/mol [166]
N_2 (gas, 25 °C) → N_2 (gas, 809 °C)	ΔH_5 = 24.77 kJ/mol [166]
H_2O (liquid, 25 °C) → H_2O (gas, 809 °C)	ΔH_6 = 73.6 kJ/mol [166]
$Si_vC_wN_xO_yH_z$ (solid, 25 °C) + (v+w-y/2+z/4) O_2 (gas, 25 °C) → v SiO_2 (cristobalite, 25 °C) + w CO_2 (gas, 25 °C) + x/2 N_2 (gas, 25 °C) + z/2 H_2O (liquid, 25 °C)	ΔH^0_{ox}
$\Delta H^0_{ox} = \Delta H_1 - v\Delta H_2 + (v+w-y/2+z/4)\Delta H_3 - w\Delta H_4 - x/2\Delta H_5 - z/2\ \Delta H_6$	
Step 2: Enthalpies of formation from the elements ($\Delta H^0_{f,\ elem}$) at 25 °C:	
$Si_vC_wN_xO_yH_z$ (solid, 25 °C) + (v+w-y/2+z/4) O_2 (gas, 25 °C) → v SiO_2 (cristobalite, 25 °C) + w CO_2 (gas, 25 °C) + x/2 N_2 (gas, 25 °C) + z/2 H_2O (liquid, 25 °C)	$\Delta H_7 = \Delta H^0_{ox}$
Si (solid, 25 °C) + O_2 (gas, 25 °C) → SiO_2 (cristobalite, 25 °C)	$\Delta H_8 = -908.346 \pm 2.1$ kJ/mol [167]
C (solid, 25 °C) + O_2 (gas, 25 °C) → CO_2 (gas, 25 °C)	$\Delta H_9 = -393.522 \pm 0.05$ kJ/mol [167]
H_2 (gas, 25 °C) + 1/2 O_2 (gas, 25 °C) → H_2O (liquid, 25 °C)	$\Delta H_{10} = -285.83 \pm 0.042$ kJ/mol [167]
v Si (solid, 25 °C) + y/2 O_2 (gas, 25 °C) + x/2 N_2 (gas, 25 °C) + w C (solid, 25 °C) + z/2 H_2 (gas, 25 °C) → $Si_vC_wN_xO_yH_z$ (solid, 25 °C)	$\Delta H^0_{f,\ elem}$
$\Delta H^0_{f,\ elem} = -\Delta H_7 + v\Delta H_8 + w\Delta H_9 + z/2\ \Delta H_{10}$	
Step 3: Enthalpies of formation from the compounds at 25 °C:	
v Si (solid, 25 °C) +y/2 O_2 (gas, 25 °C) + x/2 N_2 (gas, 25 °C) + w C (solid, 25 °C) + z/2 H_2 (gas, 25 °C) → $Si_vC_wN_xO_yH_z$ (solid, 25 °C)	$\Delta H_{11} = \Delta H^0_{f,\ elem}$
Si (solid, 25 °C) + O_2 (gas, 25 °C) → SiO_2 (cristobalite, 25 °C)	$\Delta H_{12} = -908.346 \pm 2.1$ kJ/mol [167]
3Si (solid, 25 °C) +2N_2 (gas, 25 °C) → Si_3N_4 (solid, 25 °C)	$\Delta H_{13} = -850.20 \pm 2.7$ kJ/mol [95]
Iso_SiCN5 samples: from SiO_2 (cristobalite), Si_3N_4, N_2, H_2 and C (graphite) ($\Delta H^0_{f,\ comp}$)at 25 °C	
y/2 SiO_2 (cristobalite, 25 °C) + (v-y/2)/3 Si_3N_4 (solid, 25 °C) + + [x-[4/3(v-y/2)]]/2 N_2 (gas, 25 °C) + w C (graphite, 25 °C) + z/2 H_2 (gas, 25 °C) → $Si_vC_wN_xO_yH_z$ (solid, 25 °C) $\Delta H_{f,\ comp} = \Delta H_{11} - y/2\ \Delta H_{12} - (v-y/2)/3\ \Delta H_{13}$	$\Delta H_{f,\ comp}$

SiCN1 samples: from SiO_2 (cristobalite), Si_3N_4, H_2 and C (graphite) ($\Delta H^0_{f,\ comp}$) at 25 °C	
y/2 SiO_2 (cristobalite, 25 °C) + x/4 Si_3N_4 (solid, 25 °C) + w C (graphite, 25 °C) + z/2 H_2 (gas, 25 °C)→ $Si_vC_wN_xO_yH_z$ (solid, 25 °C) $\Delta H_{f,\ comp} = \Delta H_{11} - y/2\ \Delta H_{12} - x/4\ \Delta H_{13}$	$\Delta H_{f,\ comp}$

As shown in Table 7, the thermodynamic analysis shows that all samples have negative enthalpies of formation from the components, and the ceramics pyrolyzed at 800 °C are more energetically stable than the ceramics pyrolyzed at 1100 °C. Also, the Iso_SiCN5-800 sample is somewhat more energetically stable than the SiCN1-800 PDC. Considering a recently-published study on other phenyl-containing polysilylcarbodiimides-derived ceramics [10], the materials in this work are energetically more stable than those of the previous study. The main difference between the previously studied SiCN samples and the materials investigated in this work is that the precursors in the former study contain -H, -phenyl or –methyl functional groups that form a linear chain. Here, while the SiCN1 precursor contains vinyl groups and is also a linear polymer, the Iso_SiCN5 preceramic polymer is branched. Moreover, the ceramics in the previous study have small amounts of SiC [10], whereas the ceramics in this work contain no SiC component detectable by NMR.

As discussed previously, the ^{13}C MAS NMR data indicate that, compared to the SiCN1 ceramics, the Iso_SiCN5 ceramic prepared at 800 °C contains more mixed N and C bonding (i.e., in the NC_1Si_2 environments at the interface between Si_3N_4 and sp^2 carbon nanodomains). The higher concentration of mixed bonds may also be due to the fact that the Iso_SiCN5 ceramic was derived from a branched preceramic polymer which contains a larger percentage of nitrogen. These N atoms are connected to sp^2-carbon. Combined with the calorimetry results, the higher concentration of mixed bonds between C, N, and Si atoms in the Iso_SiCN5-800 ceramic contributes to its greater energetic stability than Iso_SiCN5-1100. It can be concluded that mixed bonding in interfacial regions stabilize the structure of these PDCs. This hypothesis is consistent with the calorimetry results of Iso_SiCN5-1100 and SiCN1-1100 ceramics, which have no considerable hydrogen at the interfacial region. These materials have identical energetics within experimental error, and are less negative (less stable) than their counterparts pyrolyzed at 800 °C. Moreover, similar observations have also been made in previous studies on SiCO PDCs based on ab initio calculations that indicated that the presence of mixed Si−C−O bonds energetically stabilized the structures of these materials [96].

It is interesting to argue that, the energetic stabilization of mixed bonding coupled with its diminution at higher temperature is a thermodynamic contradiction. There must be a decrease in entropy along with the disappearance of mixed bonding and the coarsening and ordering of Si_3N_4 and C domains. This process is associated with a positive enthalpy change. As the calorimetry results suggest, the free energy of such a process would be positive too. Therefore there would be no driving force for the demixing of mixed bonds. However, hydrogen evolution also results in a change in entropy. The evolution of hydrogen gas and the disruption of the H-stabilized mixed bonding environments is then associated with positive ΔH and positive ΔS terms, and is favored with increasing temperature. The energetic stabilization of the mixed bonds may require the presence of hydrogen near the NC_1Si_2 environments. The positioning of hydrogen at mixed bonds in the interfacial region can be interpreted as stabilizing to the structure and energetic of these PDCs.

4.3.2 Structure and energetics of poly(boro)silazane-derived Si(B)CN ceramics

In this section, the effect of pyrolysis temperature (1100 °C and 1400 °C) on the structural evolution and energetics of amorphous poly(boro)silazane-derived SiCN4 and SiBCN4 PDCs is systematically investigated by solid state NMR spectroscopy and oxidative solution calorimetry in molten sodium molybdate.

Chemical compositions of the samples pyrolyzed at 1100 and 1400 °C, both in weight and atom percentages, are given in Table 9. High temperature thermogravimetric measurements of SiCN4-1100 and SiBCN4-1100 (Figure 49a) show less than 0.5 % mass loss from 1100 to 1400 °C, confirming that for both the boron-containing and boron-free samples, the amounts of the main elements, namely Si, N, C, and B (in case of boron containing-samples), remain constant with increasing pyrolysis temperature in this range. Similarly to most Si-(B-)C-N PDCs, SiCN4 and SiBCN4 ceramics pyrolyzed at 1100 °C are X-ray amorphous (Figure 49b) [21,105,136]. After heat treatment at 1400 ºC, the XRD patterns of these samples are characterized by a very broad reflection extended over the 2θ range of 30 to 50 degrees that may be caused by a change in medium-range order, for example involving the clustering of SiC_4 tetrahedra.

Table 9 Chemical compositions of SiCN4-1100, SiCN4-1400, SiBCN4-1100, and SiBCN4B-1400.

Sample	N wt%*	O wt%	C wt%	Si wt%	B wt%	H wt%	Cl wt%	Molecular Weight (g/g-atom)
SiCN4-1100	17.10 (20.49)	1.56 (1.64)	29.19 (40.81)	51.75 (31.01)	—	0.36 (6.04)	0.04 (0.02)	16.78
SiCN4-1400	17.23 (21.20)	1.44 (1.55)	29.84 (42.84)	51.283 (31.55)	—	0.165 (2.84)	0.042 (0.02)	17.23
SiBCN4-1100	13.60 (16.71)	4.63 (4.98)	28.85 (41.35)	48.36 (29.70)	4.52 (7.07)	0.01 (0.17)	0.03 (0.01)	17.20
SiBCN4-1400	14.09 (17.28)	4.59 (4.93)	28.39 (40.62)	48.20 (29.55)	4.68 (7.44)	0.01 (0.17)	0.04 (0.02)	17.17

*at. % in parentheses.

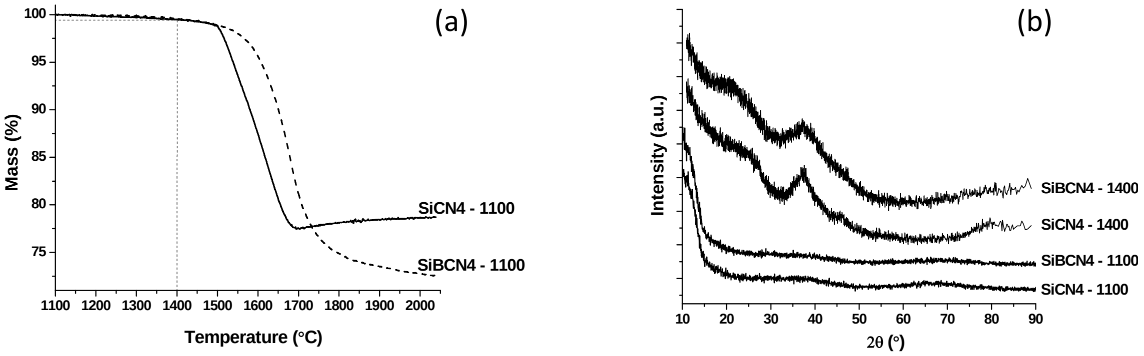

Figure 49 Characterization of the ceramic samples: (a) high temperature thermogravimetric analysis of SiCN4-1100 and SiBCN4-1100, (b) XRD patterns of SiCN4-1100, SiCN4-1400, SiBCN4-1100, and SiBCN4-1400. Reprinted from Scripta Materialia, V 69, Y. Gao, S. J. Widgeon, T. B. Tran, A. H. Tavakoli, G. Mera, S. Sen, R. Riedel, and A. Navrotsky, Effect of Demixing and Coarsening on the Energetics of Poly(boro)silazane-Derived Amorphous Si-(B-)C-N Ceramics, 347, copyright (2013), with permission from Elsevier [135].

Solid-state MAS NMR provides high-resolution structural information on amorphous materials that cannot be gleaned from XRD. The ^{29}Si MAS NMR spectra of boron free samples (SiCN4, Figure 50a) show a broad resonance that spans from ca. -70 to +10 ppm that encompasses the characteristic chemical shifts of SiN_4, $SiCN_3$, SiC_2N_2, SiC_3N, and SiC_4, species located at -48, -35, -5, +3 and -18 ppm, respectively. The relative intensity of the $SiCN_3$ peak, located at ~ -35 ppm, decreased, and concomitantly, the intensity of the SiC_4 peak increased with increasing pyrolysis temperature, suggesting that mixed SiC_xN_{4-x} bonds undergo demixing to form additional SiC_4 and SiN_4 species. The ^{13}C MAS NMR spectrum (Figure 50b) shows resonances around 140 and 122 ppm that correspond to sp^2 C-N and sp^2 C-C environments, respectively [131]. As the pyrolysis temperature is increased from 1100 to 1400 ^{o}C, the relative amount of C-N bonds decreases, and the relative amount of C-C bonds increases, again indicating the demixing of C and N and the release of low amounts of nitrogen as a gaseous by-product. As observed in previous studies, C-N bonds only exist as the interface between SiCN and carbon domains [101]. A decrease in the relative amount of C-N bonds suggests a decrease in the relative mass fraction of interdomain boundaries, and when taken together with the increase in the relative amount of C-C bonds between heat treatments at 1100 and 1400 ºC, strongly suggests the coarsening of carbon domains.

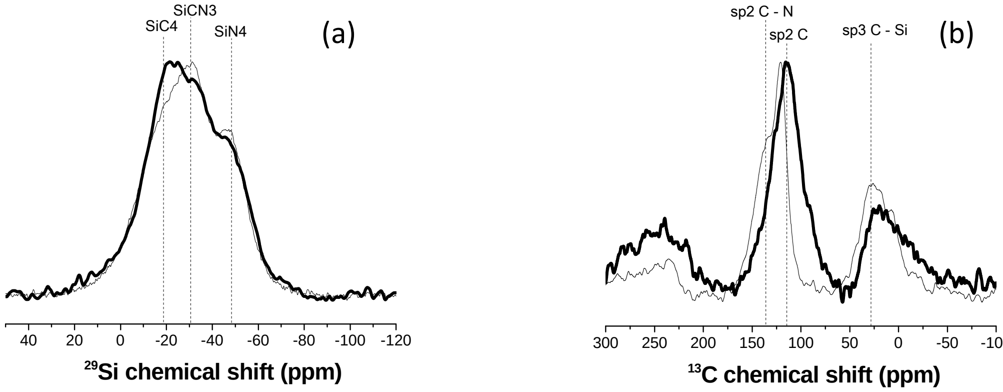

Figure 50 (a) ^{29}Si and (b) ^{13}C MAS NMR of SiCN4-1100 (thin line) and SiCN4-1400 (bold line). Reprinted from Scripta Materialia, V 69, Y. Gao, S. J. Widgeon, T. B. Tran, A. H. Tavakoli, G. Mera, S. Sen, R. Riedel, and A. Navrotsky, Effect of Demixing and Coarsening on the Energetics of Poly(boro)silazane-Derived Amorphous Si-(B-)C-N Ceramics, 347, copyright (2013), with permission from Elsevier [135].

The ^{29}Si MAS NMR spectra (Figure 51a) of the boron-containing SiBCN4 samples also show a demixing of N and C, resulting in a reduction in the relative concentration of the SiC_4N_{4-x}(x=0-4) mixed bonding environments with increasing pyrolysis temperature. This process is manifested in Figure 51a by an increase in the relative amount of SiC_4 tetrahedral environments with respect to the $SiCN_3$ environments. Since the TG analysis does not show mass loss after heating to 1400 ºC, the concentrations of Si and N remain constant, and the demixing of N and C therefore implies that, with increasing temperature, Si-N bonds break, and new B-N bonds are formed. This hypothesis is supported by the ^{11}B MAS NMR spectra (Figure 51b) showing that, with increasing pyrolysis temperature, the relative amount of BCN_2 environments (~ 40 ppm) decreases, while that of the BN_3 environments (~30 ppm) increases. Here, the C lost from the BCN_2 environments contributes to the increase in sp^2 C-C bonds in carbon domains. This is directly observed in the ^{13}C MAS NMR spectra (Figure 51c) where, similar to boron-free SiCN4 sample, the relative amount of C=C bonds increases with increasing pyrolysis temperature. Hence, these data show a decrease in the SiCN-carbon interdomain region. In addition, the ^{13}C MAS NMR spectra (Figure 51c) indicate a tremendous increase in Si-C(sp^3) bonds (~28 ppm), providing further proof that pyrolysis at 1400 °C results in more SiC_4 tetrahedral units than at 1100 °C.

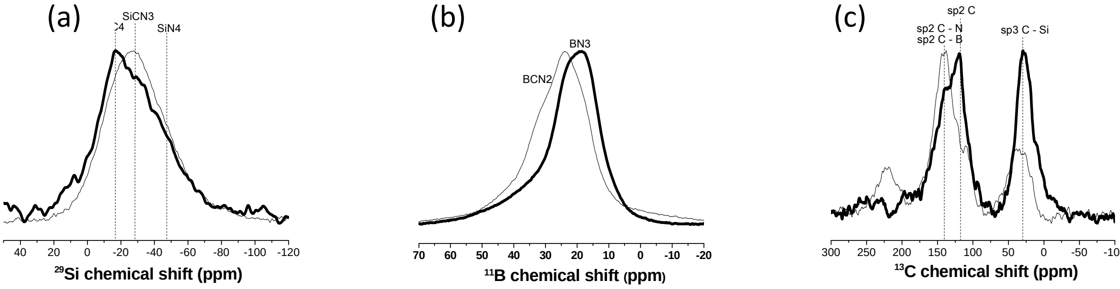

Figure 51 (a) ^{29}Si, (b) ^{11}B, and (c) ^{13}C MAS-NMR of SiBCN4-1100 (thin line) and SiBCN4-1400 (bold line). * Reprinted from Scripta Materialia, V 69, Y. Gao, S. J. Widgeon, T. B. Tran, A. H. Tavakoli, G. Mera, S. Sen, R. Riedel, and A. Navrotsky, Effect of Demixing and Coarsening on the Energetics of Poly(boro)silazane-Derived Amorphous Si-(B-)C-N Ceramics, 347, copyright (2013), with permission from Elsevier [135].

The drop solution enthalpies, ΔH_{ds}, of SiCN4 and SiBCN4 corresponding to reactions (1,2,4,5) in Table 10 are listed in the same table. As previously discussed, the compositions of SiCN4 and SiBCN4 are the same after pyrolysis at 1100 and 1400 °C. Thus, directly comparing drop solution enthalpies using the thermodynamic cycles given in Table 10 yields the enthalpy of structural evolution, $\Delta H_{\text{S-E}}$. The exothermic $\Delta H_{\text{S-E}}$ values of -13.5 ± 4.7 and -8.8 ± 5.7 kJ/g-atom obtained, respectively, for SiCN4 and SiBCN4 reveal that the ceramics heat treated at 1400 °C are energetically more stable than those pyrolyzed at 1100 °C.

Table 10 Thermodynamic cycles for calculating the enthalpies of structural evolution, $\Delta H_{S\text{-}E}$, of samples SiCN4 and SiBCN4 between 1100 and 1400 °C.

Reaction	**Enthalpy (kJ/g-atom)**
a. Enthalpy of the structural evolution of SiCN4 between 1100 and 1400 °C **($\Delta H_{S\text{-}E(SiCN4)}$)**	
(1) $Si_aC_bN_cO_dH_e$ (SiCN4-1100), 25°C + (a+b-d/2+e/4+3c/4) O_2 (gas, 802^0C) → a SiO_2 (cristobalite)* + b CO_2 (gas) + c/2 N_2 (gas) + e/2 H_2O (gas)	$\Delta H_1 = -348.6 \pm 3.5$
(2) $Si_aC_bN_cO_dH_e$ (SiCN4-1400) + (a+b-d/2+e/4+3c/4) O_2 (gas, 802^0C) → a SiO_2 (cristobalite) + b CO_2 (gas) + c/2 N_2 (gas) + e/2 H_2O (gas)	$\Delta H_2 = -335.1 \pm 3.2$
(3) $Si_aC_bN_cO_dH_e$ (SiCN4-1100) → $Si_aC_bN_cO_dH_e$ (SiCN4-1400)	$\Delta H_3 = \Delta H_{S\text{-}E(SiCN4)}$
$\Delta H_3 = \Delta H_{S\text{-}E(SiCN4)} = \Delta H_1 - \Delta H_2 = -13.5 \pm 4.7$ kJ/g-atom	
b. Enthalpy of the structural evolution of SiBCN4 between 1100 and 1400 °C **($\Delta H_{S\text{-}E(SiBCN4)}$)**	
(4) $Si_vC_wN_xO_yB_z$ (SiBCN4-1100), 25^0C + (v+w-y/2+3z/4) O_2 (gas, 802^0C) → v SiO_2 (cristobalite) + w CO_2 (gas) + x/2 N_2 (gas) + z/2 B_2O_3	$\Delta H_4 = -322.3 \pm 4.2$
(5) $Si_vC_wN_xO_yB_z$ (SiBCN4-1400), 25^0C + (v+w-y/2+3z/4) O_2 (gas, 802^0C) → v SiO_2 (cristobalite) + w CO_2 (gas) + x/2 N_2 (gas) + z/2 B_2O_3	$\Delta H_5 = -313.5 \pm 3.9$
(6) $Si_vC_wN_xO_yB_z$ (SiBCN4-1100) → $Si_vC_wN_xO_yB_z$ (SiCN4-1400)	$\Delta H_6 = \Delta H_{S\text{-}E(SiBCN4)}$
$\Delta H_6 = \Delta H_{S\text{-}E(SiBCN4)} = \Delta H_4 - \Delta H_5 = -8.8 \pm 5.7$ kJ/g-atom	

* The temperature of products in reactions (1,2,4,5) is 802°C.

In SiBCN4 ceramic prepared at 1100 °C, the presence of only BN_2C sites, combined with the lack of BNC_2 and BC_3 sites, indicates that the BN units are likely interfacial. It is suggested that the majority of the BN triangles must be bonded to SiC_xN_{4-x} (x=0~4) domains and carbon domains through Si-C-B and B-C-C (or N-C-C) bridges, respectively. When the pyrolysis temperature is increased to 1400 °C, Si-N bonds break, and B-N and Si-C bonds form. Meanwhile, the cleavage of interfacial B-C and N-C bonds leads to the formation of B-N and C-C bonds. Similarly, in the case of SiCN4 ceramic, the cleavage of C-N bonds at the interfacial regions between SiC_xN_{4-x} (x=0~4) and carbon domains occurs with increasing pyrolysis temperature. The breaking of bonds at the nanodomain interfaces results in an increase of the interface energy, providing a driving force for further nanodomain coarsening in order to compensate the increased energy of the system caused by the missing interdomain bonds. Therefore, demixing of the interfacial bonds can energetically promote coarsening of the SiC_xN_{4-x} and carbon nanodomains, as suggested by the NMR analysis.

We conclude that demixing and coarsening, occurring concurrently, stabilize the PDC structures. It is obvious that the coarsening processes reduce the total energy of a system through the elimination of interfaces. A previous NMR study on carbon-rich Si-C-N PDCs indicates that the presence of mixed bonded SiC_xN_{4-x} (x=0-4) in the interfacial region between amorphous sp^2 C and silicon nitride may contribute to thermodynamic stability only if local H atoms are present at the interface, as discussed in Section 4.3.1 (also see [136]). In the present study, Si-(B-)C-N ceramics were derived from a different precursor, poly(boro)silazane, and were pyrolyzed at higher temperatures. Since the hydrogen content in these samples is substantially lower, it is less likely to play a significant role in the structural or thermodynamic stability of the ceramics.

4.3.3 Summary

Multinuclear MAS NMR spectroscopy demonstrated that the structure of carbon rich Iso_SiCN5 and SiCN1 SiCN ceramics derived from phenyl-containing polysilylcarbodiimides consists predominantly of separate amorphous silicon nitride and sp^2 carbon nanodomains. The results of oxide melt solution calorimetry indicate that both Iso_SiCN5 and SiCN1 ceramics are energetically more stable after pyrolysis at 800 °C than after pyrolysis at 1100°C. Moreover, Iso_SiCN5 ceramics are also more energetically stable than SiCN1 ceramics. The energetic stabilization of the Iso_SiCN5 ceramic is attributed to the presence of mixed bonding between N, C, and Si atoms at the interfacial region between the Si_3N_4 and C nanodomains, which could be attributed to the nature of their precursors: Iso_SiCN5 ceramics are derived from a branched polysilsesquicarbodiimide, while SiCN1 is formed from a linear polysilylcarbodiimide. The relative concentrations of the mixed bonds between N, C, and Si atoms decrease upon an increase in the pyrolysis temperature to 1100 °C, along with a concomitant loss of hydrogen. It is hypothesized that the mixed bonds are stabilized by hydrogen bonding at the interfacial regions between the Si_3N_4 and C nanodomains, and that the loss of this hydrogen at higher temperatures provides the driving force for the destruction of mixed bonding.

The effect of pyrolysis temperature on the structural evolution of amorphous poly(boro)methylvinylsilazane-derived Si-(B-)C-N was investigated. By MAS NMR, the main processes governing structural evolution between 1100 and 1400 ºC are identified as (i) the demixing of SiC_xN_{4-x}(x=0-4) mixed bonding environments, (ii) the cleavage of mixed bonds at interdomain regions, and (iii) the coarsening of domains. Calorimetry demonstrates that this structural evolution is favorable in both enthalpy and free energy.

4.4 Solid state structure and microstructure of Si(B)CN ceramics

The existence of nanodomains in X-ray amorphous PDCs has attracted extensive attention, because nanodomains are considered to be responsible for the thermal stability, crystalline behavior, and other properties of the ceramics. In this section, we investigate the chemical environment of nanodomains and nanodomain interfaces, and the nanodomain size of the ceramics. The ceramics are characterized by (i) MAS NMR, which can probe chemical bonding information to reveal the local environment of atoms; (ii) Small angle X-ray scattering (SAXS) which can be used to determine the average nanodomain size. MAS NMR and SAXS are both integral methods and can reveal the overall structural information of the materials. This investigation is assisted by other techniques, including XRD, TEM and Raman spectroscopy. The effect of boron modification, carbon content, and precursor molecular architecture on the final nanodomain structure is discussed.

4.4.1 Solid state structure of Si(B)CN ceramics

Structural investigations by MAS NMR spectroscopy show that the segregation of N and C into separate Si tetrahedra is a characteristic of polysilylcarbodiimide-derived SiCN ceramics. This is in strong contrast to the observation of significant N and C mixing in the nearest neighbor coordination environment of Si in polysilazane-derived SiCN PDCs. The structure of nanodomain and nanodomain interfaces of the ceramics derived from tailored precursors are characterized by ^{29}Si,^{13}C and ^{11}B MAS NMR. ^{29}Si and ^{13}C MAS NMR spectra (Figure 52 and Figure 53) were measured on SiCN ceramics. ^{11}B MAS NMR (Figure 54) was additionally completed on the boron-modified SiBCN ceramics. The selected ceramics were prepared at 1100°C and 1400°C. 1100°C is the standard temperature for producing amorphous PDCs, and 1400°C is a temperature at which phase separation occurs, but no deleterious crystallization initiates.

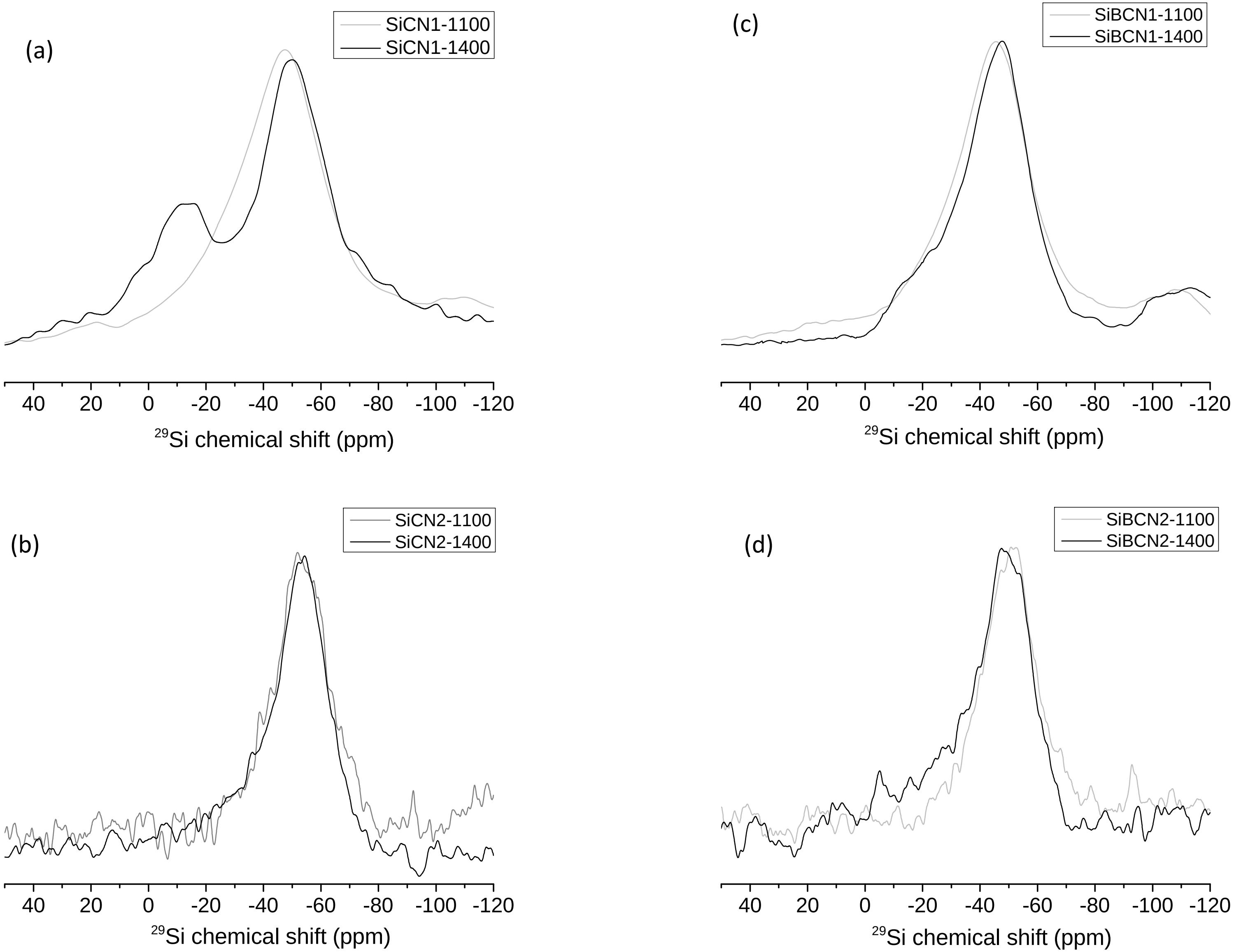

Figure 52 ^{29}Si MAS NMR spectra (to be continued)

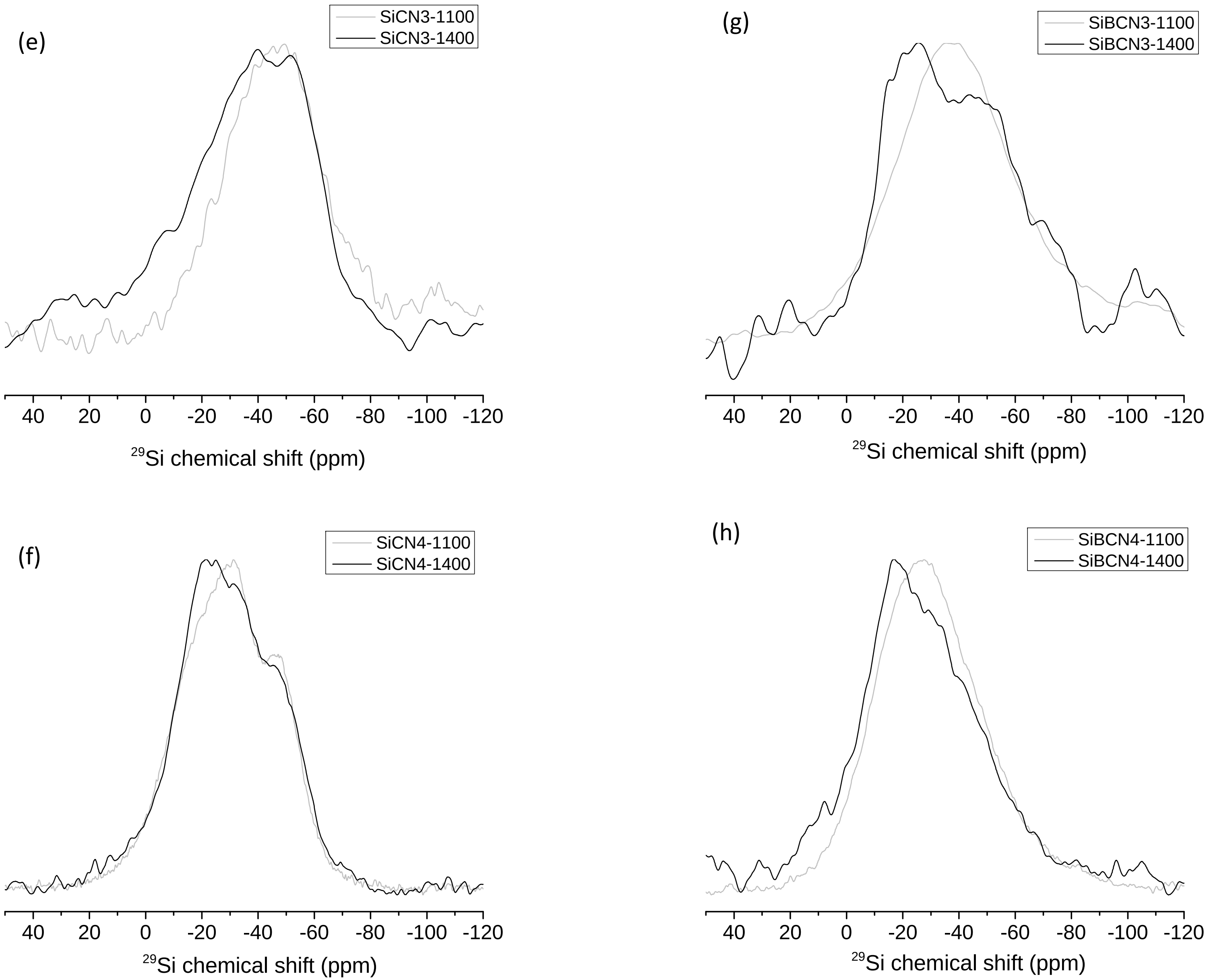

(continued) ^{29}Si MAS NMR

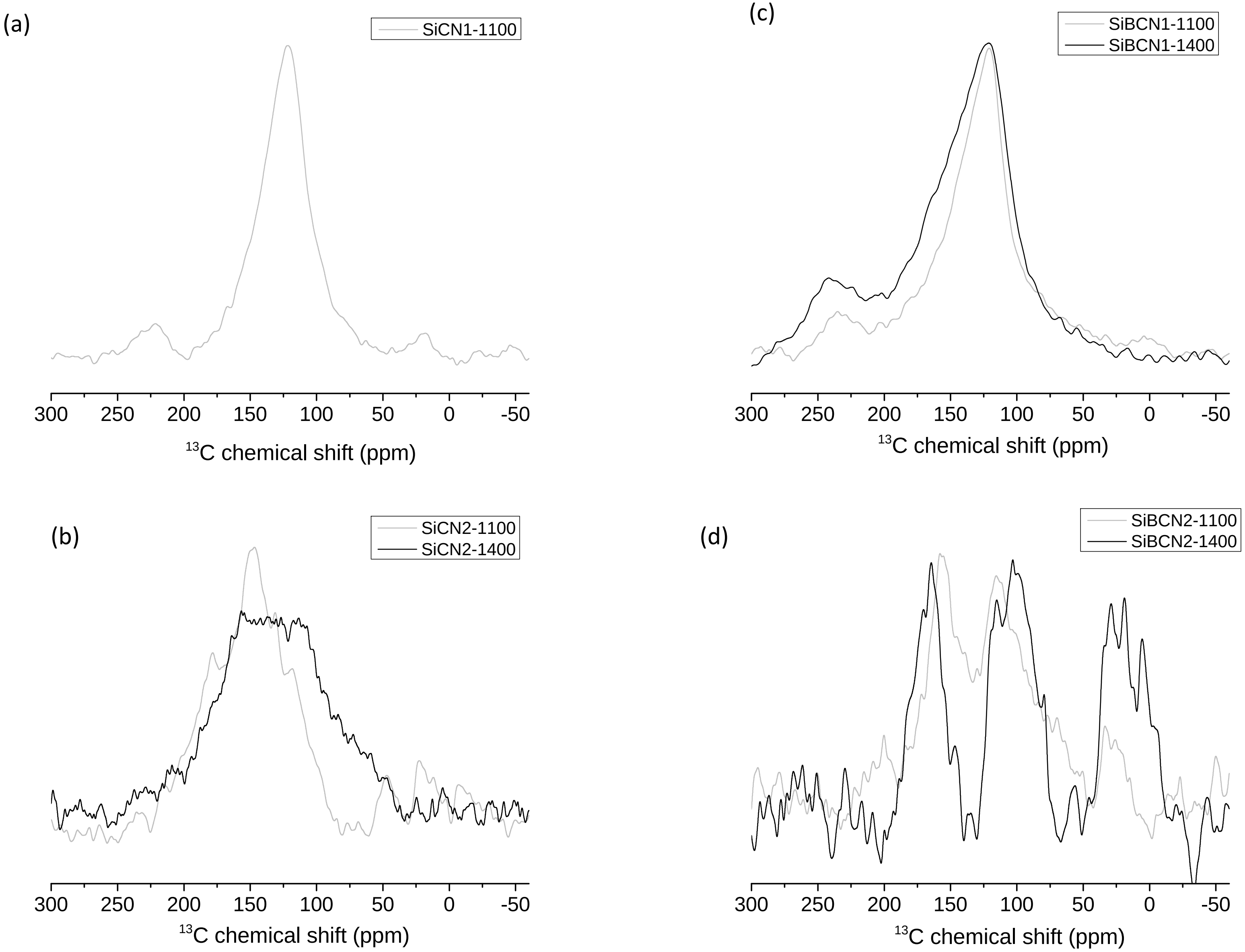

Figure 53 ^{13}C MAS NMR spectra (to be continued)

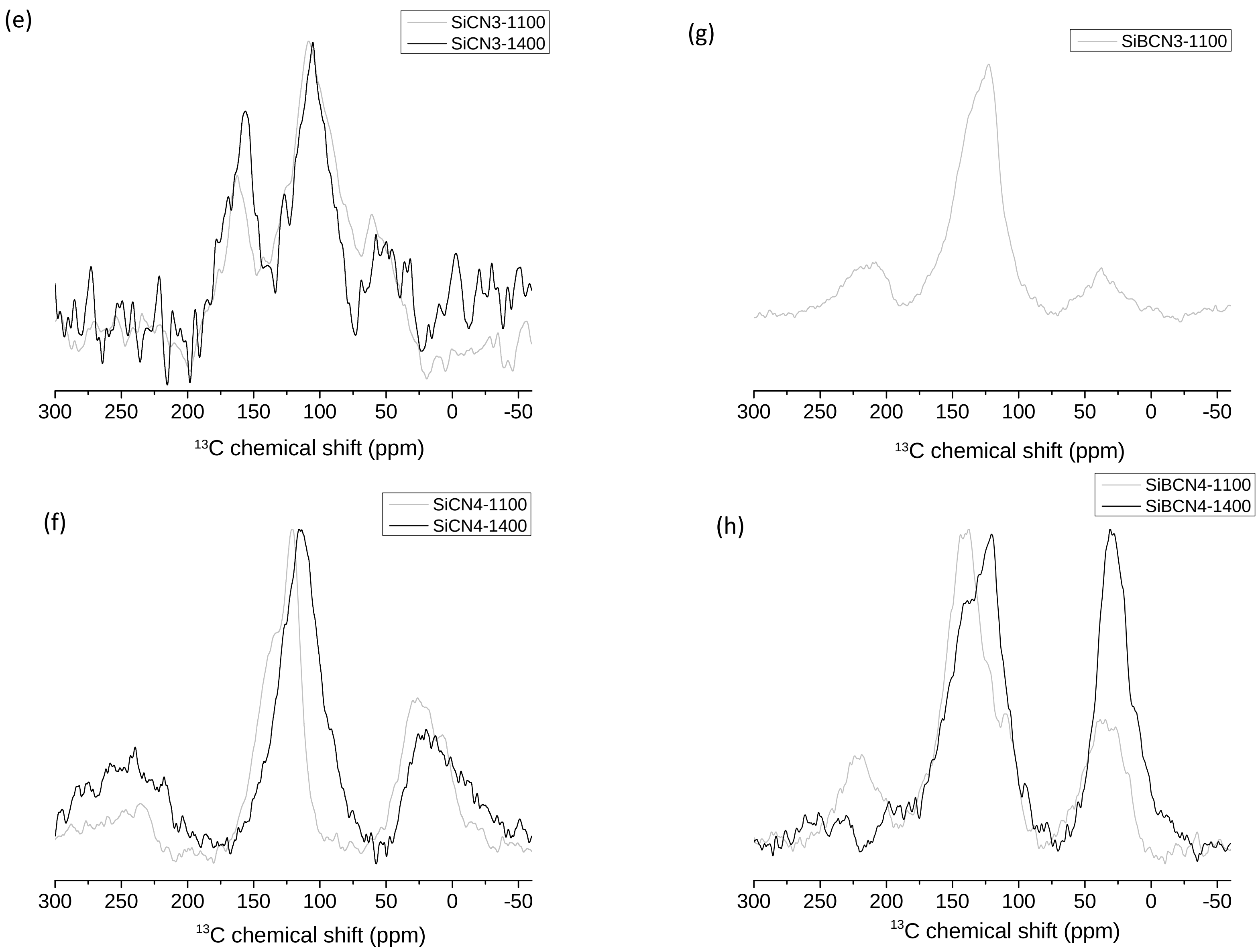

(continued) ^{13}C MAS NMR

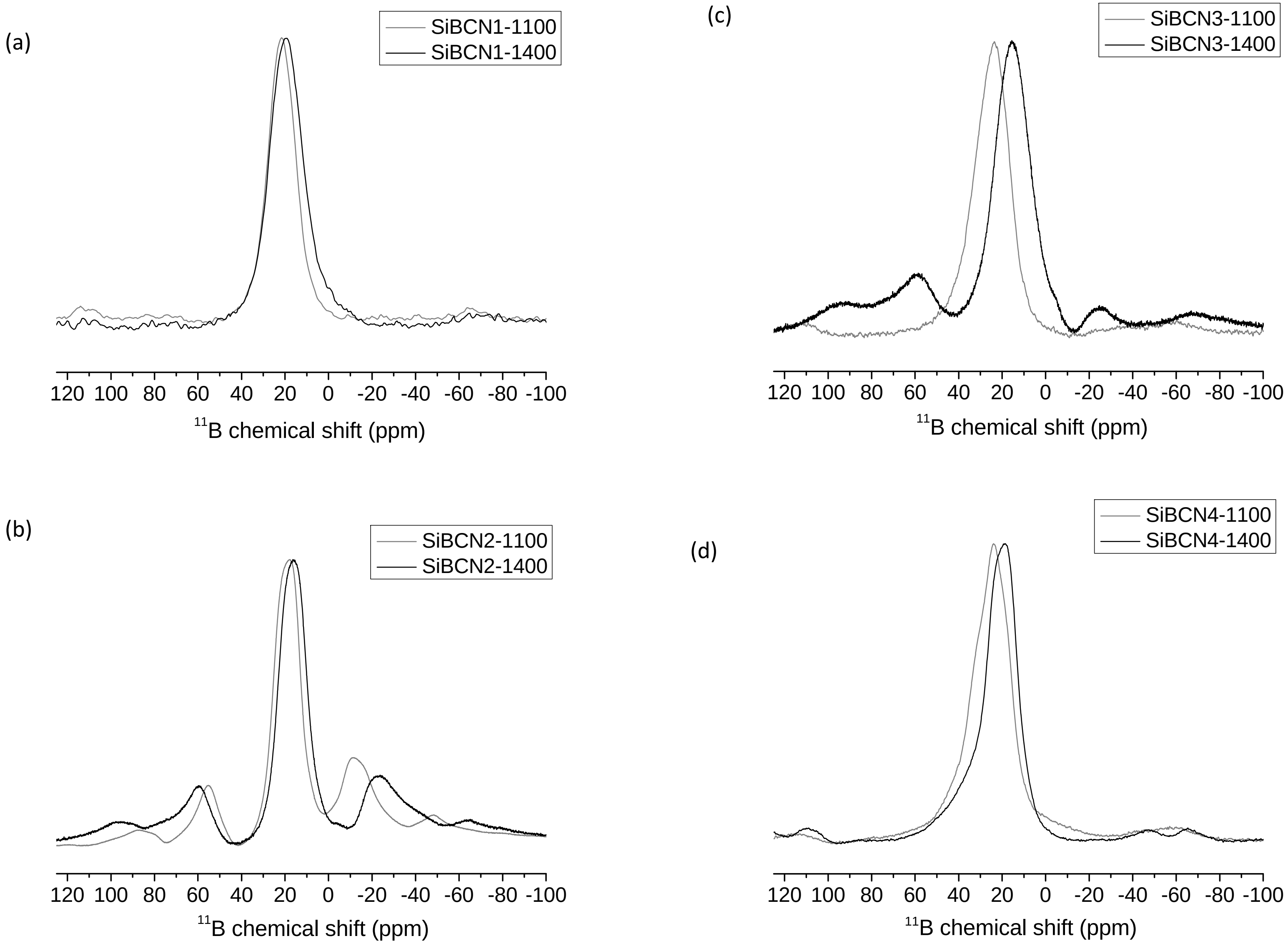

Figure 54 ^{11}B MAS NMR spectra

4.4.1.1 Solid state structure of polysilylcarbodiimide-derived SiCN1and SiCN2 ceramics

The chemical bonding environments of silicon atoms and carbon atoms were obtained by MAS NMR for polylsilylcarbodiimide-derived SiCN ceramics, i.e. SiCN1, SiCN2 ceramics. The separation of the Si_3N_4 and “free” carbon nanodomains was seen in previous structural studies of SiCN1 ceramic [136]. The ^{29}Si MAS NMR spectra (Figure 52 (a)) of these ceramics pyrolyzed at 1100ºC show mainly one heterogeneously broadened Gaussian peak with a ^{29}Si isotropic chemical shift (δ_{iso}) of ~ -48ppm, corresponding to the presence of primarily one kind of silicon environment i.e. the SiN_4 tetrahedral units that are characteristic of Si_3N_4 nanodomains. This result implies almost complete separation of nitrogen and carbon, and the formation of Si_3N_4 and “free” carbon nanodomains in the structures of these PDCs. However, some Si−C bonding may be present at the interfaces of these domains. The ^{13}C MAS NMR spectrum of the SiCN1-1100 PDC (Figure 53(a)) contains primarily one isotropic peak at δ_{iso} ~125 ppm, characteristic of sp^2 hybridized carbon network, and the broad nature of the peak indicates an amorphous structure. This means C is present primarily as amorphous sp^2-bonded carbon domains. In the ^{13}C NMR spectra of SiCN1 PDCs, the absence of any significant NMR signal near ~150 ppm, corresponding to C−N bonds, indicates a significantly smaller fraction of such carbon environments in the structure compared to that of “free” carbon. Consequently, this result also implies that the average size of the “free” carbon domains is very large in highly carbon-rich SiCN1 PDC. The “free” carbon possibly forms a continuously interconnected amorphous carbon matrix in this kind of PDC. In this case, the Si_3N_4 nanodomains are expected to be embedded in the amorphous carbon matrix in the case of the SiCN1 PDCs (Figure 55(a)).

SiCN2 ceramics were derived from $[\text{-(MeVi)Si-NCN-}]_n$, which has a methyl group and lower carbon content compared to the SiCN1 precursor. The ^{29}Si MAS NMR spectrum of SiCN2-1100 (Figure 52(b)) primarily contains SiN_4 tetrahedral units and $SiN_3(NCN)$ units. The signal of the $SiN_3(NCN)$ units are centered at ca. -60 ppm. FT-IR spectrum of SiCN2-1100 confirms the presence of –N=C=N- group which has the signal at ca. 2150cm^{-1} (Figure 56). According to the ^{13}C MAS NMR spectrum (Figure 53(b)), there is a significant amount of sp^2 C-N bonds in the structure of the SiCN2-1100 ceramic, which is different from that of SiCN1. These sp^2 C-N bonds are located at the interface between the SiN_4 and the “free” carbon nanodomains, and no considerable amount of Si-C bonding is observed. A schematic is shown in Figure 55(b).

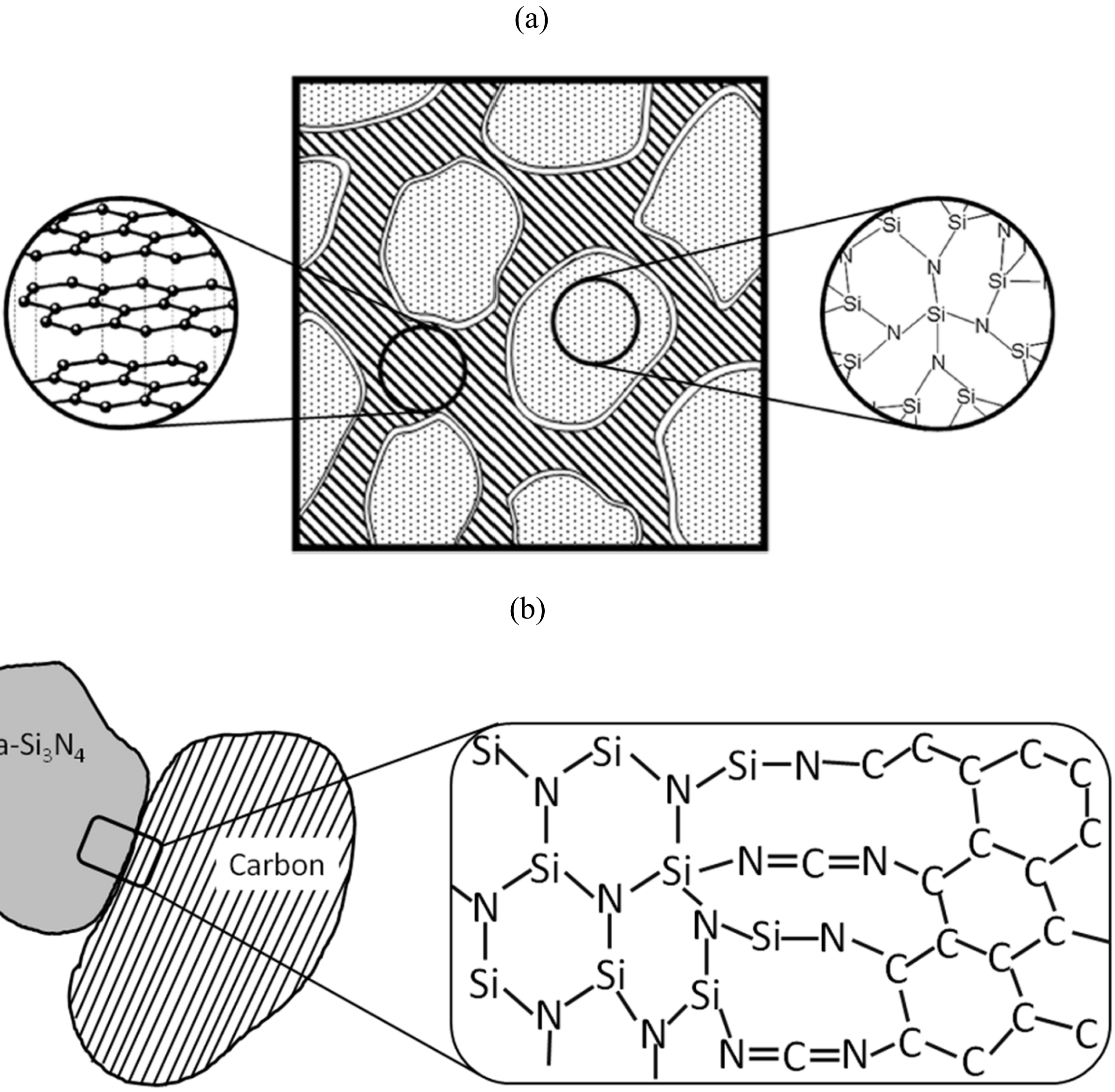

Figure 55 Schematic drawing of polysilylcarbodiimide-derived (a) SiCN1-1100. Reprinted with permission from S. Widgeon, G. Mera, Y. Gao, E. Stoyanov, S. Sen, A. Navrotsky, and R. Riedel, Chem. Mater. 24, 1181 (2012). Copyright © 2012, American Chemical Society [136]; (b) SiCN2-1100 ceramics

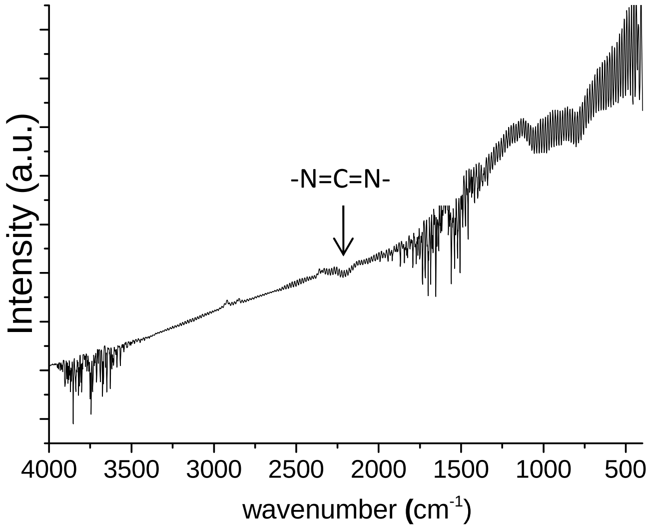

Figure 56 FT-IR spectrum of SiCN2-1100

At 1400 ºC, the ^{29}Si MAS NMR spectrum of the SiCN1-1400 PDC has two main bands representing SiC_4 and SiN_4 tetrahedra. The signal of SiC_4 environments is located at ~ -18 ppm. The formation of SiC phase is due to the carbothermal reaction of Si_3N_4 with carbon. The embedded SiN_4 nanodomains connect to “free” carbon domains via SiC_4 domains, shown in Figure 57 (a).

SiCN2-1400 shows an increase of the band at about -35 ppm in the ^{29}Si MAS spectrum, which represents SiN_3C tetrahedra. With an increase in temperature, Si-N=C=N- bonds break, nitrogen gas releases, and Si-C bonds form. ^{13}C MAS NMR spectrum shows a very broad band which is the overlap of the sp^2 C-C and sp^2 C-N bands. The schematic representation of the bonding in SiCN2-1400 is shown in Figure 57 (b).

(a)

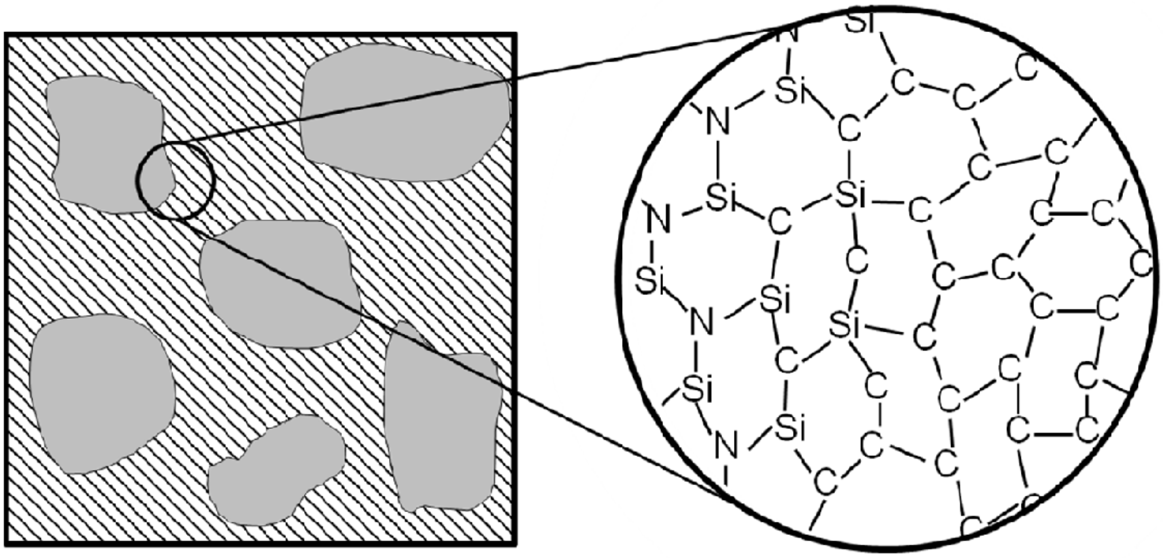

(b)

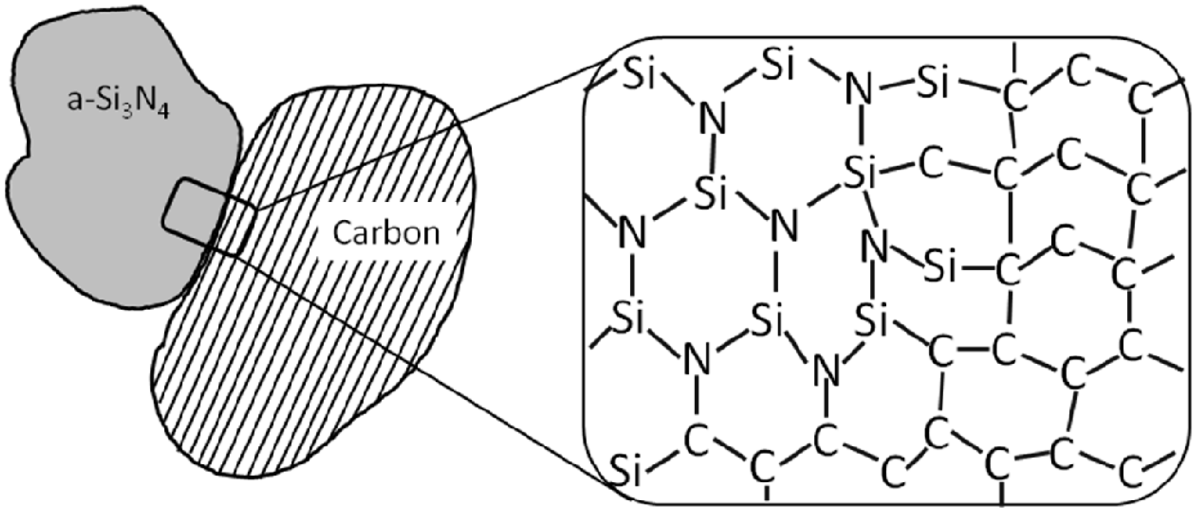

Figure 57 Schematic drawing of polysilylcarbodiimide-derived (a) SiCN1-1400, (b) SiCN2-1400 ceramics

4.4.1.2 Solid state structure of polyborosilylcarbodiimide-derived SiBCN1 and SiBCN2 ceramics

Besides ^{29}Si MAS NMR (Figure 52 (c) and (d)) and ^{13}C MAS NMR (Figure 53 (c) and (d)), the structures of polyborosilylcarbodiimide-derived SiBCN1 and SiBCN2 ceramics were also studied by ^{11}B MAS NMR (Figure 54 (a) and (b)). Similar to SiCN1-1100 ceramic, the ^{29}Si MAS NMR spectrum of SiBCN1-1100 (Figure 52 (c)) shows only one signal with a δ_{iso} near -48 ppm indicating the presence of SiN_4 tetrahedra, where silicon is bonded to four nitrogen atoms as in crystalline Si_3N_4. This leads to the formation of Si_3N_4 domains that are separated from the “free” carbon and boron nitride domains.

In SiBCN1 ceramics, sp^{2}C-bonded carbon environments, characterized by a δ_{iso} of ~ 125 ppm in the ^{13}C MAS NMR spectra (Figure 53 (c)), take great part, but about 10% of the carbon atoms are in form of C-N, which has a δ_{iso} of ~ 150 ppm. It is assumed that the C-N bonds exist as the interface between the “free” carbon and the SiC_xN_{4-x} (x=0-4) domains in SiBCN1 ceramics.

The ^{11}B MAS spectrum of the SiBCN1 ceramics show only BN_3 units characterized by a δ_{iso} of ~ 27 ppm with a lack of other BC_xN_{3-x} (x=0-3) bonds. This means that BN domains are located separately from the Si_3N_4 and C domains. Therefore, the structure of SiBCN1 ceramics consists of Si_3N_4, BN and C nanodomains, which are connected through N–B and N–C bonds. The BN domains most likely represent an interfacial phase between the Si_3N_4 and C domains, as shown in Figure 58.

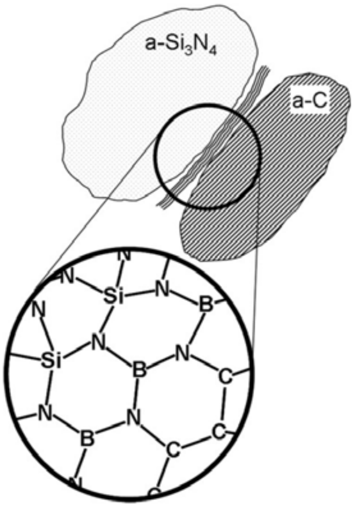

Figure 58 Schematic representation of SiBCN1-1100 and SiBCN2-1100 ceramics. From S. Widgeon, G. Mera, Y. Gao, S. Sen, A. Navrotsky, and R. Riedel, J. Am. Ceram. Soc. 96, 1651 (2013). Copyright © 2013 by John Wiley Sons, Inc. Reprinted by permission of John Wiley & Sons, Inc [131].

For SiBCN2-1100, ^{29}Si MAS NMR (Figure 52 (d)) shows only SiN_4 units without considerable Si-C bonds in the structure, while ^{13}C MAS NMR (Figure 53 (d)) reveals another signal with a δ_{iso} of ~ 150 ppm indicating C-N bonds besides the primarily sp^{2}C-bonds. The structure could be described to be the same as that of the SiBCN1 ceramic, as shown in Figure 58. Besides the similarity, SiBCN2 ceramic does show stronger intensity of the C-N band. One possible reason for this could be because the SiBCN2 ceramic has much lower carbon content, and thus a comparably higher amount of Si_3N_4 (see Chapter 3, Table 3 for the chemical compositions of ceramics), and accordingly forms a higher volume of interfaces with C-N bonds.

When the annealing temperature is increased to 1400 °C, both SiBCN1 and SiBCN2 ceramics show small bands in the ^{29}Si NMR spectra at about -18 ppm suggesting the formation of SiC domains. The signal is also increased at ca. 30 ppm in ^{13}C MAS NMR spectra which represents sp^3 C-Si bonding. This was also seen by TEM and by selected area electron diffraction (SAED) in previous studies of polyborosilylcarbodiimide-derived SiBCN ceramics. The nanocrystalline SiC results from the solid-state reaction of amorphous C with the Si_3N_4 domains (Section 4.2). Tavokoli et al. have observed the same crystallization behavior [152].

4.4.1.3 Solid state structure of polysilazane-derived SiCN3 and SiCN4 ceramics

Polysilazane-derived SiCN3 and SiCN4 ceramics prepared at 1100°C have mixed bonding environments about the Si atoms, namely SiC_xN_{4-x} (x=0~4) tetrahedra. This is in sharp contrast to the polysilylcarbodiimide-derived SiCN ceramics which have no such mixed bonding environments. In the ^{29}Si MAS NMR spectra, the chemical shifts of the $SiCN_3$, SiC_2N_2, SiC_3N tetrahedra are centered at ca. -35, -5, and 3 ppm, respectively. The ^{29}Si MAS NMR spectra of SiCN3 and SiCN4 ceramics prepared at 1100°C (Figure 52 (e) and (f)) show an overlap of several bands which are from SiC_xN_{4-x} (x=0-4) mixed bonds. The band at -18 ppm, characteristic of the SiC_4 tetrahedra, is also observed in the structure of samples pyrolyzed at 1100°C. The ^{13}C MAS NMR spectra of these two ceramics (Figure 53 (e) and (f)) show primarily two resonances at ca. 125 and 150 ppm indicating sp^2C-C environments, as well as sp^2C-N bonds. The ^{13}C MAS NMR spectra also confirm the presence of sp^3C-Si bonds which have a δ_{iso} of ~ 30 ppm. The presence of SiC_4 tetrahedra indicates the formation of SiC nanodomains at 1100°C. This is different from polysilylcarbodiimide-derived SiCN1 and SiCN2 ceramics, which contain no SiC nanodomains after pyrolysis at the same temperature. Figure 59 presents a schematic of the structure of SiCN3 and SiCN4 ceramics prepared at 1100°C. The SiC nanodomain is assumed to be the transition region between the Si_3N_4 and carbon nanodomains.

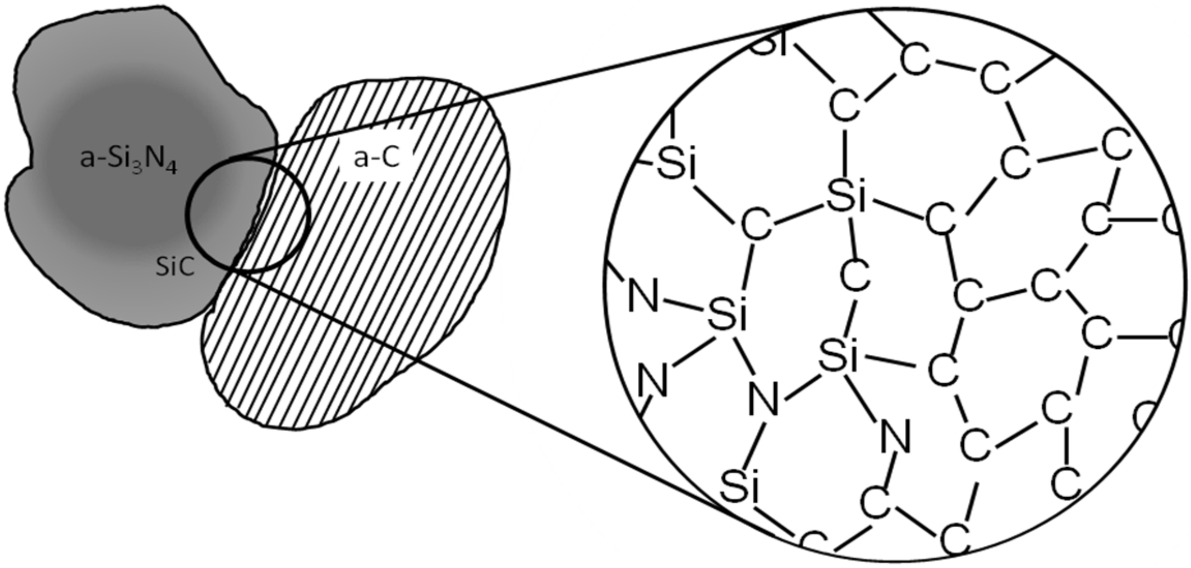

Figure 59 Schematic representation of SiCN3-1100 and SiCN4-1100 ceramics

In the ^{29}Si MAS NMR spectra of ceramics prepared at 1400°C, the intensity of the band at -18 ppm, which represents the SiC_4 tetrahedral environments, increases relative to the spectra of samples pyrolyzed at lower temperatures. This demonstrates the growth of SiC with an increase of annealing temperature.

4.4.1.4 Solid state structure of polyborosilazane-derived SiBCN3 and SiBCN4 ceramics

The ^{29}Si MAS NMR spectra of polyborosilazane-derived SiBCN3 and SiBCN4 ceramics (Figure 52 (g) and (h)) reveal the presence of significant mixed bonded SiC_xN_{4-x} tetrahedra, similar to in the boron-free analogues. SiBCN3 and SiBCN4 ceramics also show BC_xN_{3-x} mixed bonded environments (Figure 54 (c) and (d)). In comparison to the SiBCN3 ceramics, the SiBCN4 ceramic prepared at 1100°C contains a higher relative fraction of carbon-rich SiC_xN_{4-x} ($x \geq 2$) tetrahedral units, although this sample actually has a lower carbon content. This observation may be explained by the condensation reaction among methyl groups to form Si–C–Si bonds in the precursor. This condensation does not occur in the SiBCN3-1100 sample because the substitute is a phenyl group in the precursor.

The ^{29}Si CPMAS spectrum of the SiBCN4-1100 sample (Figure 60) shows that these C-rich SiC_xN_{4-x} tetrahedral units are preferentially protonated with respect to the N-rich tetrahedra. Therefore, these two types of tetrahedra must be spatially segregated in the structure. It is assumed that SiC_xN_{4-x} (x=0-4) domains have cores composed primarily of SiN_4 tetrahedra, while the carbon-rich SiC_xN_{4-x} units are located near the boundary of these domains. These units may be directly connected to the carbon domains via Si-C-C bonds, or alternatively via BN, which may make up the interface between the SiC_xN_{4-x} (x=0-4) and "free" carbon domains. In such a BN transition zone, BN_3 units are located near the core of this interface region. The BN transition zone is bonded to SiC_xN_{4-x} (x=0-4) domains via Si–C–B linkages, and to "free" carbon domains via B-C-C or N-C-C bonds. However, there is a lack of mixed BC_xN_{3-x} units, except for BCN_2 unit, which precludes the possibility of a homogeneous intermixing of B, N, and C atoms in graphene/borazine-like sheets. The ^{13}C MAS NMR spectra (Figure 53 (g) and (h)) show a sp^2 C network with significant amounts of sp^2 C–N and sp^2 C–B bonding. This is completely consistent with the structural model proposed above, for which a schematic is shown in Figure 61. Finally, the SiBCN4-1100 sample has relatively higher concentrations of interfacial sp^2 C–N and sp^2 C–B environments, as well as of BCN_2 units, compared to the SiBCN3-1100 sample. This observation suggests that low carbon concentrations lead to the formation of smaller carbon domains. Smaller carbon domains result in a higher volume fraction of interfaces among the domains, where sp^2 C–N and sp^2 C–B environments are present (also seen in Scarlett Widgeon et al. 2013).

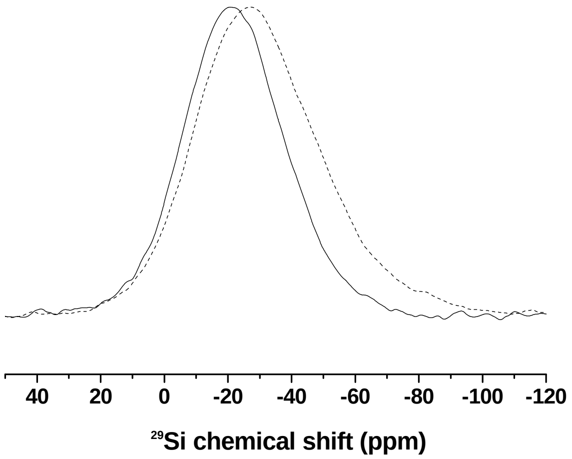

Figure 60 ^{29}Si CPMAS NMR (solid line) and ^{29}Si MAS NMR (dash line) of SiBCN4-1100 ceramic. From S. Widgeon, G. Mera, Y. Gao, S. Sen, A. Navrotsky, and R. Riedel, J. Am. Ceram. Soc. 96, 1651 (2013). Copyright © 2013 by John Wiley Sons, Inc. Reprinted by permission of John Wiley & Sons, Inc [131].

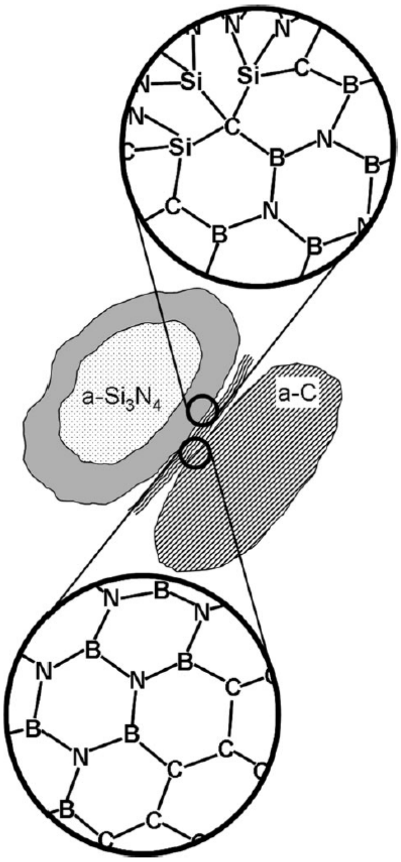

Figure 61 Schematic representation of SiBCN3-1100 and SiBCN4-1100 ceramics. From S. Widgeon, G. Mera, Y. Gao, S. Sen, A. Navrotsky, and R. Riedel, J. Am. Ceram. Soc. 96, 1651 (2013). Copyright © 2013 by John Wiley Sons, Inc. Reprinted by permission of John Wiley & Sons, Inc [131].

In SiBCN4-1400 samples, the relative amount of interfacial sp^2 C–N and sp^2 C–B bonds decreases, while that of B-N and C-C bonds increases. The intensities of the bands, which represent SiC_xN_{4-x} (x=0-4) and BC_xN_{3-x} (x=0-3) mixed bonding environments, decrease. This is to say, the ceramics undergo a demixing process and a nanodomain coarsening. Details are discussed in Section 4.3. Calorimetry demonstrates that this structural evolution is favorable in both enthalpy and free energy.

4.4.2 Microstructure of Si(B)CN ceramics

In small angle X-ray scattering (SAXS), X-rays are used to investigate the structural properties of materials. Photons interact with electrons, and provide information about the fluctuations of electronic densities in heterogeneous matter. In the SAXS of PDCs, the intensity of the scattering signal is propotional to the electronic contrast between the domains. In this way, the nanodomains of PDCs can be detected using this technique. By studying the change in scattering intensity, at least two structural levels in all ceramic samples prepared at 1100 ºC and 1400 ºC in this study were confirmed (Figure 62). Unfortunately, we were not able to collect data over the entire q range relevant for these materials. Data is lacking at low q, where the Guinier region of the first structural level (larger domain size) would be found, as well as at high q, where the Porod region for the second structural level (smaller domain size) would be found. However, relatively complete data is available for the Guinier region of the second structural level, and a fitting was performed in this region.

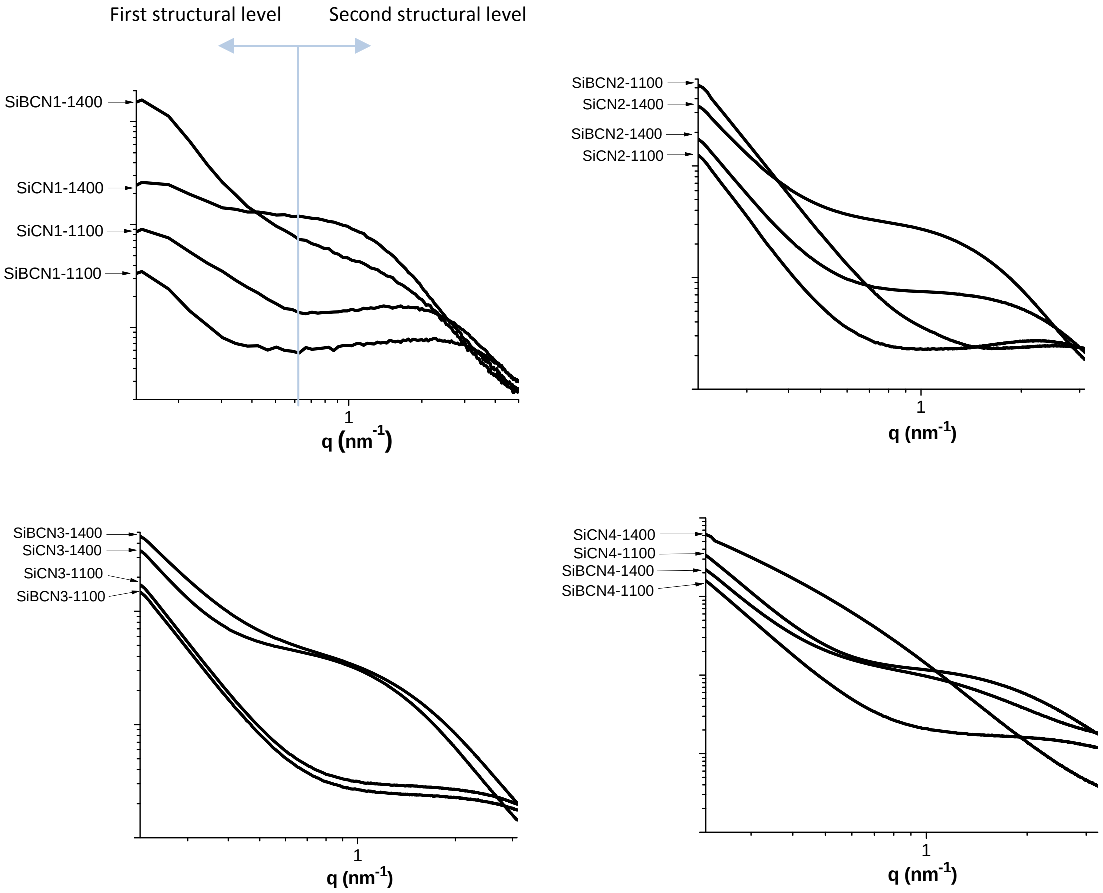

Figure 62 SAXS results of ceramics prepared at 1100°C and 1400°C

The Beaucage equation (Formula 4) was used for data fitting (Figure 63) [169]. The variables G, R, B and P were fitted using Origin 8.1 for the second structural level. Here R represents R_g, which is the radius of gyration from the domains in the second structural level.

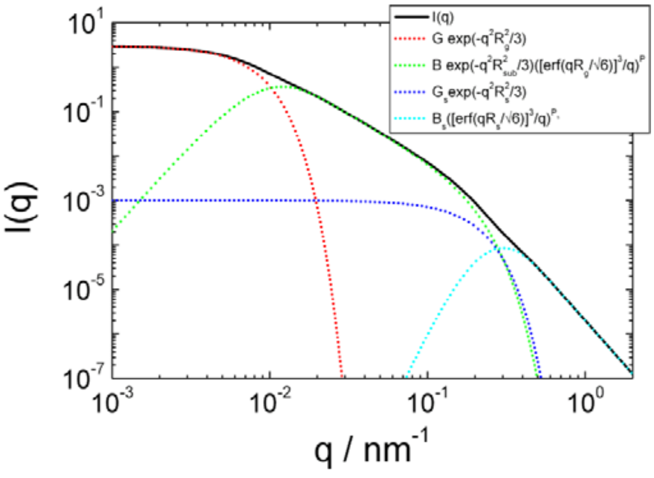

$$\begin{aligned} I_{\mathrm{Beaucage}}(Q) \simeq\ & G \exp\left(-\frac{Q^2R_g^2}{3}\right) \\ & + B \exp\left(\frac{Q^2R_{sub}^2}{3}\right)\left(\frac{\left[\operatorname{erf}\left(QkR_g/\sqrt{6}\right)\right]^3}{Q}\right)^P \\ & + G_s \exp\left(-\frac{Q^2R_s^2}{3}\right) \\ & + B_s\left(\frac{\left[\operatorname{erf}\left(Qk_sR_s/\sqrt{6}\right)\right]^3}{Q}\right)^{P_s} \end{aligned}$$

.

Figure 63 Beaucage equation for fitting SAXS data

$$\mathbf{I \cong G\exp\left(-\frac{Q^2R^2}{3}\right) + B\left(\frac{\left[\operatorname{erf}\left(\frac{qR}{\sqrt{6}}\right)\right]^3}{q}\right)^P}$$

Formula 4

The radius of gyration (R_g) values obtained from fitting the second structural level of the SAXS data are shown in Table 11. The R_g values of ceramics prepared at 1100°C are mostly 0.5 - 1.5 nm, while the R_g values of the ceramics prepared at 1400°C mostly range from 1.5 to 3 nm, indicating domain coarsening at higher pyrolysis temperatures.

Table 11 Radius of gyration of ceramics prepared at 1100°C and 1400°C

Ceramic sample	Formula of preceramic precursor	R_g(nm) of the ceramics prepared at 1100°C	R_g(nm) of the ceramics prepared at 1400°C
SiCN1	$[\text{-(PhVi)Si-NCN-}]_n$	0.69	1.26
SiBCN1	$[\text{-(MeVi)Si-NCN-}]_n$	0.45	1.19
SiCN2	$\{B[\text{-}(C_2H_4)\text{Si(Ph)-NCN-}]_3\}_n$	1.21	2.48
SiBCN2	$\{B[\text{-}(C_2H_4)\text{Si(Me)-NCN-}]_3\}_n$	1.02	1.87
SiCN3	$[\text{-(PhVi)Si-NH-}]_n$	1.37	2.98
SiBCN3	$[\text{-(MeVi)Si-NH-}]_n$	1.28	2.79
SiCN4	$\{B[\text{-}(C_2H_4)\text{Si(Ph)-NH-}]_3\}_n$	2.17	3.76
SiBCN4	$\{B[\text{-}(C_2H_4)\text{Si(Me)-NH-}]_3\}_n$	1.21	2.28

Based on previous studies, nanodomains in carbon rich polymer-derived SiCN ceramics normally consist of SiC_xN_{4-x} (x=0-4) domains and "free" carbon domains. SiBCN ceramics also have nanosized features containing B, N and C. The carbon rich ceramic samples in this work contain a large amount of "free" carbon, varying from 40 mol % to 90 mol % (Table 3). TEM observations (SiCN1-1100 and SiCN1-1400 ceramics as an example, shown in Figure 64) illustrate that the structure of these samples is amorphous, though at 1400°C, the ordering of few graphene layers is observed (Figure 64). Numerous TEM observations indicate that the stacking number of the graphene sheets is ~ 1-5 in ceramics pyrolyzed at 1100 and 1400° C.

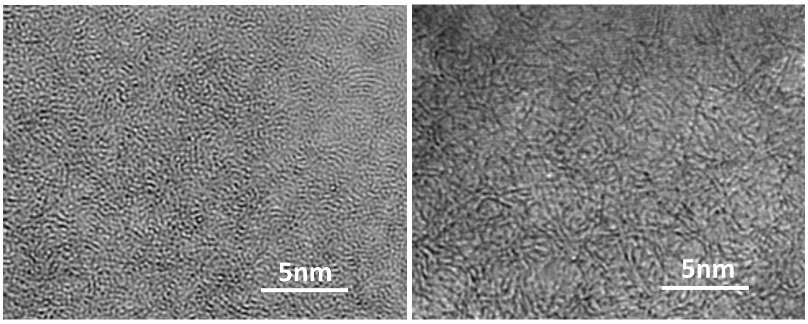

Figure 64 TEM observation of carbon rich SiCN1 PDCs prepared at (a) 1100°C and (b) 1400°C

One parameter used to characterize the extent of graphitization is “L_a,” which can be obtained from Raman spectroscopy. L_a is the average lateral size of the graphitic carbon. The formula for determining L_a and additional explanations are given in Section 4.2. The Raman spectra of ceramic samples prepared at both 1100 and 1400°C are shown in Figure 65. The calculated L_a values are also shown in the same figure. The average lateral size along the six-fold rings of graphitic carbon is in the range of 1.4-2.2 nm. It is notineable that L_a values of ceramics pyrolyzed at 1100 and 1400 ºC do not show the same trend as the R_g values determined by SAXS. R_g of ceramics pyrolyzed at 1400 ºC are always larger than those of ceramics pyrolyzed at 1100 ºC.

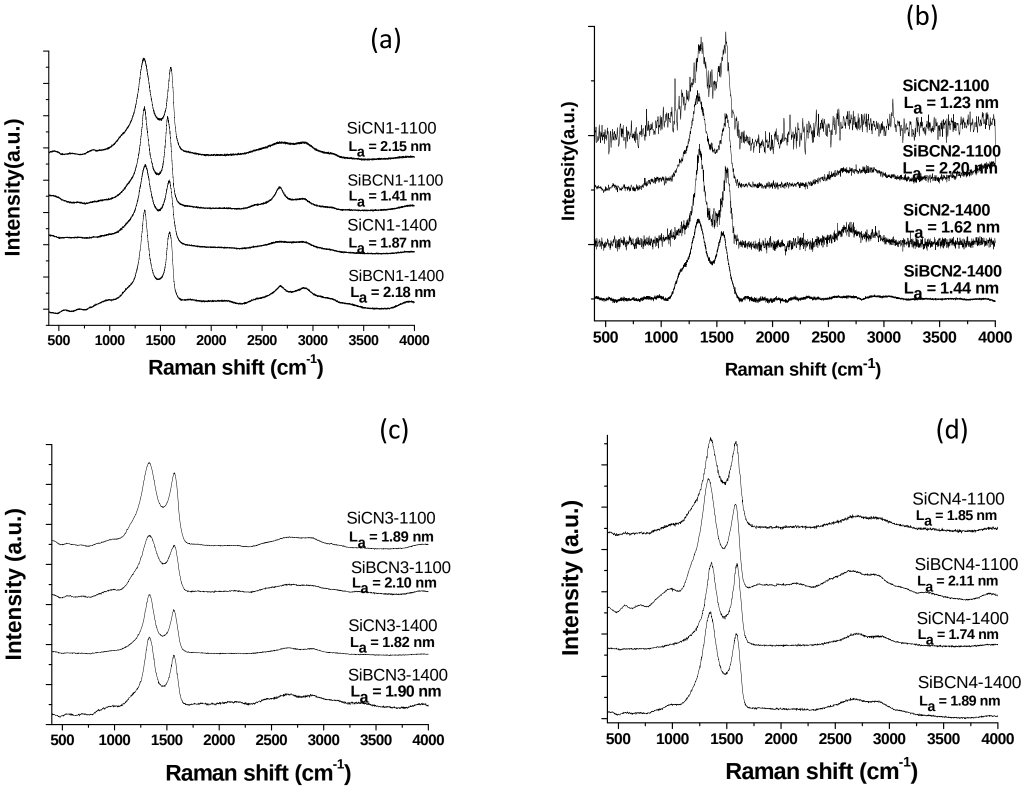

Figure 65 Raman spectroscopy of (a) SiCN1, SiBCN1, (b) SiCN2, SiBCN2, (c) SiCN3, SiBCN3, (d) SiCN4, SiBCN4 PDCs

In fact, L_a is the lateral size of graphene layers without tortuosities. L_a does not characterize the full length of the graphitic carbon if the sheets are tortuous [170]. It is observed that the graphitic carbon in carbon-rich amorphous polymer-derived ceramics is always tortuous. Thus, L_a cannot be used to characterize the carbon domain sizes in these materials. Tortuous graphene sheets with stacking numbers from 1 to 5 form a network in the polymer-derived ceramic structure. The SiC_xN_{4-x} (x=0-4) domains are located among the network of carbon sheets. A schematic of this nanodomain feature is shown in Figure 66. This schematic is also consistent with a previously published model [161].

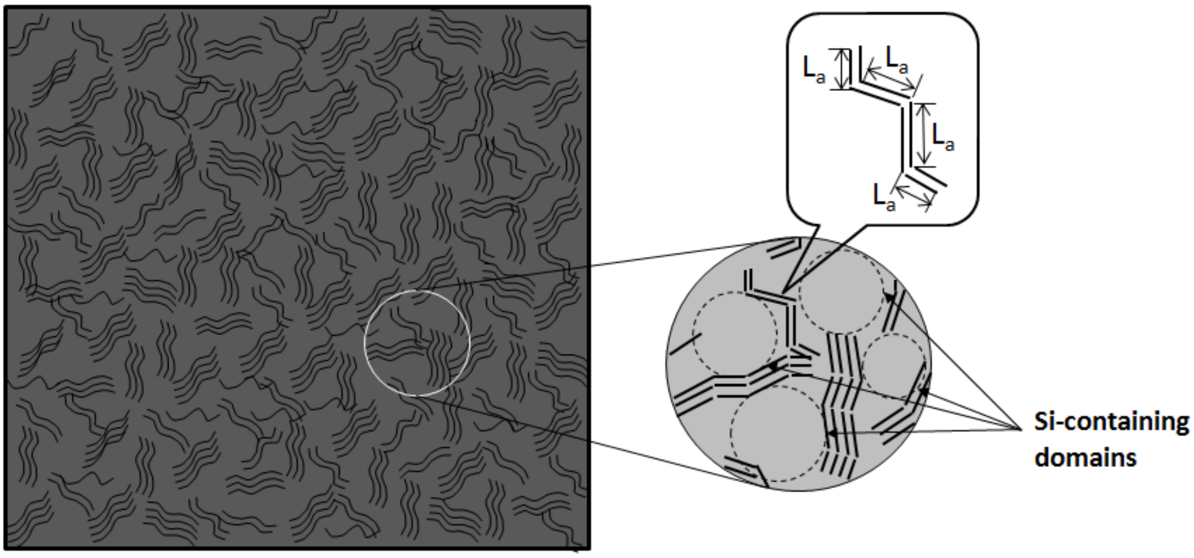

Figure 66 Schematic of nanodomain structure of carbon rich PDCs

Provided that the SiC_xN_{4-x} (x=0-4) domains are spherical, the size of these nanodomains can be calculated from R_g using the equation: $R_{sphere} = R_g \cdot \sqrt{\frac{5}{3}}$. The distribution of nanodomain sizes calculated in this way are shown in Figure 67.

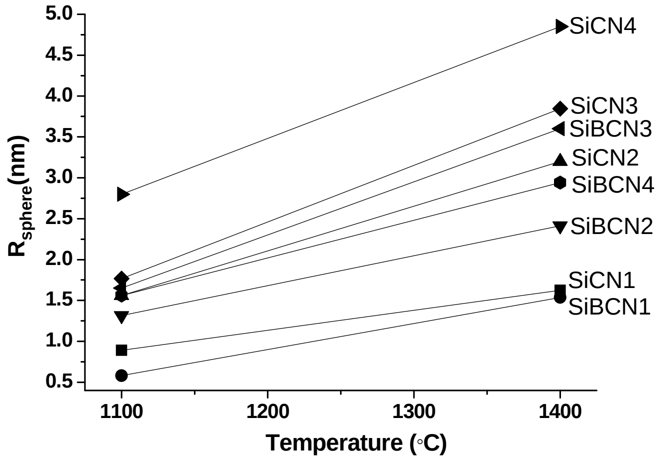

Figure 67 Si nanodomains size in ceramics prepared at 1100°C and 1400°C

As is well-known, Si(B)CN ceramics prepared at 1100 °C typically remain amorphous. This is certainly true for the materials invested in this work, as demonstrated by XRD in Figure 68. Meanwhile, some of the ceramics pyrolyzed at 1400°C show nanocrystallization, as is evidenced by broad humps in the XRD pattern. The reflections at $2\theta = 37^o, 41^o, 60^o, 72^o$ are from the (111), (200), (220), and (311) planes of SiC. The average size of the SiC crystals can be estimated using the Scherrer equation. Taking SiBCN3-1400 and SiCN4-1400 as two examples, the sizes of the SiC nanocrystals in SiBCN3-1400 and SiCN4-1400 ceramics are ca. 2.4 nm and 2.8 nm, respectively, if no other contributions to peak broadening are considered. The Si domain sizes obtained by SAXS of these two ceramics are 3.6 nm and 4.8 nm, which is bigger than the size of SiC nanocrystals. These results suggest that the nanodomain sizes obtained by SAXS are representative of the SiC_xN_{4-x} (x=0-4) nanodomains, which should be larger than the crystallites.

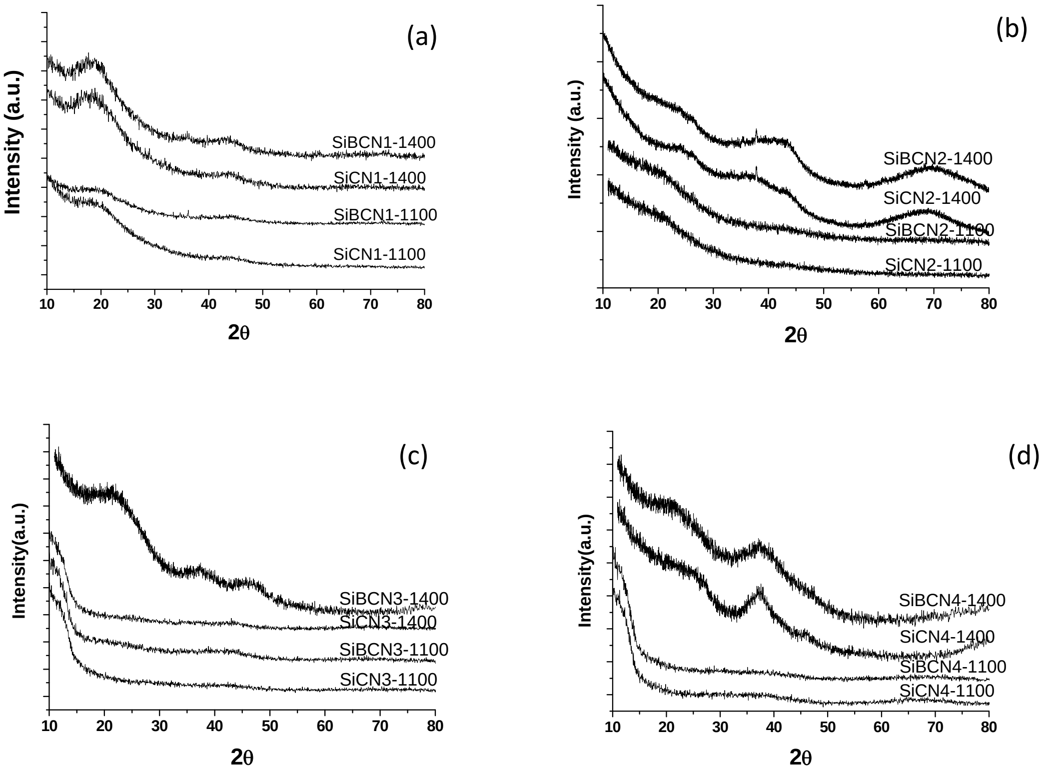

Figure 68 XRD patterns of (a) SiCN1, SiBCN1, (b) SiCN2, SiBCN2, (c) SiCN3, SiBCN3, (d) SiCN4, SiBCN4

It was also found that the average sizes of the SiC_xN_{4-x} (x=0-4) domains (Figure 67) in ceramic samples derived from different precursors show some interesting characteristic:

First, the SiC_xN_{4-x} (x=0-4) domains in all ceramic samples pyrolyzed at 1400 °C are larger than in the analogues pyrolyzed at 1100°C. This coarsening phenomenon with increasing temperature has already been studied and reported. SiC_xN_{4-x} (x=0-4) domains grow with the concomitant elimination of interfaces.

Second, boron modified ceramics have smaller SiC_xN_{4-x} (x=0-4) domains than that of the boron-free ceramics. Generally after thermolysis, boron forms BN, so fewer nitrogen atoms connect to silicon atoms to form SiN_4 tetrahedra in the SiBCN samples than in their SiCN counterparts. At the macro scale, the amount of $Si\text{-}N_4$ is reduced. BN is considered to be located at the interface between Si and "free" carbon domains. The electron density of the BN unit is similar to that of carbon, so there is no contrast under X-ray scattering. BN is considered to be in the same region as that of the carbon domains. The reduced amount of SiN_4 tetrahedra may result in smaller SiC_xN_{4-x} (x=0-4) domains, but not necessarily. Another explanation for the smaller SiC_xN_{4-x} (x=0-4) domains can be traced back to the synthesis of the boron-modified polymers. During hydroboration, boron atoms connect to vinyl groups. In this way, vinyl groups do not connect to each other, as they do during the polymerization of boron-free polymers. Therefore, in the boron-modified polymers, fewer Si atoms gather via the polymerization process, but are separated by boron atoms. These boron atoms form BN during pyrolysis. This BN "barrier" leads to smaller SiC_xN_{4-x} (x=0-4) domains in the ceramics.

A third trend revealed by SAXS is that if the preceramic precursors contain the same organic substitute attached to Si, the SiC_xN_{4-x} (x = 0-4) domains in the ceramics derived from poly(boro)silylcarbodiimides are always smaller than those in the ceramics derived from poly(boro)silazanes. One explanation for this trend is that, if the polymer is crosslinked at 100 to 300 ºC, nitrogen atoms of the Si-N(H)-Si groups in poly(boro)silazanes can connect to a third silicon atom through transamination reaction. In any case, N-H is involved in forming the network structure. In the case of poly(boro)silylcarbodiimide, the decomposition of -N=C=N- groups can still be observed even up to 950 ºC with the evolution of HCN (e.g. in [-(PhVi)Si-NCN-]$_n$ polymer as shown in Figure 69). The breaking of double bonds in N=C=N groups separates SiC_xN_{4-x} (x=0-4) domains from "free" carbon domains. This separation is also shown in the ^{29}Si MAS NMR spectra of the SiCN1 ceramics (Figure 52 (a)). A schematic is shown in Figure 55(a) [136]. The activity of the N=C=N groups causes the final SiC_xN_{4-x} (x=0-4) domains in poly(boro)silylcarbodiimides-derived ceramics to be smaller.

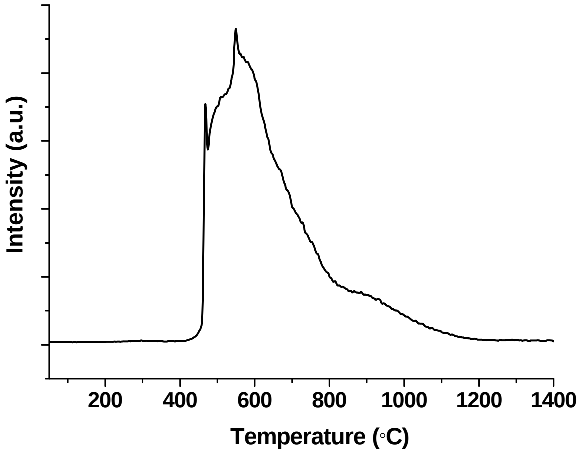

Figure 69 m/z=27 fragment in Mass Spectra of [-(PhVi)Si-NCN-]$_n$ polymer

At last, the carbon content also affects the SiC_xN_{4-x} (x=0-4) domain size in the ceramics. Most obviously, samples with lower carbon contents tend to have larger SiC_xN_{4-x} (x=0-4) domains, except the case of the SiBCN3 and SiBCN4 ceramics. Differences in carbon content arise due to the use of different substitutes in the purecursor polymers (i.e. phenyl group and methyl group). During the crosslinking process and the following pyrolysis, phenyl groups sterically hinder the connection between silicon atoms and the formation of Si networks. In other words, Si domains are restricted to relatively small sizes because phenyl groups are too large to allow Si tetrahedral units to come into close contact. However, in methyl-substituted polymers, it is easier for Si tetrahedral units to interact to form larger

SiC_xN_{4-x} (x=0-4) domains. The opposite trend was found in case of the SiBCN3 and SiBCN4 ceramics. SiBCN4-1100, which is derived from methyl-substituted polyborosilazane, has SiC_xN_{4-x} (x=0-4) domains similar in size to those of SiBCN3-1100, which is derived from phenyl-substituted polyborosilazane. SiBCN4-1400 has smaller SiC_xN_{4-x} (x=0-4) domains than SiBCN3-1400. The reason for this remains unclear.

4.4.3 Summary

The nano-scale structure of polymer-derived ceramics strongly depends on the nature of their precursor polymers. By using a suite of characterization techniques, information regarding domain composition, domain size, and interdomain bonding could be obtained. MAS NMR spectroscopic investigations support the finding that ceramics derived from polysilazanes contain silicon mixed bonding environments, namely SiC_xN_{4-x}(x=0-4) tetrahedra, while ceramics derived from polysilylcarbodiimides have no such mixed bonding. The boron-modified counterparts show the same phenomenon. While all of the synthesized ceramics are basically made up of SiN_4 and sp^2 carbon nanodomains, the nature of the transition zones between these domains differ depending on the architecture of the precursor. Polysilylcarbodiimide-derived SiCN1 and SiCN2 ceramics pyrolyzed at 1100°C contain Si_3N_4 and “free” carbon domains. The SiCN1 ceramic consists of a continuous carbon phase in which Si_3N_4 domains are embedded, but no considerable amount of chemical bonding exists between these domains. In contrast, in the SiCN2 ceramics, these domains are connected by C-N bonds. Boron-modified polyborosilylcarbodiimide-derived SiBCN1 and SiBCN2 ceramics prepared at 1100°C contain Si_3N_4 and “free” carbon domains, as well as an additional BN phase which exists at the interface between these two domains. Consequently, the Si_3N_4 and “free” carbon domains connect to the BN phase via N-B and N-C bonds. For polysilazane-derived SiCN3 and SiCN4 ceramics pyrolyzed at 1100°C, mixed SiC_xN_{4-x}(x=1~4) tetrahedra are found located interfacially between the SiN_4 and “free” carbon domains. SiC_4 tetrahedra are connected to the “free” carbon domains. The MAS NMR spectra of the polyborosilazane-derived SiBCN3 and SiBCN4 ceramics prepared at 1100°C indicate that there are SiC_xN_{4-x}(x=0~4) tetrahedra and BC_xN_{3-x} (x=0~4) mixed bonds which connect the Si_3N_4 domains to the “free” carbon domains via C-B bonds (between the SiC_4 tetrahedron and the BN phase) and B-C bonds (between the BN phase and the “free” carbon domain).

Considering results from Raman spectroscopy, XRD, and TEM, the radius of gyration values obtained by SAXS are considered to be the size of the SiC_xN_{4-x} (x=0-4) nanodomains in the amorphous PDCs. Trends in the domain size with respect to the type of precursor are summarized as follows: 1) for the materials studied, Si-containing domain sizes increase with an increase in the pyrolysis temperature from 1100 ºC to 1400 ºC, indicative of coarsening during heat treatment; 2) boron-modified ceramics have smaller Si-containing domains than that of the boron-free ceramics; 3) the SiC_xN_{4-x} (x=0-4) domains in the ceramics derived from poly(boro)silylcarbodiimides are always smaller than those derived from poly(boro)silazanes;

4) lower carbon contents result in larger SiC_xN_{4-x} (x=0-4) domains, except for polyborosilazane-derived SiBCN ceramics.

4.5 Electrical / electrochemical properties

4.5.1 Complex impedance spectra of selected polymer-derived ceramics

Complex impedance spectroscopy (IS) is a useful tool for studying the electrical behavior of composite materials [171]. Unlike DC resistance measurements, which study the average behavior of a sample, impedance spectroscopy is sensitive to phase differences. The parameters derived from IS, such as conductance and capacitance, can often be correlated to complex materials variables such as composition, microstructure, mass transport, etc. In general, each phase of a composite can be represented by an equivalent electrical sub-circuit containing a resistor and a capacitor; and the impedance of the entire composite can then be represented by a unique equivalent circuit comprised of these sub-circuits.

Polymer-derived ceramics can be considered multiphase composite materials. Their electric conduction behavior strongly depends on the distribution and conductivity of each phase. While the electrical behavior of polymer-derived ceramics has been studied to a certain extent, previous studies primarily focused on measuring the DC resistance of the entire material. This type of measurement has two main drawbacks: (i) it cannot determine the contribution of each phase to the total conductivity of the material, and (ii) it cannot be used to determine the structure based conduction mechanisms.

In this section, we study the impedance behavior of selected SiCN PDCs. If we consider a polymer-derived ceramic as a two-phase composite [172], then the possible paths for electric current depend on whether the two phases are continuous. If both phases are not continuous, as shown in Figure 70 (a1), electric current within the material will have only one possible path via both phases in series (Figure 70 (b1)). If one phase is continuous and the other is not, as shown in Figure 70 (a2), electric current has two possible paths as shown in Figure 70 (b2): conduction via the first phase (the continuous one), or conduction via the first and the second phase in series. If both phases are continuous, electric current within the material will have three possible paths as shown in Figure 70 (a3): conduction via the first phase; conduction via the first and the second phase in series, and conduction via the second phase. The corresponding equivalent circuit is shown in Figure 70 (b3). The IS results will be analyzed using this model.

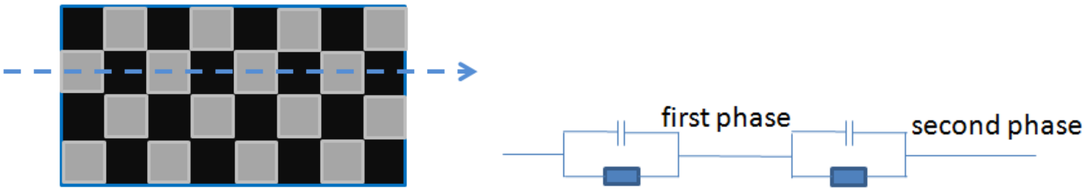

(a1) (b1)

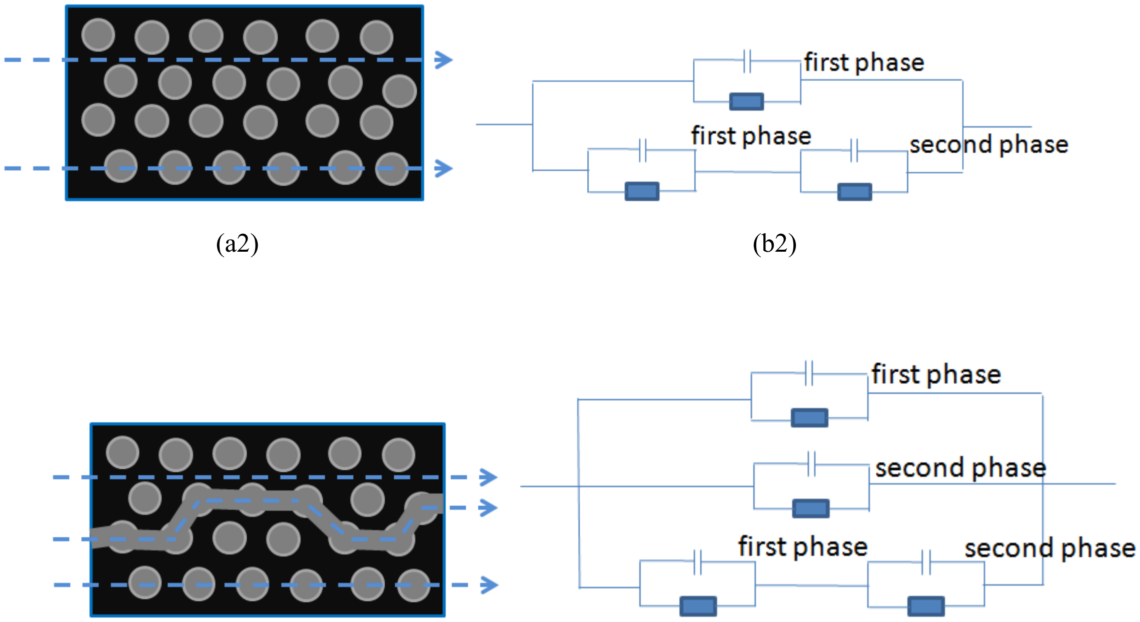

(a2) (b2)

(a3) (b3)

Figure 70 (a) Schematic models of two-phase composite with conduction paths: (a1) both phases are not continuous; (a2) one phase is continuous, the other is not; (a3) both phases are continuous; and (b) the corresponding equivalent electrical circuits of (a1), (a2) and (a3).

Three polymer-derived ceramics have been selected as model materials for studying impedance behavior: SiCN4, SiBCN2 and SiBCN4. The compositions of the three materials prepared at 1100 and 1400°C are listed in Table 12. It is seen that the major conducting phases in the studied ceramics are SiC and "free" carbon, because Si_3N_4, SiO_2 and BN are considered insulating phases. SiBCN2 and SiBCN4, in comparison to SiCN4, contain a fairly large amount of BN, while SiCN4 contains no BN phase. Besides, SiBCN4 consists mainly of "free" carbon and a SiC phase, while the major phase in SiBCN2 is "free" carbon with a small amount of SiC. As discussed in section 4.4.1.3 and 4.4.1.4, poly(boro)silazane derived Si(B)CN ceramics have domains consisting of mixed bonded SiC_xN_{4-x}(x=0-4) tetrahedra. These SiC_xN_{4-x} (x=0-4) domains have cores composed primarily of SiN_4 tetrahedra, while the SiC_4 tetrahedra are located at the boundary of these domains. In SiCN4 and SiBCN4 ceramics, a considerable amount of SiC_4 tetrahedra are present, which is revealed by the intense band centered at -18 ppm in the ^{29}Si MAS NMR spectra (Figure 52 (f) and (h)). At 1400°C, all three studied ceramic samples contain SiC nanocrystallites, as evidenced by XRD (SiBCN2 in Figure 68 (b), SiCN4 and SiBCN4 in Figure 68 (d)).

Table 12 Compositions of the samples investigated with for impedance spectroscopy∗

Preceramic polymer	Ceramic sample	Si wt% atom%	C wt% atom%	N wt% atom%	B wt% atom%	O wt% atom%	H wt% atom%	Cl wt% atom%	Empirical formula	Calculated phases (Mol%)				
										Free C	Si_3N_4	SiC	BN	SiO_2
{B[-(C_2H_4)Si(Me)-NCN-]$_3$}$_n$	SiBCN2-1100	37.71 21.78	30.41 40.98	24.67 28.50	3.00† 4.49†	4.21 4.25	—	—	$SiC_{1.88}N_{1.31}B_{0.21}O_{0.20}$	73.38	11.20	3.08	8.38	3.97
	SiBCN2-1400	39.94 23.34	30.31 41.33	23.43 27.39	3.00† 4.55†	3.32 3.40	—	—	$SiC_{1.77}N_{1.17}B_{0.19}O_{0.15}$	69.10	10.72	8.47	8.53	3.19
[-(MeVi)Si-NH-]$_n$	SiCN4-1100	51.75 31.01	29.19 40.81	17.10 20.49	—	1.56 1.64	0.36 6.04	0.04 0.02	$SiC_{1.32}N_{0.66}O_{0.05}$	55.6	11.0	31.7	—	1.8
	SiCN4-1400	51.283 31.55	29.84 42.84	17.23 21.20	—	1.44 1.55	0.165 2.84	0.042 0.02	$SiC_{1.36}N_{0.67}O_{0.05}$	57.2	10.8	30.4	—	1.6
{B[-(C_2H_4)Si(Me)-NH-]$_3$}$_n$	SiBCN4-1100	48.36 29.70	28.85 41.35	13.60 16.71	4.52 7.07	4.63 4.98	0.01 0.17	0.03 0.01	$SiC_{1.39}N_{0.56}B_{0.24}O_{0.17}$	40.1	4.5	37.5	13.3	4.7
	SiBCN4-1400	48.20 29.55	28.39 40.62	14.09 17.28	4.68 7.44	4.59 4.93	0.01 0.17	0.04 0.02	$SiC_{1.37}N_{0.58}B_{0.25}O_{0.17}$	39.5	4.6	37.2	14.0	4.7

∗ This table is a part of Table 3.

† Samples have not been measured on boron element. The values are estimated from the ratio of starters in polymer reactions and the ceramic yield.

Figure 71, Figure 72, Figure 73 show the impedance spectra of SiCN4, SiBCN2 and SiBCN4 materials, respectively, as organized by pyrolysis temperature. The complex impedance plots typically take the form of semicircular arcs. In some cases, the arcs are incomplete in the high frequency region due to limitations of the experimental facilities. The spectrum for SiCN4-1100 exhibits one big semicircle, while the spectra for SiCN4 samples prepared at 1200°C, 1300°C and 1400°C exhibit one semicircle at low frequency followed by an arc obtained at higher frequency. This arc represents the beginning of another semicircle. The two semicircles are partially overlapping. The spectra of samples containing a BN phase, namely SiBCN2 and SiBCN4, show only one semicircle or an incomplete semicircular arc.

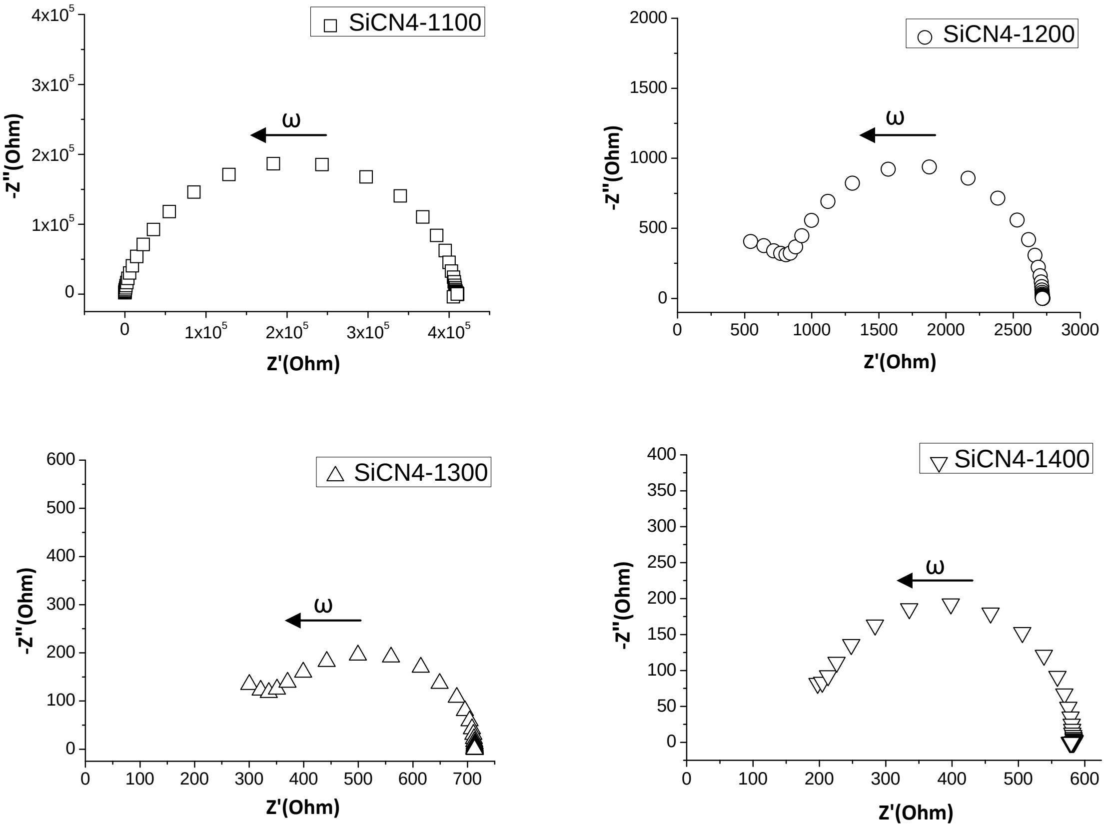

Figure 71 Complex impedance spectra of SiCN4 samples pyrolyzed at different temperatures.

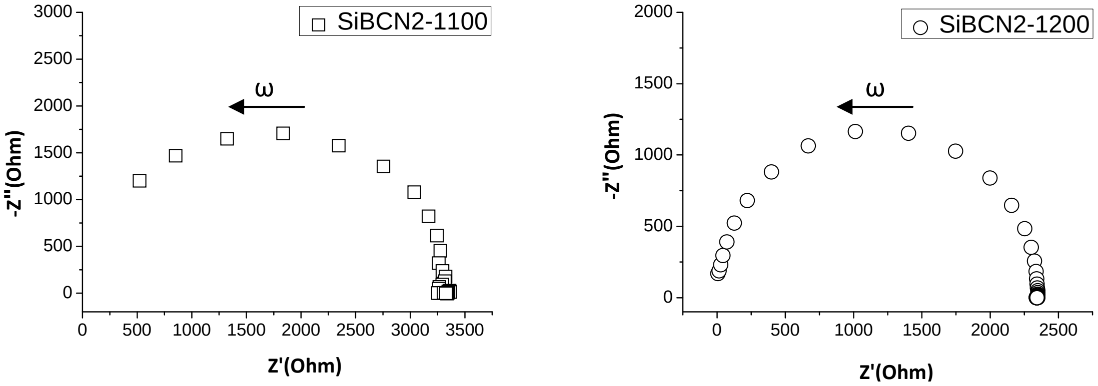

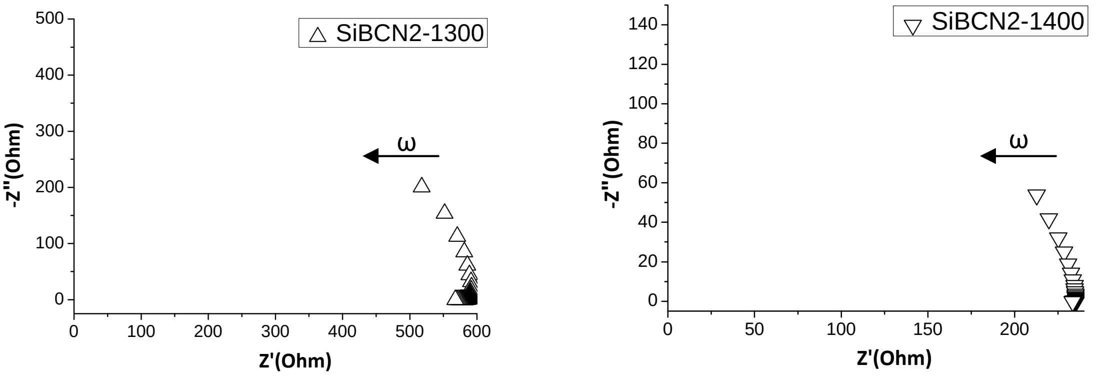

Figure 72 Complex impedance spectra of SiBCN2 samples pyrolyzed at different temperatures.

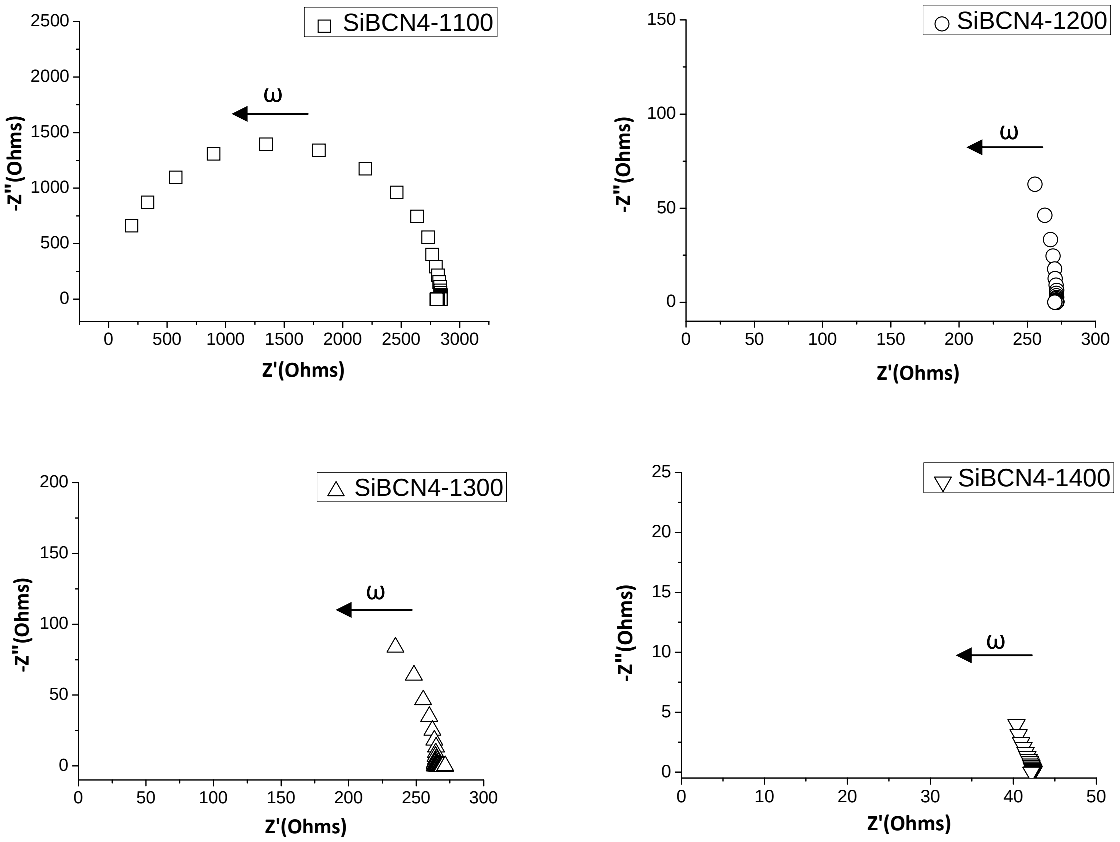

Figure 73 Complex impedance spectra of SiBCN4 samples pyrolyzed at different temperatures.

The most accepted approach to interpret the semicircle phenomena is to consider them with respect to the distribution of relaxation time. The semicircles measured for the investigated materials are modeled by an electrical equivalence consisting of a parallel resistance and capacitance circuit corresponding to the individual component of the material. The parameters which were used to obtain the best fit for the experimental results are listed in Table 13. It is found that the two-semicircle spectra obtained for SiCN4 samples can be best fitted by the equivalent circuit shown in Figure 74(a), which contains two resistor/capacitor sub-circuits in series. The same electrical equivalence is used to model the spectrum of

SiCN4-1100 sample, although its spectrum resembles one semicircle. However, analying this spectrum with only one resistor/capacitor circuit resulted in poorer fitting. The goodness of the fit is given by the parameters, “Chi-squared” and “sum of sqr”, as listed for both cases in Table 13. The equivalent circuit with two resistor/capacitor sub-circuits in series yields lower values for “Chi-squared” and “sum of sqr” (i.e. greater goodness of fit) than that of the equivalent circuit with one resistor/capacitor. The presence of two semicircles is also consistent with the spectra measured on the same ceramic prepared at other temperatures. The two semicircle phenomenon is similar to those previously measured for polymer-derived silicon oxycarbide (SiOC) ceramics [172], suggesting the presence of two phases. The semicircle measured at low frequency is considered to represent conduction in the “free” carbon phase, while the semicircle at high frequency is attributed to the Si-containing phase.

The spectra for SiBCN2 and SiBCN4 samples prepared at all studied temperatures can be estimated and best fitted as one semicircle. This semicircle represents the equivalent circuit shown in Figure 74(b), which contains one resistor/capacitor sub-circuit. Therefore, we assume that the conduction of these two samples is dominated by one phase. For some samples, suppressed semicircles are represented in the Nyquist plots. This suggests that the studied materials are not ideal capacitors, and a constant phase element (CPE) is required to obtain the best fitting (Figure 74). The suppressed semicircles have been explained by a number of phenomena, depending on the nature of the system being investigated. However, a common thread among these explanations is that some property of the system is not homogeneous, or that there is some distribution (dispersion) of the value of a physical property of the system. CPE consists of a capacitive element CPE-T and of CPE-P (0-1), which is a measure of how much the CPE deviates from an ideal capacitor. When CPE-P = 1, the CPE is an ideal capacitor and can be replaced by C.

Table 13 Properties of elements from the equivalent circuits*

Sample	Elements	1100°C	1200°C	1300°C	1400°C
SiCN4	R1(Ω)	17137	826.8	337.3	203.4
	C1/CPE1(F)	CPE-T 1.888×10^{-10} CPE-P 0.90799	1.396×10^{-11}	1.664×10^{-11}	1.822×10^{-11}
	R2 (Ω)	391640	1879	374.5	378.1
	C2/CPE2(F)	CPE-T 2.227×10^{-11} CPE-P 0.96435	4.175×10^{-10}	5.155×10^{-10}	4.335×10^{-10}
	Chi-Squared /Sum of Sqr	0.0011413 /0.1187	0.0010251 /0.057408	0.00022046 /0.012346	0.00010317 /0.0057776
	Chi-Squared /Sum of Sqr (For one RC fit)	0.015858 /1.6968	—	—	—
SiBCN2	R (Ω)	3358	2314	592.7	236
	C/CPE(F)	1.159×10^{-11}	5.265×10^{-10}	1.044×10^{-11}	CPE-T 1.398×10^{-10} CPE-P 0.88652
	Chi-Squared /Sum of Sqr	0.0013527 /0.02976	0.0013994 /0.13714	0.0000564 /0.00090315	0.0000874 /0.0020118

Sample	Elements	1100°C	1200°C	1300°C	1400°C
SiBCN4	R (Ω)	2804	271.3	264.7	42.48
	C/CPE(F)	2.299×10^{-11}	1.446×10^{-11}	2.164×10^{-11}	CPE-T 1.249×10^{-8} CPE-P 0.68394
	Chi-Squared /Sum of Sqr	0.0034681 /0.20115	0.0026268 /0.15235	0.00025252 /0.014646	0.00024328 /0.0080283

* All the values were obtained base on the normalized size of samples: diameter 8mm, thickness 0.5mm.

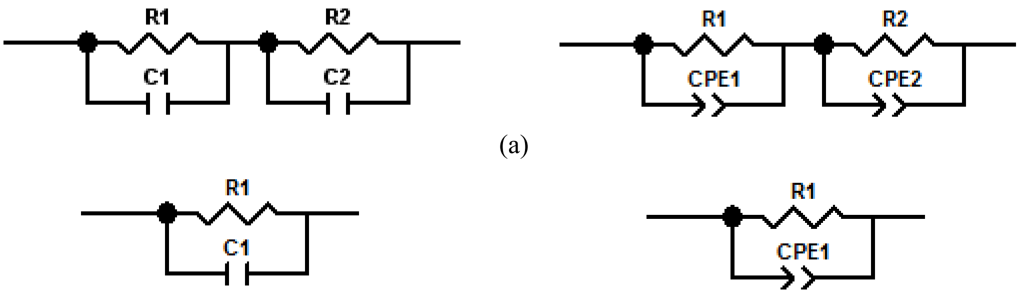

(a)

(b)

Figure 74 equivalent circuits used to fit the experimental impedance spectra.

As discussed above, the major conductive phases in the studied ceramics are SiC and “free” carbon. The impedance measurements confirm that the resistance of the ceramic decreases with increasing pyrolysis temperature. It is explained by the increased ordering of both the “free” carbon and SiC phases with increasing pyrolysis temperature, which leads to higher conductivity.In SiBCN2 samples, the major phase is “free” carbon, so it is likely the phase which dominates the conduction of SiBCN2. SiBCN4 samples have a lower “free” carbon concentration, but the overall conductance is higher than that of SiBCN2 (Figure 75). Noticing that the SiBCN4 samples contain a relatively large amount of the SiC phase, the SiC phase is considered to be responsible for their higher conductivity. This means that SiC is the dominant conductive phase in the SiBCN4 samples. The SiC dominant position is also indicated by the strong increase in conductivity after pyrolysis at 1400°C, when the sample contains nano crystalline SiC. This one-phase dominant conduction phenomenon is not found in SiCN4 samples which contain similar amount of “free” carbon and SiC, as in the SiBCN4 samples.

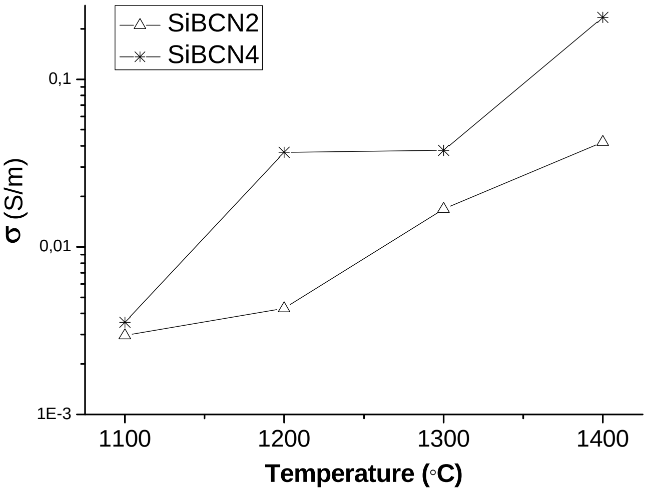

Figure 75 Comparison of overall conductance of SiBCN2 and SiBCN4 as a function of pyrolysis temperature.

To understand the different conduction mechanism in these samples, nanodomain structure is considered. As discussed in Section 4.4, NMR studies revealed that the Si-containing phase exhibits a microstructure wherein the Si_3N_4 forms a core and SiC forms a shell about it. For SiBCN samples, the BN phase is located between the Si-containing and the "free" carbon phases. Based on the structural information, we propose the following simple structural models to account for the observed conduction behavior of these materials (Figure 76). In SiCN4 (Figure 76 (a)), neither SiC nor the carbon phase forms a continuous network. Therefore, the conduction path goes via both phases in series. In SiBCN2 (Figure 76 (b)), the "free" carbon forms a continuous phase, and the BN forms at the interfacial region between the matrix "free" carbon and the isolated SiC phases. The BN phase isolates the SiC phase from the "free" carbon phase, thus the conduction path proceeds via the "free" carbon phase. In SiBCN2-1400 sample, even though the amount of SiC increases and SiC shows slight nanocrystallinity, the proposed mechanism can still be applied. In SiBCN4 (Figure 76 (c)), the SiC forms a continuous phase, and the BN forms the interfacial region between the isolated "free" carbon and the matrix SiC phases. Again, the BN phase isolates the "free" carbon phase from the SiC phase, and the conduction path goes via the SiC phase. The higher conductivity of SiBCN4 as compared to SiBCN2 is likely because the conductivity of the SiC phase is higher than that of the "free" carbon phase. This can also be seen from the SiCN4 samples: the resistance of the SiC phase (R1) is lower than that of the "free" carbon phase (R2), even though the concentrations of the two phases are similar.

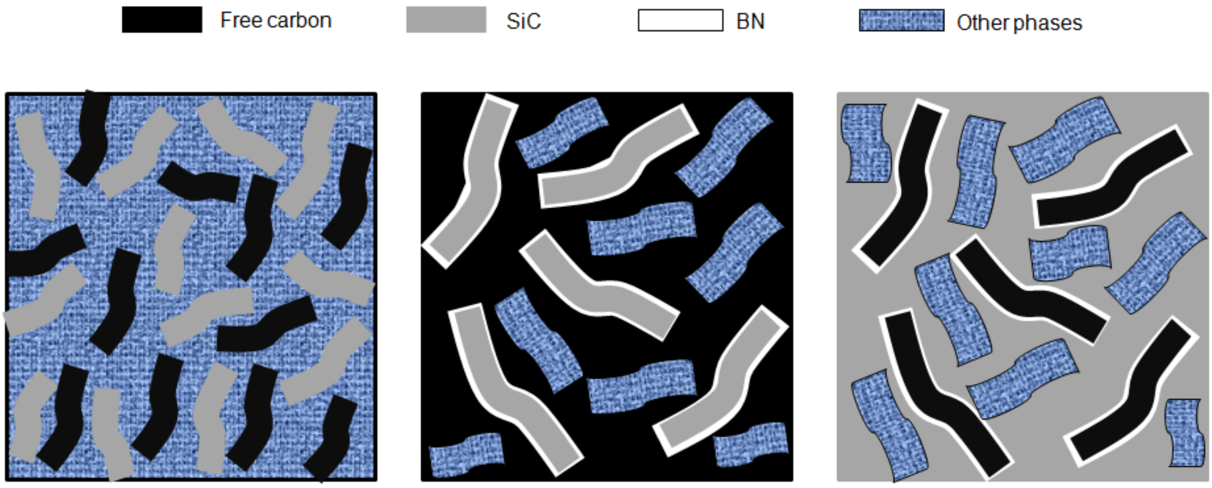

(a) SiCN4

(b) SiBCN2

(c) SiBCN4

Figure 76 Schematic model showing the microstructures for (a) SiCN4, (b) SiBCN2 and (c) SiBCN4. “Other phases” represent the non-conductive Si_3N_4, SiO_2, etc.

In summary, complex impedance spectroscopy was used to study the electrical behavior of three polymer-derived ceramics synthesized in this work. The experimental data were analyzed by modeling the processes by means of electrical equivalence circuits. By doing so, microstructure-based conduction mechanisma are revealed. In particular, we found that conduction in SiCN ceramics is via the “free” carbon and SiC phases in series, which is represented by two semicircles in the Nyquist plot. Conduction in SiBCN ceramics is dominated by one phase, and is thus represented by one semicircle in the Nyquist plot. Such difference between the SiCN and SiBCN ceramics is due to the presence of nonconducting BN formed at the interfacial region between the “free” carbon and SiC phases, and isolates the discontinuous phase from the continuous phase. Therefore, conduction is dominated by the continuous phase, whether it is “free carbon” or SiC.

4.5.2 Carbon-rich SiCN ceramics as anode material for lithium-ion batteries

This study is focused on the electrochemical investigation of four SiCN ceramics containing a high content of “free” carbon for use as anode materials for lithium-ion batteries. The studied SiCN materials are derived from pre-ceramic polymers with different molecular structures and degrees of branching. For this purpose, branched and linear polysilylcarbodiimides, as well as branched and linear polysilazanes were synthesized. As demonstrated by solid-state NMR, the pyrolysis of polysilazanes at 1100°C leads to mixed SiC_xN_{4-x}(x=0-4) bonding configurations within the amorphous SiCN ceramic, as discussed in Section 4.4. In contrast, the pyrolysis of polysilylcarbodiimides results in the formation of amorphous nanocomposites comprised of Si_3N_4, SiC and a “free” carbon phase. This work focuses on the relationship of the molecular structure of the precursor and the resulting derived microstructures on the electrochemical properties of the ceramics.

Figure 77 shows the discharge capacities of the investigated materials. The best performance, with respect to the recovered capacities, was achieved with polysilazane-derived materials, SiCN3-1100 and SiCN6-1100. Both samples recover the outstanding capacity of 700 mA hg^{-1} for low current charge/discharge, clearly exceeding the theoretical capacity of graphite. Starting with a rate of C/5, the capacity of SiCN6 tends to fade, while it remains perfectly stable for SiCN3-1100. At C/1, the average discharge capacities are 437 $mAhg^{-1}$ and 316 $mAhg^{-1}$ for SiCN3-1100 and SiCN6-1100, respectively. The capacities recovered at low current for the polysilylcarbodiimide-derived samples are much lower, namely 612 and 486 $mAhg^{-1}$ for the SiCN1-1100 and SiCN5-1100 ceramic, respectively. The SiCN5 ceramic demonstrates high irreversible capacity during the first cycle, followed by stable electrochemical cycling behavior. In contrast, SiCN1-1100 shows lower irreversible capacity during the first cycle, but significant capacity fading at current rates of C/20, C/10 and C/5. When finally charged/discharged at rates of C/2 and C/1, the capacity stabilizes, and the recovered capacity is similar to that of SiCN5-1100. The high irreversible capacity of SiCN5-1100 during the first cycle can be attributed to its high oxygen content.

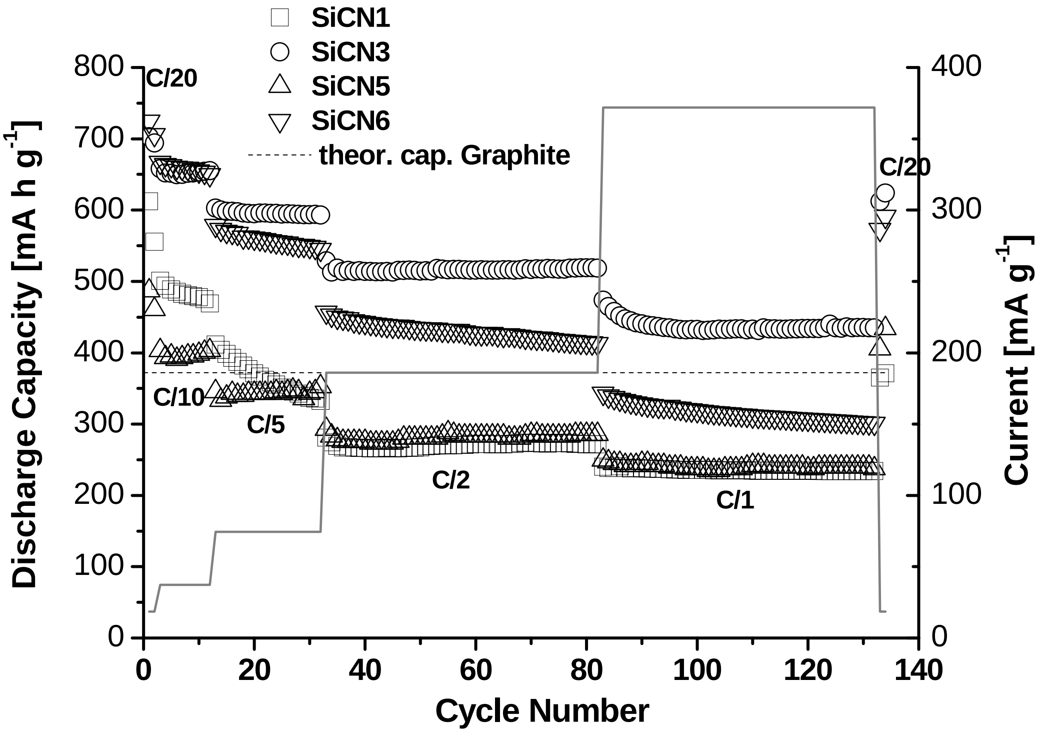

Figure 77 Discharge capacities with corresponding rates/currents for SiCN1, SiCN3, SiCN5 and SiCN6 prepared at 1100°C. Reprinted from Journal of Power Sources, V236, L. M. Reinold, M. Graczyk-Zajac, Y. Gao, G. Mera, and R. Riedel, Carbon-rich SiCN ceramics as high capacity/high stability anode material for lithium-ion batteries, 224, copyright (2013), with permission from Elsevier [137].

A summary of the corresponding specific capacity values for the 1st and 134th cycles are given in Table 14. The irreversible capacity $C_{irreversible}$ represents the amount of charge which is not recovered during the first discharging process, and the Coulombic efficiency, η, is given by the ratio ($C_{reversible}$/C_{charge}) x 100%. The efficiency, η′, was introduced in order to evaluate the cycling stability of the material, and is given by the ratio of the reversible capacity recovered after 134 cycles to that after 1 cycle, ($C_{reversible134th}$/$C_{reversible1st}$) × 100%. The averaged discharge capacities were calculated for each current step separately. All investigated ceramics exhibit promising results in terms of capacity. Our electrochemical studies clearly show no dependence of the capacity on the "free" carbon amount, and no dependence on the N/O ratio. These results are clearly in contrast to the hypothesis that a nitrogen to oxygen ratio smaller than 1 is necessary for SiC(O)N PDCs to achieve suitable capacities [129]. According to

Figure 77, there is no difference in the discharge capacity of the sample with the highest N/O ratio (SiCN5) and the sample with the lowest N/O ratio (SiCN1). Furthermore, the cycling stability of SiCN5-1100 is much better than that of sample SiCN1-1100. Nevertheless, it should be pointed out that the samples investigated in Ref. [129] contain less "free" carbon (up to 26 wt%) than the samples investigated in this work.

Table 14 First cycle charging/discharging capacity, irreversible capacity and coulombic efficiency, as well as averaged discharge capacities for different rates.

Sample	C_{charge} [mA hg^{-1}]	$C_{reversible}$ [mA hg^{-1}]	$C_{irreversible}$ [mA hg^{-1}]	η[%]	C/20_start [mA hg^{-1}]	C/10 [mA hg^{-1}]	C/5 [mA hg^{-1}]	C/2 [mA hg^{-1}]	C/1 [mA hg^{-1}]	C/20_end [mA hg^{-1}]	η′[%]
SiCN1-1100	1033	612	421	59	584	483	365	270	235	368	61
SiCN3-1100	1078	703	375	65	699	653	596	516	437	618	89
SiCN5-1100	930	486	444	52	474	397	343	281	240	420	89
SiCN6-1100	1211	724	487	60	715	659	559	430	316	582	82

4.5.3 Summary

The AC conductivity of PDCs studied by impedance spectroscopy reveals microstructure-based conduction mechanisms. The conduction in SiCN ceramics is via the "free" carbon and SiC phases in series, which is represented by two semicircles in the Nyquist plot. Conduction in SiBCN ceramics is dominated by one phase, and is thus represented by one semicircle in the Nyquist plot. Nonconducting BN forms the interfacial phase between the "free" carbon and SiC phases, and isolates the discontinuous phase from the continuous phase. Therefore, conduction in SiBCN ceramics is dominated by the continuous phase, whether it is "free carbon" or SiC.

The electrochemical study of four SiCN ceramics reveals their outstanding behavior as high capacity/high stability anode materials for lithium-ion batteries. A linear polysilazane-derived SiCN ceramic shows excellent performance in terms of cycling stability and capacity even at high currents. Furthermore, the results demonstrate that a high N/O ratio is not deleterious to the electrochemical performance of SiC(O)N ceramics. The use of different classes of precursors does not only lead to different microstructures within the ceramics, but also to differences in the electrochemical behavior. These investigations nicely bridge nanostructural features with macroscopic properties.

5. Conclusion

In this dissertation, carbon rich SiCN and SiBCN PDCs were produced from tailored polymers, including linear polysilylcarbodiimides and polysilazanes, their boron-modified counterparts, as well as branched polysilylcarbodiimide and polysilazane, aiming at obtaining ceramics with systematically varied compositions and microstructures. For synthesizing polysilazanes, the salt-free reflux route was employed using hexamethyldisilazane and dichlorosilane as the reactants and pyridine as the catalyst. NMR spectroscopic analysis confirmed the molecular structure of the polymers. Both powder and bulk ceramics were prepared. Powder samples were synthesized by directly pyrolyzing the precursors, while bulk samples were produced via warm-pressing of the polymer powder prior to pyrolysis. For thermoset polysilylcarbodiimides and polysilazanes, bulk ceramics were obtained by warm-pressing with optimized pre-crosslinking parameters. For thermoplastic polyborosilazanes, bulk samples were obtained using a modified warm-pressing with pre-pyrolyzed materials as self-fillers. These ceramics were then applied to investigate the characteristic features of carbon rich PDCs. The following conclusions can be drawn due to our studies:

1. Effects of processing route on crystallization and decomposition of PDCs

The studies of phenyl-containing poly(boro)silylcarbodiimides derived Si(B)CN powder and bulk ceramics show that the thermal stability against crystallization of the ceramics strongly depends on the processing route and the chemistry of the precursors. In SiCN and SiBCN powder samples prepared at 1400 ºC, SiC crystallites are embeded in a matrix of amorphous carbon and Si_3N_4. In contrast, the corresponding bulk ceramics remain completely amorphous at this temperature. The presence of boron in the powder SiBCN samples promotes SiC crystallization. Moreover, annealing the same powder and bulk samples up to 2100 ^{o}C, HT-TG/DTA showed that bulk ceramics exhibit less weight loss than their powder analogues, especially for SiCN. The larger surface area of the powder samples enhances the carbothermal reaction and the crystallization of silicon carbide. The boron modification was found to impede the degradation of silicon nitride.

2. Effects of structure on thermodynamic stability of PDCs

The oxide melt solution calorimetry study indicates that the ceramic derived from linear polyphenylvinylsilylcarbodiimide is energetically less stable than that of the ceramic derived from a branched polyphenylsilsesquicarbodiimide. Multinuclear NMR spectroscopy demonstrated that the structure of SiCN ceramics derived from polyphenylvinylsilylcarbodiimide consists predominantly of separate amorphous domains of silicon nitride and sp^2 carbon, while that derived from polyphenylsilsesquicarbodiimide has mixed bonds between N, C, and Si atoms at the interface between the Si_3N_4 and C nanodomains. The energetic stabilization of the latter is then attributed to the presence of such mixed bonds, the presence of which is likely due to the nature of the branched polymer used in the synthesis of these PDCs. The relative concentrations of these mixed bonds decrease upon increase of the pyrolysis temperature, along with concomitant hydrogen loss. It is suggested that the mixed bonde are stabilized via hydrogen bonds located at the interfacial regions between the Si_3N_4 and C nanodomains, and that the loss of hydrogen at higher temperature provides the entropic driving force for the destruction of the mixed bonds. The effect of pyrolysis temperature on the structural evolution of amorphous poly(boro)silazane-derived Si(B)CN was investigated as well. By MAS NMR spectroscopy, the main processes governing the structural evolution between 1100 and 1400°C are identified as (i) demixing of SiC_xN_{4-x} (x=0-4) mixed bonds, (ii) cleavage of mixed bonds at interdomain regions, and (iii) coarsening of the domain. Calorimetry studies demonstrate that this structural evolution is favorable in both enthalpy and free energy.

3. The relationship between final structure and precursor chemistry

The structure of the resultant ceramics greatly depends on the chemistry of the corresponding precursors. The results derived from MAS NMR spectroscopy support that the carbon rich amorphous Si(B)CN ceramics derived from poly(boro)silylcarbodiimides contain separate Si_3N_4 and sp^2 carbon domains, while ceramics derived from poly(boro)silazanes consist of mixed bonded SiC_xN_{4-x} (x=0-4) tetrahedra. The SiC_xN_{4-x} (x=0-4) domains consist of a core of SiN_4 tetrahedra connected to “free” carbon domains via SiN_3C, SiN_2C_2, $SiNC_3$, and SiC_4 tetrahedra. SiC_4 tetrahedra make up the most outer shell of the SiC_xN_{4-x}(x=0-4) nanodomains. The SiBCN ceramics derived from boron-modified precursors are comprised of an additional boron-containing phase which connects the Si-containing domain with that of the “free” carbon domain. SAXS results indicate that (i) for all precursors, SiC_xN_{4-x} (x=0-4) domain sizes are smaller in samples pyrolyzed at 1100 ºC than at 1400 ºC; (ii) boron-modified ceramics have smaller SiC_xN_{4-x} (x=0-4) domains than their boron-free analogues; (iii) ceramics derived from poly(boro)silylcarbodiimides have smaller SiC_xN_{4-x} (x=0-4) domains than those derived from poly(boro)silazanes; and (iv) generally, lower carbon contents contribute to the formation of larger SiC_xN_{4-x} (x=0-4) domains.

4. The AC conductivity of different phases reflecting structural information

The AC conductivity of PDCs studied by impedance spectroscopy reveals microstructure-based conduction mechanisms. Conduction in SiCN ceramics is dominated via “free” carbon and SiC phases in series, as analyzed by two semicircles in the Nyquist plot. Conduction in SiBCN ceramics is dominated by one phase, and is thus represented by one semicircle in the Nyquist plot. Nonconducting BN forms the interfacial phase between the “free” carbon and SiC phases, and isolates the discontinuous phase from the continuous phase. Therefore, conduction in SiBCN ceramics is dominated by the continuous phase, whether it is “free carbon” or SiC.

5. Electrochemical behavior for lithium-ion battery anodes

The electrochemical study of four SiCN ceramics reveals their outstanding behavior as high capacity/high stability anode materials for lithium-ion batteries. A linear polysilazane-derived SiCN ceramic shows excellent performance in terms of cycling stability and capacity, even at high currents. Furthermore, the results demonstrate that a high N/O ratio is not deleterious to the electrochemical performance of SiC(O)N ceramics. The use of different classes of precursors leads to different SiCN microstructures, which in turn explains their significant differences in electrochemical behavior.

6. Outlook

This thesis presents a systematic study of the nanodomain structures in SiCN and SiBCN PDCs synthesized from tailored polymers. New routes for polymer synthesis were explored, and their optimized bulk processing contributes valuably to the PDC field. The characterization techniques used for studying the microstructure, solid state structure, and energetic stability of these materials provide some guidelines for future studies. Detailed structural information of the ceramic nanodomains derived from the synthesized precursors can be used as reference for future studies, particularly since many common characteristics exist in the microstructure of PDCs derived from similar precursor systems.

Although this study was systematic and complete for its own purpose, additional investigations are necessary to further understand in more detail the nature of the preceramic polymers, the derived ceramics, and the polymer-to-ceramic transformation. An outline of possible investigations is recommended as follows:

1. As discussed, three types of reactions occur during pyrolysis: (i) demixing of SiC_xN_{4-x} (x=0-4) tetrahedra, (ii) diminishing of mixed bonds at interdomain regions, and (iii) coarsening of nanodomains. Calorimetry gives the total energetic consequence of these processes through the change in enthalpy. However, except for the obvious notion that nanodomain coarsening is energetically stabilizing, the energetic effects of the other processes are unclear. Whether these effects are stabilizing or destabilizing, and to what extent, remains unknown. By carrying out similar study involving materials synthesized at more intermediate pyrolysis temperatures, the structural evolution could be probed more thoroughly, in order to determine the onset of bond demixing and phase separation. Coupling these results with calorimetry studies will provide more insight into the nature of the bond demixing process.

2. The high frequency response semicircles obtained in the impedance spectroscopy investigations are not completed due to instrumental limitations. Measurements up to at least several GHz are necessary in order to obtain more detailed information. Along with improved structural characterizations of the materials, the AC conductivity contributed by each phase should be better assessed.

References

[1] P. Colombo, G. Mera, R. Riedel, and G. D. Sorarù, J. Am. Ceram. Soc. **93**, 1805 (2010).

[2] G. Mera, A. Tamayo, H. Nguyen, S. Sen, and R. Riedel, J. Am. Ceram. Soc. **93**, 1169 (2010).

[3] A. Saha, R. Raj, D. L. Williamson, and H.-J. Kleebe, J. Am. Ceram. Soc. **88**, 232 (2005).

[4] A. Saha, R. Raj, and D. L. Williamson, J. Am. Ceram. Soc. **89**, 2188 (2006).

[5] G. Mera, R. Riedel, F. Poli, and K. Müller, J. Eur. Ceram. Soc. **29**, 2873 (2009).

[6] Y. Iwamoto, W. Völger, E. Kroke, R. Riedel, T. Saitou, and K. Matsunaga, J. Am. Ceram. Soc. **84**, 2170 (2001).

[7] H. J. Seifert, H. L. Lukas, and F. Aldinger, Berichte Bunsenges. Für Phys. Chem. **102**, 1309 (1998).

[8] M. Weinmann, J. Schuhmacher, H. Kummer, S. Prinz, J. Peng, H. J. Seifert, M. Christ, K. Müller, J. Bill, and F. Aldinger, Chem. Mater. **12**, 623 (2000).

[9] H. J. Seifert, J. Peng, J. Golczewski, and F. Aldinger, Appl. Organomet. Chem. **15**, 794 (2001).

[10] R. M. Morcos, G. Mera, A. Navrotsky, T. Varga, R. Riedel, F. Poli, and K. Müller, J. Am. Ceram. Soc. **91**, 3349 (2008).

[11] R. M. Morcos, A. Navrotsky, T. Varga, D. Ahn, A. Saha, F. Poli, K. Müller, and R. Raj, J. Am. Ceram. Soc. **91**, 2391 (2008).

[12] R. M. Morcos, A. Navrotsky, T. Varga, Y. Blum, D. Ahn, F. Poli, K. Müller, and R. Raj, J. Am. Ceram. Soc. **91**, 2969 (2008).

[13] A. H. Tavakoli, J. A. Golczewski, J. Bill, and A. Navrotsky, Acta Mater. **60**, 4514 (2012).

[14] T. Varga, A. Navrotsky, J. L. Moats, R. M. Morcos, F. Poli, K. Müller, A. Saha, and R. Raj, J. Am. Ceram. Soc. **90**, 3213 (2007).

[15] A. H. Tavakoli, P. Gerstel, J. A. Golczewski, and J. Bill, Acta Mater. **58**, 6002 (2010).

[16] A. H. Tavakoli, P. Gerstel, J. A. Golczewski, and J. Bill, J. Mater. Res. **25**, 2150 (2011).

[17] Z.-C. Wang, F. Aldinger, and R. Riedel, J. Am. Ceram. Soc. **84**, 2179 (2001).

[18] P. Gerstel, A. Müller, J. Bill, and F. Aldinger, Chem. Mater. **15**, 4980 (2003).

[19] Z.-C. Wang, P. Gerstel, G. Kaiser, J. Bill, and F. Aldinger, J. Am. Ceram. Soc. **88**, 2709 (2005).

[20] R. Riedel, G. Mera, R. Hauser, and A. Klonczynski, J. Ceram. Soc. Jpn. **114**, 425 (2006).

[21] R. Riedel, G. Passing, H. Schönfelder, and R. J. Brook, Nature **355**, 714 (1992).

[22] G. Passing, H. Schönfelder, R. Riedel, and R. Brook, Br Ceram Trans **92**, 21 (1993).

[23] J. Seitz and J. Bill, J. Mater. Sci. Lett. **15**, 391 (1996).

[24] R. Haug, M. Weinmann, J. Bill, and F. Aldinger, J. Eur. Ceram. Soc. **19**, 1 (1999).

[25] Konetschny, C., J. Eur. Ceram. Soc. **19**, 2789 (1999).

[26] J. Wan, M. J. Gasch, and A. K. Mukherjee, J. Mater. Res. **15**, 1657 (2000).

[27] J. Seitz, B. Joachim, F. Aldinger, and Y. Naerheim, U.S. Patent No. 6458315 (1 October 2002).

[28] S. R. Shah and R. Raj, Acta Mater. **50**, 4093 (2002).

[29] R. Harshe, C. Balan, and R. Riedel, J. Eur. Ceram. Soc. **24**, 3471 (2004).

[30] N. Janakiraman and F. Aldinger, J. Eur. Ceram. Soc. **29**, 163 (2009).

[31] T. Jiang, A. Hill, W. Fei, Y. Wei, M. Tellam, C. Xu, and L. An, J. Am. Ceram. Soc. **93**, 3017 (2010).

[32] D. Su, Y.-L. Li, H.-J. An, X. Liu, F. Hou, J.-Y. Li, and X. Fu, J. Eur. Ceram. Soc. **30**, 1503 (2010).

[33] N. Janakiraman, M. Weinmann, J. Schuhmacher, K. Müller, J. Bill, F. Aldinger, and P. Singh, J. Am. Ceram. Soc. **85**, 1807 (2002).

[34] N. Janakiraman, A. Zern, M. Weinmann, F. Aldinger, and P. Singh, J. Eur. Ceram. Soc. **25**, 509 (2005).

[35] E. Barsoukov and J. R. Macdonald, *Impedance Spectroscopy, Theory Experiment and Applications* (John Wiley & Sons, Inc., 2005).

[36] C. Haluschka, C. Engel, and R. Riedel, J. Eur. Ceram. Soc. **20**, 1365 (2000).

[37] S. Trassl, M. Puchinger, E. Rössler, and G. Ziegler, J. Eur. Ceram. Soc. **23**, 781 (2003).

[38] D. Ahn and R. Raj, J. Power Sources **196**, 2179 (2011).

[39] R. Ralf, M. Gabriela, H. Ralf, and K. Alexander, J. Ceram. Soc. Jpn. **114**, 425 (2006).

[40] P. Colombo, *Polymer Derived Ceramics: From Nano-Structure to Applications* (DEStech Publications, Inc, 2010).

[41] B. Papendorf, K. Nonnenmacher, E. Ionescu, H.-J. Kleebe, and R. Riedel, Small **7**, 970 (2011).

[42] R. Riedel, A. Kienzle, W. Dressler, L. Ruwisch, J. Bill, and F. Aldinger, Nature **382**, 796 (1996).

[43] A. O. Gabriel, R. Riedel, S. Storck, and W. F. Maier, Appl. Organomet. Chem. **11**, 833 (1997).

[44] A. O. Gabriel, R. Riedel, W. Dressler, S. Reichert, C. Gervais, J. Maquet, and F. Babonneau, Chem. Mater. **11**, 412 (1999).

[45] R. Raj, R. Riedel, and G. D. Soraru, J. Am. Ceram. Soc. **84**, 2158 (2001).

[46] R. Riedel, E. Kroke, A. Greiner, A. O. Gabriel, L. Ruwisch, J. Nicolich, and P. Kroll, Chem. Mater. **10**, 2964 (1998).

[47] R. Riedel and A. O. Gabriel, Adv. Mater. **11**, 207 (1999).

[48] J. Schuhmacher, M. Weinmann, J. Bill, F. Aldinger, and K. Müller, Chem. Mater. **10**, 3913 (1998).

[49] J. E. Drake, R. T. Hemmings, and E. Henderson, J. Chem. Soc. Dalton Trans. 366 (1976).

[50] J. E. Drake, B. M. Glavinčevski, H. E. Henderson, and R. T. Hemmings, Synth. React. Inorg. Met.-Org. Chem. **8**, 7 (1978).

[51] P. Haag, R. Lechler, and J. Weidlein, Z. Für Anorg. Allg. Chem. **620**, 112 (1994).

[52] J. J. Moscony and A. G. MacDiarmid, Chem. Commun. Lond. 307 (1965).

[53] R. Riedel, A. Greiner, G. Miehe, W. Dressler, H. Fuess, J. Bill, and F. Aldinger, Angew. Chem. Int. Ed. Engl. **36**, 603 (1997).

[54] S. Nahar-Borchert, E. Kroke, R. Riedel, B. Boury, and R. J. P. Corriu, J. Organomet. Chem. **686**, 127 (2003).

[55] S. Nahar-Borchert, A. O. Gabriel, and R. Riedel, in *Mater. Synth.*, edited by U. Schubert, N. Hüsing, and R. M. Laine (Springer Vienna, 2004), pp. 193–198.

[56] M. Peuckert, T. Vaahs, and M. Brück, Adv. Mater. **2**, 398 (1990).

[57] D. Bahloul, M. Pereira, P. Goursat, N. S. C. K. Yive, and R. J. P. Corriu, J. Am. Ceram. Soc. **76**, 1156 (1993).

[58] Y. D. Blum, K. B. Schwartz, and R. M. Laine, J. Mater. Sci. **24**, 1707 (1989).

[59] R. J. P. C. N. S. Choong Kwet Yive, New J Chem **15**, 85 (1991).

[60] E. Kroke, Y.-L. Li, C. Konetschny, E. Lecomte, C. Fasel, and R. Riedel, Mater. Sci. Eng. R Reports **26**, 97 (2000).

[61] A. Lavedrine, D. Bahloul, P. Goursat, N. Choong Kwet Yive, R. Corriu, D. Leclerq, H. Mutin, and A. Vioux, J. Eur. Ceram. Soc. **8**, 221 (1991).

[62] D. Seyferth, G. H. Wiseman, and C. Prud'homme, J. Am. Ceram. Soc. **66**, C (1983).

[63] D. Seyferth, G. H. Wiseman, and C. Prud'homme, in *Emergent Process Methods High-Technol. Ceram.*, edited by R. F. Davis, H. P. III, and R. L. Porter (Springer US, 1984), pp. 263–269.

[64] T. Vaahs, M. Brück, and W. D. G. Böcker, Adv. Mater. **4**, 224 (1992).

[65] E. Werner, U. Klingebiel, F. Pauer, D. Stalke, R. Riedel, and S. Schaible, Z. Für Anorg. Allg. Chem. **596**, 35 (1991).

[66] W. NOLL, in *Chem. Technol. Silicones* (Academic Press, 1968).

[67] Y. D. Blum and R. M. Laine, U.S. Patent No. 4801439 (31 January 1989).

[68] Y. Blum and R. M. Laine, Organometallics **5**, 2081 (1986).

[69] C. Xu, N. Zhou, and Z. Xie, Chin. Chem. Lett. **11**, 765 (2000).

[70] J. P. Mooser, H. Nöth, and W. Tinhof, Z Naturforsch **29b**, 166 (1974).

[71] M. Weinmann, R. Haug, J. Bill, M. De Guire, and F. Aldinger, Appl. Organomet. Chem. **12**, 725 (1998).

[72] K. B. Schwartz and D. j. Rowcliffe, J. Am. Ceram. Soc. **69**, C (1986).

[73] S. Zhu, W. G. Fahrenholtz, and G. E. Hilmas, Scr. Mater. **59**, 123 (2008).

[74] S. T. Schwab, C. R. Blanchard, and R. C. Graef, J. Mater. Sci. **29**, 6320 (1994).

[75] M. Balog, J. Keckes, T. Schöberl, D. Galusek, F. Hofer, J. Krest' An, Z. Lences, J.-L. Huang, and P. Sajgalik, J. Eur. Ceram. Soc. **27**, 2145 (2007).

[76] O. Funayama, T. Kato, Y. Tashiro, and T. Isoda, J. Am. Ceram. Soc. **76**, 717 (1993).

[77] D. Seyferth and H. Plenio, J. Am. Ceram. Soc. **73**, 2131 (1990).

[78] K. Su, L. G. Sneddon, E. E. Remsen, and G. A. Zank, Chem. Mater. United States **5:4**, (1993).

[79] T. Wideman, E. Cortez, E. E. Remsen, G. A. Zank, P. J. Carroll, and L. G. Sneddon, Chem. Mater. **9**, 2218 (1997).

[80] M. Takamizawa, T. Kobayashi, A. Hayashida, and Y. Takeda, U.S. Patent No. 4604367 (5 August 1986).

[81] R. Riedel and M. Seher, J. Eur. Ceram. Soc. **7**, 21 (1991).

[82] L. L. Snead and S. J. Zinkle, Nucl. Instruments Methods Phys. Res. Sect. B Beam Interactions Mater. Atoms **191**, 497 (2002).

[83] F. Aldinger, M. Weinmann, and J. Bill, Pure Appl. Chem. **70**, 439 (1998).

[84] H.-P. Baldus, G. Passing, H. Scholz, D. Sporn, M. Jansen, and J. Göring, Key Eng. Mater. **127-131**, 177 (1997).

[85] S. Bernard, M. Weinmann, D. Cornu, P. Miele, and F. Aldinger, J. Eur. Ceram. Soc. **25**, 251 (2005).

[86] J. Bill and F. Aldinger, Adv. Mater. **7**, 775 (1995).

[87] M. Christ, G. Thurn, M. Weinmann, J. Bill, and F. Aldinger, J. Am. Ceram. Soc. **83**, 3025 (2000).

[88] M. Christ and A. Zimmermann, J. Mater. Res. **16**, 1994 (2001).

[89] A. Müller, P. Gerstel, M. Weinmann, J. Bill, and F. Aldinger, J. Eur. Ceram. Soc. 2655 (2000).

[90] R. Riedel, L. M. Ruswisch, L. An, and R. Raj, J. Am. Ceram. Soc. **81**, 3341 (1998).

[91] M. Weinmann, T. W. Kamphowe, J. Schuhmacher, K. Müller, and F. Aldinger, Chem. Mater. **12**, 2112 (2000).

[92] A. Navrotsky, Phys. Chem. Miner. **2**, 89 (1977).

[93] A. Navrotsky, Phys. Chem. Miner. **24**, 222 (1997).

[94] Y. Zhang, A. Navrotsky, and T. Sekine, J Mater Res **21**, 41 (2006).

[95] J. Liang, L. Topor, A. Navrotsky, and M. Mitomo, J Mater Res **14**, 1959 (1999).

[96] P. Kroll, J. Non-Cryst. Solids **351**, 1121 (2005).

[97] A. H. Tavakoli, P. Gerstel, J. A. Golczewski, and J. Bill, J. Mater. Res. **26**, 600 (2011).

[98] G. Mera, R. Riedel, F. Poli, and K. Müller, J. Eur. Ceram. Soc. **29**, 2873 (2009).

[99] J. Seitz, J. Bill, N. Egger, and F. Aldinger, J. Eur. Ceram. Soc. **16**, 885 (1996).

[100] S. Traßl, G. Motz, E. Rössler, and G. Ziegler, J. Am. Ceram. Soc. **85**, 239 (2002).

[101] S. Traßl, H.-J. Kleebe, H. Störmer, G. Motz, E. Rössler, and G. Ziegler, J. Am. Ceram. Soc. **85**, 1268 (2002).

[102] S. Traßl, D. Suttor, G. Motz, E. Rössler, and G. Ziegler, J. Eur. Ceram. Soc. **20**, 215 (2000).

[103] S. Traßl, G. Motz, E. Rössler, and G. Ziegler, J. Non-Cryst. Solids **293–295**, 261 (2001).

[104] J. Schuhmacher, F. Berger, M. Weinmann, J. Bill, F. Aldinger, and K. Müller, Appl. Organomet. Chem. **15**, 809 (2001).

[105] J. Bill, T. W. Kamphowe, A. Müller, T. Wichmann, A. Zern, A. Jalowieki, J. Mayer, M. Weinmann, J. Schuhmacher, K. Müller, J. Peng, H. J. Seifert, and F. Aldinger, Appl. Organomet. Chem. **15**, 777 (2001).

[106] F. Berger, A. Müller, F. Aldinger, and K. Müller, Z. Für Anorg. Allg. Chem. **631**, 355 (2005).

[107] W. Gruber, O. Starykov, W. Oppermann, and H. Schmidt, Diffus. Fundam. **8**, 9 (2008).

[108] W. Gruber, O. Starykov, and H. Schmidt, Phys. Status Solidi RRL - Rapid Res. Lett. **3**, 85 (2009).

[109] J. Haug, P. Lamparter, M. Weinmann, and F. Aldinger, Chem. Mater. **16**, 72 (2004).

[110] J. Haug, P. Lamparter, M. Weinmann, and F. Aldinger, Chem. Mater. **16**, 83 (2004).

[111] N. Resta, C. Kohler, and H.-R. Trebin, J. Am. Ceram. Soc. **86**, 1409 (2003).

[112] J. Cordelair and P. Greil, J. Eur. Ceram. Soc. **20**, 1947 (2000).

[113] C. Engel, *Elektrische Eigenschaften gefüllter Pyrolyse-Keramiken im System Si-O-C* (Shaker, 2000).

[114] S. Trassl, G. Motz, E. Rössler, and G. Ziegler, J. Non-Cryst. Solids **293–295**, 261 (2001).

[115] S. Trassl, H.-J. Kleebe, H. Störmer, G. Motz, E. Rössler, and G. Ziegler, J. Am. Ceram. Soc. **85**, 1268 (2002).

[116] J. Robertson, Adv. Phys. **35**, 317 (1986).

[117] S. Wansom, N. J. Kidner, L. Y. Woo, and T. O. Mason, Cem. Concr. Compos. **28**, 509 (2006).

[118] H. Fukui, H. Ohsuka, T. Hino, and K. Kanamura, ACS Appl. Mater. Interfaces **2**, 998 (2010).

[119] M. Graczyk-Zajac, L. Toma, C. Fasel, and R. Riedel, Solid State Ionics **225**, 522 (2012).

[120] J. Kaspar, M. Graczyk-Zajac, and R. Riedel, Solid State Ionics **225**, 527 (2012).

[121] A. M. Wilson, J. N. Reimers, E. W. Fuller, and J. R. Dahn, Solid State Ionics **74**, 249 (1994).

[122] J. R. Dahn, A. M. Wilson, W. Xing, and G. A. Zank, U.S. Patent No. US5631106 A (20 May 1997).

[123] D. Su, Y.-L. Li, Y. Feng, and J. Jin, J. Am. Ceram. Soc. **92**, 2962 (2009).

[124] Y. Feng, Electrochimica Acta **55**, 5860 (2010).

[125] J. Kaspar, G. Mera, A. P. Nowak, M. Graczyk-Zajac, and R. Riedel, Electrochimica Acta **56**, 174 (2010).

[126] M. Graczyk-Zajac, G. Mera, J. Kaspar, and R. Riedel, J. Eur. Ceram. Soc. **30**, 3235 (2010).

[127] M. Graczyk-Zajac, C. Fasel, and R. Riedel, J. Power Sources **196**, 6412 (2011).

[128] L. M. Reinold, M. Graczyk-Zajac, C. Fasel, and R. Riedel, ECS Trans. **35**, 37 (2011).

[129] D. Ahn and R. Raj, J. Power Sources **196**, 2179 (2011).

[130] I. A. Vostokov and Y. I. Dergunov, Zh Obshch Khim **47**, 1769 (1977).

[131] S. Widgeon, G. Mera, Y. Gao, S. Sen, A. Navrotsky, and R. Riedel, J. Am. Ceram. Soc. **96**, 1651 (2013).

[132] J. Liang, A. Navrotsky, V. J. Leppert, M. J. Paskowitz, S. H. Risbud, T. Ludwig, H. J. Seifert, F. Aldinger, and M. Mitomo, J. Mater. Res. **14**, 4630 (1999).

[133] H. Nguyen, Synthese und Charakterisierung von polymerabgeleiteten Si(B)CN Keramiken, Diplomarbeit, Technische Universität Darmstadt, 2010.

[134] Y. Gao, G. Mera, H. Nguyen, K. Morita, H.-J. Kleebe, and R. Riedel, J. Eur. Ceram. Soc. **32**, 1857 (2012).

[135] Y. Gao, S. J. Widgeon, T. B. Tran, A. H. Tavakoli, G. Mera, S. Sen, R. Riedel, and A. Navrotsky, Scr. Mater. **69**, 347 (2013).

[136] S. Widgeon, G. Mera, Y. Gao, E. Stoyanov, S. Sen, A. Navrotsky, and R. Riedel, Chem. Mater. **24**, 1181 (2012).

[137] L. M. Reinold, M. Graczyk-Zajac, Y. Gao, G. Mera, and R. Riedel, J. Power Sources **236**, 224 (2013).

[138] A. C. Ferrari and J. Robertson, Phys. Rev. B **61**, 14095 (2000).

[139] M. A. Pimenta, G. Dresselhaus, M. S. Dresselhaus, L. G. Cançado, A. Jorio, and R. Saito, Phys. Chem. Chem. Phys. **9**, 1276 (2007).

[140] A. C. Ferrari, J. C. Meyer, V. Scardaci, C. Casiraghi, M. Lazzeri, F. Mauri, S. Piscanec, D. Jiang, K. S. Novoselov, S. Roth, and A. K. Geim, Phys. Rev. Lett. **97**, (2006).

[141] A. C. Ferrari, Solid State Commun. **143**, 47 (2007).

[142] L. G. Cançado, K. Takai, T. Enoki, M. Endo, Y. A. Kim, H. Mizusaki, A. Jorio, L. N. Coelho, R. Magalhães-Paniago, and M. A. Pimenta, Appl. Phys. Lett. **88**, 163106 (2006).

[143] A. Sadezky, H. Muckenhuber, H. Grothe, R. Niessner, and U. Pöschl, Carbon **43**, 1731 (2005).

[144] G. A. Zickler, B. Smarsly, N. Gierlinger, H. Peterlik, and O. Paris, Carbon **44**, 3239 (2006).

[145] R. Saito, A. Jorio, A. G. Souza Filho, G. Dresselhaus, M. S. Dresselhaus, and M. A. Pimenta, Phys. Rev. Lett. **88**, 027401 (2002).

[146] M. M. Lucchese, F. Stavale, E. H. M. Ferreira, C. Vilani, M. V. O. Moutinho, R. B. Capaz, C. A. Achete, and A. Jorio, Carbon **48**, 1592 (2010).

[147] E. H. Martins Ferreira, M. V. O. Moutinho, F. Stavale, M. M. Lucchese, R. B. Capaz, C. A. Achete, and A. Jorio, Phys. Rev. B **82**, 125429 (2010).

[148] A. Jorio, E. H. Martins Ferreira, L. G. Cançado, C. A. Achete, and R. B. Capaz, in *Phys. Appl. Graphene - Exp.*, edited by S. Mikhailov (InTech, 2011).

[149] H.-J. Kleebe, Phys. Status Solidi **166**, 297 (1998).

[150] C. Turquat, H.-J. Kleebe, G. Gregori, S. Walter, and G. D. Sorarù, J. Am. Ceram. Soc. **84**, 2189 (2001).

[151] H. Bréquel, J. Parmentier, S. Walter, R. Badheka, G. Trimmel, S. Masse, J. Latournerie, P. Dempsey, C. Turquat, A. Desmartin-Chomel, L. Le Neindre-Prum, U. A. Jayasooriya, D. Hourlier, H.-J. Kleebe, G. D. Sorarù, S. Enzo, and F. Babonneau, Chem. Mater. **16**, 2585 (2004).

[152] A. H. Tavakoli, P. Gerstel, J. A. Golczewski, and J. Bill, J. Non-Cryst. Solids **355**, 2381 (2009).

[153] S. Martinez-Crespiera, E. Ionescu, H.-J. Kleebe, and R. Riedel, J. Eur. Ceram. Soc. **31**, 913 (2011).

[154] A. Müller, P. Gerstel, M. Weinmann, J. Bill, and F. Aldinger, J. Eur. Ceram. Soc. **21**, 2171 (2001).

[155] A. H. Tavakoli, Thermodynamic and Kinetic Studies on the Thermal Stability of Amorphous Si-(B-)C-N Ceramics, 2010.

[156] J. Dürr, S. Schempp, P. Lamparter, J. Bill, S. Steeb, and F. Aldinger, Solid State Ionics **101**, 1041 (1997).

[157] A. Saha, R. Raj, and D. L. Williamson, J. Am. Ceram. Soc. 060428035142017 (2006).

[158] E. Leonova, J. Grins, M. Shariatgorji, L. L. Ilag, and M. Edén, Solid State Nucl. Magn. Reson. **36**, 11 (2009).

[159] E. Kolehmainen, K. Laihia, J. Korvola, V. S. Kaganovich, M. I. Rybinskaya, and Z. A. Kerzina, J. Organomet. Chem. **487**, 215 (1995).

[160] V. A. Du, G. N. Stipicic, and U. Schubert, Eur. J. Inorg. Chem. **2011**, 3365 (2011).

[161] A. Scarmi, G. D. Sorarù, and R. Raj, J. Non-Cryst. Solids **351**, 2238 (2005).

[162] Y. H. Sehlleier, A. Verhoeven, and M. Jansen, J. Mater. Chem. **17**, 4316 (2007).

[163] W. J. Gammon, D. I. Malyarenko, O. Kraft, G. L. Hoatson, A. C. Reilly, and B. C. Holloway, Phys. Rev. B **66**, 153402 (2002).

[164] H. Imai, P. K. Babu, E. Oldfield, A. Wieckowski, D. Kasuya, T. Azami, Y. Shimakawa, M. Yudasaka, Y. Kubo, and S. Iijima, Phys. Rev. B **73**, 125405 (2006).

[165] C. Gervais, F. Babonneau, L. Ruwisch, R. Hauser, and R. Riedel, Can. J. Chem. **81**, 1359 (2003).

[166] C. W. Bale, P. Chartrand, S. A. Degterov, G. Eriksson, K. Hack, R. Ben Mahfoud, J. Melançon, A. D. Pelton, and S. Petersen, Calphad **26**, 189 (2002).

[167] R. A. Robie and B. S. Hemingway, *Thermodynamic Properties of Minerals and Related Substances at 295.15K and 1 Bar (105 Pa) Pressure and at Higher Temperatures* (1995).

[168] S. Widgeon, G. Mera, Y. Gao, S. Sen, A. Navrotsky, and R. Riedel, J Am Ceram Soc (2013).

[169] G. Beaucage, S. Rane, D. W. Schaefer, G. Long, and D. Fischer, J. Polym. Sci. Part B Polym. Phys. **37**, 1105 (1999).

[170] N. Larouche and B. L. Stansfield, Carbon **48**, 620 (2010).

[171] J. R. Macdonald, *Impedance Spectroscopy: Emphasizing Solid Materials and Systems* (Wiley, 1987).

[172] K. Wang, B. Ma, Y. Wang, and L. An, J. Am. Ceram. Soc. **96**, 1363 (2013).

Curriculum Vitae

Yan GAO
Address： Rabenaustr. 9
64293, Darmstadt
Germany
E-mail：gao@materials.tu-darmstadt.de

Personal status

Gender: Female
Date of Birth: 04/24/1981
Citizenship: China

Scientific background

- **1999-2003 Bachelor in Materials Science & Engineering, Tsinghua University, P.R. China**

Thesis: Gel-casting of fused silica ceramic

Advisor: Prof. Zhipeng Xie

- **2003-2006 Master in Materials Science & Engineering, Tsinghua University, P.R. China**

Thesis: Injection molding of silicon carbide and zirconia and the removal of water-soluble binders

Advisor: Prof. Zhipeng Xie

- **2010-2013 Ph.D. in Material Science, Technische Universität Darmstadt (TUD), Germany**

Thesis: Nanodomain structure and energetics of carbon rich SiCN and SiBCN polymer-derived ceramics

Advisor: Prof. Ralf Riedel

Research experiences

- **2010-2013 Research Assistant, Universität Darmstadt**
  - Synthesized the preceramic polymers with tailored compositions and structures, and the isotope counterparts.
  - Developed the processing technology that can make compact bulk ceramics derived from polymers.
  - Studied the structural evolution of polymer-derived ceramics depending on their unique polymer chemistry. Investigated the influenc of the nanostructures of polymer-

derived amorphous ceramics on their thermodynamic stabilities.

  - Investigated the electrical and electrochemical behavior of amorphous ceramics derived from different precursors. Developed fundamental understandings of these properties.

- **03-04/2011 and 08-09/2012 Research Assistant, University of California, Davis**
  - Investigated on the thermal stability of amorphous PDCs using oxidative drop solution calorimetry and high-temperature TGA.
  - Studied nanodomain structures of amorphous PDCs with solid state MAS NMR.
- **2003-2006 Research Assistant, Tsinghua University**
  - Developed a new organic system based on partially water-soluble binders and associated debinding technique for injection molding of ceramics. The efficiency of the debinding process was greatly improved compared to the traditional process using wax based binders. Optimized the process of injection molding. Improved the mechanical properties and micro-structures of molded parts.
  - Developed a novel processing technique for making fine and/or bio-compatible ceramic components/parts, such as dental posts, dental brackets, optical fiber sleeves, fan shafts and razors. The technique has been transferred to industries and the fabricated components/parts have been put into applications in hospitals and industries.
- **2003 Research Assistant, Tsinghua University**
  - Studied and improved colloidal system for Gel-casting process applications.
  - Improved dispersibility of the colloidal suspension by optimizing process parameters, such as pH value, particle size and its distribution, etc. Fabricated amorphous fused silica ceramic with good mechanical properties.

Working experience

- 2006-2010 Engineer, China Aerospace Science and Technology Corporation
  - Carried out the investigation on the development and potential use of composites.
  - Studied the functionality of space materials, complying with the safe applications in the extreme space environment, such as high/low temperature, thermal cycling, vacuum and radiation, etc.
  - Served as a technical support for qualification approval of the manufacturers of space used composite materials.
- 2005 Internship, Foxconn Technological Corporation
  - Developed a new organic system for injection molding, which reduced the manudacturing cost.

- ➢ Fabricated zirconia optical fiber connectors, reduced the defects of products.

Activities

- Teaching the lab courses of "Polymer-derived SiOC ceramic" and "Silicon Nitride ceramic" in 2011/2012/2013 at TU Darmstadt.
- Supervise the "School girls" program in 2010/2011/2012, at TU Darmstadt

Publications

- ***Ph.D.***

1) **Y. Gao**, G. Mera, H. Nguyen, K. Morita, H-J. Kleebe, and R. Riedel. Processing route dramatically influencing the nanostructure of carbon-rich SiCN and SiBCN polymer-derived ceramics. Part I: Low temperature thermal transformation *J. Eur. Ceram. Soc.*, 32[9], 1857-1866 (2012).

2) **Y. Gao**, S. Widgeon, T. Tran, A. H. Tavakoli, G. Mera, S. Sen, R. Riedel, and A. Navrotsky. Effect of Demixing and Coarsening on the Energetics of Poly(boro)silazane-Derived Amorphous Si-(B-)C-N Ceramics, Scr. Mater. 69, 347(2013).

3) S. Widgeon, G. Mera, **Y. Gao**, E. Stoyanov, S. Sen, A. Navrotsky, and R. Riedel. Nanostructure and Energetics of Carbon-Rich SiCN Ceramics Derived from Polysilylcarbodiimides: Role of the Nanodomain Interfaces. *Chem. Mater.*, 24, 1181 (2012).

4) S. Widgeon, G. Mera, **Y. Gao**, S. Sen, A. Navrotsky, and R. Riedel. Effect of precursor on speciation and nanostructure of SiBCN polymer derived ceramics. *J. Am. Ceram. Soc.*, 96, 1651 (2013).

5) L. M. Reinold, M. Graczyk-Zajac, **Y. Gao**, G. Mera, and R. Riedel. Carbon-rich SiCN ceramics as high capacity/high stability anode material for lithium ion batteries. *Journal of Power Sources*, 236, 224–229 (2013).

6) **Y. Gao**, M. Bazarjani, S. Sen, R. Riedel. Nanodomain Characteristic in Polymer-Derived Si(B)CN Ceramics. To be submitted.

7) **Y. Gao**, H. Nguyen, Y. Xu, G. Buntkowsky and R. Riedel. Development of Thermoplastic Polyborosilazanes for Polymer-Derived SiBCN Ceramic Monoliths. In preparation.

- ***Master & Bachelor***

8) **Y. Gao**, K. Huang, Z. Fan, and Z. Xie. Water-soluble binder based Injection molding of zirconia. Key Eng. Mater., 336-338, 1017-1020, 2007.

9) **Y. Gao**, Z. Xie, and Y. Huang. Gel-casting of fused silica ceramic and its sintering process. Rare Metal Mater. and Eng., 34, 438-442, 2005.

10) J. Luo, Z. Yi, B. Xiao, **Y. Gao**, Z. Xie, J. Li, and Y. Huang. Injection molding of ultra-fine zirconia(Y-TZP) powders. J. Ceram. Proc. Tech., 7[1], 14-19, 2006.

11) Z. Xie, B. Xiao, **Y. Gao**, J. Li, and Y. Huang. Injection molding of high performance ceramic parts. Adv. Manuf. Mater. Appl. Tech., 4, 13-16, 2005.

- ***Conference Presentation***

12) Y. Gao, G. Mera, H. Nguyen, K. Morita, H-J. Kleebe, and R. Riedel. Processing of Bulk Carbon-Rich SiCN and SiBCN Ceramics Derived from Polysilylcarbodiimides and Polyborosilylcarbodiimides Presentation in "the seventh Intenational Conference on High-performance Ceramics", Xiamen, China, Nov. 4-7, 2011.

- ***Other Publications:***

13) As Editor, English-Chinese Dictionary of Composite Materials Technology, ISBN 7-5025-9295-4, Chemical Industry Press, Jan. 2007, the First Edition.

14) **Y. Gao**, Plan for the aerospace composite materials standards, Standards and Civilian Aerospace, 2007.

15) **Y. Gao** et al. Space systems - safety and compatibility of materials - Part 1-Part 5: Aerospace Standards of China.

16) **Y. Gao**, Aerospace composites materials assurance practice, Aerospace Standardization, 2009(4), pp. 43~46.

17) Z. Gao and **Y. Gao**, Evaluation requirements for qualified composite material supplier of space products, Aerospace Standards of China.

18) H. Zhang, Y. Zhu, J. Yan, Z. Gao, and **Y. Gao**. The classification and code of space materials, Aerospace Standards of China.

Awards & Honors

- 2000 Third Class Kang-hong Scholarship for Excellent Students of Tsinghua University.
- 2005 Third Class Scholarship for Excellent Integrated Graduate Students of Tsinghua University.
- 2005 Excellent League Member of Tsinghua University.
- 2007 Outstanding Employee of CASI
- 2008 Advanced Individual of CASI
- 2009 Second Class Technical Achievement of CASI

M. Sc. Yan Gao

Rabenaustr. 9

64293 Darmstadt

Eidesstattliche Erklärung

Hiermit erkläre ich an Eides statt, dass ich die vorliegende Dissertation selbstständig und nur mit den angegebenen Hilfsmitteln angefertigt habe. Von mir wurde weder an der Technischen Universität Darmstadt noch einer anderen Hochschule ein Promotionsversuch unternommen.

Darmstadt, den 09.10.2013

Yan Gao